UNIVERSITY OF SOUTHAMPTON

# Radio Observations of the UK Deep X-ray Survey Area

Nick Seymour

Submitted for the degree of Doctor of Philosophy

DEPARTMENT OF PHYSICS AND ASTRONOMY
FACULTY OF SCIENCE

November 27, 2002

UNIVERSITY OF SOUTHAMPTON

ABSTRACT

FACULTY OF SCIENCE

DEPARTMENT OF PHYSICS AND ASTRONOMY

Doctor of Philosophy

# Radio Observations of the UK Deep X-ray Survey Area

by Nick Seymour

In this thesis results of VLA radio observations of the UK Deep X-ray Survey Area are presented. To a $4\sigma$ peak flux detection limit at 1.4 GHz of 30 $\mu$Jy/beam a total of 462 sources are found. The log(N)-log(S) differential source count confirms the results of other deep radio surveys at 1.4 GHz showing an upturn in source counts below 1 mJy. Data at 4.86 GHz is also available to a $3\sigma$ peak flux detection limit of 100 $\mu$Jy/beam which found 116 sources of which 53 had 1.4 GHz counterparts allowing two-point radio spectral indices to be accurately determined. For other sources at either frequency it possible to determine upper or lower limits to the two-point radio spectral index.

The correlation of the radio sources with the deep optical data is also presented ($R \sim 27$ and $B \sim 26.5$). In $R-$band 83% of the radio sources had optical counterparts and 64% had $B-$band counterparts. The radio sources show a wide range of radio to optical flux ratios ($0.01 - 10^4$) consistent with many different types of sources with a large range of properties contributing to the radio background. For radio sources with optical $R-$band counterparts with $R \leq 20.5$, 96 out of 124 have optical spectra. These optical counterparts are dominated by Narrow Emission Line galaxies, but also include quasars, normal galaixes and clusters.

From a deep *Chandra* survey 68 of 214 X-ray sources are found to have radio counterparts. Examples of how a well sampled spectral energy distribution is vital in understanding the emission mechanisms of the faint X-ray/radio population are given. It is found that many classes of object make up the X-ray background radiation including quasars, BL Lacs, starburst galaxies, clusters, normal galaxies and galaxies with both AGN and starburst activity.

# Contents

# List of Figures

# List of Tables

# Preface

The work presented in this thesis has been carried out by the author, in collaboration with others, at the University of Southampton between October 1999 and October 2002. This research has been performed as part of a collaborative multi-wavelength extra-galactic survey. Chapter 2 presents the VLA 1.4 GHz radio data of which the A-configuration was calibrated by Tom Muxlow and the B-configuration by Ian M$^{c}$Hardy. All subsequent analysis of the radio data was performed by the author.

The $R-$band optical data presented in chapter 4 was obtained and reduced by Tadafumi Takata and Kaz Sekiguchi. The $B-$band data in the same chapter was donated to the survey team by Scott Croom. However correlation of the radio data with the optical data was solely performed by the author.

The *Chandra* data in chapter 5 was taken from M$^{c}$Hardy et al. (2002a), but again the correlation of the radio and X-ray data was performed by the author.

For further copies or any queries please contact the author at ns@astro.soton.ac.uk or go to the author's website (http://www.astro.soton.ac.uk/ ns/) to download a hard copy or to view the electronic version.

NS 28/11/02

# Chapter 1

# Introduction

In this chapter I provide a brief overview of the history of radio astronomy followed by a description of the Unified AGN Model. The details and results of the original UK Deep *ROSAT* X-ray Survey are presented. The content and structure of the thesis is then outlined.

## 1.1 A Brief History of Radio Astronomy

### 1.1.1 Early Origins

Radio Astronomy can trace its history back over a hundred years. After Maxwell had formulated his equations of electromagnetism based on the work of Faraday and others, experimentation in the transmission and receiving of electromagnetic waves began.

There is evidence (Ghigo, 2002) that Edison first proposed observing the sun with the aim of detecting emission of electromagnetic waves at long wavelengths. Several experiments were attempted (Sir Oliver J. Lodge 1897-1900, Wilsing and Scheiner 1896, Nordman 1900), but all were unsuccessful due to lack of sensitivity. Experiments were further discouraged by theoretical predictions. Max Planck's explanation of the thermal radiation curve by the quantised nature of light implied that the emission of electromagnetic radiation from the Sun at long wavelengths would be very faint. Also Oliver Heaviside predicted that the ionisation of the outer atmosphere would not only reflect radio waves internally, but also externally as well. After little success in detecting extra-terrestrial sources of radio waves scientific interest waned in the 1920s.

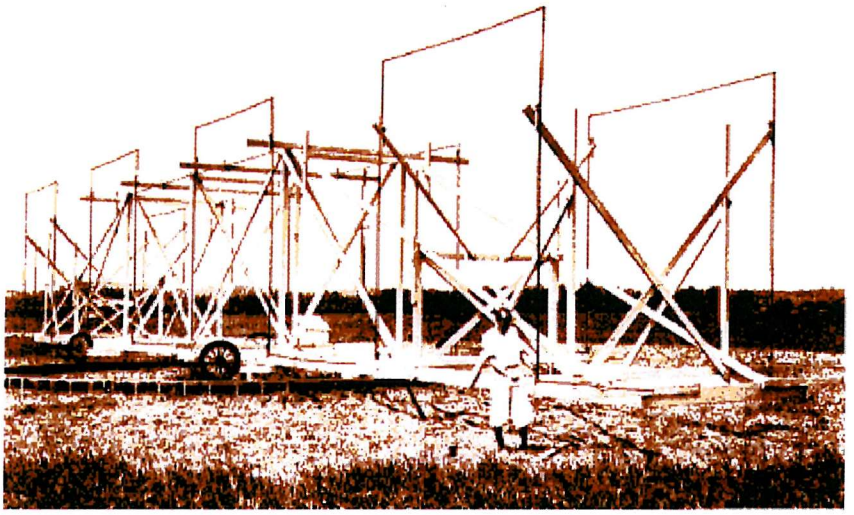

Figure 1.1: Karl Jansky and his rotating wire frame Antenna

Short wave radio technology was kept alive by ham radio operators who were not allowed to use longer wavelengths which were reflected most by the ionosphere and reserved for commercial uses. Forced to be inventive these amateur radio operators advanced the technology of short-wave transmitters and receivers. As the use of radio communications grew commercial companies began to look at using the shorter wavelengths. Karl Jansky was working on the identification of sources of interference at radio wavelengths for Bell Telephone Laboratories in 1931 (at 15-30MHz frequencies) when he succeeded where others had failed. Jansky was using a rotating wire frame antennae that allowed him to follow the source of any static, and he detected three separate groups of static: local thunderstorms, distant thunderstorms and a steady hiss-type static of unknown origin. Jansky noticed that this third type of noise started at the same time each day. After monitoring it for a few weeks, he noticed that it started 4 minutes earlier each day. This was a clue that he was detecting emission outside the Solar System (a sidereal day is 4mins less than a solar day). Jansky quickly established that this source of radio waves was located at the galactic centre.

Jansky wrote 3 papers on his findings (Jansky 1982a,b & c), but his work was largely ignored by the astronomical community. The field of radio astronomy was continued by another American radio engineer, Grote Rebe. He had heard of Jansky's work and in 1937 built a 9.5m parabolic dish in his own backyard. Rebe operated his dish for many years looking for astronomical sources of radio waves at several wavelengths. Working alone he finally detected emission at about 7 GHz from the galactic plane and was later able to produce the first radio map of the sky.

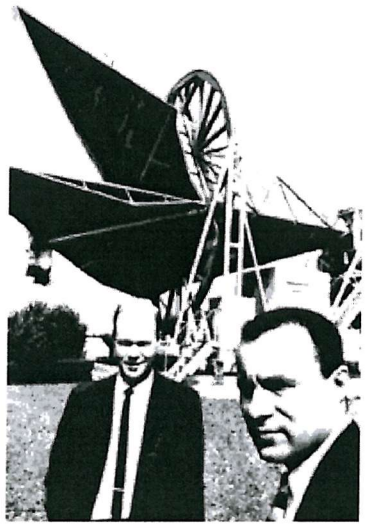

Figure 1.2: Penzias and Wilson in front of their horn antenna

### 1.1.2 Post Second World War

The Second World War had accelerated the development of radio with the need for better communications and accurate early warning radar. A scientist working with the British Army Operational Research Group, J.S. Hey, was working on sources of jamming when in 1942 he concluded that the Sun was a source of intense radio emission. Soon after, G.C. Southworth made the first successful observations of thermal radio emission from the sun at centimetre Giga-Hertz frequencies. After the war many of these scientists returned to academia to continue their study of extraterrestrial radio sources. In 1946 Hey, along with S.J. Parsons and J.W. Phillips observed fluctuations in the intensity of cosmic radio waves from the constellation Cygnus. In the next ten years thousands of discrete radio sources were identified, including galaxies and supernovae.

In 1944 J Oort and his student, H.C. Van de Hulst, predicted that one of the main sources of radio emission might be the hyperfine transition of neutral hydrogen in the ground state at 1420 MHz, or 21cm (hydrogen being the most abundant element universe). The 21cm emission line due to hydrogen was finally detected by H Ewen and E Purcell in 1951 which they used to map the galaxy.

### 1.1.3 The Discovery of the Cosmic Microwave Background

Later on new discoveries in radio astronomy were again being made serendipitously. Arno Penzias and Robert Wilson were assigned by Bell Laboratories to trace radio noise that was interfering with the development of communications satellites. They

found that there was always a non-zero noise strength no matter where they pointed their antenna. Having convinced themselves that the signal was real and not from any known galactic sources they concluded that the source of this microwave radiation must be extragalactic. Astronomers had been considering looking for radiation at microwave wavelengths ever since George Gamow predicted isotropic radiation left over from the big bang that would have cooled to a few degrees above absolute zero. This cosmic microwave background (CMB) radiation matched that predicted by Gamow and added further credence to the Big Bang theory.

### 1.1.4 The Development of Multi-Element Interferometers

Since the end of the war, radio receivers had been developed in many places across the world including Jodrell Bank, USA, Australia and the Netherlands. The long wavelengths of radio waves led to poor resolution of the sky from individual radio dishes. A technique was soon developed where two or more dishes observed a radio source in the sky simultaneously, effectively acting like a single dish with a size equivalent to the baseline separation of the individual dishes. The signals from each dish are correlated and sophisticated mathematical techniques are used to reconstruct the sky brightness distribution.

### 1.1.5 The Future; eVLA, eMERLIN and the SKA

The two great northern hemisphere radio arrays, MERLIN and the VLA are both undergoing upgrades to become eMERLIN and eVLA respectively. For MERLIN the main improvement will be new high-frequency receivers and a new correlator which in combination with the newly resurfaced 76m Lovell telescope, will give a 30-fold increase in sensitivity. The eVLA project involves the upgrade of many of the electronics including the receivers and the addition of possibly up to eight new antennae increasing the maximum baseline to 250 km. These developments will lead to approximately a factor of 10 improvement in both resolution and sensitivity of the VLA.

These arrays will be both superseded by the Square Kilometre Array project (SKA) due to begin construction in 2010. The SKA is so called as it is intended to be an array of antennae with a collecting area of one square kilometre and is an international project undergoing development with the involvement of all the major astronomical communities world wide.

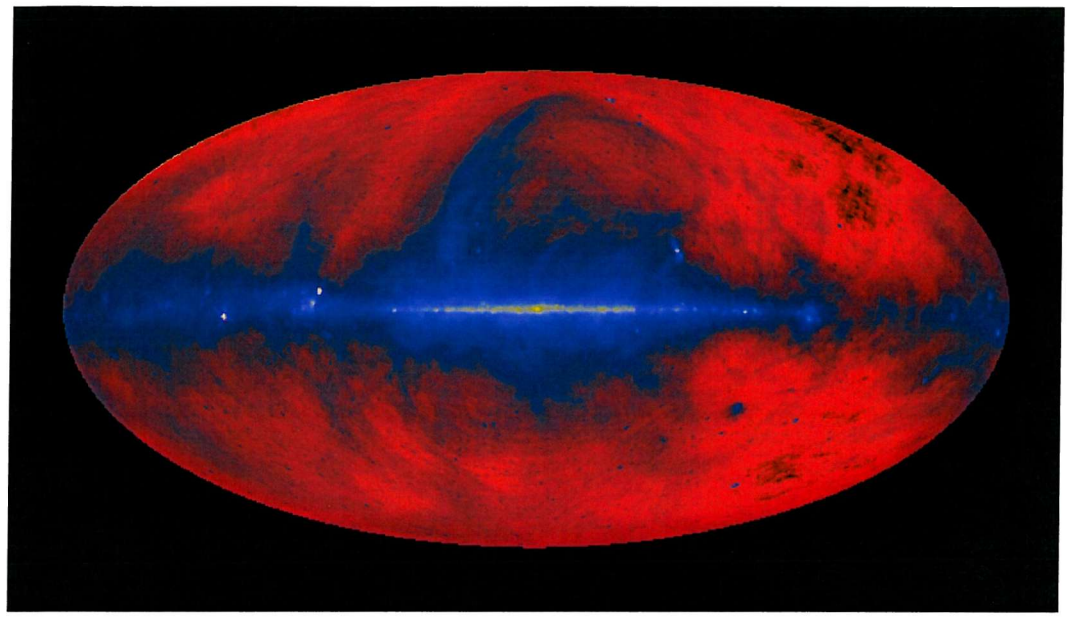

Figure 1.3: A map of the radio sky at 408 MHz in galactic coordinates (C. Haslam et al., 2002).

## 1.2 The Unified Active Galactic Nuclei Model

Although not completely satisfactory the unification scheme of Active Galactic Nuclei (AGN) does seem to explain the many observed features of extragalactic sources that were once thought to be completely different types of objects. To help illustrate this scheme a brief taxonomy of various types of AGN is presented. Historically the differences between the main classes of AGN (Seyferts and quasars) are due to the methods by which they were first isolated. Undoubtedly some of the differences noted below are due more to the way they are observed than fundamental differences between the types.

### 1.2.1 Seyfert Galaxies

Seyfert galaxies were first selected as being different to normal galaxies because they had a bright point-like core, although the host spiral galaxy is clearly visible. Optical spectra of the cores are found to be dominated by high excitation nuclear emission lines which are very broad (full width at half maximum, FWHM, $1000 - 10000\,\mathrm{km\,s^{-1}}$) with the hydrogen lines broader still. Two conclusions were drawn from these unusual spectra. As the nuclei are unresolved they must be less than 100 pc in size. If the material in the nucleus is gravitationally bound then its mass must be very high. From simple virial arguments (Woltjer, 1959):

$$M \approx \frac{v^2 r}{G} \tag{1.1}$$

The velocity dispersion obtained from the widths of the emission lines is of the order of $10^3\,\mathrm{km\,s^{-1}}$ (if assumed to be due to Doppler broadening). With an upper limit on the radius of $\leq 100\,\mathrm{pc}$ and with a lower limit from the fact that the emission lines are typical of a low density gas ($r \sim 1\,\mathrm{pc}$) we have a constraint on the mass of the nucleus:

$$M \approx 10^{9\pm1} M_\odot \tag{1.2}$$

It became clear that there were two types of Seyfert galaxies based on their optical spectra (which is now the defining characteristic, but most are still spiral galaxies). Some Seyferts have two sets of emission line, superposed on one another. The first set of lines has widths of $100 - 1000\,\mathrm{km\,s^{-1}}$ which are characteristic of a low density ionised gas (electron density, $n_e \approx 10^{3-6}\,\mathrm{cm^{-3}}$) and are known as 'narrow lines'. Another set of broad lines is seen in permitted lines only (Freyer, 2002). These 'broad lines' have widths of $1000 - 10000\,\mathrm{km\,s^{-1}}$ and the absence of forbidden lines indicates that the gas is of higher density ($n_e \geq 10^9\,\mathrm{cm^{-3}}$) . Both sets of lines are seen in type 1 Seyfert galaxies, but only the narrow lines are present in type 2 Seyferts (Khachikian and Weedman, 1974).

Examples of Seyfert galaxy spectra are presented in figures 1.4, 1.5 and 1.6. They are taken from Bradley Peterson's 'An Introduction to Active Galactic Nuclei'. Figure 1.4 shows the optical spectrum and figure 1.5 the ultraviolet spectrum of the Seyfert 1 galaxy NGC 5548. The prominent broad lines are labelled, as are strong absorption features of the host galaxy spectrum. The vertical scale is expanded in the lower panels to show the weaker features.

Figure 1.6 shows the optical spectrum of the Seyfert 2 galaxy NGC 1667, with important emission lines identified (Ho, Filippenko, and Sargent 1993). Some strong absorption lines that arise in the host galaxy rather than the AGN itself are also identified. This spectrum can be compared with the spectrum shown in figure 1.6. The units are: wavelength (Å) for the x-axis and flux ($\mathrm{erg\,cm^{-2}\,s^{-1}\,\AA^{-1}}$) for the y-axis.

In some extragalactic sources that were originally thought to be Seyfert 2s weak broad lines were eventually detected particularly in polarised light (Antonucci and Miller, 1985). It is clear that the distinction between type 1s and type 2s is not absolute. Some observations of Seyfert 1s have shown that the broad line components can sometimes fade dramatically, almost disappearing (Penston and Perez, 1984). Osterbrock (1981) introduced intermediate sub-classes of Seyferts: 1.5, 1.8 and 1.9

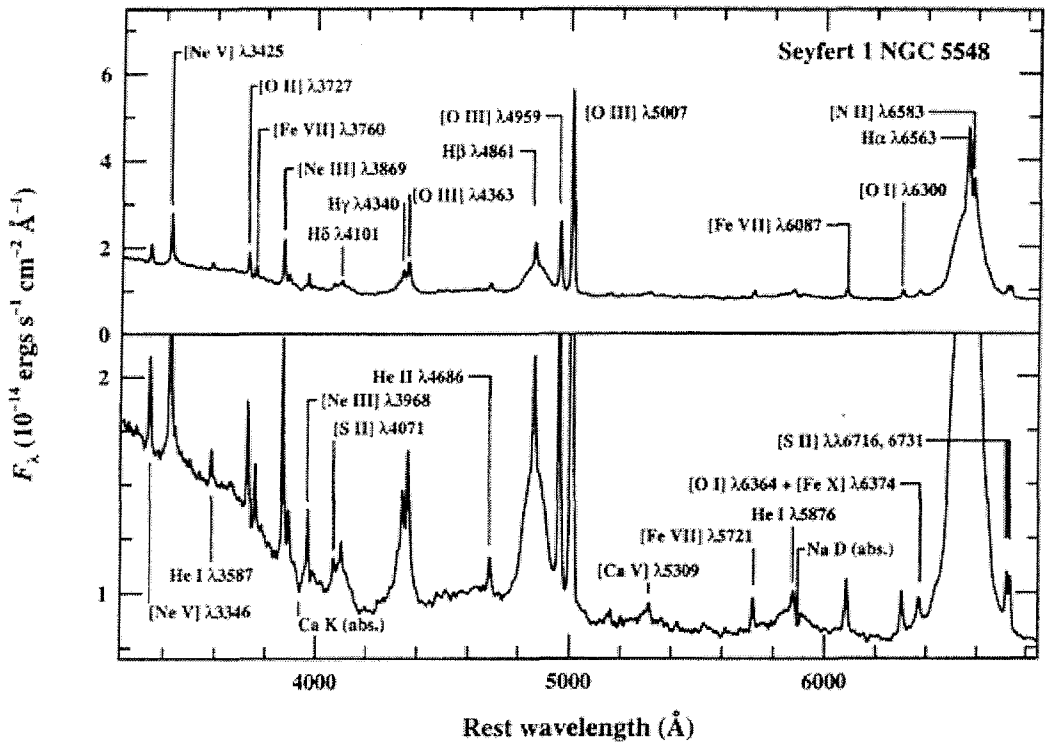


Figure 1.4: The optical spectrum of the Seyfert 1 galaxy NGC 5548. The prominent broad lines are labelled, as are strong absorption features of the host galaxy spectrum. The vertical scale is expanded in the lower panel to show the weaker features.The full width at half maximum (FWHM) of the broad components is about $5900\,\mathrm{km\,s^{-1}}$, and the width of the narrow components is about $400\,\mathrm{km\,s^{-1}}$. The strong rise shortward of 4000Å is the long-wavelength end of the 'small blue bump' feature which is a blend of Balmer continuum and FeII line emission. This spectrum is the mean of several observations made during 1993 with the 3-m Shane Telescope and Kast spectrograph at the Lick Observatory. Image taken from Bradley Peterson's 'An Introduction to Active Galactic Nuclei'.

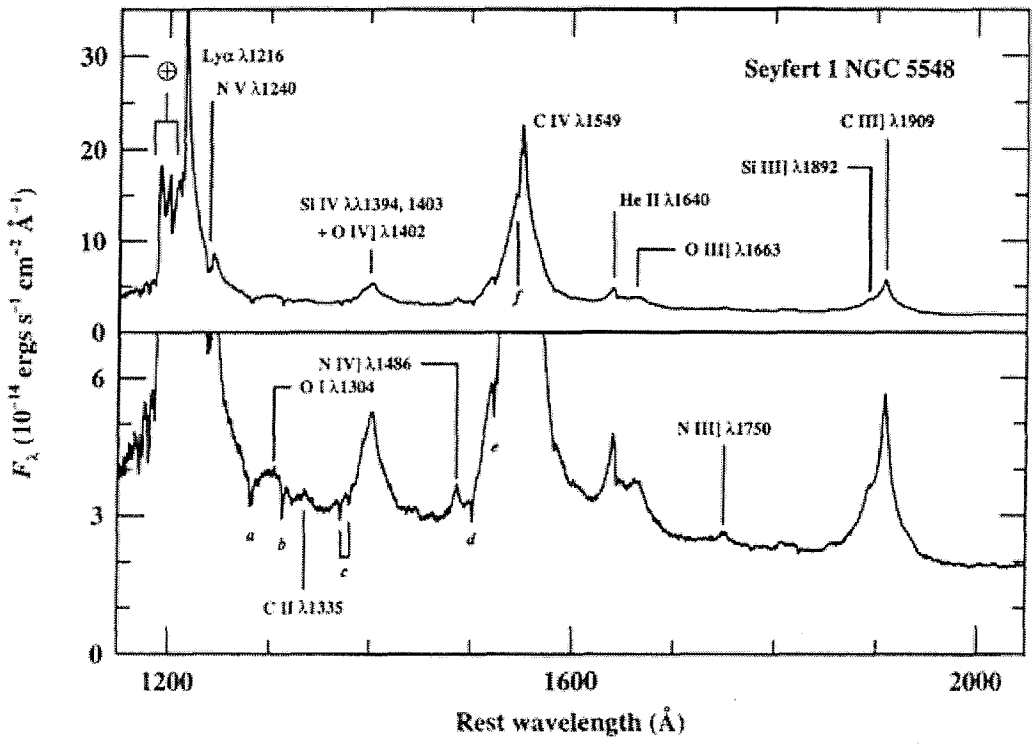


Figure 1.5: The ultraviolet spectrum of the Seyfert 1 galaxy NGC 5548. The prominent broad lines are labelled. The emission labelled with the Earth symbol (⊕) arises in the extended upper atmosphere of the Earth and is known as 'geocoronal' emission. Most of the labelled absorption features arise in our own Galaxy and thus appear blueshifted from their rest wavelengths since the spectrum has been corrected for the redshift of NGC 5548 (z = 0.017). The labelled absorption features are OII λ1302 (a), CII λ1335 (b), SiIV λλ1394, 1403 (c), SiII λ1527 (d), and CIV λλ1548, 1551 (e). Another weak CIV λ1548, 1551 doublet (f) is only slightly displaced shortward of line centre and presumably arises in NGC 5548 itself. This spectrum is the mean of several observations obtained with the Faint Object Spectrograph on the Hubble Space Telescope in 1993. Image taken from Bradley Peterson's 'An Introduction to Active Galactic Nuclei'.

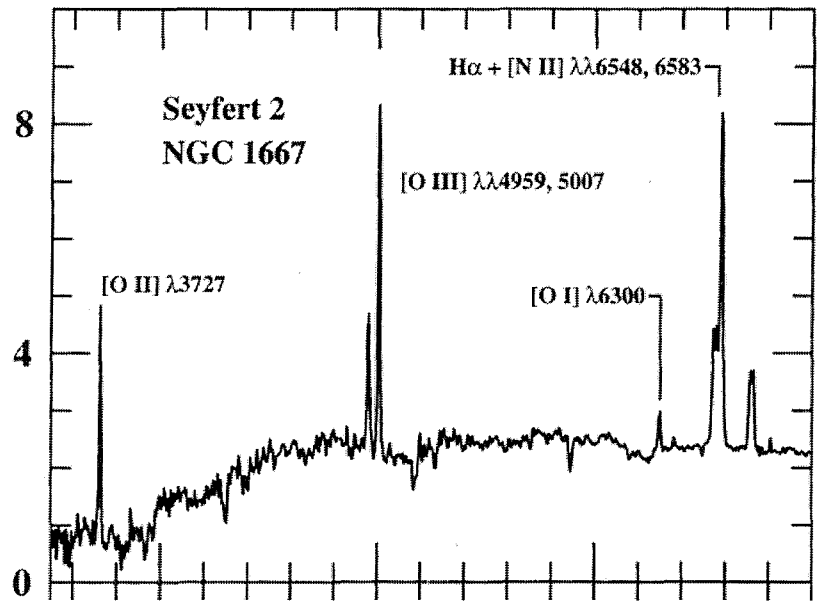


Figure 1.6: The optical spectrum of the Seyfert 2 galaxy NGC 1667 is shown, with important emission lines identified (Ho, Filippenko, and Sargent 1993).

where numerically larger sub-classes have weaker broad line components relative to the narrow lines.

### 1.2.2 Quasars

Quasars were originally identified as unresolved optical counterparts to sources from the first radio surveys. Although most radio sources were resolved galaxies, some only had star-like counterparts and were dubbed 'quasi-stellar radio sources', or quasar. Optical spectra of these early quasars showed very broad emission lines which couldn't initially be identified, see figures 1.7 and 1.8. It was eventually realised that these lines were highly redshifted relative to most objects known at the time. These redshifts were interpreted as being due to the cosmological expansion of the universe. If this was the case, then their intrinsic luminosities must be very large, approximately 100 × more luminous than local spiral galaxies (Schmidt 1963, and Greenstein and Matthews, 1963).

Schmidt (1969) defined the properties of quasars as follows:

1. star-like object identified with radio source
2. time-variable continuum flux
3. large UV flux

4. broad emission lines

5. large redshifts

Although not all objects we now call AGN have these properties this list indicated a way for quasars to be found without searching through fields of radio sources. The relatively large UV fluxes compared to stars meant that any objects with a relative excess in a $U-$band filter compared to a $B-$band filter was worth investigating. This method along with others was so successful that 'radio-quiet' quasars now make up over 90% of the quasar population.

Another of the modern characteristics of a quasar is their very broad spectral energy distribution (SED). Quasars are amongst the most luminous objects in the sky at any wavelength. Their SEDs are so unlike stars or galaxies that they cannot be described in terms of thermal processes. Non-thermal processes, primarily synchrotron radiation, are believed to be at work.

#### 1.2.2.1 Radio Properties of Quasars

The morphology of quasars at radio wavelengths can generally be described by two components: a compact, normally unresolved component at the optical position of the quasar and an extended component which normally takes the form of symmetric lobes about the optical centre. The extended component can be divided in two classes based on luminosity and morphology (Fanaroff and Riley, 1974). FR I sources are generally weaker and have the bright emission of the lobes near the centre and with decreasing surface brightness towards the edge. FR II sources have regions of enhanced emission either at the edge of the radio structure or embedded in it. Compact radio sources are typically unresolved with sizes $\leq 0.01\,\mathrm{pc}$ and have flat radio spectra if a power law is assumed. The extended components tend to have steep radio spectra. This diagnostic will be very important later on in this thesis whilst determining the nature of the faint radio and X-ray sources.

#### 1.2.2.2 Distinction between Quasars and Seyferts

Quasars are defined by objects having broad emission lines ($\geq 1000\,\mathrm{km\,s^{-1}}$) and an absolute magnitude of $M_B \leq -23$. They are additionally distinguished from the fainter Seyfert galaxies by the fact that they are generally unresolved on the Palomar Sky Survey Photographs (i.e. have angular sizes smaller than $\sim 7''$). However some of these quasars are surrounded by a low-surface brightness halo and more recently there has been direct detection of a quasar host galaxy (Bahcall et al. 1995, McLeod & Reicke 1995, McLure & Dunlop, 2000).

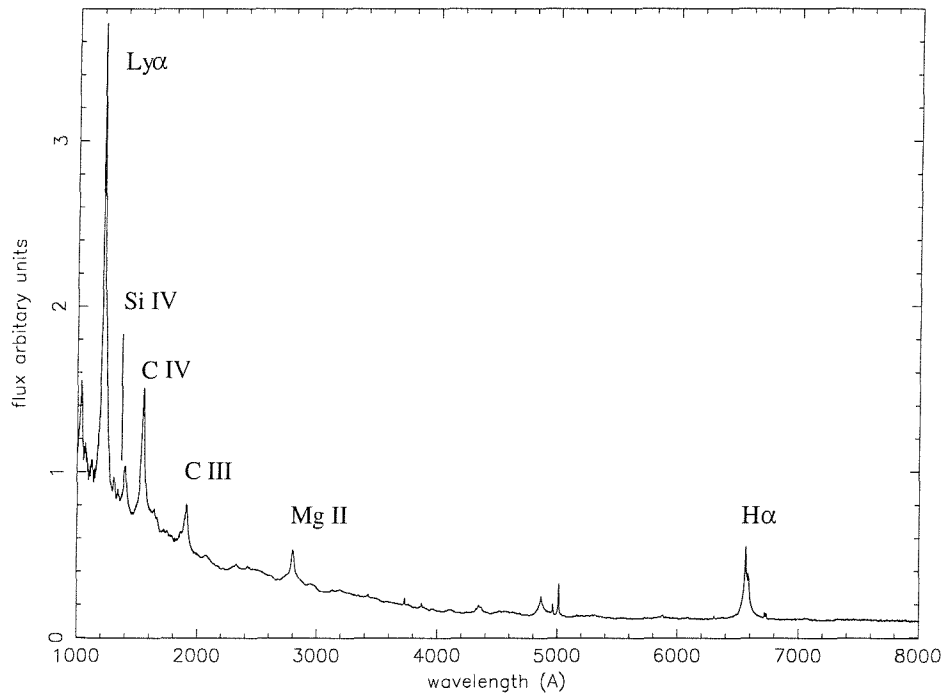


Figure 1.7: The combination ultraviolet to optical spectrum of a HST radio-quiet quasar composite (Telfer et al., 2002) and the Sloan Digital Sky Survey median composite. Below 1275 Angstroms this is the HST composite, above 2000 Angstroms it is the Sloan composite, and in between it is the mean of the two.

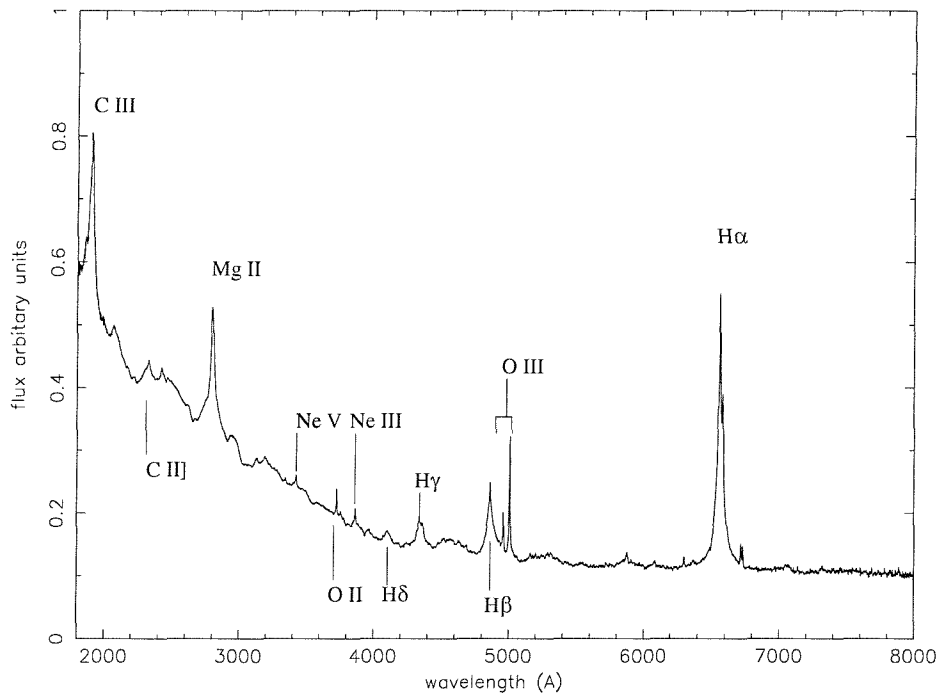


Figure 1.8: A close up of the previous figure highlighting the relatively weaker features of a generic radio-quiet quasar optical spectrum.

### 1.2.3 Radio Galaxies

Radio loud sources, if not quasars, are typically hosted by giant elliptical galaxies. Some of these objects show emission lines from the nuclear region indicating AGN activity. Analogous to the situation with Seyfert galaxies they come in two types; broad-line radio galaxies (BLRGs) and narrow-line radio galaxies (NLRGs). These are equivalent to type 1 and type 2 Seyfert galaxies respectively although as a class there are some other differences. Otherwise they can generally be considered radio-loud Seyferts, except that they are not found in spirals like most Seyferts.

### 1.2.4 LINERS

Low-ionisation nuclear emission line regions (LINERs) are spectroscopically similar to Seyfert 2s, but with relatively strong low-ionisation lines. They are very common and may be detectable in nearly half of all spiral galaxies. To distinguish them from HII regions the intensity ratio of at least two, closely spaced pairs of emission lines are needed. This helps to determine if the original ionising spectra is a blackbody (HII region) or a power-law (AGN origin).

### 1.2.5 BL Lac objects and Optically Violent Variables

There is a subset of AGN which show very rapid variation compared to 'standard' AGN (e.g. $\Delta m \geq 0.1$mag in visible wavelengths in timescales of a day or so). Additionally they also tend to have relatively high polarisation of a few percent compared to most AGN (which normally have polarisation $\leq 1\%$). This high polarisation also varies with magnitude and position angle. These sources are known as 'optically violent variables' (OVV) and are always radio loud.

'BL Lac' objects, named after the prototype of this class BL Lacertae have similar properties. The prototype was originally identified as a variable star (hence the variable star name). As well as sharing some of the properties of OVVs they are also characterised by the absence of strong emission or absorption lines in their optical spectra, although in high quality optical spectra weak features can generally be detected. Together 'BL Lac Objects' and 'optically violent variables' are known as Blazars.

The spectral energy distribution of Blazars has broad two peaks in a plot of $\nu F_\nu$ vs $\nu$. The first, thought to be due to synchrotron radiation emission, is located in the IR to soft X-ray band whilst the second due to inverse Compton scattering by the same population of electrons producing the synchrotron radiation is located above

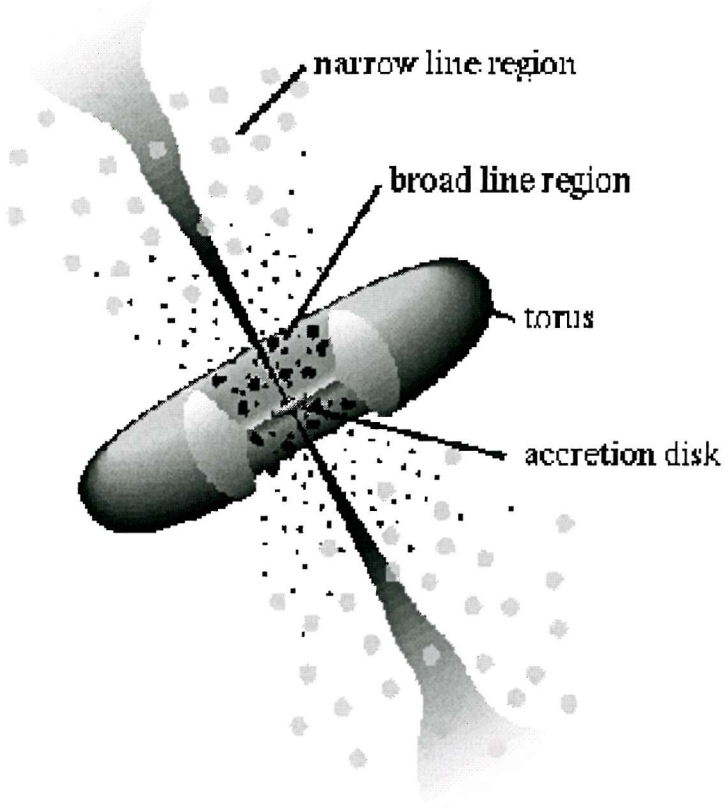


Figure 1.9: A schematic view of the current paradigm for AGN unification (Urry & Padovani, 1995).

energies of 10 keV. The $0.1 - 10$ keV range falls between these two peaks and hence the X-ray spectra of Blazars is a very useful diagnostic in examining the dominating mechanism in a particular source. If a blazar has steep power-law ($F_\nu \propto \nu^{-\alpha}$, $\alpha > 1$) then it is due to the tail of the synchrotron spectrum, whilst if it has a flatter power-law ($\alpha < 1$) then the contribution of the inverse Compton processes is dominating. In the latter case, the Blazar will have a higher bolometric luminosity and the peak of the inverse Compton scattering will be at lower frequencies and hence dominate the $0.1 - 10$ keV range. A source would normally then be classified as a OVV and in the former, steep X-ray spectrum case, a source would be called a BL Lac.

### 1.2.6 Unified AGN Model

It is now generally thought that that AGN are powered by gravitational accretion onto a supermassive black hole (SMB). Although there is not yet direct proof of the existence of SMB, energetic arguments as to how can so much energy be generated

in such a small volume, rule out dense clusters of stars and other scenarios put forward. A qualitative description was put forward by Eddington, who defined a characteristic luminosity (now known as the Eddington luminosity) of a source as being the maximum luminosity of source being fuelled by spherical accretion onto a central object. From the precept that the inward gravitational force acting on a gas must balance or exceed the outward radiation pressure, the Eddington limit is defined thus,

$$L_E = \frac{4\pi G c m_p}{\sigma_e} M \tag{1.3}$$

where $\sigma_e$ is the Thompson scattering cross-section for an electron with a photon. For a typical quasar luminosity of $L_{QSO} \sim 10^{46}\,\mathrm{erg\,s^{-1}}$, a central mass in excess of $M \sim 10^8\,\mathrm{M_\odot}$ is required.

The key to a unifying scheme of AGN is that they are not spherically symmetric, but are anisotropic and display axial symmetry (Antonucci 1993, Urry & Padovani 1995). It was clear from early on that radio sources were not spherically symmetric due to the presence of geometrically opposing extended lobes. Additionally it was long suspected that intrinsically there was only one type of Seyfert galaxy, but in some cases we do not see the broad line region (BLR) as it is obscured. Osterbrock (1978) was the first to suggest that an orientation effect may be obscuring the central region. It is now generally excepted that the obscuring medium forms a torus around the central source, which heavily obscures the BLR when not observed from near the torus axis (Urry & Padovani 1995). Away from this axis the narrow line regions (NLR) would still be seen as they are not hidden by the torus and only very weak emission would be seen from the BLR.

Evidence for this came from observations of the polarised optical spectra of Seyfert 2s where very weak broad line features were more prominent than in the total flux optical spectra implying that the broad line features are scattered (and thus polarised) by material close to the torus axis (Antonucci and Miller, 1985). Later, is was found that Seyfert 2s have significantly lower hard X-ray luminosities compared to Seyfert 1s (Lawrence and Elvis, 1982) implying that they are highly attenuated (if the torus[1] is blocking our line of sight).

#### 1.2.6.1 'Grand' Unified AGN Model

Figure 1.9 illustrates the basic precepts of the unified model and it is clear that any observer looking side on will only see the narrow line regions and not see the broad

[1]The obscuring matter is referred to as a torus, but there is no direct evidence to indicate whether it is actually a torus or some other distribution (e.g. a warped disk)

line regions directly. Any 'grand' unified scheme will be based on the fewest number of different properties of a source plus the relative orientation of the torus axis. The basic tenets are:

1. The primary difference between Seyferts and quasars is the luminosity of the central source. Quasars tend to be much brighter than Seyferts and normally outshine their host galaxy to such an extent that they are difficult to detect. Why do very few quasars have type 2 optical spectra?[2] Possibilities include smaller or non-existent tori in the brightest sources, diminished by the bright central emission or that they are so obscured we can't see even the narrow line regions (e.g. ultra-luminous far-infrared galaxies, Januzzi et al. 1994)
2. Seyferts are intrinsically all the same except that in some, due to the line of sight at which an object is observed, the broad line regions are obscured by dust in the form of a torus around the central engine. The same is true for BLRGs and NLRGs.
3. Blazars are radio-loud AGNs viewed along a line of sight close to that of the radio axis. They have flat radio spectra due to observations being made down the jet axis. This allows regions of gas of many different densities along the jet to be seen at once. As the radio spectra of each region turns over at different frequencies, a superposition of humps is observed combining to give a net flat spectrum. They have very steep X-ray spectra if they are BL Lacs or flatter spectra if OVVs.
4. Some AGN are radio-loud and some are not. Why this should be is not clear. The creation of jets which lead to the extended lobe emission is poorly understood. Strong magnetic fields are needed to create the amount of collimation seen at the highest resolutions. These are to believed to be related to the rate of spin of the central blackhole, which are sped up by mergers (Wilson and Colbert, 1995).

Thus, although it is possible to find many objects that do not fit in to this scheme, we at least have a framework in which one can begin to understand AGN.

## 1.3 The UK Deep *ROSAT* X-ray Survey

### 1.3.1 Original Motivation

The motivation for the original X-ray survey was to investigate the X-ray sources that contribute to the cosmic soft X-ray background (XRB). The excellent fit of

[2]Only very recently have such objects been found, e.g. Norman et al.(2002).

the microwave background, as observed by *COBE* , to a pure blackbody spectrum undistorted by Compton Scattering from energetic electrons, has ruled out a major contribution to the XRB ($\geq$ a few percent) from diffuse hot gas (Mather et al., 1990) so there must be a number of discrete X-ray sources responsible. Early investigations into this work seemed to indicate that there were different contributions to the XRB at soft energies ($0.5 - 2\,\mathrm{keV}$) and at higher energies ($2 - 10\,\mathrm{keV}$). Less deep X-ray surveys with *ROSAT* had found that the source counts were dominated by QS0s (Shanks et al. 1991, Boyle et al. 1993).

### 1.3.2 The Observations

The field at RA 13 34 37 Dec 37 54 44 (hereafter, the 13hr field) was originally observed by the *ROSAT* satellite using the position-sensitive proportional counter (*PSPC* ). This field was chosen for its extremely low obscuration by galactic dust (i.e. $N_H = 6.5{\times}10^{19}\mathrm{cm}^{-2}$ Stark et al. 1992) and lack of $100\mu$m cirrus (from *IRAS* maps) not because of sparseness of bright X-ray or radio sources (see sections 2.2.2 and 6.3.1.1).

Observations of the 13hr field with the *ROSAT PSPC* detector reached a flux limit of $1.6 \times 10^{-15}\,\mathrm{erg\,cm^{-2}\,s^{-1}}$ (0.5-2.0 keV), M$^{\mathrm{c}}$Hardy et al.(1998). A total of 70 X-ray sources were found in the 15arcminute radius field of view above a flux limit of $2 \times 10^{-15}\,\mathrm{erg\,cm^{-2}\,s^{-1}}$ (corresponding to $\sim 3.5\sigma$ significance). This observation resolved approximately half the X-ray background at 1 keV. Optical data and optical spectra were collected both before and after the *ROSAT* observations.

### 1.3.3 Results and Conclusions

Of the 70 X-ray sources, 59 were optically spectroscopically identified and a further 5 had tentative identifications. At bright fluxes ($\geq 10^{-14}\,\mathrm{erg\,cm^{-2}\,s^{-1}}$), the results of previous less deep X-ray surveys were confirmed (Shanks et al., 1991), with 84% of the X-ray sources being quasars. Near the faint flux limit this survey was dominated by a population of galaxies with narrow emission lines (NELGs). If the observed X-ray source counts could be reliably extrapolated to fainter fluxes, clusters will contribute almost nothing more to the XRB and quasars will contribute only a small amount more. NELGs, though, will contribute double to the XRB at a flux limit of a factor of 4 lower.

The NELGs also have harder X-ray spectra than quasars, with a spectral index similar to that of the XRB (Almaini et al. 1996, Romero-Colmerero et al. 1996). If their X-ray spectra can be smoothly extrapolated to higher energies they will be significant contributors to the XRB at those energies. This means that NELGs

should be detectable in large numbers in *XMM* and *Chandra* surveys.

Morphologically the nearby NELGs appeared to be spirals, although this does not preclude others being elliptical. All the NELGs lie at a redshift $\leq 0.6$ and some appeared to be part of disturbed or interacting systems. The absolute magnitudes of NELGs lie in the range $M_R$=-20 to 23 mag, typical of large spirals or ellipticals. However, their X-ray luminosities lie in the range $3 \times 10^{41}$ to $5 \times 10^{42}\,\mathrm{erg\,s^{-1}}$, an order of magnitude or two larger than that of spirals and at the highest values for large non-cluster ellipticals. The X-ray spectra were consistent with the idea that the emission mechanism could be advection-dominated accretion onto a SMB.

The conclusion was that the NELGs, both as a sample and individually, appear to be a mixture of starburst galaxies and AGN. This was based on some of the emission line ratios and the X-ray spectra. A possible scenario is that starburst/X-ray binary activity dominates the X-ray emission from the lower luminosity NELGs, but that AGN activity dominates those with higher luminosity. This implies that the fainter NELGs are simply more luminous members of the normal field galaxy population.

### 1.3.4 Motivation for extending the X-ray survey to other wavelengths

One of the key questions thrown up by the *ROSAT* survey was how much do starbursts contribute to the X-ray emission of the NELGs. Radio observations are a useful independent determination of the star-formation rate in NELGs as radio imaging can distinguish starburts, which are generally resolved with steep radio spectra, from AGN, which are compact, have flat radio spectra and high brightness temperatures. Combined with the X-ray and optical data, the radio data would provide excellent determinations of the contribution of starburst emission to the whole spectral energy distribution.

The chance to improve the quality of the *ROSAT* data came with the launch of two state of the art X-ray telescopes in 2000. *Chandra* was launched by NASA and has unprecedented resolution of $0.5 - 1''$ in the $0.1 - 2\,\mathrm{keV}$ band. This increase in resolution is a great improvement over *ROSAT* and would lead to unambiguous optical identifications of X-ray sources in most cases. *XMM* -Newton was launched by ESA around the same time and has a resolution of $6''$, and the advantage of $4\times$ greater throughput than *Chandra* which allows relatively good quality X-ray spectra of even faint objects. The combinations of positions (from *Chandra*) and spectra (from *XMM*) is vital for expanding the UK Deep X-ray survey and understanding the XRB.

## 1.4 Thesis Outline

The work presented here is part of a collaboration involving many people. However the author's contribution is the analysis of all the radio data and the correlation with the optical and X-ray data (which was collected and reduced by others). The initial analysis of the 1.4 GHz data performed by others is hopefully made clear in the text.

In the following chapter details of the 1.4 GHz radio data are presented. There are approximately 24hours of data from the VLA in both A and B-configurations. The calibration, image construction and source extraction is explained. In chapter three the analysis of the 4.86 GHz data (also from the VLA) is discussed consisting of 51 pointings to cover the 30′ field of view. Chapter four concerns the correlation of the radio data with the optical data (both images and spectra). In chapter five the correlation of the radio and optical data with the *Chandra* data is discussed, and highlights are presented of NELGs and Blazars in the 13hr field which have involved the use of *XMM* and *MERLIN* data. The conclusions are presented in chapter six.

# Chapter 2

# The 13hr field 1.4 GHz radio data

In this chapter the calibration and imaging of the 1.4 GHz radio data are discussed. The source extraction and construction of the logN-logS plot are also described. Additionally some of the technical aspects of the calibration and image construction are explained. Down to a 30 $\mu$Jy ($4\sigma$ limit) 462 sources were found. To avoid incompleteness in the log(N)-log(S) plot only sources with a $4\sigma$ peak flux and an integrated flux $> 50\,\mu$Jy were included. The log(N)-log(S) shows an up-turn of sources at sub- mJy fluxes above the Euclidean normalised slope: $S \sim dN/dS(S^{2.5})$ confirming the results of other recent deep surveys at 1.4 GHz.

## 2.1 Motivation for the Radio Survey

Results from the *ROSAT* survey indicated that Narrow Emission Line Galaxies could contribute significantly to the X-ray Background at fluxes fainter than the X-ray survey limit (i.e. $< 2 \times 10^{-15}\,\mathrm{erg\,cm^{-2}\,s^{-1}}$ (0.5-2.0 keV) M$^{c}$Hardy et al., 1998) and in harder energy bands (i.e. $2 - 10$ keV). It was found that NELGs probably contain a starburst component. Radio emission is a key independent indicator of starburst activity. Radio spectra can help distinguish between starburst emission (resolved, steep spectra) and AGN activity (unresolved flat spectra). To obtain two-point radio spectra it was decided that observations at 1.4 GHz and 4.86 GHz should be made.

The observations were made using the National Radio Astronomy Observatory's[1] (NRAO) Very Large Array (VLA) in New Mexico. The VLA was chosen as it is one of the world's most sensitive radio arrays due to it's large collecting area from

[1]The National Radio Astronomy Observatory is a facility of the National Science Foundation operated under cooperative agreement by Associated Universities, Inc.

27 antennae. At 1.4 GHz the field of view of the VLA is 30′ diameter which exactly matches that of *ROSAT*. 1.4 GHz is a useful frequency with which to observe many of the physical processes in NELGs like starburst emission and AGN activity (e.g. synchrotron radiation from either supernova remnants or AGN activity). Observations could then be made at 4.86 GHz in order to derive 2-point radio spectral indices.

Initially observations were made with a 10 hour observation of the field by the VLA in B-configuration[2] at 1.4 GHz and multiple pointings at 4.86 GHz in D-configuration. Initial correlation of the B-configuration 1.4 GHz data with the *ROSAT* catalogue showed considerable overlap, see figure 2.1. The success of the initial radio observations to detect faint X-ray sources (and hence determine their emission mechanism) further radio observations being requested. A much deeper radio observation at 1.4 GHz was obtained with the VLA in the higher resolution A-configuration. Additionally a very deep survey of the 13hr field was made with four pointings of the Multi-Element Radio Linked Interferometer Network (MERLIN). In this chapter the VLA A and B-configuration 1.4 GHz data are presented. The 4.86 GHz is presented in Chapter 3. The MERLIN data is only touched upon in a few places as it is not yet fully analysed.

### 2.1.1 Software

The analysis of the radio data was carried out using the Astronomical Image Processing System (AIPS) developed by the NRAO in Charlottesville, Virginia USA. It is a freely available software package for the editing and calibration of radio interferometric data and for the construction and analysis of astronomical images made from those data using Fourier synthesis methods.

## 2.2 Observations and Data Reduction

In November 1995 the 13hr field was observed for a total of 10 hours at 1.4 GHz in the B-configuration of the VLA. Observations were made in pseudo-continuum spectral line mode (see following paragraphs) with $8 \times 3.125$ MHz channels centred on intermediate frequencies 1365 MHz and 1435 MHz to minimise chromatic aberration. Each frequency channel was composed of two independent circular polarisations.

These observations were followed up in August 1998 by a deeper observation of 30hrs in the A-configuration of the VLA. This observation was also made in pseudo-

[2]At 1.4 GHz the B-configuration of the VLA has a resolution of 6″ and the A-configuration has a resolution of 1.4″.

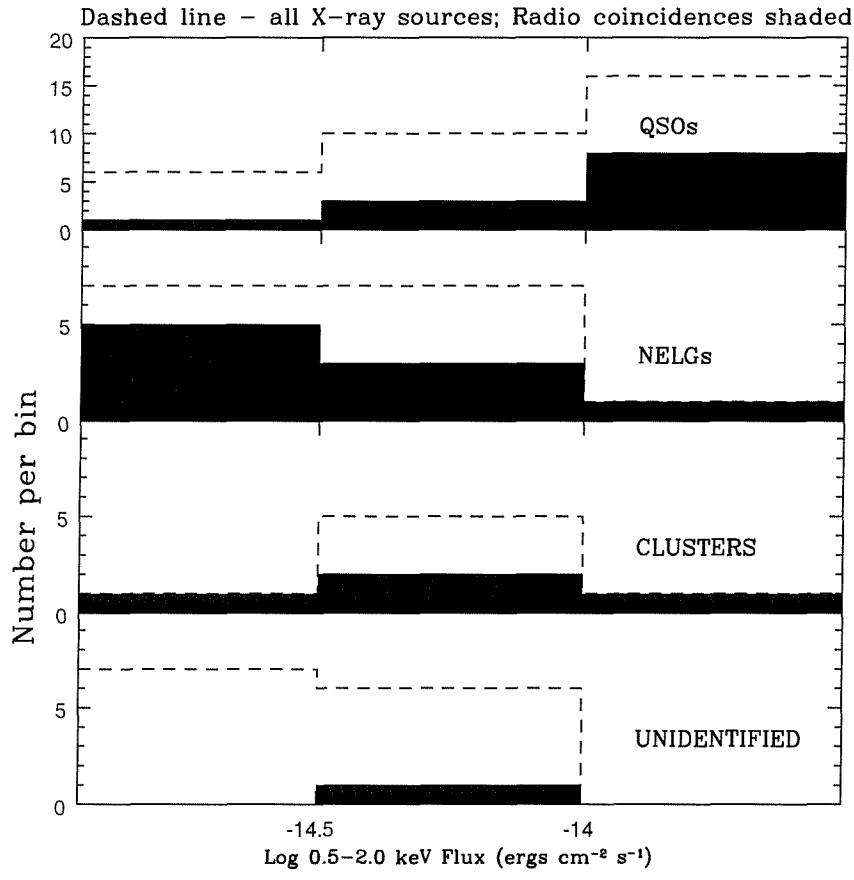


Figure 2.1: Number of *PSPC* sources in the original *ROSAT* survey identified with various optical spectroscopic classes of object. Shaded areas indicate where an identification is also detected in preliminary B-configuration radio data.

continuum spectral line mode with 8 x 3.125 MHz channels centred on intermediate frequencies 1365 MHz and 1435 MHz, again with two independent circular polarisations.

The observing of these data sets in this manner is known as '4 IF' observing mode due to the 4 data streams; 1365 MHz right-hand circular polarisations (RCP), 1365 MHz left-hand circular polarisation (LCP), 1435 MHz RCP and 1435 MHz LCP. Each of these IFs has a total bandwidth of 25 MHz divided into eight channels. However the effective bandwidth is reduced due to bandpass roll-off which requires discarding the first channel for signal to noise reasons leaving seven channels of 3.125 MHz (the first channel is then replaced by a pseudo-continuum form of the data known as 'channel 0'). The spectral line information of the radio sources was not a concern (although it would be interesting, but the vast majority of the sources in the field of view would be too faint), but spectral line mode was used because of its increased sensitivity and potential to make images of high dynamic range. Each of the seven channels will occupy a slightly different place on the the Fourier transform plane (known as the *uv* plane in radio interferometry parlance) for each visibility[3] due to the slightly different median frequency of each channel. This improves the coverage of the *uv* plane and hence makes the deconvolution of the sky plane from the synthesis beam easier.

The principles upon which synthesis imaging are based are strictly valid only for monochromatic radiation so when radiation from a finite bandwidth is accepted and gridded, as if monochromatic, aberrations in the image will result. This is known as chromatic aberration or 'band-width smearing'. This takes the form a radial smearing which worsens with increased distance from the pointing centre of the field of view. The peak response to a point source simultaneously declines in a way that keeps the integrated flux constant. The net effect is a radial degradation in the resolution and sensitivity of the array. The amount of bandwidth smearing increases with the size of the individual channels. 'Pseudo-continuum spectral line mode' helps reduce bandwidth smearing so that larger fields of view can be used without distortion. However using too many channels reduces sensitivity again. It has been found that the particular combination of number of channels and channel bandwidth used here gives the optimum balance between sensitivity and chromatic aberration (Richards, 2000).

[3]A visibility is a single record of interferometric radio data consisting of the correlation of the signals from one pair of antennae for one channel at a particular frequency and with a particular polarisation over a certain integration time. In these observations an integration time of 3.3secs was used.

### 2.2.1 Initial Data Reduction

Both the A and B-configuration observations were calibrated with the same primary and secondary calibrators, 1331+305 and 1310+323, for amplitude and phase respectively. As the observations were made in spectral line mode bandpass calibrators were also needed, 1310+323 for the A-configuration data and 1331+305 for the B-configuration data. Spectral line data differs from continuum data in that the antenna gains have to be determined as a function of frequency as well as time. Bandpass calibration is required to determine these antenna-based complex bandpass functions using a suitable calibrator source.

The B-configuration data was observed in one run and was calibrated by the standard recipe with AIPS for spectral line data. The A-configuration data was observed over 3 nights in runs of ten hours each. On top of the normal flagging of bad data the last half of the second night was unusable due to thunder storms. Combined with other problems only 14 hours of data were used. The data were then also calibrated in the usual fashion.

The initial calibration of the B-configuration was performed by Ian M$^{c}$Hardy and that of the A-configuration was performed by Tom Muxlow using the standard AIPS recipe. All subsequent analysis on the radio data was done by the author.

### 2.2.2 Self-calibration of the data

Initial mapping of both sets of data showed side-lobes from bright sources within and outside the field. The most significant of these was a bright extended source to the western edge of the primary beam (source J133328.7+375553 in the FIRST radio survey (White et al., 1997) with a flux of 92 mJy, hereafter referred to as source 1 from table 2.2). It was extended to $35-40''$ which is just beyond the limit of extended structure resolvable by the VLA A-configuration. Additionally it was the brightest source in the field by almost an order of magnitude. For the B-configuration data it was not a problem if the main field was shifted a few arcminutes to the east and separate images made of this source, its environment and the handful of other off-field confusing sources. However for the A-configuration data this strategy did not completely remove the side lobes from maps of the rest of the field. Additionally the next 3 brightest sources in the main field could not be deconvolved properly from the beam and caused ripples from their side-lobes across the field due to apparent phase errors in the calibration. These problems limited the dynamic range of the maps and did not allow the theoretical thermal rms noise to be obtained.

It was decided to self-calibrate the A-configuration data to help improve the phase errors and dynamic range. Self-calibration is an iterative process whereby the input

*uv* data is compared with the predictions of a source model - a point-source initial guess or the best current set of Clean components - in order to compute a set of antenna based amplitudes and phase corrections as a function of time which would bring the data into better agreement with the current model (AIPS Cookbook, 1999, ed, Eric Greisen). Typically self-calibration is performed on observations with one or a few bright sources near the centre of the field, but more recently it has been seen as a way of improving the calibration and dynamic range of observations of fields with many relatively faint sources as is common in radio survey work (Ivison et al. 2002, Smail et al. 2002 and references therein).

Self-calibration is generally more successful for an array like the VLA with a larger number of elements which results in less information being lost when allowing the calibration to be variable. Also sources are generally simple and can be well represented by a small number number of degrees of freedom (even in the 13hr field although there are hundreds of sources, they are virtually all essentially point-sources). The basic requirement is that the total number of degrees of freedom (the number of free gains plus the number of free parameters in the model of the sky brightness distribution) should not be greater than the number of independent visibility measurements (Synthesis Imaging, Perley et al., 1986). The A-configuration data contained $\sim 4.2 \times 10^6$ visibilities (before self-calibration) so although they are not all independent they satisfy this requirement by having a very well sampled *uv* plane. Additionally there is a large enough dynamic range of $\sim$ 500 : 1 from an rms of $\sim 15\,\mu$Jy/beam to a peak flux of 8 mJy/beam (for source 1) to make self-calibration worth while. '4 IF' observing mode makes it possible to obtain dynamic ranges of up to 1000:1 at 1.4 GHz.

For the input model all of the current, best set of Clean components from the maps were used including those of 3 sources outside the field of view (see figure 2.3 for their locations). There are different views on how many Clean components to take for the self-calibration process. In some situations it's best to only take those up to the first negative component so that you are confident your input model is an accurate representation of the real sky surface brightness (as is usually the case for bright sources which are not too extended). This helps to avoid the fabrication of weak sources in cases where your input images are already limited by the receiver noise. In others you may want to include all the Clean components in order to use an input model which is a significantly good representation of the true sky brightness. In cases where the source is significantly different to the model, self-calibration can fail hence in this case all the Clean components were chosen to be used (including those of the off-field sources) to have the best representation of the sky plane possible.

CALIB was run twice in the self-calibration procedure each time using all the components from the best map from the previous *uv* data sets. The maps at this stage consisted of $4 \times 4096$ maps with $0.22''$ pixels made from $10^5$ CLEAN iterations (plus a few small maps of off-field sources). Each time CALIB was run the clean

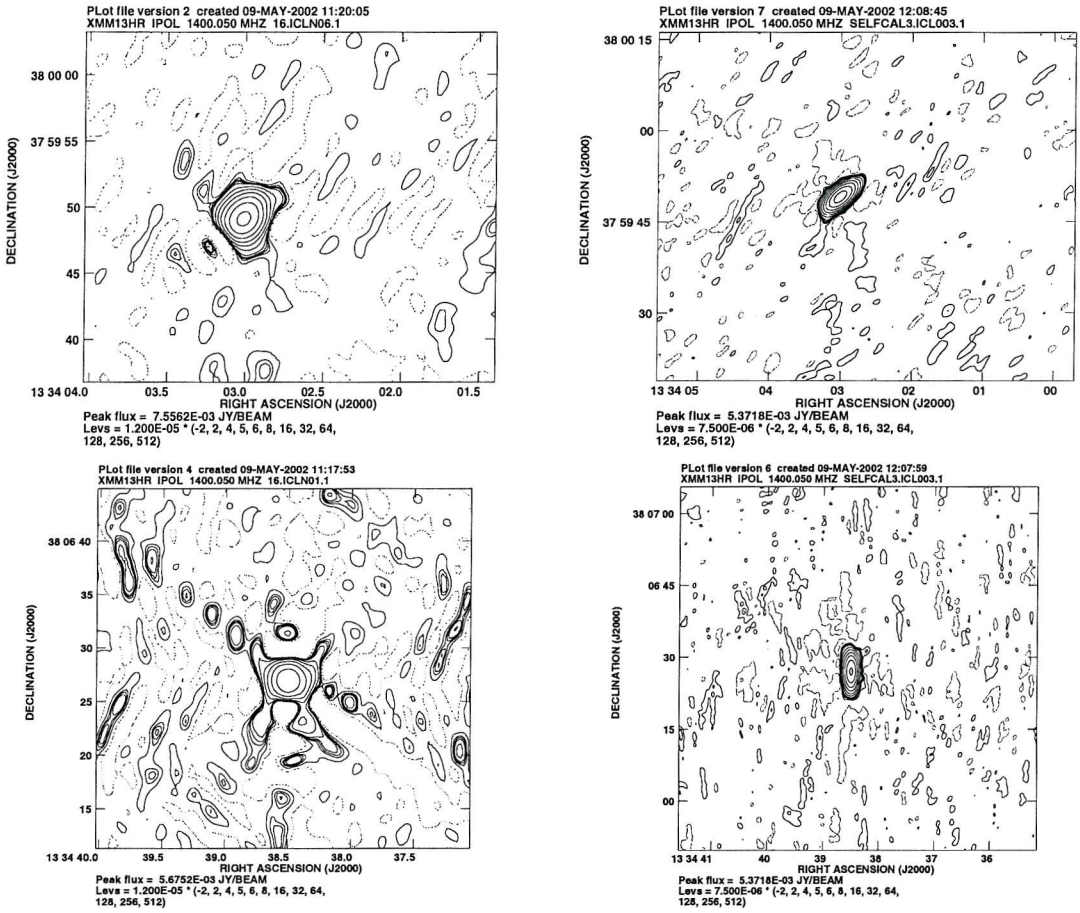


Figure 2.2: The improvements in the imaging of radio sources 2, top, and 4, bottom, from self-calibration. The figures on the left are before self-calibration and the those on the right after the second iteration of self-calibration. The sources are listed in table 2.2 and are ordered according to the integrated flux (e.g. these are the second and fourth brightest sources respectively). The effect of bandwidth smearing can been seen in source 4 which is 235″ due north of the centre of the field of view.

component solutions were solved for phase weighted by amplitude; the first time with a solution interval of 60mins and the second time with one of 20mins (to be roughly comparable with the frequency of observations of the phase calibrator). A $uv$ range of $20 - 500k\lambda$ was used where the the model best represented the sky brightness (i.e. not on the very smallest or largest angular scales). The data outside this range was given a relative weight of 0.1.

The first run of CALIB found 1920 good solutions (and failed on 8) and reduced the number of visibilities from 4,245,987 to 4,229,374. The second run of CALIB found 4003 good solutions (and failed 307) further taking the number of visibilities down to 3,996,971. This meant 6.9% of the A-configuration data was lost, but the improvement in the calibration of the sources can be seen in figure 2.2 and the rms noise of the image decreased to $\sim 10\,\mu$Jy/beam.

## 2.3 The Image Construction

To obtain the very best (ie deepest and with fewest side-lobes) images from AIPS the *uv* data set was deconvolved in 'Direct Fourier Transform' mode (DFT) which is computationally expensive. Self-calibration also had to be done in 'DFT' mode. If this option is not chosen then AIPS choses the fastest of the two options for doing the Fourier transform which is generally the slightly less accurate gridded Fast-Fourier-Transform (FFT) interpolation model.

The A and B-configurations were combined using the AIPS algorithm DBCON. The relative weighting of the data sets which needs to be specified is found by making dirty images (ie Fourier transform them, but do not deconvolve the beam) in the exact manner in which the final images will made. The algorithm IMAGR reports the 'sum of the gridding weights' in the message file. This is the sum of the weights after all corrections are applied. These values should be used to specify the REWEIGHT parameters in DBCON where REWEIGHT(1) is inversely proportional to the 'sum of the gridding weights' for the second data set and vice-versa for REWEIGHT(2). In case this the 'sum of the gridding weights' was 170 078 000 and 195 842 000 for the A and B-configuration data respectively leading to REWEIGHT = 1, 0.868445.

To cover the 30′ diameter field of view without having any part of an image too far from a tangent point of the field with the sky a square array of $9 \times 2048$ pixel maps was used with 0.33″/pixel in order to have Nyquist sampling of the A-configuration restoring beam, 1.4″. These maps were shifted about 100″ west to avoid source 1 that had caused problems in the calibration. The slice of the circular field of view that was missed was imaged separately with four 1024 by 1024 maps in a vertical stripe. The mapping strategy is shown in figure 2.3. The maps overlapped so to restore Clean components to all fields to which they contribute a value of OVERLAP = 2 was used in IMAGR .

The final maps were made using natural weighting of the *uv* data which gave a restoring beam for the combined data of 3.35″. Natural weighting gives each *uv* data point equal weighting whereas the other extreme, uniform weighting, gives a data point weighting depending on the local density of points on the *uv* plane. Uniform weighting gives equal weighting per unit area of the *uv* plane, so typically the points further from the centre which are less densely spaced get a higher relative weighting. These points though correspond to the pairs of antennae with the longest baselines and hence are responsible for the highest resolution data. This effectively down weights any extended structure at the expense of sensitivity to give you a higher resolution image. Therefore to get maximum sensitivity natural weighting was used in the maps. The final set of 13 maps (figure 2.3) were constructed with $10^6$ CLEAN iterations and a GAIN value of 0.1.

The histograms of the pixel intensity of each field after the sources have been

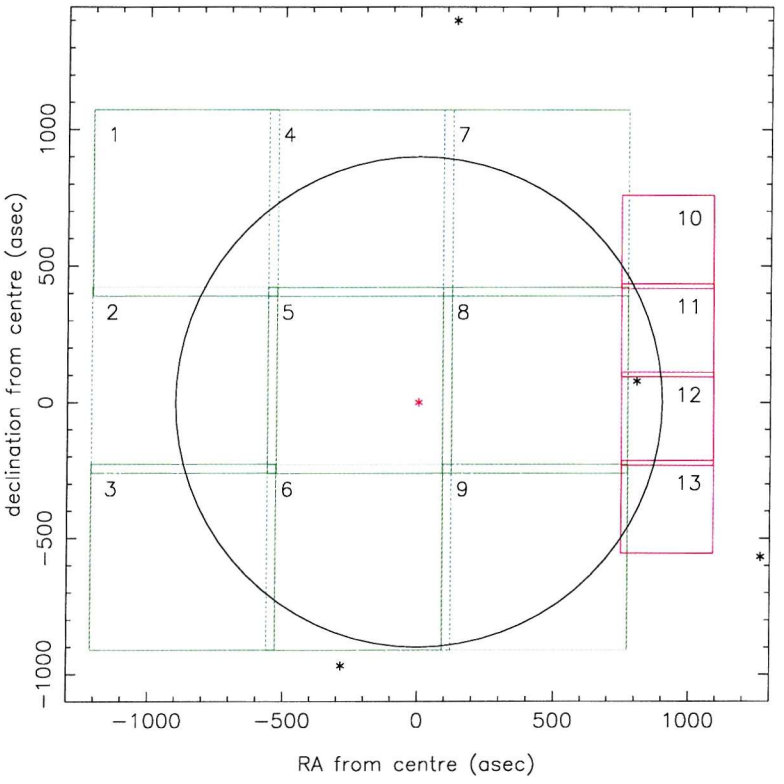


Figure 2.3: A figure to show the mapping strategy. The red star represents the centre of the field and the black stars indicate the main confusing sources (including source 1 just in the field on the right). The 30′ diameter field of view is represented by the circle. The pixel size was chosen at 0.33″/pixel and the 2048 pixel and 1024 pixel fields are represented by the green and red squares respectively.

removed is shown in figure 2.4. The rms noise distribution is, to first order, reasonably Gaussian. For each field the rms fitted to the Gaussian and the rms calculated directly from the data are given both in units of $\mu$Jy/beam. It was decided that a final rms of $7.5\,\mu$Jy/beam was a reasonable representation of the whole field of view.

### 2.3.1 Weighty Issues

Within the IMAGR task in AIPS it is possible to use a hybrid of natural and uniform weighting (see IMAGR explain file and Briggs, 1995). Essentially uniform weighting is used, but slightly tempered by a robustness parameter. If this parameter, ROBUST, equals five then natural weighting weighting is obtained and if ROBUST equals minus five uniform weighting is recovered. Values in between give one a trade off between sensitivity and resolution. Several display maps were created (as in the 4k map, figure 2.5, with $4096 \times 1024$ pixel fields flanking each side) to investigate the use of ROBUST, not just on the combined data, but also the A and B-configuration separately. The CMETHOD parameter in IMAGR was left blank allowing the task to chose the faster of the two Fourier transform methods; the more accurate direct Fourier transform (DFT) or the gridded fast Fourier transform interpolation model computation.

The motivation for this was to have higher resolution images of particular sources of interest not only for material in this thesis, but for the future use of the UK Deep X-ray Survey as a whole. It was found that a value of ROBUST=0 was the best compromise of improved angular resolution against worsening noise. For the combined data this gave us a resolution of $1.69''$ whilst increasing the noise only fractionally to $8.5\,\mu$Jy/beam.

## 2.4 The Complete Source List

### 2.4.1 Source Extraction

A final image of almost Gaussian noise was obtained with an average rms of $7.5\,\mu$Jy /beam. There were some minor artifacts usually caused by side-lobes from the brighter sources in the field. The AIPS algorithm SAD (Search and Destroy) was used to detect any point sources in the maps. SAD works by finding areas of local maximum flux and then tries to fit this area with a 2 dimensional elliptical Gaussian. SAD then returns the source's position, size, orientation, peak flux and integrated flux. This task is poor at extended sources which have been fitted by hand with

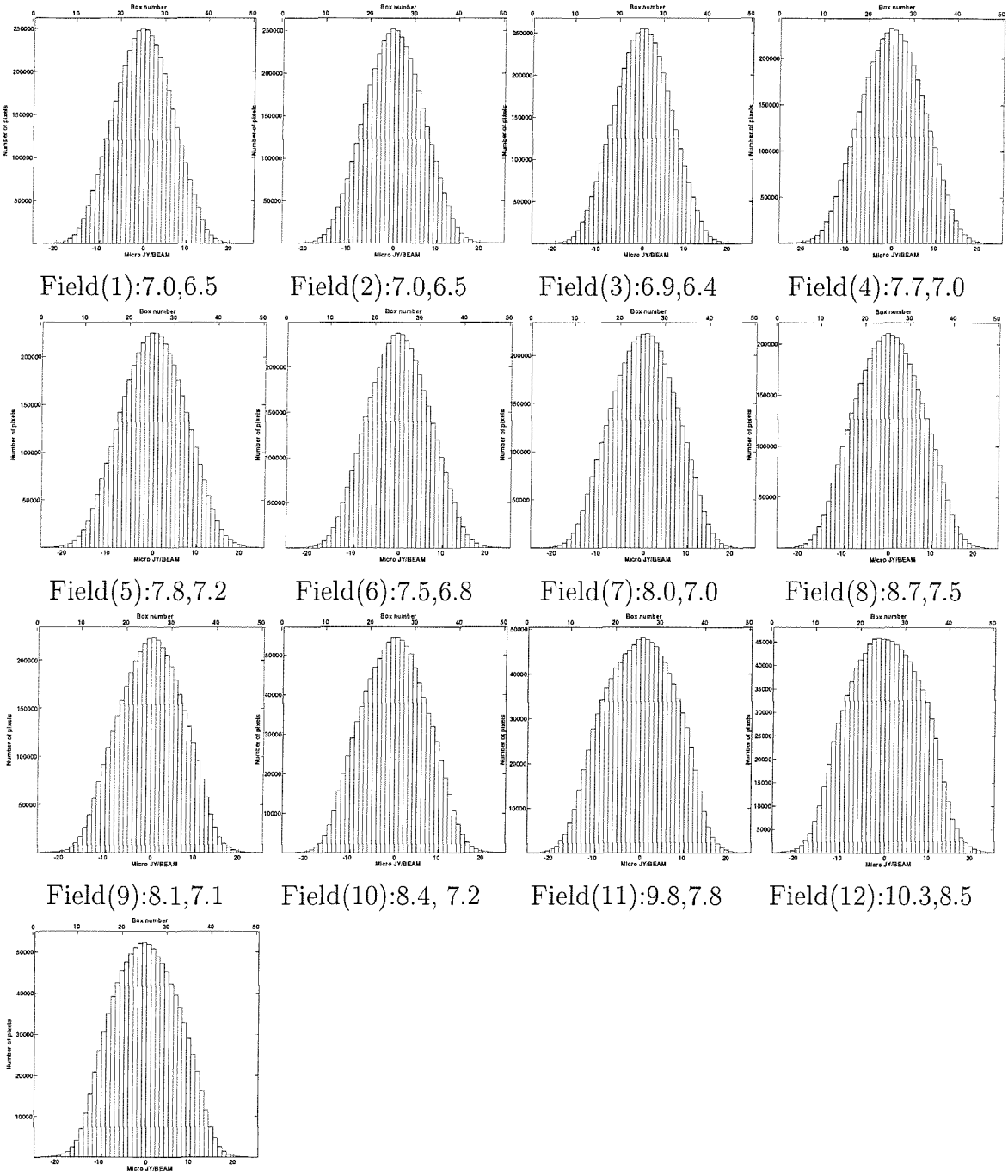


Figure 2.4: Distribution of pixel fluxes for each field showing that all the fields are very close to having Gaussian noise. For each plot the field number (from figure 2.3) is given below each histogram along with the rms fitted to a Gaussian distribution and the rms calculated directly from the data (both in $\mu$Jy/beam). Note that the problem source, source one, was in field 12 very close to field 13 which is why these two fields slightly deviate from a Gaussian distribution.

Figure 2.5: An inverse greyscale image of the inner 22.8′ by 22.8′ of the 1.4 GHz map. This map has a pixel size of 0.33″, is 4096 pixels square and was made with an effective resolution is 3.35″ with an rms of 10 $\mu$Jy/beam. This map made for display purposes only. Note that this image has not been corrected for primary beam attenuation.

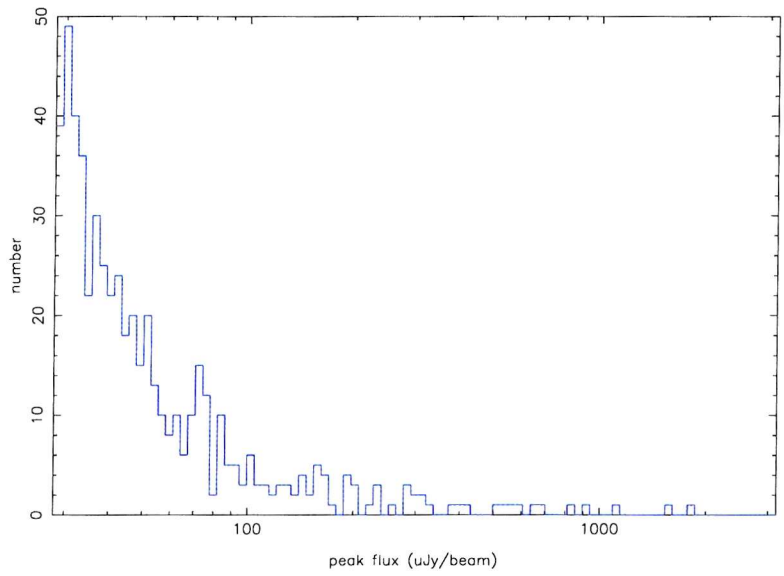


Figure 2.6: A Histogram of peak fluxes of the 1.4 GHz sources

the AIPS algorithm TVSTAT (which finds the total flux in an irregular area defined by the user). However there were only 6 sources where SAD failed due to extended morphology (discussed further in section 4.1.3.2). SAD was initially instructed to search for sources above a three sigma peak flux (ie 22.5 $\mu$Jy/beam).

Each source was checked to see if it was spurious (e.g. part of a side-lobe) and a dozen or so were discarded. Additionally all the maps were checked for possible real sources with four sigma peak flux which had not been found by SAD . This led to only 3 more sources being included in the four to five sigma range. Ultimately only sources with a $4\sigma$ peak flux were included. The histogram showing the distribution of empirical peak fluxes is shown in figure 2.6.

#### 2.4.1.1 The 6″ Resolution Map

In order to look for any possible low surface brightness objects in the field a map was constructed in exactly the same fashion as before except it was tapered to have a resolution of 6″ (thereby increasing the sensitivity to low surface brightness sources). This was done by setting the parameter in IMAGR UVTAP to 35 35. This parameter specifies the widths, in the U and V directions of the *uv* data in units of kilowavelength, of a Gaussian function used to weight down long baseline data points. It causes an image to be relatively more sensitive to larger scale structure. This has the effect of increasing the restoring beam and hence decreasing the resolution. The tapered image had an rms of 12.5 $\mu$Jy and a natural restoring beam of 6.07″. The sources were extracted with SAD and the list correlated with the original list to look for new sources. Six new, slightly extended sources with a peak flux above $4\sigma$

(50 $\mu$Jy) were discovered and added to the final catalogue in table 2.2.

## 2.4.2 Bias

### 2.4.2.1 SAD Bias

There is a known bias in the SAD elliptical fitting algorithm (Condon, 1997) which at low signal/noise overestimates a source's angular size due to fluctuations in the noise at the edge of a source. The total flux is calculated from the total angular size and the peak flux (which is not affected by this bias) and hence the total flux is overestimated. This effect was investigated by a number of simulations where 64 fake sources of a particular flux were inserted into each of the nine residual images left over from the running of SAD (i.e. the original maps with all the sources found by SAD removed). These sources were inserted with the task IMMOD and then extracted by SAD (having been visually inspected to check that no sources were coincident with any artifacts in the residual maps caused by the initial execution of SAD). This was repeated three times each for peak fluxes of 140 $\mu$Jy down to 21 $\mu$Jy at intervals of 7 $\mu$Jy. It was then possible to plot the average overestimate of the total flux of a source as function of peak flux.

Figure 2.7 shows the fractional overestimate increasing with decreasing flux. An empirical polynomial curve was fitted to this plot which was then used to correct for the total flux of every source. It was also possible to calculate the fraction of the model sources that were undetected by SAD as a function of peak flux due to the noise in the maps (see figure 2.8). This was also fitted with an empirical polynomial curve. This later came in useful for calculating the completeness of the log(N)-log(S) source counts, see section 2.5.

### 2.4.2.2 Instrumental Correction

There are 4 instrumental biases which need to be considered; the Primary Beam, Chromatic Aberration (Bandwidth Smearing), Time Delay Smearing and 3D Smearing. These are discussed below.

1. The Primary Beam

   The ultimate limiting factor to the field of view is the diffraction-limited response of the individual antennas. For the *VLA* at 1.4 GHz the full width at half power is $\sim 30'$ which was taken to be limit of the field of view. This causes a decrease in sensitivity away from the pointing centre (i.e. the attenuation of the primary beam) as a function of radial distance which was used to correct

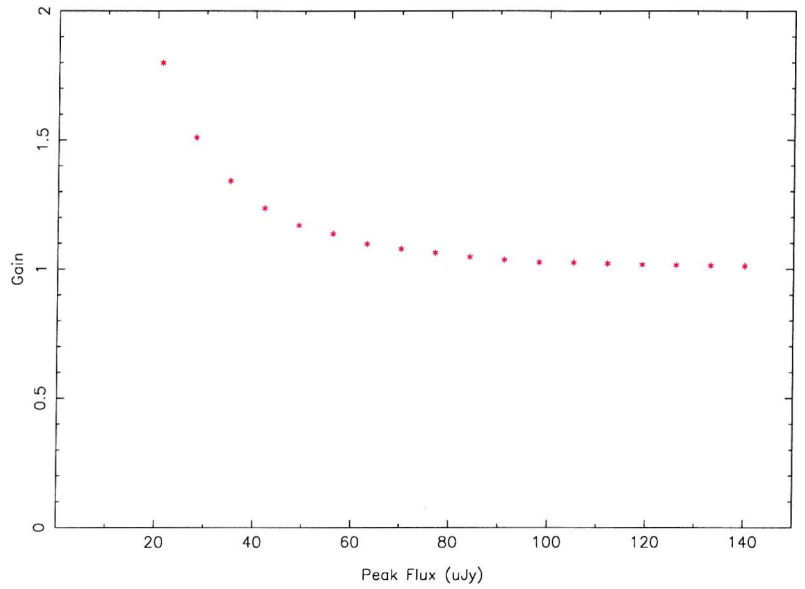


Figure 2.7: A plot of the average measured fractional increase in total flux for model point sources inserted into the residual data shown as a function of the input peak flux.

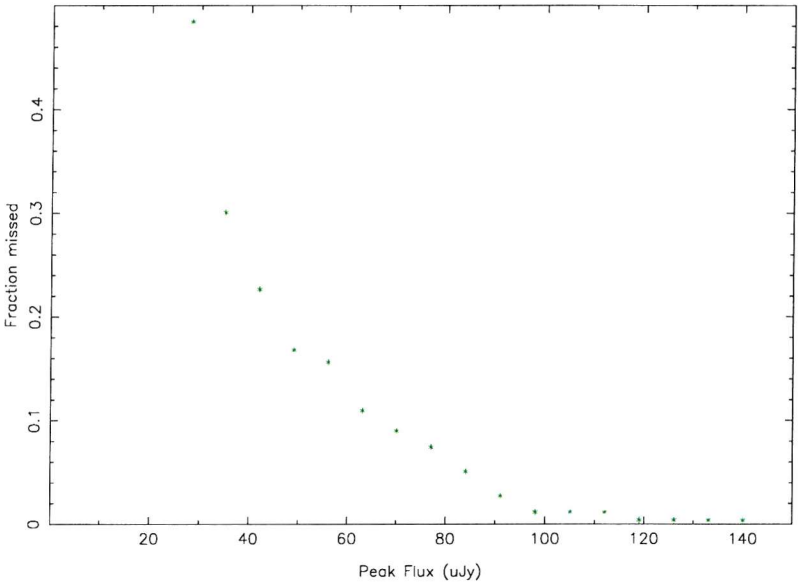


Figure 2.8: A plot of the average fraction of sources inserted into the residual data which are not detected by SAD shown as a function of the input peak flux.

the integrated flux. The empirically measured primary beam attenuation as given by Rick Perly in the explain file for the AIPS task PBCOR was used to correct for the measured peak and integrated flux of the sources (although the signal to noise given in table 2.2 is the empirically measured one).

2. Chromatic Aberration

   Chromatic aberration was discussed in section 2.2. The empirically measured function by Richards (2000) was used as a reasonable approximation to the effect on the data[4]. Theoretical and measured models for chromatic aberration are not available for combined arrays so the Richards formula for the A-configuration at 20cm was used to estimate the fraction of sources missed in each bin of the log(N)-log(S) plot. The effect of bandwidth smearing on the empirical data is shown in figure 2.9. The mean ratio of peak over integrated fluxes given as a function of radial distance. Each bin includes many resolved sources so even the most central bin does not approach unity.

3. Time Delay Smearing

   The sampled coherence function of an object not at the pointing centre varies slowly with time due to the slowly changing geometry of the array relative to the sky. Therefore over a certain observing interval there is a decrease in amplitude compared to a shorter observing interval. The sky was observed with 3.3second visibility sampling intervals (the minimum available with a full array) in both the A and B-configurations and by not averaging this any effect of time-delay smearing was minimised.

4. 3D smearing

   The procedures of creating most images in Fourier Synthesis imaging are based on the assumptions that all antenna pairs are in the same plane, but this only strictly true for east-west interferometers which the VLA is not. This problem reveals itself in errors on sources the further away from the centre of the field they are. This becomes serious at distances where the product of the angular offset in radians times the angular offset in units of the synthesized beam exceeds unity. For these observations this corresponds to a distance of 831.3″ for the combined data set with a restoring beam of 3.35″ and 537.4″ for just the A-configuration data which has a restoring beam 1.4″.

   Although this effect is only noticeable at 1.4 GHz in certain instances a multi-faceted observing strategy (section 2.3) was used so that no part of the survey field was more than 482.7″ away from the centre of a map. Due to the computing power available it was possible to deconvolve each field simultaneous in IMAGR and use the DO3D option (available in more recent versions of AIPS).

[4]The formula used was $S_{peakflux}/S_{integratedflux} = (1+(r/k)^2)^{-0.5}$ where r is the distance from the field centre and k was found to be 16.19′ from a least squares fit to the off-axis measurements of the peak and integrated flux of the calibrator source 1400+621 as a function of distance from the image centre.

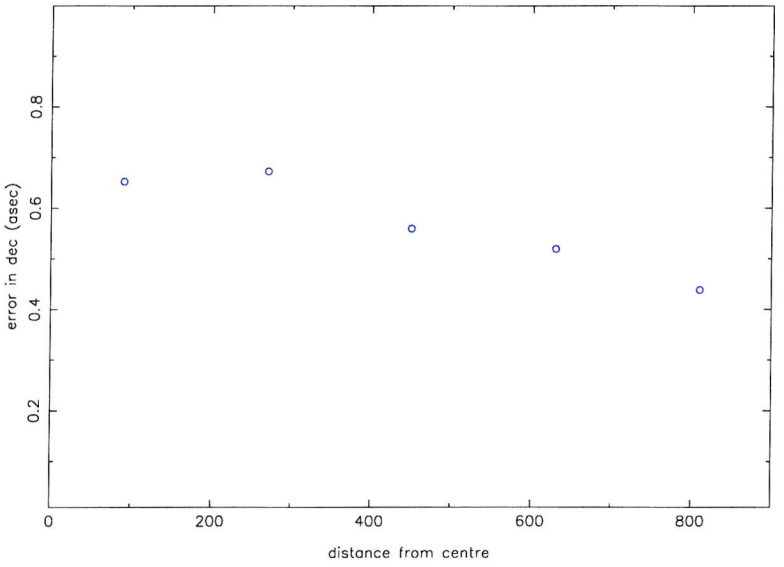


Figure 2.9: Plot to show the effect of bandwidth smearing by showing the mean peak flux to total flux ratio as a function of radial distance of the empirically observed data. Each bin includes all sources with many resolved sources and is not corrected for any other effects (e.g. primary beam attenuation) so even the most central bin does not approach unity.

Additionally the positions of sources measured from maps made with large Fields of view (e.g. figure 2.5) were compared with those measured from 30″ 'postage-stamp' images centred on the source (see appendix). It was found that the discrepancies in position were virtually all better than 0.3″. No corrections for the annual aberration effect were made which leads to an discrepancy of almost an order of magnitude less than the error due to 3D smearing. Total positional errors are discussed more in section 2.4.2.4.

#### 2.4.2.3 The distribution of angular sizes

In figures 2.10 and 2.11 the distribution of the deconvolved angular size (as determined by SAD) is presented as a function of peak and total radio luminosity. If a source has a measured minor axis smaller than the beam (3.35″) then SAD returns a nominal deconvolved angular size of zero (i.e. unresolved). The angular size of a source was defined as the mean of the major and minor axis of the fitted elliptical Gaussian. Unresolved sources have been given a nominal size of 1″. At low signal to noise SAD overestimates the size of a source (section 2.4.2.1) so it is unwise to interpret the angular sizes of sources below 100 $\mu$Jy as being accurate. They are probably smaller than indicated on the plots and would continue the trend of decrease in angular size observed by Richards, 2000. As SAD calculates the total

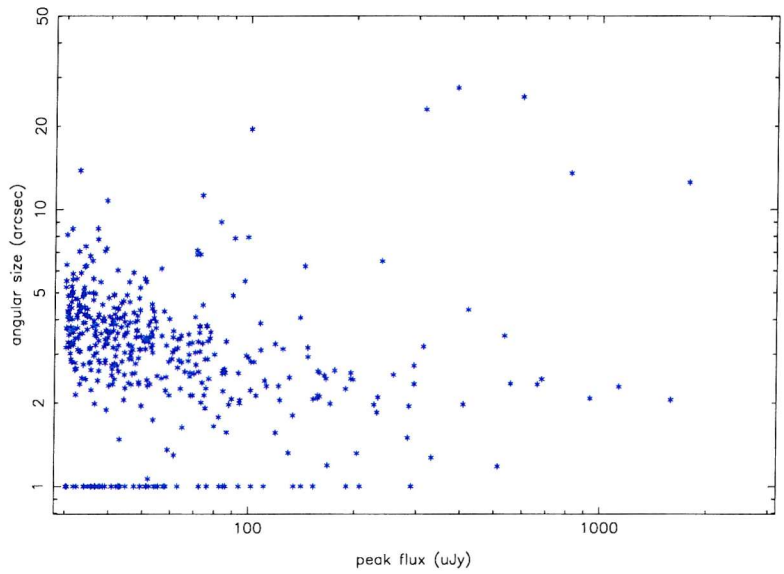


Figure 2.10: Plot to show the angular size of a source against peak flux. All sources unresolved by SAD are given a nominal value of 1″. At low signal to noise SAD overestimates the size of a source (section 2.4.2.1) so it is unwise to interpret the angular sizes of sources below 100 $\mu$Jy as being accurate.

flux from the deconvolved angular size and the peak flux, figure 2.11 illustrates the surface brightness limit of source at low signal to noise.

#### 2.4.2.4 Other issues and the final source list

In different radio surveys there have been different methods for determining whether two nearby unresolved sources are actually doubles (e.g. flux ratio $\leq$ 2 and the separation $\leq$ 2$\times$ the restoring beam, Ciliegi et al., 1999 and nearest neighbour density pair distribution function, Prandoni et al., 2000. Very few of the sources (21 pairs) could be considered to be double by the first of these criteria and many pairs of sources with small separations have both been found to each have optical counterparts suggesting that they are pairs of separate galaxies rather than extended emission from just one (optical spectra have shown that some pairs of galaxies are physically related, i.e. at similar redshifts). The optical data are presented in chapter 4 and optical 'postage-stamp' images with radio contours of all sources are included in the appendix.

The systematic error in the position of each sources was taken to be 0.1″ (which is a conservative estimate for the VLA under normal conditions, VLA Observational Status Summary, 2002). The random error in a source is defined by the point-spread function (i.e. the FWHM of the restoring beam, 3.35″) divided by twice the signal to noise ratio (although this only strictly valid for unresolved or only slightly

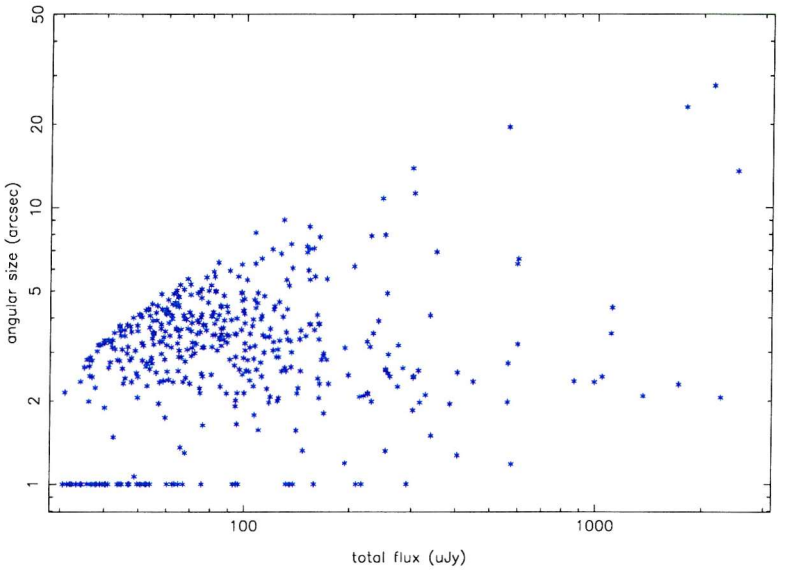


Figure 2.11: Plot to show the angular size of a source against total flux. All sources unresolved by SAD are given a nominal value of 1″. The surface brightness limit of a source at low signal to noise is illustrated here by the lack sources in the upper left of this plot.

resolved sources, see Condon (1997) for a thorough discussion). With a $4\sigma$ source limit of $30\,\mu$Jy/beam this means that the maximum statistical error is 0.42″ giving a maximum total error of 0.43″ for a $4\sigma$ source. In the final list of sources an error in the source position is not given, but it is only noted that the error is in the range $0.1 - 0.43''$ depending on the signal to noise. For the six extended sources originally mentioned in section 2.4.1, and discussed in detail in section 4.1.3.2, the positions given are those of the optical counterparts which are accurate to 0.3″.

The full list of sources is presented in table 2.2 at the end of this chapter. This list contains 462 sources above a $4\sigma$ peak flux limit of $30\,\mu$Jy/beam. The first column is the source number, the next six columns are the Right Ascension and declination (J2000), the eighth column is the angular size of the source (zero means it is unresolved), the ninth column is the signal to noise ratio, the tenth column in the peak flux corrected for primary beam attenuation, and the final two columns are the total integrated flux and its error from SAD both also corrected for primary beam attenuation.

# 2.5 The Source Counts

## 2.5.1 The log(N)-log(S) plot background

Interpretation of radio sources counts has been subject of intensive study for over 40 years. Early on in the analysis of the Cambridge Radio Surveys it was realised that evolution of luminous radio sources was required to explain the 178 MHz source counts (Longair, 1966). His initial suggestion was that density evolution of the populations of radio loud quasars could be responsible. It was later suggested and then confirmed that luminosity evolution was more likely to be the main culprit. It was shown that the quasar population undergoes strong luminosity evolution in the the redshift range $0 \leq z \leq 2$ for an optically selected sample (Boyle et al., 1988). Between redshifts 2 and 5 the space density of quasars seems to be approximately constant (McMahon et al., 1992).

Assuming we are in a flat Euclidean universe, with no evolution of the luminosity function, the surface density of galaxies (the number per unit area of sky) observed at a given wavelength plotted as a function of their apparent brightness will have a shape proportional to $S^{-2.5}$ ($S$=observed flux) . Therefore for a plot of real data normalised by $S^{2.5}$ any deviation would imply that either or both of the previous assumptions is false. By modelling known local luminosity functions for certain classes of radio sources (e.g.AGN and starburst) and assuming that they apply to more distant sources except with either evolution in their luminosity or density we can hope to match the observed source counts.

With deeper radio surveys the modelling of faint source counts has advanced a lot in the past ten years. Fits to the current deepest radio surveys at 1.4 GHz (Hopkins et al. 1998 and references therein) seem to show that both starburst and AGN components are required to explain the radio source counts across the flux range $S_{1.4\,\mathrm{GHz}} = 10^{-1} - 10^{4}$ mJy with a modest amount of luminosity evolution of the starburst galaxies.

The determination of evolutionary models is beyond the scope of this thesis. As this survey does not increase the parameter space of the log(N)-log(S) plot, it only adds to an already well sampled part of it, the replication of sophisticated models would be unnecessary. Here just the determination of the plot is presented and comparisons with other plots discussed.

| Bin ($\mu$Jy) | $< S_{1.4} >$ ($\mu$Jy) | $N_{sources}$ | Correction | $dN/dS(S^{2.5})\mathrm{sr}^{-1}\,\mathrm{Jy}^{1.5}$ |
|---|---|---|---|---|
| 50-64.9 | 56.96 | 42 | 2.86 | 3.30 $\pm$0.51 |
| 64.9-82 | 72.95 | 47 | 1.69 | 3.53 $\pm$0.51 |
| 82-100.5 | 90.78 | 52 | 1.20 | 4.42 $\pm$0.61 |
| 100.5-121.6 | 110.55 | 36 | 1.0 | 3.66 $\pm$0.61 |
| 121.6-148 | 134.15 | 32 | 1.0 | 4.22 $\pm$0.75 |
| 148-188.9 | 167.20 | 26 | 1.0 | 3.84 $\pm$0.75 |
| 188.9-263 | 222.89 | 25 | 1.0 | 4.18 $\pm$0.84 |
| 263-327 | 293.26 | 10 | 1.0 | 3.85 $\pm$1.27 |
| 327-600 | 442.94 | 15 | 1.0 | 3.79 $\pm$0.98 |
| 600-100000 | 7745.97 | 17 | 1.0 | 15.10 $\pm$3.66 |

Table 2.1: The differential sources counts, normalised to a Euclidean, non-expanding universe. The first column shows the bin range, the second one the bin centre (both in $\mu$Jy), the third column the number of sources found in that range, the fourth column shows the multiplicative correction for the biases described in the text and the final column shows the normalised source counts per steradian for each bin with Poisson errors derived from the number of sources in each bin.

### 2.5.2 Completeness

For the statistically complete sample a 5 sigma peak detection (*i.e.* 37.5 $\mu$Jy/beam) was chosen before the primary beam correction had been applied and an integrated flux limit of 50 $\mu$Jy (after correcting for the primary beam) to minimise the corrections needed at very low signal to noise. All these sources were binned in flux density space and the source counts were based on the number of sources in each bin. It was necessary to correct for the effective area over which a source could have been detected due to the attenuation of the primary beam and chromatic aberration reducing the sensitivity of the survey away from the centre of the field. Additionally each bin was multiplied by a factor to correspond to the number of sources missed by the source extraction algorithm and the non-Gaussian nature of the noise of the maps (as explained in section 2.4.2.1). The total correction for these effects for each bin is shown in table 2.5.2. This table presents the differential source counts for the complete flux limited sample. The sources were binned so that they were better sampled at the faint end where the number of sources is more dense. The table shows the bin range, bin centre (both in $\mu$Jy), the number of sources found in that range, the multiplicative corrections for the biases described in section 2.4.2 and then the normalised source count of sources per steradian for each bin with a Poisson error derived from the number of sources in each bin.

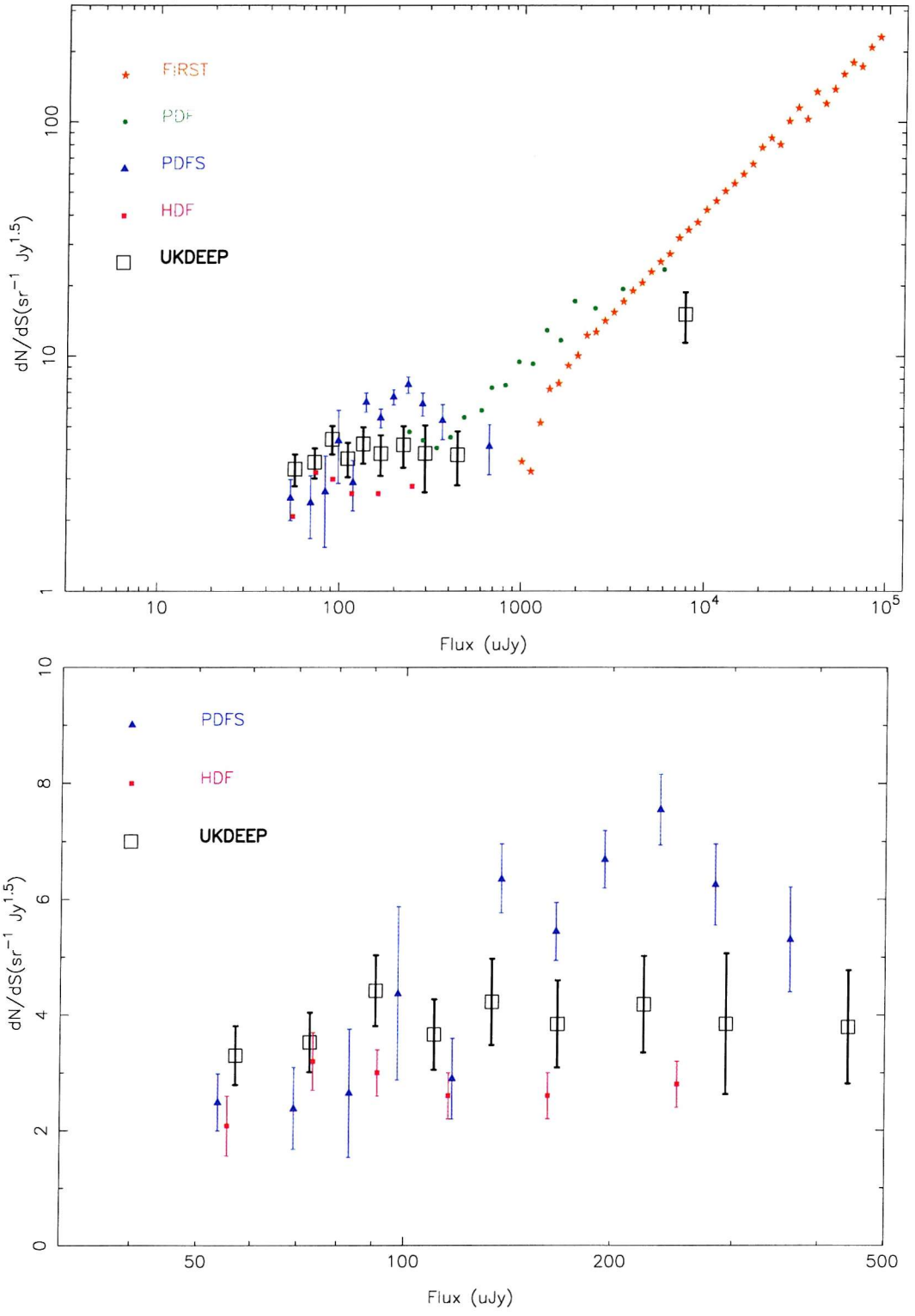


Figure 2.12: The 1.4 GHz Differential Source Counts of this survey (normalised to a Euclidean, non-expanding universe) compared to other surveys; the FIRST survey (White et al., 1997), the Phoenix Deep Field (PDF) and Phoenix Deep Field Subregion (PDFS) (Hopkins et al., 1998), and the Hubble Deep Field (HDF) (Richards 2000). The lower panel shows a close up of the sub-500 mJy region with a linear vertical scale.

### 2.5.3 Comparison of our log(N)-log(S) data with other results

The differential log(N)-log(S) plot is shown in figure 2.12 (normalised to a Euclidean, non-expanding universe) along with other recent results. From $100 - 1$ mJy the source counts from the 'Faint Images of the Radio Sky at Twenty centimetres' (FIRST) survey (White et al., 1997) are plotted as stars. As circles and triangles the results of the Phoenix Deep Field (PDF) survey and Phoenix Deep Field Subregion (PDFS) survey respectively are shown (Hopkins et al., 1998). As squares the results from the Hubble Deep Field are shown (Richards, 2000) whilst the results from the UK Deep X-ray survey are shown as large open squares. All the surveys below 1 mJy show an up turn above a Euclidean normalised slope. This also seen in other deep surveys at 1.4 GHz (e.g. Windhorst et al. 1990, Prandoni et al. 2001 and Gruppioni et al. 1999), but these are not shown to avoid overcrowding the plot. This upturn is interpreted as the presence of population of faint sources revealing themselves. These sources tend to be relatively low luminosity galaxies at moderate redshifts (i.e. $z \leq 1$) Samples of faint galaxies have revealed signs of star formation in their optical spectra, indicating that they are related to local objects detected in 60$\mu$m surveys (Benn et al., 1993). This observation combined with the evidence of a radio(1.4 GHz)-FIR(60$\mu$m) correlation (Helou et al., 1985)[5], implies that a significant portion of the faint radio population are starburst galaxies.

Apart from the up turn the most noticeable feature of the sub-mJy counts is the relatively wide scatter in values at a given flux below 1 mJy (see the close up in the lower panel of figure 2.12). Around a few hundred $\mu$Jy there is a scatter of over a magnitude in normalised source counts. Interestingly the surveys seem to re-converge below 100 $\mu$Jy. Why there is this scatter is unclear, but the most obvious answer is some kind of selection effect is at work. The sub- mJy reconverging must be taken with a pinch of salt because at low signal noise the affects of biases described earlier are most strong. The PDF was selected to have a larger area (2° radius) than previous very deep radio surveys to avoid the problem of selecting an unrepresentative pencil-beam wedge of the sky, but the PDFS only has an radius of 35′ similar to the UK Deep Survey. As a designated radio survey it was also chosen to be free of bright radio sources ($>$ 100 mJy at 4.55 MHz[6]) to avoid problems that would be caused by having a bright source in the field (see section 2.2.2). The HDF region has a similar area, 40′, and was also chosen to be free of radio sources, but with a more stringent limit: no sources $>$ 1 mJy at 8.3 GHz. Additionally the HDF was selected to be a multi-wavelength survey so it was chosen to be free of bright sources at other wavelengths (especially free from foreground stars and bright nearby clusters). This further increased the selection effects as all sources emit to

[5]continued by Garrett, 2002, to $z \sim 1.3$

[6]Although this criteria and the one for the HDF were for the lack of objects at frequencies higher than 1.4 GHz the reader should be reminded that these surveys here were conducted at 1.4 GHz.

some degree over the whole spectral energy range so de-selecting bright sources at one wavelength must slightly affect the numbers of sources at other wavelengths. By minimising the number of bright sources in your field you are probably decreasing the number of faint sources in your field as it is likely that bright and faint sources have the similar distributions in space due to large scale clustering. This strong selection effect is probably why the HDF source counts are so much lower than the others.

The UK Deep survey has different criteria being selected initially purely as an X-ray survey region. The general area in the sky was selected by the low neutral hydrogen column density ($N_H = 6.5 \times 10^{19}\,\mathrm{cm}^{-2}$) and finally pinned down by having low 100$\mu$m cirrus (M$^{\mathrm{c}}$Hardy et al., 1998). There was no selection based on the presence of radio sources at all. In fact there are over 50 sources that break the selection criteria for the PDF, extrapolating their limit to 1.4 GHz assuming a radio spectrum of $\alpha \sim 0.7$. It is most likely that the scatter in source counts is due to real field to field variations between the different surveys. This is consistent with the idea that many of the faint sources are relatively nearby sources of modest radio luminosity due to star formation activity and possibly very quiet AGN activity.

## 2.6 Summary

From a total of $\sim$ 25hours of data from the VLA at 1.4 GHz in both A and B-configuration, 462 sources are detected down to a peak flux 4$\sigma$ limit of 30 $\mu$Jy in a circular field with a 30′ diameter. The full source list is presented in table 2.2. This is one of the most sensitive surveys ever made at this frequency and resolution comparable to 7.5 $\mu$Jy/beam rms noise with 1.8″ resolution of the HDF (Richards, 2000) and the 4.8 & 9.2 $\mu$Jy/beam rms noise with 1.4″ resolution of the Lockman Hole East and the ELIAS N2 surveys (Ivison et al., 2002). Other comparably deep surveys have been performed with lower resolution arrays, e.g. the C or D-configuration of the VLA, the Australia Telescope Compact Array and the Westerbork Synthesis Radio Telescope. The log(N)-log(S) confirms the trend of other surveys covering similar parameter space of an upturn of the Euclidean normalised source counts below 1 mJy, believed to be due to the emergence of a new population of faint radio sources.

## 2.7 The complete 1.4 GHz source list

In this section the complete 1.4 GHz source list is presented. Sources are ordered by total flux and the first column gives a source's position in the list. The next two columns are the Right Ascension and Declination (J2000). The fourth column is the

mean angular size of a source. The fifth column is the signal to noise ratio before corrections are made for the attenuation of the primary beam. The final 3 columns are the peak flux, integrated flux and the error of the total flux all corrected for the primary bream attenuation.

Table 2.2: Complete 1.4 GHz Source List (see previous page for details).

| Source | Right Ascension hh mm ss | Declination ° ′ ″ | $\theta_{dec}$ (″) | $\sigma_{snr}$ | $S_{peak}$ ($\mu$Jy) | $S_{integrated}$ ($\mu$Jy) | $\Delta S$ ($\mu$Jy) |
|---|---|---|---|---|---|---|---|
| 1 | 13 33 29.040 | 37 55 57.90 | 35.0 | 1117.9 | 13985.2 | 92681.0 | 256.5 |
| 2 | 13 34 3.011 | 37 59 49.18 | 1.8 | 1160.7 | 10539.6 | 11624.0 | 20.6 |
| 3 | 13 34 38.496 | 38 06 27.01 | 2.1 | 999.9 | 10980.8 | 10939.0 | 23.4 |
| 4 | 13 35 16.664 | 38 00 8.19 | 3.5 | 515.7 | 4946.5 | 8017.0 | 26.9 |
| 5 | 13 33 59.951 | 37 49 11.64 | 12.5 | 236.3 | 2227.9 | 3918.8 | 498.8 |
| 6 | 13 34 57.650 | 37 50 29.40 | 25.5 | 79.4 | 653.0 | 3680.7 | 0.0 |
| 7 | 13 34 38.015 | 37 57 10.33 | 13.5 | 109.3 | 833.1 | 2510.5 | 178.6 |
| 8 | 13 35 6.603 | 38 03 48.64 | 2.0 | 210.7 | 2176.6 | 2260.0 | 22.0 |
| 9 | 13 34 49.260 | 38 05 52.50 | 27.5 | 51.7 | 555.8 | 2146.9 | 108.4 |
| 10 | 13 35 25.340 | 38 05 33.90 | 23.0 | 42.0 | 569.8 | 1790.6 | 125.5 |
| 11 | 13 34 38.106 | 37 41 33.46 | 2.3 | 150.1 | 1836.5 | 1715.0 | 26.1 |
| 12 | 13 35 35.475 | 37 53 14.30 | 2.1 | 124.5 | 1359.6 | 1362.4 | 21.8 |
| 13 | 13 34 13.571 | 37 45 39.30 | 4.3 | 56.0 | 557.8 | 1112.0 | 33.8 |
| 14 | 13 34 5.407 | 38 07 37.99 | 3.5 | 70.9 | 955.0 | 1103.2 | 38.0 |
| 15 | 13 33 46.583 | 38 00 22.26 | 2.4 | 90.5 | 974.2 | 1041.9 | 27.1 |
| 16 | 13 34 58.392 | 38 04 29.88 | 2.3 | 88.0 | 900.9 | 989.1 | 22.6 |
| 17 | 13 35 49.175 | 37 51 35.33 | 2.3 | 74.0 | 1019.9 | 865.5 | 28.8 |
| 18 | 13 33 59.951 | 37 49 11.64 | 6.5 | 31.7 | 298.5 | 597.5 | 73.4 |
| 19 | 13 35 44.626 | 37 57 42.78 | 3.2 | 41.7 | 530.6 | 596.7 | 30.2 |
| 20 | 13 35 16.292 | 37 56 21.43 | 6.2 | 19.1 | 169.9 | 593.9 | 43.1 |
| 21 | 13 34 42.846 | 37 57 34.12 | 1.2 | 68.1 | 523.6 | 574.0 | 15.0 |
| 22 | 13 34 39.874 | 37 57 2.66 | 19.5 | 13.4 | 102.1 | 560.4 | 21.1 |
| 23 | 13 33 49.923 | 38 03 34.41 | 2.7 | 39.2 | 465.8 | 560.3 | 139.4 |
| 24 | 13 35 13.273 | 37 48 57.21 | 2.0 | 54.3 | 512.4 | 559.0 | 19.4 |
| 25 | 13 34 40.030 | 37 42 52.48 | 2.3 | 39.3 | 435.9 | 446.4 | 24.2 |
| 26 | 13 34 53.824 | 37 48 16.32 | 1.3 | 44.1 | 381.0 | 403.3 | 16.5 |
| 27 | 13 34 51.997 | 37 57 43.56 | 2.5 | 34.3 | 269.5 | 402.9 | 18.7 |
| 28 | 13 34 57.310 | 37 47 59.01 | 1.9 | 38.0 | 336.5 | 383.9 | 18.0 |
| 29 | 13 34 47.565 | 37 40 56.53 | 6.9 | 9.7 | 126.0 | 350.5 | 70.0 |
| 30 | 13 34 13.642 | 37 57 32.89 | 1.5 | 37.7 | 305.3 | 339.7 | 17.6 |
| 31 | 13 34 1.322 | 37 48 29.16 | 4.1 | 18.6 | 177.6 | 336.8 | 30.6 |
| 32 | 13 33 58.546 | 37 56 9.09 | 2.1 | 31.0 | 272.5 | 327.3 | 21.0 |
| 33 | 13 35 1.685 | 37 47 26.09 | 2.0 | 30.2 | 278.9 | 315.4 | 19.1 |
| 34 | 13 35 0.786 | 37 44 8.48 | 2.6 | 25.9 | 281.9 | 312.3 | 24.6 |
| 35 | 13 33 48.906 | 37 43 31.16 | 11.2 | 9.8 | 136.4 | 302.8 | 117.0 |
| 36 | 13 35 48.319 | 37 58 52.13 | 2.4 | 25.9 | 359.4 | 302.8 | 28.9 |
| 37 | 13 34 46.491 | 37 42 47.43 | 2.4 | 26.3 | 296.4 | 302.2 | 24.7 |
| 38 | 13 34 40.642 | 37 55 45.57 | 1.8 | 30.8 | 231.8 | 301.4 | 16.0 |
| 39 | 13 33 28.072 | 37 59 20.82 | 13.8 | 4.4 | 58.9 | 299.2 | 182.8 |
| 40 | 13 34 26.260 | 37 56 23.22 | 0.0 | 38.6 | 294.9 | 290.0 | 14.8 |
| 41 | 13 35 4.775 | 37 49 2.92 | 2.6 | 23.3 | 206.9 | 282.1 | 20.1 |
| 42 | 13 35 48.866 | 37 51 15.11 | 3.2 | 19.5 | 270.0 | 273.9 | 32.6 |

Table 2.2: Complete 1.4 GHz Source List (continued)

| Source | Right Ascension hh mm ss | Declination ° ′ ″ | $\theta_{dec}$ (″) | $\sigma_{snr}$ | $S_{peak}$ ($\mu$Jy) | $S_{integrated}$ ($\mu$Jy) | |
|---|---|---|---|---|---|---|---|
| 43 | 13 33 48.194 | 37 53 54.16 | 2.2 | 25.1 | 242.5 | 272.8 | 23.5 |
| 44 | 13 35 14.814 | 38 01 10.26 | 2.4 | 22.1 | 215.5 | 259.2 | 23.3 |
| 45 | 13 33 58.842 | 37 43 21.32 | 2.9 | 19.6 | 248.7 | 256.6 | 32.5 |
| 46 | 13 34 32.592 | 37 58 2.73 | 2.5 | 21.8 | 168.5 | 256.0 | 18.4 |
| 47 | 13 34 13.669 | 37 59 44.70 | 4.9 | 12.0 | 101.6 | 254.1 | 33.7 |
| 48 | 13 34 20.980 | 37 59 30.75 | 1.3 | 27.0 | 221.3 | 252.6 | 18.2 |
| 49 | 13 33 48.390 | 37 54 57.52 | 2.6 | 21.1 | 203.3 | 252.4 | 24.9 |
| 50 | 13 35 0.206 | 37 56 33.14 | 2.6 | 20.9 | 167.2 | 251.8 | 19.4 |
| 51 | 13 35 31.909 | 37 45 35.76 | 7.9 | 13.2 | 175.7 | 250.4 | 82.1 |
| 52 | 13 34 11.575 | 38 01 19.36 | 10.8 | 5.2 | 47.2 | 245.9 | 77.3 |
| 53 | 13 34 22.738 | 37 55 25.25 | 3.9 | 14.3 | 109.8 | 240.2 | 25.5 |
| 54 | 13 34 0.259 | 37 49 23.64 | 3.5 | 8.5 | 79.8 | 232.1 | 15.3 |
| 55 | 13 34 41.819 | 38 00 11.09 | 2.0 | 22.7 | 184.5 | 229.9 | 17.7 |
| 56 | 13 33 44.489 | 38 03 43.66 | 7.9 | 12.1 | 154.3 | 228.4 | 78.8 |
| 57 | 13 33 42.740 | 37 52 39.77 | 3.1 | 16.6 | 172.9 | 227.6 | 29.9 |
| 58 | 13 33 57.045 | 37 51 25.78 | 2.1 | 21.1 | 193.2 | 224.2 | 21.9 |
| 59 | 13 34 17.587 | 37 44 32.93 | 2.1 | 20.9 | 216.9 | 224.0 | 23.2 |
| 60 | 13 35 18.698 | 37 55 31.62 | 3.3 | 15.8 | 142.5 | 223.0 | 24.7 |
| 61 | 13 34 14.025 | 37 57 12.82 | 2.1 | 20.9 | 167.9 | 218.3 | 19.1 |
| 62 | 13 34 36.240 | 37 51 6.68 | 0.0 | 25.2 | 196.0 | 215.9 | 15.3 |
| 63 | 13 35 14.124 | 37 51 28.12 | 2.1 | 20.3 | 181.0 | 212.3 | 19.8 |
| 64 | 13 34 33.169 | 37 52 21.28 | 0.0 | 27.5 | 210.0 | 208.4 | 13.8 |
| 65 | 13 34 14.506 | 38 04 46.88 | 6.1 | 7.5 | 78.2 | 204.6 | 49.6 |
| 66 | 13 34 27.505 | 38 08 32.46 | 2.5 | 17.3 | 225.6 | 197.5 | 29.5 |
| 67 | 13 34 9.906 | 37 54 31.84 | 1.2 | 22.3 | 180.5 | 193.5 | 17.2 |
| 68 | 13 33 42.365 | 38 03 36.17 | 3.1 | 14.4 | 187.2 | 192.9 | 34.1 |
| 69 | 13 34 47.374 | 37 59 49.84 | 2.3 | 16.2 | 131.4 | 173.4 | 18.6 |
| 70 | 13 33 45.243 | 37 58 8.19 | 5.5 | 12.9 | 133.1 | 171.2 | 49.6 |
| 71 | 13 33 36.753 | 37 53 4.53 | 2.8 | 13.8 | 154.1 | 171.0 | 30.4 |
| 72 | 13 34 30.945 | 37 47 32.47 | 1.8 | 17.7 | 153.4 | 168.3 | 17.1 |
| 73 | 13 35 29.639 | 37 51 27.90 | 3.0 | 13.1 | 136.1 | 167.7 | 23.6 |
| 74 | 13 35 0.294 | 38 01 57.84 | 2.9 | 13.3 | 121.5 | 167.5 | 22.3 |
| 75 | 13 34 43.450 | 37 49 21.55 | 2.8 | 13.5 | 109.7 | 165.5 | 19.1 |
| 76 | 13 35 35.883 | 37 57 38.23 | 2.3 | 14.9 | 166.6 | 163.4 | 22.8 |
| 77 | 13 34 49.882 | 37 53 36.71 | 3.8 | 10.1 | 77.5 | 163.0 | 23.4 |
| 78 | 13 34 24.003 | 38 00 30.49 | 2.0 | 16.3 | 136.0 | 162.9 | 19.6 |
| 79 | 13 33 32.018 | 37 56 51.08 | 7.8 | 4.9 | 59.4 | 162.8 | 92.8 |
| 80 | 13 35 14.374 | 37 45 40.50 | 3.3 | 11.5 | 125.8 | 162.5 | 28.4 |
| 81 | 13 33 26.742 | 37 57 13.05 | 3.8 | 10.1 | 132.8 | 162.4 | 47.4 |
| 82 | 13 34 50.016 | 37 49 48.10 | 2.4 | 14.8 | 120.2 | 161.6 | 17.7 |
| 83 | 13 35 30.245 | 37 56 39.02 | 4.1 | 9.4 | 96.1 | 160.7 | 29.0 |
| 84 | 13 34 33.689 | 37 47 19.92 | 5.6 | 6.7 | 58.5 | 158.3 | 35.9 |

Table 2.2: Complete 1.4 GHz Source List (continued)

| Source | Right Ascension hh mm ss | Declination ° ′ ″ | $\theta_{dec}$ (″) | $\sigma_{snr}$ | $S_{peak}$ ($\mu$Jy) | $S_{integrated}$ ($\mu$Jy) | |
|---|---|---|---|---|---|---|---|
| 85 | 13 34 53.141 | 37 50 43.94 | 0.0 | 20.3 | 163.6 | 158.1 | 14.9 |
| 86 | 13 35 17.277 | 37 54 15.92 | 3.6 | 10.4 | 92.2 | 157.8 | 26.1 |
| 87 | 13 35 33.819 | 37 48 31.96 | 7.1 | 9.5 | 112.5 | 156.8 | 60.8 |
| 88 | 13 34 17.114 | 38 00 39.97 | 3.8 | 9.6 | 82.8 | 153.7 | 28.1 |
| 89 | 13 35 30.518 | 38 04 4.96 | 5.5 | 6.8 | 89.3 | 153.0 | 49.3 |
| 90 | 13 34 26.509 | 38 00 27.97 | 3.8 | 9.7 | 80.0 | 152.8 | 26.9 |
| 91 | 13 33 41.280 | 37 54 27.02 | 7.1 | 5.2 | 54.0 | 152.7 | 65.8 |
| 92 | 13 33 36.839 | 37 56 48.00 | 8.5 | 4.2 | 46.7 | 152.2 | 92.7 |
| 93 | 13 33 36.377 | 38 02 44.15 | 5.9 | 6.2 | 84.4 | 151.6 | 61.8 |
| 94 | 13 33 57.795 | 38 06 4.26 | 6.9 | 9.5 | 120.8 | 150.2 | 69.0 |
| 95 | 13 34 44.879 | 37 41 46.75 | 7.2 | 5.2 | 63.1 | 149.9 | 64.5 |
| 96 | 13 34 22.710 | 37 46 56.94 | 3.4 | 10.3 | 93.1 | 149.2 | 25.4 |
| 97 | 13 34 41.143 | 37 51 16.15 | 1.3 | 17.3 | 133.9 | 146.9 | 15.4 |
| 98 | 13 34 30.272 | 37 55 25.84 | 3.6 | 9.6 | 72.7 | 144.4 | 22.0 |
| 99 | 13 33 56.464 | 38 04 6.96 | 2.6 | 12.4 | 142.5 | 144.3 | 27.4 |
| 100 | 13 34 45.975 | 37 40 1.77 | 3.3 | 10.2 | 143.2 | 143.5 | 36.7 |
| 101 | 13 35 1.209 | 37 59 37.44 | 2.2 | 13.5 | 114.5 | 142.1 | 19.4 |
| 102 | 13 34 45.107 | 37 55 42.51 | 2.1 | 14.0 | 105.7 | 141.1 | 16.8 |
| 103 | 13 34 39.770 | 37 58 15.38 | 1.6 | 15.9 | 123.0 | 140.6 | 15.8 |
| 104 | 13 34 52.419 | 37 42 45.41 | 0.0 | 12.5 | 143.6 | 138.0 | 25.3 |
| 105 | 13 33 40.756 | 37 54 45.61 | 6.0 | 5.6 | 59.1 | 136.4 | 54.4 |
| 106 | 13 34 0.893 | 37 47 5.84 | 3.0 | 10.6 | 107.5 | 136.0 | 26.2 |
| 107 | 13 34 1.210 | 37 55 24.39 | 2.6 | 11.4 | 97.6 | 135.6 | 22.8 |
| 108 | 13 33 23.151 | 37 58 16.76 | 7.4 | 4.5 | 64.9 | 135.2 | 104.6 |
| 109 | 13 34 13.095 | 38 02 7.81 | 3.3 | 9.8 | 90.7 | 134.9 | 25.0 |
| 110 | 13 34 33.204 | 37 55 10.02 | 0.0 | 18.8 | 141.2 | 134.9 | 13.3 |
| 111 | 13 34 29.790 | 37 54 40.64 | 0.0 | 17.9 | 134.6 | 134.6 | 13.8 |
| 112 | 13 34 57.733 | 38 03 37.30 | 5.2 | 6.5 | 63.5 | 133.5 | 37.2 |
| 113 | 13 35 24.718 | 37 51 19.51 | 3.3 | 9.6 | 94.3 | 132.4 | 24.0 |
| 114 | 13 34 57.836 | 37 50 6.42 | 4.3 | 7.6 | 63.5 | 132.1 | 26.2 |
| 115 | 13 35 12.871 | 37 52 39.78 | 0.0 | 14.7 | 127.8 | 131.5 | 17.9 |
| 116 | 13 34 58.953 | 37 40 47.57 | 3.5 | 9.0 | 123.9 | 131.3 | 37.4 |
| 117 | 13 33 38.535 | 37 47 33.80 | 5.5 | 6.1 | 76.8 | 131.2 | 53.7 |
| 118 | 13 35 14.684 | 37 48 38.99 | 2.6 | 11.4 | 110.3 | 131.1 | 21.8 |
| 119 | 13 35 12.267 | 37 51 31.16 | 2.6 | 11.2 | 98.7 | 130.0 | 21.4 |
| 120 | 13 34 2.402 | 38 03 6.02 | 9.0 | 11.0 | 114.1 | 128.8 | 64.6 |
| 121 | 13 35 48.525 | 37 54 49.98 | 4.0 | 7.9 | 104.5 | 128.3 | 37.0 |
| 122 | 13 33 44.295 | 37 57 52.66 | 2.6 | 11.2 | 116.2 | 127.4 | 26.7 |
| 123 | 13 33 31.064 | 37 59 24.91 | 6.8 | 4.7 | 60.3 | 126.5 | 85.7 |
| 124 | 13 35 12.280 | 37 49 47.20 | 3.3 | 9.2 | 83.9 | 125.6 | 23.6 |
| 125 | 13 34 54.194 | 37 46 41.72 | 4.5 | 7.0 | 64.9 | 125.2 | 30.3 |
| 126 | 13 34 15.602 | 38 03 4.88 | 2.0 | 12.6 | 119.5 | 125.0 | 20.7 |

Table 2.2: Complete 1.4 GHz Source List (continued)

| Source | Right Ascension hh mm ss | Declination ° ′ ″ | $\theta_{dec}$ (″) | $\sigma_{snr}$ | $S_{peak}$ ($\mu$Jy) | $S_{integrated}$ ($\mu$Jy) | |
|---|---|---|---|---|---|---|---|
| 127 | 13 34 43.508 | 37 50 27.45 | 2.9 | 10.2 | 80.3 | 124.7 | 20.1 |
| 128 | 13 34 31.416 | 37 48 31.27 | 3.1 | 9.7 | 80.6 | 124.2 | 20.5 |
| 129 | 13 34 28.690 | 37 46 47.35 | 2.0 | 12.5 | 112.4 | 124.0 | 18.4 |
| 130 | 13 34 14.678 | 37 46 14.36 | 2.9 | 10.0 | 96.3 | 123.0 | 24.4 |
| 131 | 13 34 46.605 | 37 45 29.62 | 4.4 | 7.1 | 67.4 | 121.4 | 30.6 |
| 132 | 13 34 11.425 | 37 52 39.34 | 4.3 | 7.1 | 58.0 | 121.0 | 29.4 |
| 133 | 13 35 16.732 | 37 51 29.40 | 3.3 | 9.0 | 81.8 | 120.6 | 24.9 |
| 134 | 13 35 6.236 | 38 02 32.98 | 3.0 | 9.4 | 90.9 | 120.2 | 24.4 |
| 135 | 13 33 32.880 | 37 57 6.11 | 7.1 | 4.4 | 52.0 | 119.5 | 82.8 |
| 136 | 13 35 9.324 | 37 55 3.53 | 2.1 | 11.9 | 99.5 | 118.2 | 18.4 |
| 137 | 13 34 36.831 | 37 56 20.24 | 3.6 | 8.1 | 61.3 | 118.1 | 22.2 |
| 138 | 13 34 14.131 | 38 04 39.31 | 3.4 | 8.5 | 88.0 | 117.3 | 29.0 |
| 139 | 13 34 29.999 | 37 56 40.17 | 2.0 | 11.7 | 89.1 | 117.2 | 16.9 |
| 140 | 13 34 28.929 | 37 53 32.66 | 2.2 | 11.3 | 85.3 | 115.5 | 17.1 |
| 141 | 13 33 51.965 | 38 02 29.77 | 3.4 | 8.4 | 92.1 | 114.4 | 30.5 |
| 142 | 13 34 0.017 | 37 58 55.85 | 4.8 | 6.5 | 58.8 | 113.5 | 34.7 |
| 143 | 13 34 54.429 | 38 03 0.05 | 3.0 | 9.0 | 83.9 | 113.3 | 23.3 |
| 144 | 13 34 40.580 | 38 07 54.60 | 3.5 | 8.1 | 99.2 | 112.4 | 33.3 |
| 145 | 13 34 23.323 | 38 03 0.55 | 2.4 | 10.2 | 94.3 | 111.7 | 21.4 |
| 146 | 13 34 7.019 | 37 48 44.77 | 4.1 | 7.1 | 64.8 | 111.6 | 28.8 |
| 147 | 13 35 3.560 | 38 05 2.84 | 6.5 | 4.8 | 51.7 | 111.3 | 51.9 |
| 148 | 13 34 56.543 | 38 04 28.12 | 3.9 | 7.2 | 73.3 | 111.0 | 30.4 |
| 149 | 13 34 58.329 | 38 06 37.25 | 2.7 | 9.4 | 110.3 | 110.9 | 27.9 |
| 150 | 13 35 19.399 | 37 50 12.37 | 1.6 | 11.5 | 110.8 | 109.6 | 19.3 |
| 151 | 13 34 33.995 | 37 57 39.15 | 4.9 | 6.0 | 45.9 | 108.7 | 28.9 |
| 152 | 13 35 20.180 | 37 50 33.35 | 4.5 | 9.8 | 94.3 | 108.4 | 41.5 |
| 153 | 13 35 14.764 | 37 52 58.32 | 2.6 | 9.6 | 84.2 | 108.0 | 21.2 |
| 154 | 13 34 8.220 | 37 59 6.04 | 4.3 | 6.5 | 56.1 | 107.2 | 31.3 |
| 155 | 13 34 33.619 | 38 05 42.98 | 6.3 | 4.6 | 47.8 | 106.9 | 50.9 |
| 156 | 13 35 36.236 | 37 54 43.00 | 8.1 | 4.0 | 44.1 | 106.7 | 57.0 |
| 157 | 13 34 30.986 | 37 56 57.90 | 3.2 | 8.3 | 63.6 | 106.7 | 20.5 |
| 158 | 13 33 58.769 | 37 49 52.74 | 1.8 | 10.9 | 102.2 | 106.6 | 20.3 |
| 159 | 13 35 23.825 | 38 03 32.44 | 4.6 | 6.1 | 72.0 | 106.4 | 41.0 |
| 160 | 13 35 3.429 | 37 45 29.14 | 2.8 | 8.9 | 91.5 | 106.0 | 24.1 |
| 161 | 13 35 11.565 | 37 45 47.83 | 2.3 | 10.1 | 107.1 | 105.9 | 22.9 |
| 162 | 13 34 46.011 | 37 40 47.92 | 3.9 | 7.0 | 91.5 | 105.4 | 38.6 |
| 163 | 13 34 46.940 | 38 04 27.15 | 3.7 | 7.2 | 71.0 | 104.9 | 28.2 |
| 164 | 13 35 8.565 | 37 59 47.68 | 3.5 | 7.5 | 67.1 | 103.3 | 25.6 |
| 165 | 13 33 55.842 | 37 51 54.64 | 2.4 | 9.8 | 89.9 | 103.3 | 22.7 |
| 166 | 13 34 14.380 | 37 46 47.12 | 3.1 | 8.2 | 76.9 | 103.1 | 24.9 |
| 167 | 13 34 13.275 | 38 00 17.18 | 2.5 | 9.3 | 80.4 | 102.5 | 22.1 |
| 168 | 13 34 28.822 | 37 53 39.99 | 2.8 | 8.6 | 64.9 | 101.8 | 19.2 |

Table 2.2: Complete 1.4 GHz Source List (continued)

| Source | Right Ascension hh mm ss | Declination ° ′ ″ | $\theta_{dec}$ (″) | $\sigma_{snr}$ | $S_{peak}$ ($\mu$Jy) | $S_{integrated}$ ($\mu$Jy) | |
|---|---|---|---|---|---|---|---|
| 169 | 13 34 12.189 | 38 01 17.91 | 5.5 | 5.0 | 45.1 | 101.2 | 38.5 |
| 170 | 13 34 46.118 | 37 43 9.47 | 2.6 | 9.1 | 99.5 | 100.8 | 24.8 |
| 171 | 13 34 24.984 | 37 40 7.09 | 3.0 | 8.1 | 113.7 | 100.1 | 36.9 |
| 172 | 13 35 25.076 | 37 48 14.24 | 3.8 | 6.9 | 74.6 | 99.9 | 28.3 |
| 173 | 13 35 3.581 | 37 43 52.26 | 3.2 | 7.8 | 87.3 | 99.8 | 28.7 |
| 174 | 13 34 55.899 | 37 58 10.43 | 4.1 | 6.4 | 51.5 | 99.6 | 26.3 |
| 175 | 13 34 1.008 | 37 54 5.08 | 2.1 | 10.0 | 85.6 | 99.5 | 20.6 |
| 176 | 13 34 29.429 | 37 52 18.57 | 4.7 | 5.8 | 44.8 | 99.4 | 27.7 |
| 177 | 13 34 40.887 | 38 03 53.66 | 4.2 | 6.3 | 59.1 | 99.1 | 30.2 |
| 178 | 13 34 1.130 | 38 01 51.39 | 2.9 | 8.4 | 83.1 | 99.0 | 24.7 |
| 179 | 13 34 26.841 | 38 09 23.97 | 4.2 | 6.3 | 88.1 | 98.8 | 46.2 |
| 180 | 13 34 49.303 | 38 06 57.76 | 2.5 | 9.0 | 104.7 | 98.4 | 26.4 |
| 181 | 13 34 33.277 | 37 40 19.62 | 4.6 | 5.8 | 78.5 | 98.0 | 45.9 |
| 182 | 13 34 32.556 | 38 01 51.52 | 6.2 | 4.5 | 38.9 | 97.8 | 39.4 |
| 183 | 13 34 25.177 | 38 04 46.10 | 4.9 | 5.5 | 55.0 | 97.7 | 37.8 |
| 184 | 13 35 24.552 | 37 47 39.96 | 4.9 | 5.5 | 60.6 | 97.7 | 35.9 |
| 185 | 13 34 23.472 | 37 49 14.56 | 3.6 | 7.0 | 58.2 | 97.5 | 24.2 |
| 186 | 13 34 34.234 | 37 47 45.86 | 2.6 | 8.8 | 74.9 | 96.4 | 19.3 |
| 187 | 13 34 37.417 | 37 51 28.59 | 0.0 | 11.5 | 88.4 | 95.9 | 15.4 |
| 188 | 13 33 44.542 | 38 00 13.65 | 5.6 | 4.8 | 52.5 | 95.5 | 51.6 |
| 189 | 13 34 19.543 | 37 40 15.75 | 2.1 | 9.2 | 130.5 | 95.1 | 32.3 |
| 190 | 13 33 48.657 | 37 56 11.65 | 1.6 | 10.6 | 102.5 | 95.0 | 21.6 |
| 191 | 13 35 13.052 | 38 00 0.30 | 4.0 | 6.4 | 59.4 | 94.8 | 29.3 |
| 192 | 13 34 38.608 | 37 57 42.12 | 0.0 | 11.3 | 86.9 | 94.6 | 15.3 |
| 193 | 13 34 43.962 | 38 05 29.80 | 3.5 | 7.1 | 73.4 | 94.4 | 28.3 |
| 194 | 13 33 50.477 | 37 53 25.45 | 2.0 | 9.8 | 92.4 | 94.2 | 22.3 |
| 195 | 13 34 51.453 | 37 46 19.63 | 2.9 | 8.0 | 74.6 | 94.0 | 22.1 |
| 196 | 13 34 39.217 | 37 54 39.81 | 1.9 | 10.0 | 75.2 | 94.0 | 16.1 |
| 197 | 13 35 50.986 | 37 51 31.31 | 3.5 | 7.0 | 100.0 | 93.5 | 35.9 |
| 198 | 13 34 21.051 | 37 50 23.39 | 2.7 | 8.3 | 67.6 | 93.4 | 19.7 |
| 199 | 13 35 2.307 | 37 58 5.15 | 0.0 | 11.0 | 90.9 | 92.7 | 16.6 |
| 200 | 13 34 23.650 | 37 50 55.16 | 0.0 | 13.6 | 107.7 | 92.7 | 14.8 |
| 201 | 13 33 53.662 | 37 49 59.94 | 3.9 | 6.3 | 61.4 | 91.3 | 30.2 |
| 202 | 13 34 5.438 | 37 49 27.96 | 2.8 | 7.9 | 70.7 | 90.5 | 22.5 |
| 203 | 13 33 54.028 | 38 02 10.95 | 5.9 | 4.4 | 47.0 | 90.4 | 48.7 |
| 204 | 13 34 54.790 | 37 49 35.17 | 3.4 | 6.9 | 57.5 | 89.9 | 22.0 |
| 205 | 13 33 39.847 | 37 50 15.49 | 4.2 | 5.9 | 66.7 | 89.3 | 37.1 |
| 206 | 13 34 35.987 | 37 40 21.59 | 3.2 | 7.1 | 95.5 | 88.9 | 34.8 |
| 207 | 13 34 39.648 | 38 02 4.37 | 3.5 | 6.8 | 58.9 | 88.8 | 23.6 |
| 208 | 13 35 30.131 | 37 46 42.99 | 4.4 | 5.7 | 69.4 | 88.7 | 36.1 |
| 209 | 13 34 1.139 | 37 53 49.52 | 2.1 | 9.1 | 78.2 | 88.7 | 20.5 |
| 210 | 13 35 22.343 | 37 59 29.16 | 3.9 | 6.1 | 60.6 | 87.2 | 27.3 |

Table 2.2: Complete 1.4 GHz Source List (continued)

| Source | Right Ascension hh mm ss | Declination ° ′ ″ | $\theta_{dec}$ (″) | $\sigma_{snr}$ | $S_{peak}$ ($\mu$Jy) | $S_{integrated}$ ($\mu$Jy) | |
|---|---|---|---|---|---|---|---|
| 211 | 13 34 12.430 | 38 04 0.40 | 4.8 | 5.3 | 53.7 | 87.0 | 36.3 |
| 212 | 13 35 47.973 | 37 54 52.85 | 3.3 | 6.9 | 90.1 | 87.0 | 31.9 |
| 213 | 13 34 5.401 | 38 01 55.30 | 3.7 | 6.4 | 61.5 | 86.6 | 28.1 |
| 214 | 13 34 27.288 | 38 05 37.34 | 3.5 | 6.6 | 69.0 | 85.5 | 28.8 |
| 215 | 13 34 49.855 | 37 55 45.45 | 3.2 | 7.0 | 53.6 | 85.4 | 20.6 |
| 216 | 13 35 49.094 | 37 53 34.70 | 4.4 | 5.6 | 75.4 | 85.4 | 39.5 |
| 217 | 13 35 45.303 | 37 56 48.53 | 3.6 | 6.4 | 80.9 | 85.3 | 32.8 |
| 218 | 13 34 29.355 | 38 03 59.30 | 2.2 | 8.5 | 81.0 | 85.1 | 21.4 |
| 219 | 13 35 18.174 | 37 53 59.81 | 4.4 | 5.5 | 49.2 | 85.0 | 30.9 |
| 220 | 13 34 57.739 | 37 49 33.97 | 3.4 | 6.7 | 56.3 | 84.9 | 22.1 |
| 221 | 13 34 20.039 | 37 56 29.28 | 3.3 | 6.7 | 52.3 | 84.3 | 23.2 |
| 222 | 13 35 21.599 | 37 55 9.59 | 4.1 | 5.8 | 53.6 | 84.2 | 29.9 |
| 223 | 13 35 47.281 | 37 51 48.79 | 6.3 | 4.0 | 53.3 | 83.8 | 57.0 |
| 224 | 13 35 14.390 | 37 54 57.54 | 3.0 | 7.1 | 61.4 | 83.2 | 22.8 |
| 225 | 13 35 17.297 | 37 44 10.34 | 3.9 | 5.9 | 72.4 | 83.0 | 36.0 |
| 226 | 13 35 0.606 | 38 00 47.57 | 5.0 | 4.8 | 42.0 | 82.4 | 34.4 |
| 227 | 13 35 18.166 | 37 48 10.95 | 5.0 | 4.9 | 49.1 | 82.2 | 36.4 |
| 228 | 13 34 9.257 | 37 50 42.25 | 3.5 | 6.4 | 54.1 | 82.1 | 26.1 |
| 229 | 13 34 9.537 | 37 43 18.48 | 5.6 | 4.3 | 50.4 | 81.8 | 51.6 |
| 230 | 13 34 0.866 | 37 51 55.39 | 3.8 | 6.0 | 52.6 | 81.8 | 28.7 |
| 231 | 13 34 26.838 | 38 03 49.28 | 5.9 | 4.2 | 39.7 | 81.3 | 41.2 |
| 232 | 13 35 41.819 | 37 54 34.02 | 4.2 | 5.5 | 65.4 | 81.0 | 34.4 |
| 233 | 13 35 25.342 | 38 01 10.38 | 3.5 | 6.3 | 68.7 | 80.9 | 27.1 |
| 234 | 13 35 1.084 | 37 52 56.74 | 4.0 | 5.7 | 45.7 | 80.5 | 25.6 |
| 235 | 13 35 8.704 | 37 44 23.85 | 3.1 | 6.7 | 76.0 | 80.4 | 28.2 |
| 236 | 13 33 59.042 | 37 49 46.23 | 2.5 | 7.7 | 72.3 | 80.2 | 22.0 |
| 237 | 13 35 21.358 | 37 55 22.70 | 4.0 | 5.6 | 51.9 | 80.0 | 29.7 |
| 238 | 13 35 35.654 | 37 51 8.74 | 5.2 | 4.5 | 50.9 | 79.8 | 40.6 |
| 239 | 13 34 59.219 | 38 06 21.67 | 5.0 | 4.7 | 53.7 | 78.6 | 43.1 |
| 240 | 13 34 35.177 | 37 47 12.94 | 4.5 | 5.1 | 44.4 | 78.3 | 28.8 |
| 241 | 13 33 34.097 | 37 55 55.17 | 5.6 | 4.2 | 48.3 | 77.5 | 54.3 |
| 242 | 13 34 46.701 | 38 01 25.64 | 3.6 | 6.0 | 51.2 | 77.5 | 24.0 |
| 243 | 13 34 14.807 | 37 59 7.53 | 3.8 | 5.8 | 47.8 | 76.7 | 27.1 |
| 244 | 13 35 17.583 | 37 47 5.69 | 3.1 | 6.5 | 68.8 | 76.2 | 26.2 |
| 245 | 13 35 21.642 | 37 55 34.12 | 1.6 | 8.6 | 79.9 | 76.0 | 19.5 |
| 246 | 13 35 16.256 | 37 44 39.64 | 3.8 | 5.8 | 68.0 | 75.9 | 33.2 |
| 247 | 13 35 5.081 | 37 48 51.46 | 2.5 | 7.5 | 67.1 | 75.7 | 19.6 |
| 248 | 13 35 10.161 | 37 43 21.40 | 3.1 | 6.5 | 79.3 | 75.5 | 30.3 |
| 249 | 13 35 3.355 | 37 57 47.55 | 0.0 | 10.1 | 83.8 | 75.4 | 15.4 |
| 250 | 13 34 29.035 | 37 52 7.40 | 4.1 | 5.3 | 41.0 | 75.1 | 24.9 |
| 251 | 13 34 1.992 | 38 01 27.80 | 2.5 | 7.3 | 70.5 | 75.1 | 24.7 |
| 252 | 13 33 52.068 | 37 53 2.49 | 4.7 | 4.8 | 44.8 | 75.0 | 36.5 |

Table 2.2: Complete 1.4 GHz Source List (continued)

| Source | Right Ascension hh mm ss | Declination ° ′ ″ | $\theta_{dec}$ (″) | $\sigma_{snr}$ | $S_{peak}$ ($\mu$Jy) | $S_{integrated}$ ($\mu$Jy) | |
|---|---|---|---|---|---|---|---|
| 253 | 13 34 53.668 | 38 05 37.50 | 5.1 | 4.5 | 48.2 | 75.0 | 40.2 |
| 254 | 13 35 45.833 | 37 51 58.21 | 4.0 | 5.4 | 70.5 | 74.7 | 35.9 |
| 255 | 13 34 34.649 | 37 44 37.54 | 2.1 | 7.9 | 78.5 | 74.5 | 20.6 |
| 256 | 13 33 35.739 | 37 50 7.14 | 3.5 | 5.9 | 70.8 | 74.3 | 34.6 |
| 257 | 13 34 40.297 | 37 47 20.63 | 2.2 | 7.7 | 67.1 | 74.2 | 18.4 |
| 258 | 13 33 29.384 | 37 48 52.51 | 5.0 | 4.5 | 61.9 | 74.1 | 56.3 |
| 259 | 13 34 23.135 | 38 04 15.59 | 3.8 | 5.6 | 54.6 | 73.6 | 29.6 |
| 260 | 13 34 52.541 | 37 40 29.09 | 4.9 | 4.5 | 61.8 | 73.2 | 49.6 |
| 261 | 13 33 47.482 | 37 52 45.33 | 3.9 | 5.5 | 53.7 | 72.9 | 32.7 |
| 262 | 13 34 15.468 | 37 59 27.43 | 3.5 | 5.9 | 49.1 | 72.8 | 25.7 |
| 263 | 13 34 19.797 | 37 44 9.15 | 3.2 | 6.2 | 65.2 | 72.5 | 28.5 |
| 264 | 13 35 45.146 | 37 49 58.27 | 3.0 | 6.1 | 82.3 | 71.8 | 31.2 |
| 265 | 13 34 31.107 | 38 05 56.96 | 3.2 | 6.0 | 64.4 | 70.7 | 27.9 |
| 266 | 13 34 55.463 | 37 48 21.72 | 3.1 | 6.2 | 53.9 | 70.6 | 21.5 |
| 267 | 13 34 36.139 | 37 43 20.59 | 4.1 | 5.1 | 55.1 | 70.5 | 32.4 |
| 268 | 13 33 39.640 | 37 45 53.96 | 3.8 | 5.4 | 72.7 | 70.3 | 41.2 |
| 269 | 13 34 40.076 | 37 49 21.34 | 2.9 | 6.5 | 52.3 | 70.3 | 19.4 |
| 270 | 13 34 41.647 | 37 48 30.03 | 3.6 | 5.6 | 47.0 | 70.1 | 22.7 |
| 271 | 13 34 46.112 | 37 56 16.30 | 4.8 | 4.5 | 34.0 | 69.8 | 28.5 |
| 272 | 13 34 7.651 | 37 55 5.29 | 5.3 | 4.1 | 34.0 | 69.7 | 35.7 |
| 273 | 13 34 56.392 | 38 07 22.51 | 2.3 | 6.8 | 83.9 | 69.5 | 28.2 |
| 274 | 13 33 36.282 | 37 50 27.86 | 4.2 | 5.0 | 58.7 | 69.5 | 41.8 |
| 275 | 13 34 20.961 | 38 07 48.82 | 3.6 | 5.5 | 68.5 | 68.7 | 36.5 |
| 276 | 13 33 24.279 | 37 58 58.14 | 5.5 | 4.0 | 57.1 | 68.5 | 69.9 |
| 277 | 13 34 15.994 | 38 06 12.56 | 3.1 | 6.1 | 69.8 | 68.4 | 29.5 |
| 278 | 13 35 33.245 | 37 52 15.64 | 3.9 | 5.2 | 55.3 | 67.9 | 29.5 |
| 279 | 13 34 20.047 | 38 00 27.50 | 2.4 | 6.8 | 57.6 | 67.7 | 21.5 |
| 280 | 13 34 22.657 | 37 57 33.20 | 1.3 | 8.2 | 63.9 | 67.6 | 17.1 |
| 281 | 13 34 57.355 | 37 51 12.99 | 2.8 | 6.3 | 51.3 | 67.5 | 20.5 |
| 282 | 13 35 18.808 | 37 54 18.16 | 4.0 | 5.1 | 45.9 | 67.1 | 28.3 |
| 283 | 13 34 12.221 | 38 04 56.99 | 5.0 | 4.2 | 44.8 | 66.9 | 41.0 |
| 284 | 13 34 36.226 | 37 54 58.75 | 0.0 | 7.0 | 52.2 | 66.8 | 17.4 |
| 285 | 13 34 39.078 | 37 44 25.48 | 4.1 | 4.9 | 49.7 | 66.7 | 30.3 |
| 286 | 13 34 6.970 | 37 51 21.34 | 2.3 | 7.0 | 59.2 | 66.6 | 21.0 |
| 287 | 13 35 25.265 | 37 54 34.23 | 2.9 | 6.2 | 59.2 | 65.8 | 21.5 |
| 288 | 13 34 29.015 | 37 45 52.66 | 1.4 | 7.8 | 73.2 | 65.6 | 18.1 |
| 289 | 13 34 0.531 | 38 03 4.26 | 3.6 | 5.3 | 56.0 | 65.6 | 30.4 |
| 290 | 13 35 21.859 | 37 58 26.53 | 5.2 | 4.0 | 38.6 | 65.2 | 34.0 |
| 291 | 13 33 58.155 | 37 56 56.01 | 3.4 | 5.5 | 49.2 | 65.0 | 26.9 |
| 292 | 13 35 17.897 | 37 56 54.25 | 3.0 | 5.9 | 53.4 | 64.8 | 23.9 |
| 293 | 13 35 28.200 | 37 50 40.16 | 0.0 | 7.2 | 74.8 | 64.8 | 20.1 |
| 294 | 13 34 31.096 | 37 45 49.22 | 4.4 | 4.6 | 43.1 | 64.8 | 29.8 |

Table 2.2: Complete 1.4 GHz Source List (continued)

| Source | Right Ascension hh mm ss | Declination °′″ | $\theta_{dec}$ (″) | $\sigma_{snr}$ | $S_{peak}$ ($\mu$Jy) | $S_{integrated}$ ($\mu$Jy) | |
|---|---|---|---|---|---|---|---|
| 295 | 13 34 18.946 | 37 44 1.00 | 2.9 | 6.1 | 64.8 | 64.7 | 27.2 |
| 296 | 13 33 40.632 | 37 49 7.92 | 4.7 | 4.3 | 50.0 | 64.6 | 42.2 |
| 297 | 13 34 57.168 | 37 58 26.31 | 4.4 | 4.5 | 36.7 | 64.5 | 28.2 |
| 298 | 13 35 12.663 | 38 02 49.87 | 2.6 | 6.3 | 64.9 | 64.5 | 24.3 |
| 299 | 13 34 27.502 | 38 00 31.88 | 3.6 | 5.3 | 44.2 | 64.5 | 24.1 |
| 300 | 13 34 47.989 | 37 44 10.36 | 4.8 | 4.3 | 44.0 | 64.4 | 35.8 |
| 301 | 13 34 48.404 | 37 47 30.86 | 3.2 | 5.7 | 49.5 | 64.1 | 22.3 |
| 302 | 13 33 26.090 | 37 59 50.46 | 5.0 | 4.2 | 58.9 | 63.6 | 62.9 |
| 303 | 13 34 7.666 | 37 59 4.27 | 3.7 | 5.2 | 44.9 | 63.6 | 27.4 |
| 304 | 13 33 31.511 | 37 58 58.72 | 3.6 | 5.2 | 66.3 | 63.6 | 43.6 |
| 305 | 13 34 4.949 | 37 58 0.01 | 4.9 | 4.1 | 35.2 | 63.4 | 35.3 |
| 306 | 13 34 0.318 | 37 55 55.34 | 4.4 | 4.5 | 38.7 | 63.3 | 32.2 |
| 307 | 13 34 31.979 | 37 46 30.30 | 4.5 | 4.4 | 39.4 | 63.2 | 30.1 |
| 308 | 13 34 22.269 | 37 56 2.06 | 0.0 | 8.4 | 64.4 | 63.1 | 15.9 |
| 309 | 13 33 44.076 | 37 58 0.06 | 4.9 | 4.2 | 43.4 | 62.4 | 41.6 |
| 310 | 13 34 9.929 | 37 52 1.72 | 2.3 | 6.5 | 53.5 | 62.4 | 20.9 |
| 311 | 13 35 21.625 | 38 00 27.66 | 0.0 | 7.6 | 77.6 | 62.4 | 20.8 |
| 312 | 13 35 19.305 | 37 52 20.20 | 4.5 | 4.4 | 40.1 | 62.0 | 32.4 |
| 313 | 13 35 0.207 | 38 01 9.28 | 4.0 | 4.8 | 42.6 | 61.9 | 28.0 |
| 314 | 13 35 2.756 | 38 07 48.56 | 4.1 | 4.7 | 61.5 | 61.7 | 40.6 |
| 315 | 13 35 16.876 | 38 04 12.02 | 3.1 | 5.6 | 63.9 | 61.5 | 29.4 |
| 316 | 13 35 17.437 | 37 47 46.83 | 3.4 | 5.3 | 53.8 | 60.9 | 27.0 |
| 317 | 13 33 43.159 | 38 03 15.41 | 3.8 | 4.9 | 62.1 | 60.5 | 38.0 |
| 318 | 13 34 20.474 | 37 54 22.33 | 2.4 | 6.5 | 49.9 | 60.5 | 19.1 |
| 319 | 13 34 45.414 | 37 48 56.10 | 4.2 | 4.5 | 37.4 | 60.3 | 25.5 |
| 320 | 13 35 3.444 | 37 55 56.51 | 4.2 | 4.5 | 36.6 | 60.3 | 26.8 |
| 321 | 13 33 39.669 | 37 48 41.82 | 4.6 | 4.1 | 49.4 | 60.3 | 43.0 |
| 322 | 13 34 24.841 | 37 50 57.12 | 0.0 | 9.6 | 76.2 | 60.1 | 14.1 |
| 323 | 13 33 57.802 | 37 53 54.81 | 2.5 | 6.2 | 54.7 | 59.9 | 22.6 |
| 324 | 13 35 33.854 | 37 59 20.37 | 3.2 | 5.5 | 61.7 | 59.7 | 26.7 |
| 325 | 13 34 8.561 | 37 57 14.42 | 4.1 | 4.6 | 38.2 | 59.7 | 28.7 |
| 326 | 13 35 11.170 | 37 55 43.09 | 4.3 | 4.4 | 37.3 | 59.6 | 28.8 |
| 327 | 13 35 30.642 | 37 44 47.63 | 4.1 | 4.6 | 63.0 | 59.3 | 37.8 |
| 328 | 13 34 57.088 | 37 55 41.94 | 1.7 | 7.1 | 55.7 | 59.2 | 16.5 |
| 329 | 13 34 26.086 | 38 06 37.02 | 3.6 | 5.0 | 56.8 | 59.0 | 32.2 |
| 330 | 13 34 20.598 | 37 55 29.59 | 2.8 | 5.8 | 44.7 | 59.0 | 20.9 |
| 331 | 13 34 16.502 | 37 48 5.95 | 3.4 | 5.2 | 45.7 | 58.5 | 24.6 |
| 332 | 13 34 3.172 | 37 53 22.11 | 2.4 | 6.1 | 51.5 | 58.5 | 21.9 |
| 333 | 13 35 40.127 | 37 46 25.26 | 3.3 | 5.3 | 75.4 | 57.9 | 33.6 |
| 334 | 13 33 58.491 | 37 47 1.66 | 4.3 | 4.4 | 45.2 | 57.9 | 34.4 |
| 335 | 13 34 18.835 | 37 56 9.71 | 3.0 | 5.6 | 43.3 | 57.7 | 21.7 |
| 336 | 13 34 36.578 | 37 53 4.52 | 4.9 | 4.1 | 30.6 | 57.6 | 27.3 |

Table 2.2: Complete 1.4 GHz Source List (continued)

| Source | Right Ascension hh mm ss | Declination ° ′ ″ | $\theta_{dec}$ (″) | $\sigma_{snr}$ | $S_{peak}$ ($\mu$Jy) | $S_{integrated}$ ($\mu$Jy) | |
|---|---|---|---|---|---|---|---|
| 337 | 13 34 1.824 | 37 53 28.21 | 3.8 | 4.8 | 40.9 | 57.6 | 27.8 |
| 338 | 13 34 54.346 | 37 53 10.80 | 3.6 | 4.9 | 37.9 | 57.5 | 23.0 |
| 339 | 13 34 40.562 | 38 01 21.05 | 2.3 | 6.2 | 52.1 | 57.0 | 18.8 |
| 340 | 13 35 1.422 | 37 55 0.88 | 3.3 | 5.2 | 41.6 | 57.0 | 21.9 |
| 341 | 13 34 33.978 | 38 01 2.14 | 1.9 | 6.6 | 55.0 | 56.8 | 18.3 |
| 342 | 13 34 11.146 | 38 07 19.27 | 4.4 | 4.1 | 52.4 | 56.2 | 43.1 |
| 343 | 13 34 9.935 | 37 42 19.89 | 3.9 | 4.5 | 57.0 | 55.9 | 39.0 |
| 344 | 13 35 37.250 | 38 00 44.43 | 2.5 | 5.9 | 72.8 | 55.8 | 26.0 |
| 345 | 13 34 3.670 | 37 50 23.53 | 4.2 | 4.3 | 38.1 | 55.7 | 29.1 |
| 346 | 13 34 24.319 | 37 50 26.37 | 3.5 | 4.8 | 38.7 | 54.9 | 24.8 |
| 347 | 13 33 47.991 | 38 00 23.56 | 3.5 | 4.9 | 51.7 | 54.9 | 32.5 |
| 348 | 13 35 6.161 | 37 49 52.47 | 3.2 | 5.1 | 44.9 | 54.8 | 22.1 |
| 349 | 13 34 44.185 | 37 56 44.51 | 3.9 | 4.5 | 34.2 | 54.5 | 23.7 |
| 350 | 13 33 48.015 | 37 59 23.12 | 8.5 | 4.9 | 50.6 | 54.5 | 31.1 |
| 351 | 13 33 21.353 | 37 54 15.75 | 3.4 | 5.0 | 70.6 | 54.4 | 48.6 |
| 352 | 13 33 59.519 | 37 54 0.79 | 2.7 | 5.6 | 48.9 | 54.3 | 23.0 |
| 353 | 13 35 33.018 | 37 49 39.88 | 4.5 | 4.1 | 46.3 | 54.3 | 33.3 |
| 354 | 13 34 41.834 | 37 49 26.16 | 2.9 | 5.2 | 42.1 | 54.0 | 20.1 |
| 355 | 13 34 31.717 | 37 56 31.57 | 2.8 | 5.5 | 41.8 | 53.9 | 19.0 |
| 356 | 13 34 37.028 | 37 53 9.51 | 0.0 | 7.3 | 54.9 | 53.7 | 14.8 |
| 357 | 13 33 55.979 | 38 06 56.98 | 4.1 | 4.3 | 59.8 | 53.5 | 43.6 |
| 358 | 13 34 0.288 | 37 53 31.54 | 3.7 | 4.6 | 39.9 | 53.4 | 27.7 |
| 359 | 13 35 9.293 | 37 48 43.60 | 2.6 | 5.7 | 52.3 | 53.4 | 20.9 |
| 360 | 13 35 17.152 | 37 43 32.62 | 4.3 | 4.1 | 52.2 | 53.0 | 40.3 |
| 361 | 13 34 58.883 | 37 48 3.13 | 4.3 | 4.1 | 36.0 | 52.8 | 28.2 |
| 362 | 13 34 28.778 | 37 57 50.48 | 2.3 | 5.9 | 45.8 | 52.6 | 19.1 |
| 363 | 13 34 36.385 | 38 00 36.84 | 0.0 | 7.7 | 63.6 | 52.6 | 15.0 |
| 364 | 13 35 13.454 | 37 52 55.67 | 0.0 | 7.7 | 67.1 | 52.4 | 15.9 |
| 365 | 13 34 38.210 | 37 49 53.03 | 2.7 | 5.4 | 43.3 | 52.3 | 18.6 |
| 366 | 13 35 30.290 | 38 01 23.92 | 2.6 | 5.4 | 62.7 | 52.1 | 25.2 |
| 367 | 13 35 28.079 | 37 58 17.30 | 4.2 | 4.1 | 41.7 | 52.1 | 30.1 |
| 368 | 13 34 6.256 | 37 57 50.27 | 0.0 | 4.7 | 40.3 | 51.9 | 25.8 |
| 369 | 13 34 31.233 | 37 57 54.39 | 3.2 | 4.7 | 36.3 | 51.2 | 21.9 |
| 370 | 13 34 19.427 | 37 59 26.68 | 2.8 | 5.2 | 42.6 | 50.9 | 22.5 |
| 371 | 13 35 9.749 | 37 48 5.90 | 0.0 | 5.8 | 54.6 | 50.8 | 20.5 |
| 372 | 13 35 9.758 | 37 47 36.26 | 3.2 | 4.9 | 46.9 | 50.7 | 24.6 |
| 373 | 13 34 39.874 | 37 56 0.97 | 4.0 | 4.2 | 31.4 | 50.7 | 24.0 |
| 374 | 13 34 35.087 | 37 57 52.68 | 0.0 | 6.6 | 50.5 | 50.4 | 15.8 |
| 375 | 13 34 14.194 | 37 59 19.22 | 4.1 | 4.1 | 34.5 | 50.3 | 28.9 |
| 376 | 13 35 45.138 | 37 58 30.59 | 4.1 | 4.0 | 52.7 | 49.9 | 37.3 |
| 377 | 13 34 42.827 | 37 50 49.07 | 0.0 | 6.8 | 53.6 | 49.6 | 15.4 |
| 378 | 13 34 29.852 | 37 46 24.56 | 3.6 | 4.5 | 40.5 | 49.5 | 24.8 |

Table 2.2: Complete 1.4 GHz Source List (continued)

| Source | Right Ascension hh mm ss | Declination ° ′ ″ | $\theta_{dec}$ (″) | $\sigma_{snr}$ | $S_{peak}$ ($\mu$Jy) | $S_{integrated}$ ($\mu$Jy) | |
|---|---|---|---|---|---|---|---|
| 379 | 13 34 30.003 | 37 58 47.07 | 2.4 | 5.5 | 43.4 | 49.5 | 18.6 |
| 380 | 13 34 17.115 | 37 54 3.50 | 2.0 | 5.9 | 46.0 | 49.5 | 18.7 |
| 381 | 13 34 41.407 | 38 03 59.71 | 3.7 | 4.3 | 41.0 | 49.3 | 27.4 |
| 382 | 13 34 2.521 | 37 51 29.34 | 2.5 | 5.4 | 47.4 | 49.0 | 22.4 |
| 383 | 13 34 6.017 | 37 46 53.89 | 3.0 | 4.9 | 48.1 | 48.7 | 25.7 |
| 384 | 13 34 11.492 | 37 56 19.51 | 1.1 | 6.9 | 55.7 | 48.7 | 16.7 |
| 385 | 13 33 37.461 | 37 51 15.39 | 4.0 | 4.1 | 46.5 | 48.0 | 38.4 |
| 386 | 13 35 31.880 | 37 54 27.94 | 2.3 | 5.5 | 56.5 | 47.6 | 21.2 |
| 387 | 13 35 38.914 | 37 59 49.76 | 2.8 | 5.0 | 60.9 | 47.5 | 27.5 |
| 388 | 13 34 19.637 | 37 57 34.41 | 3.5 | 4.4 | 34.6 | 47.5 | 24.5 |
| 389 | 13 35 14.045 | 37 46 50.03 | 0.0 | 6.3 | 65.0 | 47.1 | 19.7 |
| 390 | 13 34 7.390 | 38 02 42.88 | 3.7 | 4.2 | 41.3 | 47.1 | 28.9 |
| 391 | 13 35 8.538 | 38 06 2.19 | 2.8 | 5.0 | 59.9 | 47.0 | 28.7 |
| 392 | 13 34 20.956 | 37 50 1.97 | 0.0 | 4.9 | 39.8 | 46.7 | 20.8 |
| 393 | 13 34 28.786 | 38 01 41.63 | 3.1 | 4.7 | 40.2 | 46.4 | 22.9 |
| 394 | 13 33 49.795 | 37 50 41.71 | 3.8 | 4.1 | 41.1 | 46.2 | 32.2 |
| 395 | 13 34 26.529 | 37 59 55.46 | 3.0 | 4.8 | 39.2 | 46.1 | 22.5 |
| 396 | 13 34 37.120 | 37 54 27.61 | 2.4 | 4.9 | 37.0 | 45.6 | 18.7 |
| 397 | 13 34 49.709 | 37 49 34.06 | 3.4 | 4.3 | 35.6 | 45.5 | 21.7 |
| 398 | 13 35 32.946 | 37 48 5.33 | 3.6 | 4.2 | 50.3 | 45.4 | 29.9 |
| 399 | 13 34 13.198 | 37 52 30.79 | 2.3 | 5.3 | 42.8 | 45.1 | 19.9 |
| 400 | 13 34 21.746 | 37 48 30.89 | 2.6 | 5.0 | 42.4 | 44.8 | 20.7 |
| 401 | 13 34 25.917 | 37 52 39.63 | 0.0 | 7.4 | 56.6 | 44.7 | 14.1 |
| 402 | 13 35 31.088 | 38 01 43.31 | 3.1 | 4.4 | 52.0 | 44.7 | 28.7 |
| 403 | 13 34 42.220 | 37 55 39.29 | 0.0 | 6.8 | 51.3 | 44.6 | 13.9 |
| 404 | 13 34 40.903 | 37 59 30.52 | 3.4 | 4.3 | 33.9 | 44.3 | 22.7 |
| 405 | 13 34 26.372 | 37 53 27.70 | 0.0 | 5.1 | 39.1 | 44.1 | 19.2 |
| 406 | 13 35 3.921 | 37 57 2.16 | 3.6 | 4.1 | 33.9 | 44.0 | 23.9 |
| 407 | 13 34 43.170 | 37 58 16.05 | 3.7 | 4.0 | 31.3 | 44.0 | 23.4 |
| 408 | 13 34 8.825 | 37 57 21.29 | 3.7 | 4.0 | 33.5 | 43.9 | 26.5 |
| 409 | 13 35 1.992 | 37 55 54.23 | 2.8 | 4.7 | 37.5 | 43.9 | 20.6 |
| 410 | 13 34 59.993 | 37 49 52.46 | 0.0 | 5.7 | 48.1 | 43.6 | 16.8 |
| 411 | 13 34 42.345 | 38 03 29.73 | 2.8 | 4.7 | 43.6 | 43.3 | 22.4 |
| 412 | 13 35 19.099 | 37 56 8.72 | 3.1 | 4.4 | 39.7 | 42.6 | 24.5 |
| 413 | 13 34 41.371 | 37 56 16.27 | 3.5 | 4.1 | 30.9 | 42.4 | 21.8 |
| 414 | 13 34 12.239 | 37 53 9.23 | 1.5 | 5.7 | 46.0 | 42.3 | 17.9 |
| 415 | 13 35 27.265 | 37 52 12.18 | 3.3 | 4.2 | 42.0 | 42.0 | 24.3 |
| 416 | 13 34 27.526 | 37 55 24.48 | 3.1 | 4.3 | 32.8 | 41.9 | 20.4 |
| 417 | 13 35 45.129 | 37 52 52.08 | 3.2 | 4.2 | 53.1 | 41.4 | 30.5 |
| 418 | 13 34 45.269 | 37 51 17.33 | 2.8 | 4.5 | 35.0 | 41.3 | 20.0 |
| 419 | 13 34 14.327 | 37 52 33.74 | 0.0 | 4.8 | 38.4 | 41.0 | 20.6 |
| 420 | 13 34 23.500 | 37 59 30.93 | 3.3 | 4.2 | 33.7 | 40.9 | 24.0 |

Table 2.2: Complete 1.4 GHz Source List (continued)

| Source | Right Ascension hh mm ss | Declination ° ′ ″ | $\theta_{dec}$ (″) | $\sigma_{snr}$ | $S_{peak}$ ($\mu$Jy) | $S_{integrated}$ ($\mu$Jy) | |
|---|---|---|---|---|---|---|---|
| 421 | 13 34 35.717 | 38 08 20.10 | 2.6 | 4.7 | 59.8 | 40.9 | 29.4 |
| 422 | 13 34 17.548 | 37 57 22.65 | 0.0 | 6.2 | 47.0 | 40.5 | 11.5 |
| 423 | 13 34 44.764 | 37 47 39.91 | 0.0 | 5.1 | 44.3 | 40.4 | 18.0 |
| 424 | 13 34 12.900 | 37 58 49.78 | 0.0 | 5.7 | 47.6 | 40.4 | 18.1 |
| 425 | 13 34 24.741 | 38 00 48.02 | 0.0 | 5.8 | 48.4 | 40.1 | 18.1 |
| 426 | 13 34 43.471 | 37 56 4.47 | 1.9 | 5.2 | 39.7 | 39.9 | 16.4 |
| 427 | 13 34 38.240 | 37 52 44.30 | 3.2 | 4.1 | 31.4 | 39.9 | 20.6 |
| 428 | 13 34 15.017 | 38 04 31.57 | 3.3 | 4.1 | 41.8 | 39.8 | 28.1 |
| 429 | 13 34 27.035 | 37 55 15.07 | 3.2 | 4.1 | 31.2 | 39.6 | 20.7 |
| 430 | 13 34 36.597 | 38 05 31.96 | 0.0 | 5.4 | 56.3 | 39.5 | 20.6 |
| 431 | 13 35 22.813 | 37 58 30.76 | 0.0 | 6.0 | 58.0 | 38.9 | 18.6 |
| 432 | 13 35 2.980 | 37 43 33.76 | 3.2 | 4.0 | 45.9 | 38.8 | 29.5 |
| 433 | 13 34 34.586 | 37 56 39.24 | 3.2 | 4.1 | 30.8 | 38.6 | 20.6 |
| 434 | 13 34 31.686 | 38 02 20.51 | 3.2 | 4.1 | 35.8 | 38.3 | 22.6 |
| 435 | 13 34 27.645 | 37 58 52.27 | 0.0 | 5.0 | 39.6 | 38.0 | 18.7 |
| 436 | 13 33 54.275 | 38 00 35.24 | 3.0 | 4.1 | 41.2 | 38.0 | 28.3 |
| 437 | 13 35 33.451 | 37 56 16.11 | 0.0 | 5.0 | 53.7 | 37.6 | 20.2 |
| 438 | 13 35 16.278 | 37 52 25.76 | 2.2 | 4.7 | 42.4 | 37.6 | 20.5 |
| 439 | 13 34 24.011 | 37 49 12.29 | 0.0 | 4.5 | 37.5 | 36.9 | 19.5 |
| 440 | 13 34 56.600 | 37 56 0.65 | 2.8 | 4.3 | 33.3 | 36.7 | 19.7 |
| 441 | 13 35 17.194 | 37 42 48.81 | 2.4 | 4.6 | 61.6 | 36.7 | 29.5 |
| 442 | 13 33 29.211 | 37 54 2.43 | 0.0 | 4.7 | 59.1 | 36.6 | 34.3 |
| 443 | 13 34 56.648 | 38 08 49.64 | 2.9 | 4.1 | 57.2 | 36.3 | 33.8 |
| 444 | 13 34 26.158 | 38 02 3.38 | 2.5 | 4.5 | 39.1 | 36.3 | 20.6 |
| 445 | 13 34 43.251 | 37 56 32.07 | 2.7 | 4.3 | 32.6 | 36.1 | 18.7 |
| 446 | 13 34 51.099 | 37 52 34.60 | 2.0 | 4.9 | 37.6 | 36.0 | 17.0 |
| 447 | 13 33 35.194 | 38 01 16.14 | 2.8 | 4.2 | 53.6 | 36.0 | 32.2 |
| 448 | 13 34 52.124 | 38 03 36.07 | 0.0 | 4.3 | 41.1 | 35.7 | 22.1 |
| 449 | 13 35 4.930 | 37 58 57.61 | 2.8 | 4.2 | 35.5 | 35.6 | 21.4 |
| 450 | 13 33 40.769 | 38 02 46.05 | 2.6 | 4.3 | 54.2 | 35.0 | 30.5 |
| 451 | 13 34 38.570 | 37 56 50.51 | 0.0 | 5.2 | 39.5 | 34.4 | 15.2 |
| 452 | 13 34 29.151 | 37 53 53.96 | 0.0 | 4.9 | 36.8 | 34.2 | 16.0 |
| 453 | 13 34 39.034 | 37 48 35.03 | 2.3 | 4.4 | 36.5 | 34.1 | 18.0 |
| 454 | 13 34 29.298 | 37 51 42.96 | 0.0 | 4.0 | 31.1 | 33.3 | 20.6 |
| 455 | 13 34 45.290 | 38 00 42.21 | 0.0 | 4.1 | 33.7 | 32.4 | 20.1 |
| 456 | 13 34 44.316 | 37 55 53.51 | 0.0 | 5.6 | 42.4 | 32.4 | 0.0 |
| 457 | 13 35 1.172 | 37 51 50.63 | 0.0 | 4.7 | 38.0 | 32.1 | 17.3 |
| 458 | 13 35 4.589 | 37 45 19.25 | 0.0 | 4.5 | 47.3 | 31.9 | 20.9 |
| 459 | 13 34 34.463 | 37 59 2.98 | 0.0 | 4.9 | 38.6 | 31.3 | 15.7 |
| 460 | 13 34 45.113 | 38 08 27.12 | 2.1 | 4.3 | 55.1 | 30.8 | 27.5 |
| 461 | 13 35 47.234 | 37 52 9.80 | 0.0 | 4.2 | 55.9 | 30.5 | 25.9 |
| 462 | 13 34 32.904 | 37 56 6.76 | 0.0 | 5.0 | 38.0 | 30.3 | 14.4 |

# Chapter 3

# The 13hr field 4.86 GHz radio data and radio spectra

In this chapter the calibration and imaging of the 4.86 GHz radio data is discussed. Down to a $3\sigma$ survey limit of 100 $\mu$Jy 105 sources are found within the 30′ diameter field of view. Two-point radio spectral indices are derived for 51 sources which have counterparts at 1.4 GHz and the results examined. For sources detected only at one frequency, upper limits for the flux at the second frequency are estimated leading to lower limits of the two-point radio spectral indices for sources detected at 1.4 GHz and upper limits for sources detected at 4.86 GHz.

## 3.1 Introduction

The nature of the radio emission across the whole radio band (i.e. from frequencies of around 10 GHz and lower) can be a very useful diagnostic of the emission mechanism. Of the two most common emission mechanisms, synchrotron radiation from relativistic electrons has a steep spectrum (i.e. getting fainter toward higher frequencies) and free-free emission from electron/proton interactions has a flat spectrum. Over the range 1 GHz to 100 GHz the observed flux due to synchrotron radiation decreases by a factor of 100 whilst free-free emission flux is roughly constant. The 13hr field was observed by the VLA at 4.86 GHz in D-configuration on the 25th May 1991. Although previously calibrated the 4.86 GHz data have never been published so the archived data was requested from the VLA, re-calibrated and re-imaged.

## 3.2 Data Calibration

As the primary beam of the VLA at 4.86 GHz is 9′ (FWHM), the observations consisted of many separate pointings to cover the *XMM*/VLA 30′ diameter field of view. The pointings were made on a rectangular grid with a separation of about 250″ to Nyquist sample the interferometer and single dish coverage of the sky (i.e. to produce suitable overlap for uniform sensitivity across the field). These resulting 51[1] pointings included a guard band of a few arcminutes around the edge of the field to ensure uniform sensitivity out to the edge of the field of view (see figure-3.1). Each pointing was observed 4 times in a rotation of consecutive snapshots to get good *uv* coverage, and very similar coverage for each pointing.

Each individual snapshot lasted 2.5mins and after 10 pointings the phase calibrator 1331+305 (known alternatively as 3C286) was observed for 2mins. For a reason unknown to the author the flux calibrator was only observed twice, both near the beginning of the observation run and hence was unsuitable. Luckily 3C286 was also suitable as a flux calibrator as its flux is reasonably well known and relatively constant (7.47 Jy at 4.86 GHz). This though meant that the flux was set with the AIPS task SETJY on 3C286 near the beginning of the calibration process and GETJY was not used later on unlike the normal procedure when using separate flux and phase calibrators. Apart from this 'trick' the data were calibrated in the standard way for continuum data.

## 3.3 Image Construction and Tessellation

As radio objects tend to have the largest projections on the sky (other than the Sun, Moon and Milky Way) mosaicing has long been necessary skill of radio astronomers and therefore there are several tasks within AIPS (VTESS, LTESS and FLATN) for mosaicing offset observations. LTESS is the simplest and makes linear combinations of nearby overlapping maps correcting for the primary beam attenuations of individual pointings. Individual maps of the 51 pointings from the calibrated data set were made using a pixel size of 2″ to sample the 14″ synthesis beam of the D-configuration at this frequency. LTESS requires that each input image must reside on the same grid with the same projection. Therefore each map was offset so that they all covered the same area of sky, had a coincident central pixel and covered the full 30 arcminutes diameter field. A 2048 by 2048 pixel field was used for each pointing and then CLEANed for 1000 iterations with IMAGR. LTESS was left to choose the appropriate primary beam size from the headers of the input files. The default is the 7% primary beam attenuation distance which was calculated to be 546.3″.

[1] $N = (30 \times 60)^2/250^2 \sim 51$

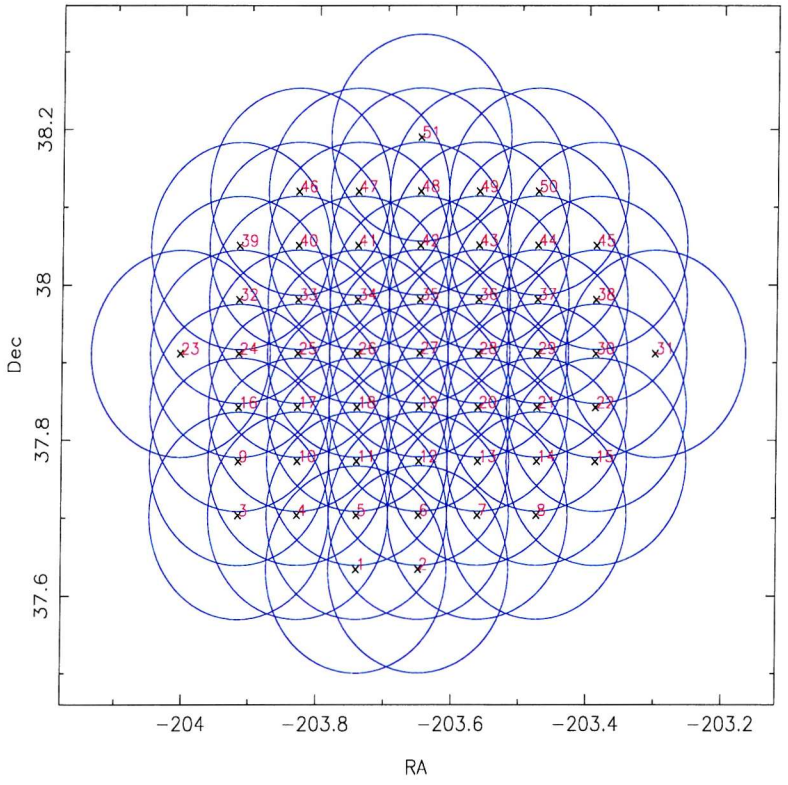


Figure 3.1: Figure to show the pointing strategy to cover the whole 30 arcminutes field at 4.86 GHz.

The 51 pointings were combined using LTESS, blanking out any area of sky beyond this primary beam limit and linearly combing any overlapping areas, producing the image seen in figure 3.2. This map has a naturally weighted resolution of 14″ and a sensitivity of 33 $\mu$Jy/beam.

## 3.4 Source Extraction

Source extraction was performed in a similar fashion to that used for the 1.4 GHz data using the AIPS task SAD (Search and Destroy), see section 2.4 for a fuller description. Again SAD was initially used to find all sources with a peak flux above our $3\sigma$ limit of 100 $\mu$Jy, checking by eye that no spurious sources were included and that no apparently 'real' sources were missed. Most of the biases considered before were not a concern here, since the primary beam correction has already been performed by LTESS. Also bandwidth smearing is not so much of a problem as the synthesis beam is much larger relative to the primary beam for 4.86 GHz and most sources will have contributions from more than one map. Sources with a peak flux less than $6.5\sigma$ were assumed to be unresolved unless they were broadened by more than 50% of the beam size, in which case I let the flux stand (Richards et al. 1998). This solution was to avoid the problems of bias at low signal to noise as discussed in Chapter 2, but without doing any modelling. The errors in the latter case were taken to be 25% of the integrated flux. The 116 sources found are presented in table 3.3.

## 3.5 Correlation with the 1.4 GHz data

The 4.86 GHz sources were correlated with the 1.4 GHz source list by searching for any sources separated by less than 7″. Of the 116 4.86 GHz sources 53 were found to have 1.4 GHz counterparts for which radio spectral indices could be directly calculated. However due to the large time (7 years) between the 4.86 GHz observations and the 1.4 GHz observations it is possible that the radio spectra derived here may not all be correct due to intrinsic variability of the radio sources. Any variability will be dominated by AGN which will vary on these timescales, whilst starburst emission from a whole galaxy does not. The radio spectral index, $\alpha_R$, was defined in the standard way:

$$S_\nu = k\nu^{-\alpha_R} \tag{3.1}$$

and hence $\alpha_R$ is calculated simply from

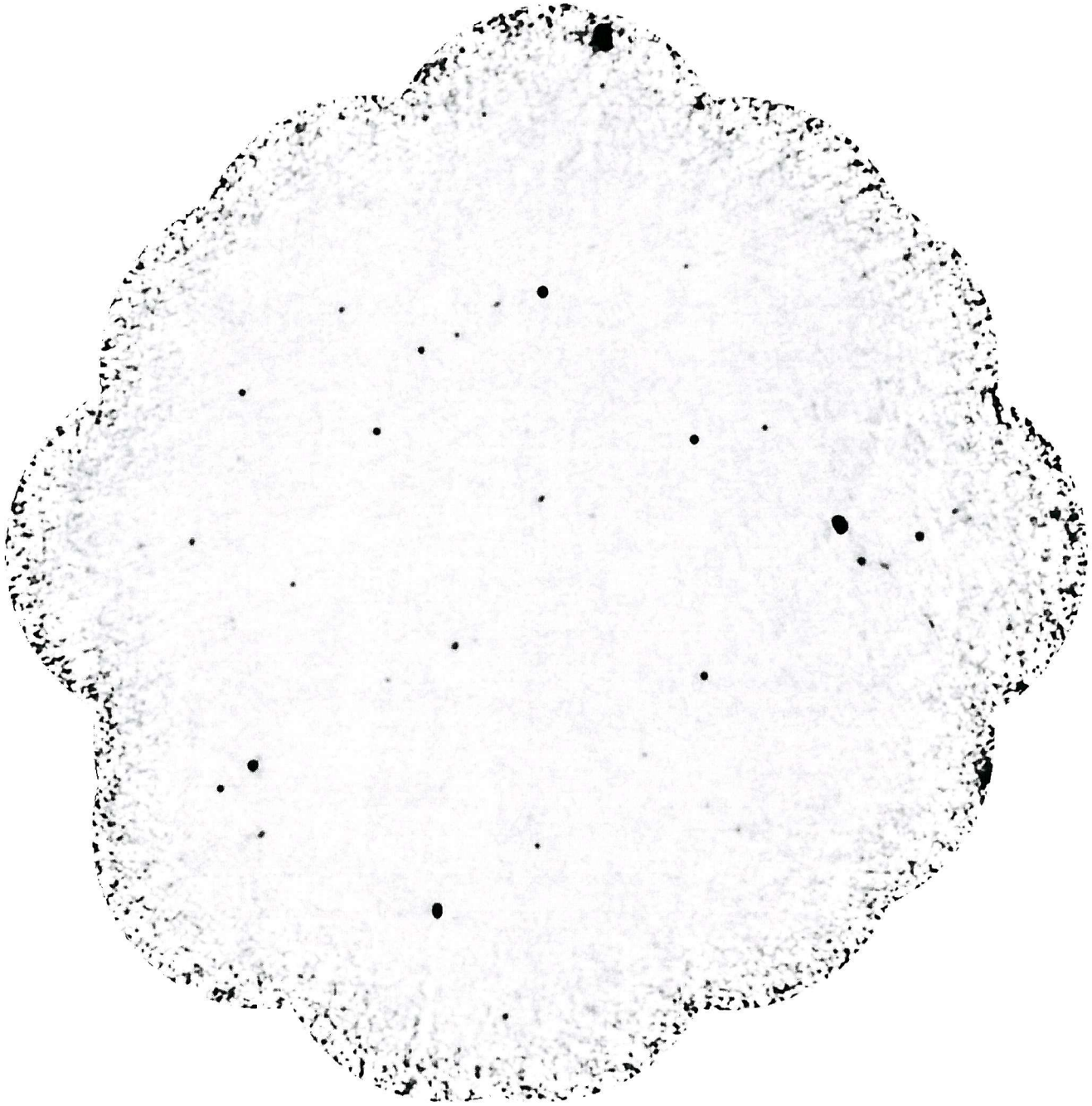

Figure 3.2: An inverse greyscale image of the 4.86 GHz map made from all 51 pointings combined with the AIPS task LTESS. The effective resolution is 14″ with an rms of 33 $\mu$Jy/beam.

$$\frac{S_{1.4}}{S_{4.86}} = \left(\frac{1.4}{4.86}\right)^{-\alpha_R} \tag{3.2}$$

$$\alpha_R = 1.85 \log_{10}\left(\frac{S_{1.4}}{S_{4.86}}\right) \tag{3.3}$$

The radio spectral indices for the 53 sources are presented in table 3.1. The positions given are those of the 1.4 GHz sources which will be easier to use to find the optical counterpart due to the higher resolution of the 1.4 GHz data. The errors were found by calculating $\alpha_R$ with one flux plus its error and the other flux minus its error and vice-versa to get the extreme possible values for $\alpha_R$. This list is by no means a complete sample in a statistical sense.

It was also possible to obtain lower limits on the radio spectral index, $\alpha_R$, for all the 1.4 GHz sources. Where there was not a 4.86 GHz counterpart a conservative $3\sigma$ upper limit of 100 $\mu$Jy for the flux was taken to calculate a lower limit $\alpha_R$ (figure 3.4). The lower limited, marked with up arrows, form a line representing the $3\sigma$ upper limit for a counterpart of a 1.4 GHz source for a given spectral index. The upper limit of a source has only been marked if it is meaningful (i.e. if it confirms that a source has a steep spectrum, $\alpha_R \geq 0.5$). The displacement in RA and dec between the positions of sources that appear at both frequencies is shown in figure 3.3. As can the seen there is no systematic offset between our fields. For table 3.1 $\alpha_R$ is plotted against 4.86 GHz in figure 3.5. Upper limits for the radio spectral index of 4.86 GHz sources without 1.4 GHz counterparts are not shown as they are all consistent with those source having a radio spectral index of $\alpha_R < 0.5$. This figure implies that at a given flux a majority of radio sources have flat spectra, $\alpha_R < 0.5$.

There is also a strong selection effect in that steep spectrum sources are less likely to be detected as the higher frequency observations at 4.86 GHz are not as sensitive as the lower frequency observations at 1.4 GHz. Variability of the core component of AGN at radio frequencies is typically of the order of a $10-20\%$ leading to a change in $\alpha_R$ of $\Delta\alpha_R \sim 0.2$ for steep spectrum sources. For flat spectrum sources variability of this magnitude can have a much greater effect inducing a change of $\Delta\alpha_R \sim 1-2$. Therefore sources which are observed to have steep spectra are probably intrinsically steep, but sources with flatter spectrum have a larger uncertainty due to possible variability if they are dominated by emssion from the core. For fainter, slightly extended sources it is not always possible to tell if radio emission is core dominated or lobe dominated.

Table 3.1: The 1.4 GHz sources with radio spectral indices, $\alpha_R$

| Source | Right Ascension hh mm ss | Declination ° ′ ″ | $S_{1.4\,\mathrm{GHz}}$ ($\mu$Jy) | $S_{4.86\,\mathrm{GHz}}$ ($\mu$Jy) | $\alpha_R$ |
|---|---|---|---|---|---|
| 1 | 13 33 29.040 | 37 55 57.90 | 92681.00 | 43073.00 | $0.616^{+0.005}_{-0.005}$ |
| 2 | 13 34 3.011 | 37 59 49.18 | 11624.00 | 4783.00 | $0.714^{+0.017}_{-0.017}$ |
| 3 | 13 34 38.496 | 38 06 27.01 | 10939.00 | 14762.00 | $-0.241^{+0.007}_{-0.007}$ |
| 4 | 13 35 16.664 | 38 00 8.19 | 8017.00 | 2156.00 | $1.055^{+0.040}_{-0.038}$ |
| 5 | 13 33 59.951 | 37 49 11.64 | 3918.80 | 2502.00 | $0.361^{+0.181}_{-0.186}$ |
| 6 | 13 34 57.650 | 37 50 29.40 | 3680.70 | 1798.00 | $0.576^{+0.137}_{-0.141}$ |
| 7 | 13 34 38.015 | 37 57 10.33 | 2510.50 | 1315.59 | $0.519^{+0.133}_{-0.131}$ |
| 8 | 13 35 6.603 | 38 03 48.64 | 2260.00 | 1785.00 | $0.190^{+0.054}_{-0.051}$ |
| 9 | 13 34 49.260 | 38 05 52.50 | 2146.90 | 1038.41 | $0.584^{+0.143}_{-0.133}$ |
| 10 | 13 35 25.340 | 38 05 33.90 | 1790.60 | 1060.88 | $0.421^{+0.141}_{-0.137}$ |
| 11 | 13 34 38.106 | 37 41 33.46 | 1715.00 | 813.61 | $0.599^{+0.109}_{-0.099}$ |
| 12 | 13 35 35.475 | 37 53 14.30 | 1362.43 | 761.28 | $0.468^{+0.119}_{-0.107}$ |
| 13 | 13 34 13.571 | 37 45 39.30 | 1111.95 | 513.66 | $0.621^{+0.207}_{-0.174}$ |
| 14 | 13 34 5.407 | 38 07 37.99 | 1103.21 | 671.51 | $0.399^{+0.152}_{-0.137}$ |
| 15 | 13 33 46.583 | 38 00 22.26 | 1041.91 | 1020.00 | $0.017^{+0.096}_{-0.090}$ |
| 16 | 13 34 58.392 | 38 04 29.88 | 989.05 | 909.60 | $0.067^{+0.103}_{-0.095}$ |
| 17 | 13 35 49.175 | 37 51 35.33 | 865.50 | 854.83 | $0.010^{+0.242}_{-0.197}$ |
| 18 | 13 33 59.951 | 37 49 11.64 | 597.50 | 2502.00 | $-1.151^{+0.178}_{-0.182}$ |
| 19 | 13 35 44.626 | 37 57 42.78 | 596.68 | 114.47 | $1.327^{+0.271}_{-0.221}$ |
| 20 | 13 35 16.292 | 37 56 21.43 | 593.88 | 140.89 | $1.156^{+0.287}_{-0.240}$ |
| 21 | 13 34 42.846 | 37 57 34.12 | 574.05 | 114.75 | $1.294^{+0.252}_{-0.201}$ |
| 23 | 13 33 49.923 | 38 03 34.41 | 560.28 | 198.04 | $0.836^{+0.410}_{-0.409}$ |
| 24 | 13 35 13.273 | 37 48 57.21 | 559.02 | 564.57 | $-0.008^{+0.191}_{-0.164}$ |
| 25 | 13 34 40.030 | 37 42 52.48 | 446.41 | 211.56 | $0.600^{+0.274}_{-0.224}$ |
| 26 | 13 34 53.824 | 37 48 16.32 | 403.32 | 158.84 | $0.749^{+0.263}_{-0.213}$ |
| 27 | 13 34 51.997 | 37 57 43.56 | 402.86 | 191.35 | $0.598^{+0.268}_{-0.218}$ |
| 28 | 13 34 57.310 | 37 47 59.01 | 383.89 | 202.53 | $0.514^{+0.708}_{-0.399}$ |
| 34 | 13 35 0.786 | 37 44 8.48 | 312.27 | 512.27 | $-0.398^{+0.394}_{-0.301}$ |
| 36 | 13 35 48.319 | 37 58 52.13 | 302.78 | 308.97 | $-0.016^{+0.321}_{-0.269}$ |
| 37 | 13 34 46.491 | 37 42 47.43 | 302.17 | 395.94 | $-0.217^{+0.618}_{-0.394}$ |
| 40 | 13 34 26.260 | 37 56 23.22 | 290.01 | 445.75 | $-0.345^{+0.286}_{-0.230}$ |
| 42 | 13 35 48.866 | 37 51 15.11 | 273.92 | 210.65 | $0.211^{+0.431}_{-0.340}$ |
| 45 | 13 33 58.842 | 37 43 21.32 | 256.62 | 449.67 | $-0.451^{+0.331}_{-0.291}$ |
| 55 | 13 34 41.819 | 38 00 11.09 | 229.89 | 216.94 | $0.047^{+0.291}_{-0.244}$ |
| 57 | 13 33 42.740 | 37 52 39.77 | 227.58 | 171.55 | $0.227^{+0.330}_{-0.292}$ |
| 62 | 13 34 36.240 | 37 51 6.68 | 215.87 | 169.75 | $0.193^{+0.286}_{-0.238}$ |
| 64 | 13 34 33.169 | 37 52 21.28 | 208.39 | 133.13 | $0.360^{+0.283}_{-0.235}$ |
| 66 | 13 34 27.505 | 38 08 32.46 | 197.49 | 385.62 | $-0.538^{+0.442}_{-0.363}$ |
| 76 | 13 35 35.883 | 37 57 38.23 | 163.42 | 103.13 | $0.370^{+0.336}_{-0.300}$ |
| 81 | 13 33 26.742 | 37 57 13.05 | 162.40 | 308.45 | $-0.515^{+0.518}_{-0.501}$ |
| 83 | 13 35 30.245 | 37 56 39.02 | 160.74 | 152.50 | $0.042^{+0.365}_{-0.339}$ |
| 85 | 13 34 53.141 | 37 50 43.94 | 158.08 | 323.99 | $-0.577^{+0.354}_{-0.287}$ |

Table 3.1: The 1.4 GHz sources with radio spectral indices, $\alpha_R$ (continued)

| Source | Right Ascension hh mm ss | Declination ° ′ ″ | $S_{1.4\,\mathrm{GHz}}$ ($\mu$Jy) | $S_{4.86\,\mathrm{GHz}}$ ($\mu$Jy) | $\alpha_R$ |
|---|---|---|---|---|---|
| 107 | 13 34 0.893 | 37 47 5.84 | 135.99 | 706.02 | $-1.323^{+0.603}_{-0.463}$ |
| 135 | 13 35 6.236 | 38 02 32.98 | 120.20 | 118.87 | $0.009^{+0.380}_{-0.362}$ |
| 163 | 13 34 46.011 | 37 40 47.92 | 105.40 | 161.53 | $-0.343^{+0.482}_{-0.545}$ |
| 167 | 13 34 14.380 | 37 46 47.12 | 103.08 | 125.70 | $-0.159^{+0.405}_{-0.401}$ |
| 180 | 13 34 26.841 | 38 09 23.97 | 98.77 | 139.84 | $-0.279^{+0.540}_{-0.686}$ |
| 190 | 13 34 19.543 | 37 40 15.75 | 95.08 | 201.58 | $-0.604^{+0.466}_{-0.513}$ |
| 227 | 13 35 17.297 | 37 44 10.34 | 83.01 | 135.89 | $-0.396^{+0.521}_{-0.636}$ |
| 249 | 13 34 46.701 | 38 01 25.64 | 77.48 | 113.23 | $-0.305^{+0.448}_{-0.476}$ |
| 254 | 13 35 16.256 | 37 44 39.64 | 75.89 | 149.05 | $-0.542^{+0.523}_{-0.642}$ |
| 337 | 13 33 43.159 | 38 03 15.41 | 60.49 | 647.30 | $-1.905^{+0.943}_{-1.117}$ |
| 390 | 13 34 58.883 | 37 48 3.13 | 52.83 | 100.26 | $-0.515^{+0.575}_{-0.792}$ |

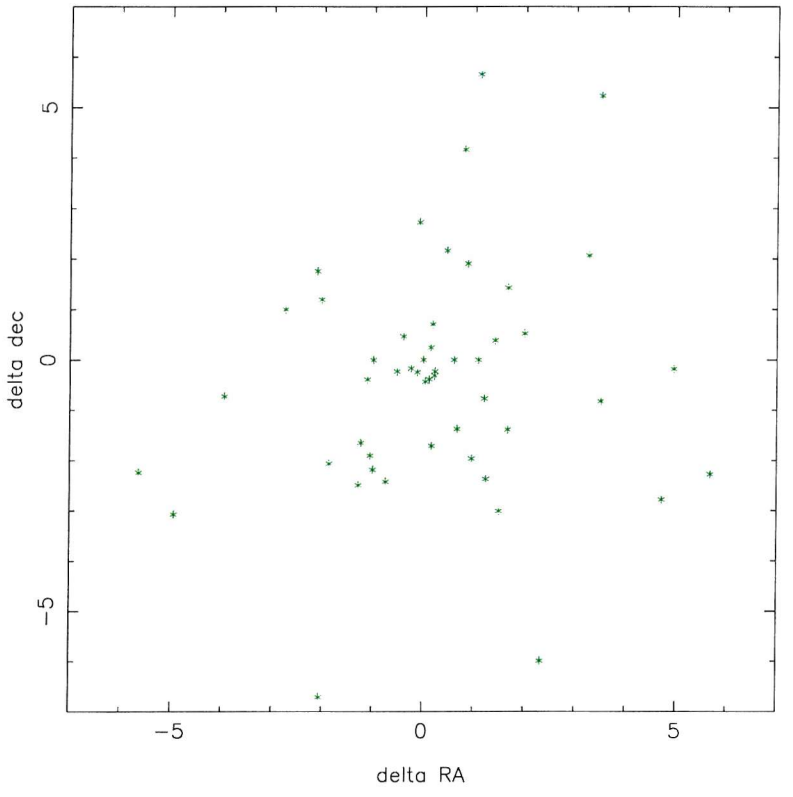


Figure 3.3: Figure showing the positional offsets in arcseconds for the correlations between the 1.4 GHz sources and the 4.86 GHz sources (for sources with a seperation of $< 7''$).

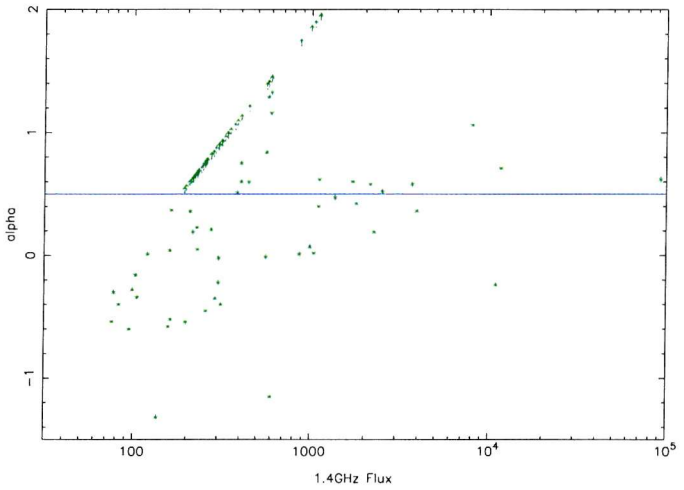


Figure 3.4: The two-point radio spectral index plotted against 1.4 GHz flux. Upper limits given for 1.4 GHz sources with no 4.86 GHz sources above a $3\sigma$ detection limit of 100 $\mu$Jy/beam. The upper limits of the radio spectral indices were calculated from the 4.86 GHz detection upper limits limit of 100 $\mu$Jy/beam and are only shown in cases where it is meaningful (i.e. that the radio spectra, $\alpha_R \geq 0.5$. This shows that for sources detected at both frequencies, their radio spectra are usually flat. Many of the sources not detected at 4.86 GHz at $\alpha_R \geq 0.5$ meaning that they are either starburst galaxies or moderately distant lobe dominated sources. Additionally many sources had lower limits consistent with being flat or steep spectrum sources. These sources are not shown for clarity.

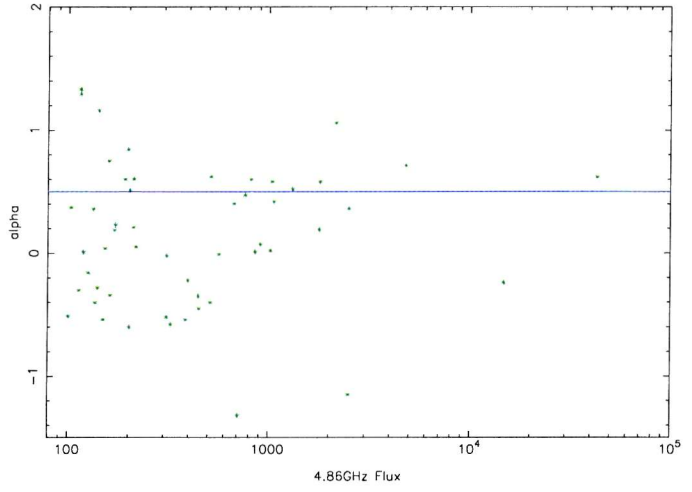


Figure 3.5: The two-point radio spectral index plotted against 4.86 GHz flux. Upper limits for the radio spectral index of 4.86 GHz sources without 1.4 GHz counterparts are not shown as they are all consistent with those source having a radio spectral index of $\alpha_R < 0.5$. Both this figure an the previous one are subject to large selection effects.

## 3.6 Extended sources and core radio spectral indices

Radio sources with extended morphologies are known to have variations in radio spectral index throughout the extended structure. As mentioned in section 1.2.2.1 the radio spectra of the extended component is steep. For a homogeneous source with a constant magnetic field, $B$, a power-law continuum (typically $\alpha_R \sim 0.75$) can be generated by the synchrotron emission mechanism by an initial power-law distribution of electron energies. At high frequencies, where the extended component is optically thin, synchrotron self-absorption is not important, but at lower frequencies the gas becomes optically thick and the increase in flux with the decrease in frequency turns over to yield, $S_\nu \propto \nu^{5/2}$.

The core component is usually flat ($\alpha_{core} \leq 0.5$). A synchrotron spectrum is only approximately flat near the turn over frequency and then only for a limited frequency range unless the the electron distribution is quite flat and different from that which drives the extended component. The flatness of compact sources over several orders of magnitude of frequency would imply the central source to have either some inhomogeneity or the presence of a number of unresolved parts. Either way the integrated spectrum is flat over a broad frequency range due to different parts of the compact region becoming optically thick at different frequencies (depending on the local electron density).

As the brighter sources in this survey are reasonably extended the radio spectra of their cores has been estimated, as the previously calculated radio spectra are for the whole source and hence have a contribution from the extended components as well as the cores. Very Long Baseline interferometry (VLBI) has shown upper limits on the size of the compact source of AGN to be $\sim$ 0.01pc (Rantakyro et al., 1998). Even at moderately low redshifts of sources in our sample (see section 4.2.7) this corresponds to $10^{-5}$ arcseconds well below the resolution of these data. If a source is a combination of an extended component and an unresolved core component then if the core component is brighter than the peak flux of the extended component it is possible to take the 1.4 GHz peak flux as the flux of the unresolved core[2]. Then the difference between the total flux and peak flux is that of the extended component. The flux of the extended component at 4.86 GHz can be calculated from that at 1.4 GHz assuming a steep spectrum of $\alpha \sim 0.75$. The flux of the core at 4.86 GHz is then the difference between the total flux and that of the extended component. The spectra of the core can then be calculated from the core fluxes at 1.4 GHz and 4.86 GHz. This was done for the ten brightest sources at 1.4 GHz and the results are presented in table 3.2

[2]As peak flux equals total flux for an unresolved source and the total flux of an extended source is a function of it's peak flux, angular extent and morphology

Table 3.2: The radio spectra of the cores of the ten brightest 1.4 GHz sources

| Source | Right Ascension hh mm ss | Declination ° ′ ″ | $S_{1.4\,\mathrm{GHz}}$ ($\mu$Jy) | $S_{4.86\,\mathrm{GHz}}$ ($\mu$Jy) | $\alpha_{core}$ |
|---|---|---|---|---|---|
| 1 | 13 33 29.040 | 37 55 57.90 | 8384.00 | 9927.00 | $-0.136^{+0.107}_{-0.114}$ |
| 2 | 13 34 3.011 | 37 59 49.18 | 8705.00 | 3635.23 | $0.702^{+0.021}_{-0.021}$ |
| 3 | 13 34 38.496 | 38 06 27.01 | 7499.00 | 13409.37 | $-0.467^{+0.006}_{-0.006}$ |
| 4 | 13 35 16.664 | 38 00 8.19 | 3868.00 | 524.59 | $1.605^{+0.167}_{-0.139}$ |
| 5 | 13 33 59.951 | 37 49 11.64 | 1772.00 | 1657.87 | $0.053^{+0.252}_{-0.229}$ |
| 6 | 13 34 57.650 | 37 50 29.40 | 595.41 | 584.85 | $0.014^{+0.404}_{-0.317}$ |
| 7 | 13 34 38.015 | 37 57 10.33 | 820.04 | 650.90 | $0.186^{+0.278}_{-0.246}$ |
| 8 | 13 35 6.603 | 38 03 48.64 | 1580.00 | 1517.62 | $0.032^{+0.058}_{-0.055}$ |
| 9 | 13 34 49.260 | 38 05 52.50 | 387.89 | 346.76 | $0.090^{+0.466}_{-0.346}$ |
| 10 | 13 35 25.340 | 38 05 33.90 | 314.73 | 480.56 | $-0.340^{+0.307}_{-0.264}$ |

### 3.6.1 Discussion

The morphologies of sources are shown on the first page of the appendix. For seven of the ten sources (1,4-10) the spectra of the core is steeper than that of the whole source. Source 2 has no extended component so the spectra index is unchanged. Source 3 is more inverted (i.e. $\alpha$ become more negative) and source 4 becomes even steeper than before. The sources are discussed below:

1. Source 1 ($\alpha_{core} = -0.136$) is discussed more in section 4.1.3.2, but as a bright radio source with steep spectrum lobes, the flat spectrum of the core is not too surprising. It is a good example of Fanaroff-Riley class II object with bright, hotspots towards the edge of the lobes. The assumption that the peak flux corresponds to the core is not strictly be true here as the peak flux does not coincide with the core, but with a hotspot. The higher resolution MERLIN data (see section 6.3.1.2) shows the position of the core. Taking the flux of the core as the unresolved flux of the MERLIN image and using the same assumptions as before gives you an extremely inverted spectrum, $\alpha_{core} = -2.1$. This method of estimating the core flux is probably not valid in this case as the flux of the whole source is dominated so much by the lobes.

2. Source 2 ($\alpha_{core} = 0.702$) is only just resolved to 1.8″ and therefore the spectra of the core is very similar to that of the whole source. As this source is radio loud ($\log(R_O) \sim 4$), see section 4.1.6.1, with a steep radio spectrum then it is most likely a Steep Spectrum Lobe-Dominated (SSLD) radio source (Antonucci, 1993).

3. Source 3 ($\alpha_{core} = -0.467$) is also just resolved to 2.1″, but the core has an even more inverted spectrum than the whole source. It has a very bright optical counterpart with $R \sim 17.7$, $B - R = 2.2$ and has been spectroscopically

identified as a NELG (see table 4.2). It is also detected as a *Chandra* source. It is also believed to be a BL Lac and is discussed further in section 5.5.

4. Source 4 ($\alpha_{core} = 1.605$) has an even steeper core spectrum than the whole source and is sightly extended to 3.5″. It has a $R$–band magnitude of 20.9 and is reasonably blue $B - R = 0.7$. As it is radio loud, $\log(R_O) \sim 3$, it is probably a SSLD radio source like source 2.

5. Source 5 ($\alpha_{core} = 0.053$) has a flatter component in the core than as a whole and is also detected by *Chandra* . It is believed to be a BL Lac and is discussed further in section 5.5.

6. Source 6 ($\alpha_{core} = 0.014$) also has a flatter core compared to its whole. This is consistent with it being a flat spectrum core dominated source (in this case a head-tail source with its lobes swept back by intra-cluster medium). It is associated with a previously known *ROSAT* source believed to be a cluster, and is discussed further in section 4.1.3.2.

7. Source 7 ($\alpha_{core} = 0.186$) is a double lobed radio source, and unsurprisingly has a flat core. It is a typical FRII radio source (see section 4.1.3.2).

8. Source 8 ($\alpha_{core} = 0.032$) is only just resolved (2.0″) so it's core is only very slightly flatter than the extended component. It is most likely a QSO with faint extended emission and a bright core with a flat spectrum (known as a Flat Spectrum Core Dominated quasar, Antonucci 1993).

9. Source 9 ($\alpha_{core} = 0.090$) is a good example of an FR II object. Again the peak flux may not be equivalent to the flux of the core here, but are result here is consistent with the core having a flat spectrum and the lobes having a steep spectrum. As for source one the lobes dominate to such an extent that this method may not be valid.

10. Source 10 ($\alpha_{core} = -0.340$) is an X-ray detected NELG with a possibly interacting partner. It has a flat core, but as noted in section 4.1.3.2 the radio emission appears to trace out star-formation in the spiral arms. The assumption that the peak flux is the flux of the core may not be true (see figure 5.13, but it is likely that core does have a flat spectrum and that the radio emission is dominated by that from starburst regions in the spiral arms.

## 3.7 Conclusions

In this chapter, data from 4.86 GHz has been presented whereby 116 sources have been found to a $3\sigma$ flux limit of $100\,\mu$Jy. Of these sources 53 were found to have 1.4 GHz counterparts from the catalogue in chapter 2. The sources show a wide

range of two-point radio spectral indices $-1 < \alpha < 1$. For extended sources it has been shown that consideration of the distribution of flux is important in the determination of the spectra of the core and of the extended component. The radio spectra combined with information at other wavelengths will be an important diagnostic parameter when determining the nature of the faint radio and X-ray populations.

## 3.8 The complete 4.86 GHz source list

In this section the complete 4.86 GHz source list is presented. Sources are ordered by total flux and the first column gives a source's position in the list. The next two columns are the Right Ascension and Declination (J2000). The fourth column is the mean angular size of a source. The fifth column is the signal to noise ratio. The final 3 columns are the peak flux, integrated flux and the error of the total flux all corrected for the primary bream attenuation.

Table 3.3: Complete 4.86 GHz Source List (see previous page for details).

| Right Ascension hh mm ss | Declination ° ′ ″ | $\theta_{dec}$ (″) | $\sigma_{snr}$ | $S_{peak}$ ($\mu$Jy) | $S_{integrated}$ ($\mu$Jy) | |
|---|---|---|---|---|---|---|
| 13 33 28.983 | 37 55 59.28 | 15.7 | 645.6 | 21519.0 | 43073.0 | 144.0 |
| 13 34 38.507 | 38 06 27.25 | 1.9 | 435.4 | 14515.0 | 14762.0 | 91.0 |
| 13 34 3.001 | 37 59 49.56 | 1.9 | 140.5 | 4684.0 | 4783.0 | 91.0 |
| 13 34 0.035 | 37 49 11.64 | 0.0 | 56.8 | 1894.0 | 2502.0 | 250.2 |
| 13 35 16.685 | 38 00 8.36 | 4.6 | 58.2 | 1941.0 | 2156.0 | 97.0 |
| 13 33 23.997 | 37 54 22.59 | 0.0 | 47.5 | 1583.0 | 2135.0 | 213.5 |
| 13 34 57.755 | 37 50 31.05 | 13.4 | 30.0 | 1000.0 | 1798.0 | 130.0 |
| 13 35 6.648 | 38 03 48.87 | 6.2 | 45.8 | 1525.0 | 1785.0 | 99.0 |
| 13 34 38.194 | 37 57 8.58 | 11.4 | 24.1 | 803.1 | 1315.6 | 122.1 |
| 13 35 25.235 | 38 05 36.27 | 8.6 | 23.4 | 781.3 | 1060.9 | 108.6 |
| 13 34 49.118 | 38 05 53.89 | 11.8 | 18.3 | 608.8 | 1038.4 | 125.3 |
| 13 33 46.571 | 38 00 22.01 | 2.9 | 30.3 | 1009.0 | 1020.0 | 91.0 |
| 13 34 58.341 | 38 04 29.88 | 7.4 | 22.2 | 739.2 | 909.6 | 0.0 |
| 13 35 49.509 | 37 51 36.05 | 23.2 | 7.7 | 257.1 | 854.8 | 201.4 |
| 13 34 38.004 | 37 41 34.23 | 3.2 | 23.5 | 783.1 | 813.6 | 92.3 |
| 13 35 35.456 | 37 53 14.61 | 3.4 | 21.3 | 709.9 | 761.3 | 94.3 |
| 13 34 1.530 | 37 47 10.07 | 41.9 | 3.8 | 125.2 | 706.0 | 308.4 |
| 13 34 5.315 | 38 07 37.99 | 5.3 | 18.0 | 600.3 | 671.5 | 96.9 |
| 13 33 42.760 | 38 03 18.20 | 34.0 | 3.3 | 109.4 | 647.3 | 321.4 |
| 13 35 13.259 | 37 48 58.92 | 7.4 | 13.5 | 448.7 | 564.6 | 103.8 |
| 13 34 46.478 | 37 45 12.48 | 26.5 | 4.6 | 154.4 | 563.1 | 216.5 |
| 13 34 13.568 | 37 45 39.74 | 7.3 | 12.1 | 402.6 | 513.7 | 104.6 |
| 13 35 0.369 | 37 44 8.66 | 20.2 | 5.6 | 187.3 | 512.3 | 173.9 |
| 13 33 42.309 | 37 51 32.22 | 20.9 | 5.2 | 171.7 | 499.7 | 182.1 |
| 13 33 58.950 | 37 43 23.81 | 10.3 | 9.2 | 305.2 | 449.7 | 114.2 |
| 13 34 26.492 | 37 56 22.23 | 11.0 | 8.7 | 288.6 | 445.8 | 117.6 |
| 13 34 46.664 | 37 42 54.14 | 23.8 | 3.7 | 122.3 | 395.9 | 197.4 |
| 13 34 27.209 | 38 08 27.23 | 11.3 | 6.4 | 214.0 | 385.6 | 129.9 |
| 13 35 42.721 | 37 59 56.38 | 17.8 | 4.2 | 138.6 | 342.5 | 161.6 |
| 13 35 7.318 | 37 43 31.99 | 41.4 | 3.1 | 102.9 | 338.7 | 200.0 |
| 13 34 53.204 | 37 50 46.36 | 4.3 | 8.9 | 295.3 | 324.0 | 95.7 |
| 13 35 50.190 | 37 55 2.25 | 19.5 | 3.5 | 117.3 | 312.7 | 170.8 |
| 13 35 48.413 | 37 58 52.52 | 0.0 | 10.7 | 356.5 | 309.0 | 81.8 |
| 13 33 26.615 | 37 57 16.06 | 8.0 | 7.9 | 263.9 | 308.5 | 99.4 |
| 13 33 31.450 | 38 00 56.34 | 19.4 | 3.5 | 118.3 | 306.0 | 167.0 |
| 13 33 43.365 | 37 51 5.16 | 14.3 | 4.7 | 156.2 | 299.7 | 135.4 |
| 13 34 59.033 | 37 53 40.14 | 19.4 | 3.1 | 104.5 | 286.9 | 174.5 |
| 13 34 59.758 | 37 43 41.56 | 94.5 | 4.6 | 152.7 | 278.6 | 131.0 |
| 13 35 1.927 | 38 07 34.25 | 24.3 | 3.4 | 114.8 | 277.8 | 159.1 |
| 13 34 9.072 | 38 06 30.75 | 20.4 | 3.0 | 100.5 | 273.5 | 173.3 |
| 13 35 27.291 | 38 03 7.66 | 16.8 | 3.2 | 106.0 | 240.5 | 152.0 |
| 13 35 37.148 | 38 03 29.73 | 13.3 | 3.5 | 118.2 | 239.6 | 140.6 |

Table 3.3: Complete 4.86 GHz Source List (continued).

| Right Ascension hh mm ss | Declination ° ′ ″ | $\theta_{dec}$ (″) | $\sigma_{snr}$ | $S_{peak}$ ($\mu$Jy) | $S_{integrated}$ ($\mu$Jy) | |
|---|---|---|---|---|---|---|
| 13 34 48.808 | 38 06 45.16 | 15.3 | 3.7 | 122.5 | 234.7 | 135.4 |
| 13 34 6.154 | 38 06 9.09 | 15.9 | 3.3 | 109.4 | 232.7 | 145.4 |
| 13 34 41.678 | 38 00 9.66 | 7.2 | 6.5 | 216.9 | 216.9 | 54.2 |
| 13 34 39.861 | 37 42 51.96 | 9.6 | 6.3 | 211.6 | 211.6 | 52.9 |
| 13 35 48.900 | 37 51 14.65 | 2.4 | 8.8 | 291.9 | 210.6 | 72.8 |
| 13 34 57.395 | 37 48 1.20 | 31.8 | 4.1 | 136.4 | 202.5 | 114.7 |
| 13 34 58.273 | 38 09 0.54 | 8.1 | 6.1 | 201.8 | 201.8 | 50.4 |
| 13 34 19.462 | 37 40 17.71 | 5.5 | 6.0 | 201.6 | 201.6 | 50.4 |
| 13 33 49.803 | 38 03 34.03 | 11.9 | 5.9 | 198.0 | 198.0 | 49.5 |
| 13 34 2.264 | 38 03 16.51 | 15.2 | 3.1 | 104.4 | 191.9 | 131.7 |
| 13 34 51.978 | 37 57 43.79 | 10.0 | 5.7 | 191.3 | 191.3 | 47.8 |
| 13 34 56.476 | 38 05 50.76 | 52.4 | 4.1 | 138.0 | 188.3 | 108.9 |
| 13 34 43.186 | 38 05 59.44 | 5.9 | 5.5 | 185.0 | 185.0 | 46.2 |
| 13 34 28.956 | 37 57 24.91 | 14.8 | 3.1 | 102.5 | 184.5 | 129.9 |
| 13 33 59.828 | 38 01 53.50 | 13.1 | 4.1 | 135.5 | 179.3 | 106.9 |
| 13 34 21.726 | 38 08 4.91 | 0.0 | 5.3 | 176.4 | 176.4 | 44.1 |
| 13 34 34.493 | 37 40 1.00 | 12.5 | 3.2 | 106.1 | 176.1 | 123.1 |
| 13 35 1.977 | 38 03 13.50 | 0.0 | 5.2 | 172.3 | 172.3 | 43.1 |
| 13 33 42.464 | 37 52 37.71 | 9.6 | 5.1 | 171.5 | 171.5 | 42.9 |
| 13 34 36.247 | 37 51 3.96 | 7.0 | 5.1 | 169.8 | 169.8 | 42.4 |
| 13 34 57.399 | 38 08 7.49 | 0.0 | 5.1 | 169.3 | 169.3 | 42.3 |
| 13 34 46.169 | 37 40 49.99 | 7.9 | 4.8 | 161.5 | 161.5 | 40.4 |
| 13 34 53.995 | 37 48 15.13 | 6.1 | 4.8 | 158.8 | 158.8 | 39.7 |
| 13 33 30.650 | 37 58 28.12 | 15.7 | 4.7 | 157.8 | 157.8 | 39.4 |
| 13 35 30.049 | 37 56 45.01 | 12.3 | 4.6 | 152.5 | 152.5 | 38.1 |
| 13 35 16.189 | 37 44 35.48 | 8.0 | 4.5 | 149.1 | 149.1 | 37.3 |
| 13 35 51.002 | 37 56 22.13 | 6.6 | 4.4 | 146.4 | 146.4 | 36.6 |
| 13 33 42.210 | 38 01 14.96 | 13.6 | 3.1 | 103.6 | 146.1 | 111.1 |
| 13 33 41.313 | 37 49 26.84 | 14.9 | 4.3 | 144.5 | 144.5 | 36.1 |
| 13 34 44.549 | 37 40 2.98 | 10.7 | 4.3 | 144.0 | 144.0 | 36.0 |
| 13 34 22.142 | 38 01 42.41 | 9.4 | 4.3 | 143.2 | 143.2 | 35.8 |
| 13 35 15.615 | 37 56 16.88 | 14.5 | 4.2 | 140.9 | 140.9 | 35.2 |
| 13 34 26.545 | 38 09 24.79 | 0.0 | 4.2 | 139.8 | 139.8 | 35.0 |
| 13 34 14.521 | 38 08 48.81 | 9.8 | 4.1 | 137.1 | 137.1 | 34.3 |
| 13 35 17.282 | 37 44 9.64 | 14.4 | 4.1 | 135.9 | 135.9 | 34.0 |
| 13 34 48.369 | 38 05 32.63 | 10.4 | 4.1 | 135.1 | 135.1 | 33.8 |
| 13 35 13.085 | 37 48 33.31 | 9.5 | 4.0 | 133.4 | 133.4 | 33.4 |
| 13 34 33.645 | 37 52 23.52 | 11.1 | 4.0 | 133.1 | 133.1 | 33.3 |
| 13 34 12.242 | 38 08 39.86 | 5.3 | 3.8 | 127.7 | 127.7 | 31.9 |
| 13 34 55.378 | 37 45 57.70 | 10.9 | 3.8 | 127.3 | 127.3 | 31.8 |
| 13 33 43.284 | 38 05 0.44 | 0.0 | 3.8 | 126.3 | 126.3 | 31.6 |
| 13 34 14.287 | 37 46 41.47 | 17.4 | 3.8 | 125.7 | 125.7 | 31.4 |

Table 3.3: Complete 4.86 GHz Source List (continued).

| Right Ascension hh mm ss | Declination °′″ | $\theta_{dec}$ (″) | $\sigma_{snr}$ | $S_{peak}$ ($\mu$Jy) | $S_{integrated}$ ($\mu$Jy) | |
|---|---|---|---|---|---|---|
| 13 33 54.239 | 37 47 43.47 | 0.0 | 3.7 | 123.4 | 123.4 | 30.8 |
| 13 34 23.926 | 37 53 13.89 | 15.3 | 3.6 | 120.6 | 120.6 | 30.2 |
| 13 35 5.504 | 38 02 32.84 | 8.7 | 3.6 | 118.9 | 118.9 | 29.7 |
| 13 35 31.348 | 37 56 26.61 | 6.1 | 3.5 | 116.9 | 116.9 | 29.2 |
| 13 34 27.123 | 37 46 44.25 | 12.6 | 3.5 | 116.5 | 116.5 | 29.1 |
| 13 34 23.683 | 37 52 41.81 | 10.6 | 3.5 | 115.7 | 115.7 | 28.9 |
| 13 34 55.033 | 38 02 10.02 | 2.7 | 3.5 | 115.5 | 115.5 | 28.9 |
| 13 35 17.163 | 37 52 56.80 | 14.8 | 3.5 | 115.2 | 115.2 | 28.8 |
| 13 33 38.105 | 37 54 20.78 | 13.8 | 3.4 | 115.0 | 115.0 | 28.7 |
| 13 35 9.702 | 38 05 27.26 | 2.5 | 3.4 | 114.8 | 114.8 | 28.7 |
| 13 34 42.935 | 37 57 36.02 | 8.5 | 3.4 | 114.8 | 114.8 | 28.7 |
| 13 35 44.587 | 37 57 40.62 | 13.9 | 3.4 | 114.5 | 114.5 | 28.6 |
| 13 35 46.394 | 37 58 39.00 | 5.7 | 3.4 | 114.3 | 114.3 | 28.6 |
| 13 34 46.585 | 38 01 33.32 | 11.7 | 3.4 | 113.2 | 113.2 | 28.3 |
| 13 34 49.195 | 37 44 53.07 | 5.1 | 3.3 | 110.4 | 110.4 | 27.6 |
| 13 35 5.663 | 38 03 6.87 | 11.1 | 3.3 | 109.9 | 109.9 | 27.5 |
| 13 34 25.125 | 37 53 40.73 | 7.1 | 3.3 | 108.8 | 108.8 | 27.2 |
| 13 34 44.367 | 38 00 17.96 | 5.4 | 3.2 | 107.9 | 107.9 | 27.0 |
| 13 34 7.214 | 38 05 25.07 | 13.0 | 3.2 | 107.8 | 107.8 | 27.0 |
| 13 34 33.368 | 38 03 2.05 | 8.0 | 3.2 | 107.6 | 107.6 | 26.9 |
| 13 34 1.948 | 37 41 58.80 | 10.9 | 3.2 | 107.0 | 107.0 | 26.8 |
| 13 34 49.953 | 38 02 55.45 | 2.5 | 3.2 | 106.5 | 106.5 | 26.6 |
| 13 34 51.451 | 37 53 10.27 | 13.8 | 3.2 | 106.3 | 106.3 | 26.6 |
| 13 34 19.652 | 38 06 26.00 | 9.7 | 3.2 | 106.2 | 106.2 | 26.6 |
| 13 34 28.266 | 38 06 3.19 | 4.0 | 3.1 | 104.4 | 104.4 | 26.1 |
| 13 35 30.511 | 37 59 29.06 | 10.5 | 3.1 | 103.3 | 103.3 | 25.8 |
| 13 35 35.404 | 37 57 40.50 | 10.9 | 3.1 | 103.1 | 103.1 | 25.8 |
| 13 35 18.578 | 37 54 44.40 | 10.7 | 3.1 | 102.9 | 102.9 | 25.7 |
| 13 34 17.091 | 37 55 0.90 | 14.4 | 3.1 | 102.7 | 102.7 | 25.7 |
| 13 34 16.998 | 38 04 41.98 | 10.6 | 3.1 | 101.9 | 101.9 | 25.5 |
| 13 34 59.301 | 37 48 6.20 | 3.2 | 3.0 | 100.3 | 100.3 | 25.1 |

# Chapter 4

# Optical counterparts to the Radio Sources

In this chapter the optical data and the correlation of the optical with the radio data are presented. The radio data are correlated with deep $R-$band data ($R \leq 27$) from the Subaru Telescope and deep $B-$band data ($B \leq 26.5$) from the Isaac Newton Telescope. Existing optical spectra from the William Herschel Telescope and from follow up observations of potential *ROSAT* counterparts during the original survey provide spectroscopic identifications of some of the optically brighter radio sources. The general properties of the radio/optical sample are shown including radio to optical flux ratio, colour and stellarity. The properties of an almost complete sample of bright galaxies with optical spectra is also examined.

## 4.1 The Images

### 4.1.1 The $R-$band Data

On the 23 December 2000 the 13hr field was observed for one hour using the Prime Focus Camera, SuperimeCam, on the 8.2m Japanese Subaru Telescope with a standard $R-$band filter by Japanese collaborators of the Deep Survey team. SuperimeCam (Miyazaki et al., 1998) consists of ten closely butted MIT/Lincoln Labs 4096x2038 CCDs, with a scale of 0.2 arcseconds/pixel, giving an overall field of view of $34' \times 27'$. The observations were dithered in order to fill the small gaps between the CCDs, resulting in an overall field of $39' \times 31'$. At the time of observation only nine of the CCDs were operational, hence part of the south-east corner of the field was not covered. An overview of the image is shown in figure 4.1, with a $15'$ radius circle representing the VLA/*XMM* fields overlaid. The limiting magnitude

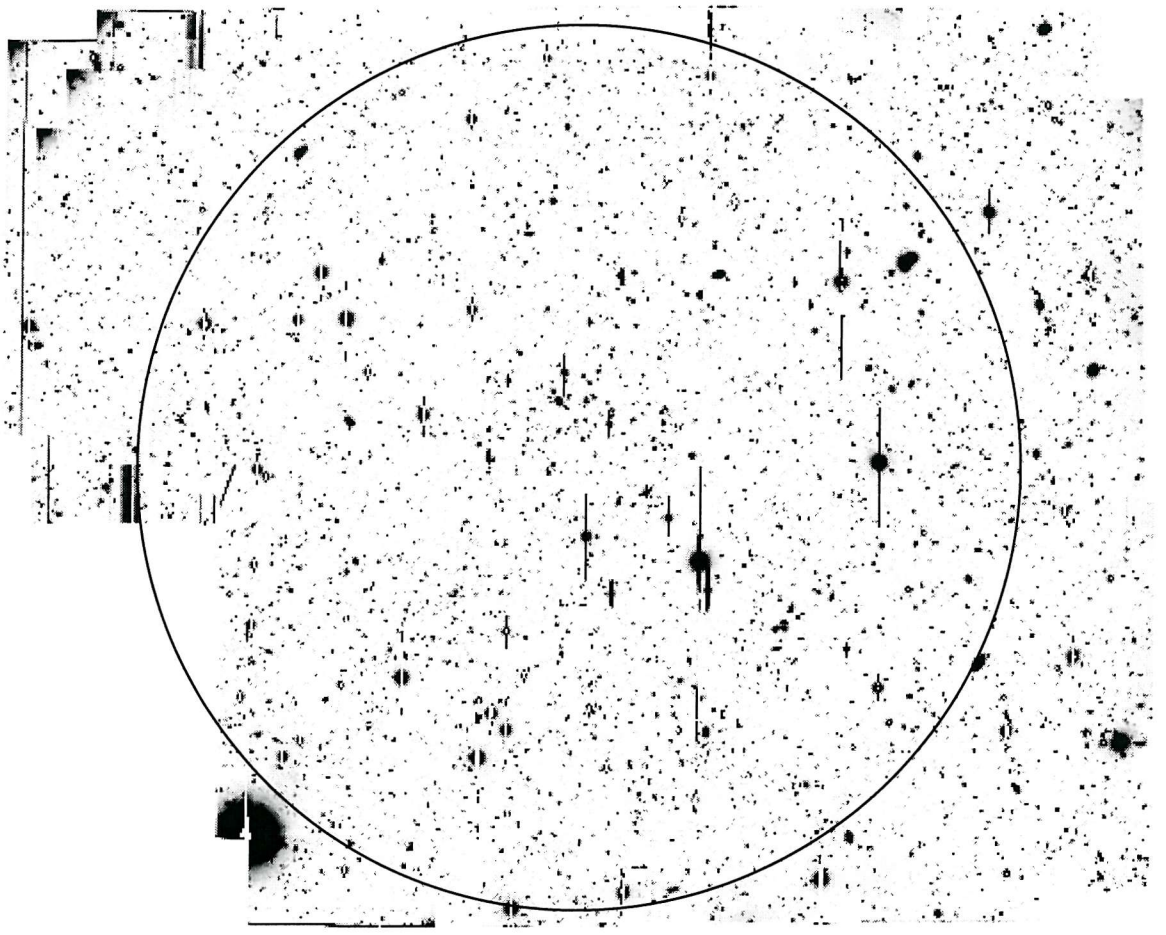

Figure 4.1: Subaru SuprimeCam $R$-band image of the 13hr field, with the VLA/*XMM* 15′ radius field-of-view superimposed with a large circle.

for this observation is $R \sim 27$ ($5\sigma$ significance), higher for confused sources. The average seeing was $0.9''$.

### 4.1.2 CCD Photometry

Full details are given in M$^{c}$Hardy et al.(2002). A brief overview is presented here.

#### 4.1.2.1 Registration of the Subaru Coordinate Frame

The initial coordinate frame of the CCD observations was set to by reference to USNO-A2.0 star catalogue and also to the HST Guide Star Catalog (Ver 1.2) which have an accuracy to better than an arcsecond. The coordinate frame was refined using second epoch Palomar Sky Survey J plates scanned by the Cambridge Auto-

matic Plate Measuring Machine, which is accurately tied to the FK5 system. The resulting positional accuracy was 0.3″ in both Right Ascension and declination.

#### 4.1.2.2 The Source Extraction

The software package SExtractor (Bertin & Arnouts 1996) was used to determine the magnitudes, positions and approximate morphologies of all objects in the SuperimeCam image. The version used was that in the Starlink package GAIA. The main morphological parameter returned was the stellarity parameter, which indicates how confident this software is that a certain object is 'stellar' in appearance (i.e. unresolved). The standard interpretation is that bright objects with stellarity $> 0.5$ are stars or QSOs and objects with stellarity $< 0.5$ are galaxies, however this is quite conservative and an object brighter than the confusion limit with a stellarity $< 0.9$ is almost certainly not stellar.

By comparison with results from Bertin & Arnouts (1996) it was estimated that almost all objects brighter than $R \sim 23$ should be correctly classified and that ~80% of objects with $23 < R < 25$ should be correctly classified. Beyond that magnitude, the large majority of objects in the high latitude extragalactic sky should be galaxies (Smail et al. 1995), but SExtractor cannot give a reliable classification in our data.

### 4.1.3 Correlation with the Radio Sources

To show the full range of optical morphologies and to give an informative view of the optical identifications 30″ × 30″ 'postage-stamp' images of the optical counterparts to all 462 radio sources are presented in the Appendix (including non-detections). Each postage-stamp has radio contours starting at -2 (dashed lines) times the rms noise (7.5 $\mu$Jy/beam) and then going in the following multiples (solid lines) of the rms; 2, 3, 4, 5, 8, 16, 32, 64, 128, 256, 512, 1024 and are of the combined A and B-configuration naturally weighted display maps (figure 2.5). Optical identifications were made by selecting any optical source found by SExtractor which was within a 2″ radius of a radio position found on the 1.4 GHz source list. The extremely accurate independent coordinate frames allow such a search radius to be taken. This led to 385 out of 462 radio sources having optical counterparts )including the extended radio sources).

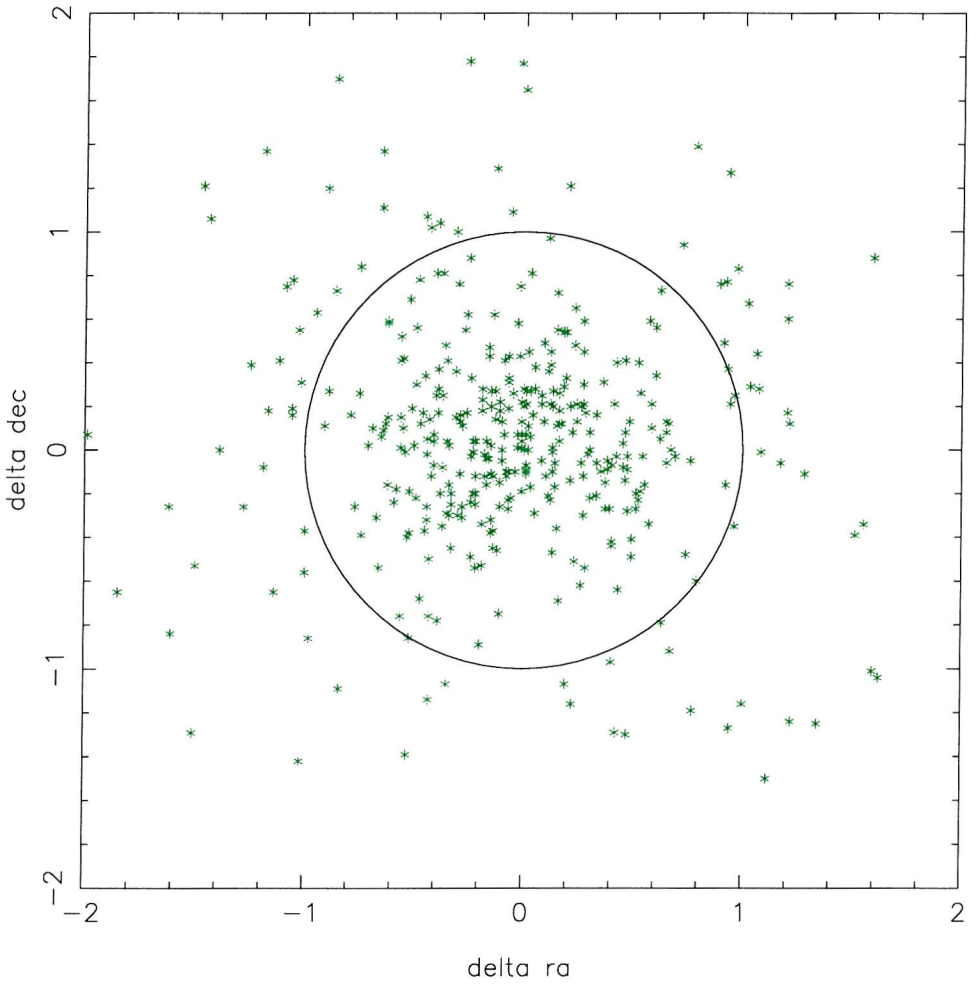


Figure 4.2: Diagram of the offset in RA and dec (arcseconds) of the $R$–band optical positions with the radio positions. There appears to be no systematic offset between the coordinate frames.

#### 4.1.3.1 Radio-optical position offsets

Figures 4.2, 4.3 and 4.4 indicate the radio-optical positional offsets. There is no obvious systematic difference between the coordinate frames and the amount of scatter has a rms-value of 0.60″ in Right Ascension and 0.58″ in declination. The vast majority of sources (297 out of 385) are within the 1″ radius marked on figure 4.2. This confirms that the two coordinate frames are in good agreement and therefore the chance of an optical source randomly having an unresolved radio source within 2″ is 0.23%. This means that only a few of 462 radio sources is likely to have false optical counterpart, allowing for possible mis-identifications of extended radio sources.

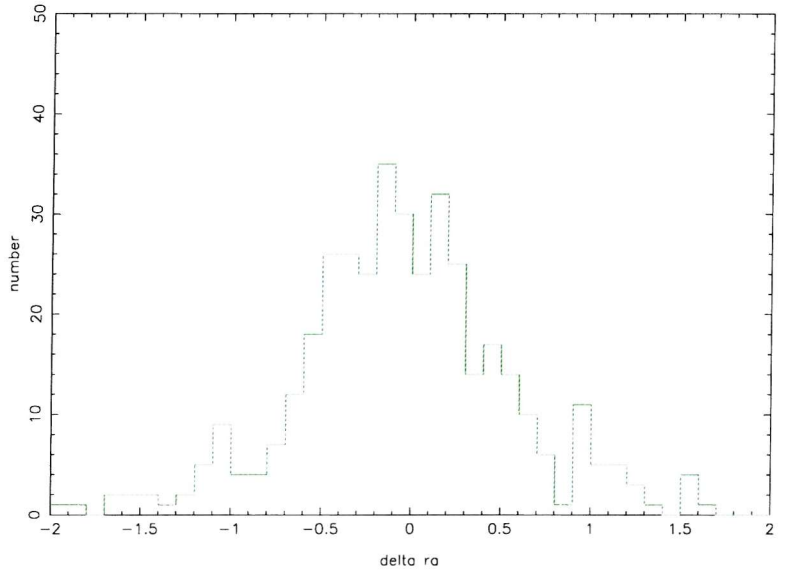


Figure 4.3: Distribution of Right Ascension offsets in arcseconds.

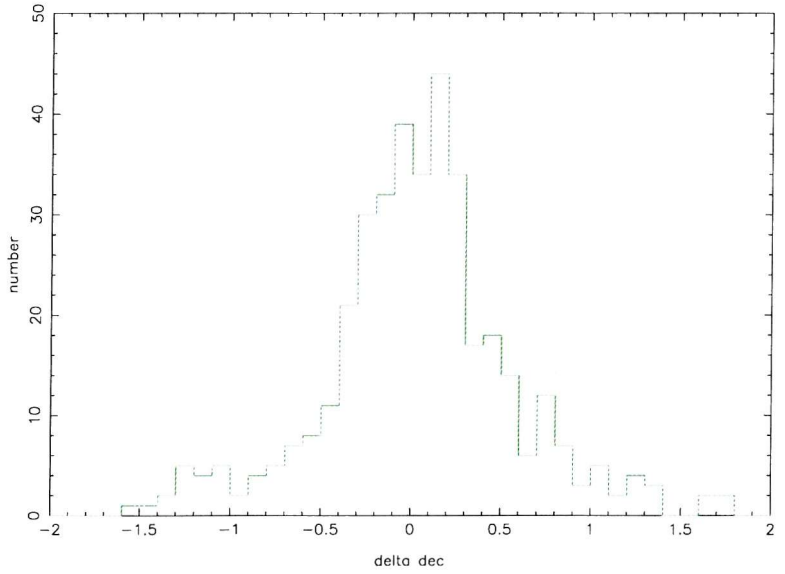


Figure 4.4: Distribution of the declination offsets in arcseconds.

#### 4.1.3.2 Extended Radio Sources

In six cases where radio sources were significantly extended the optical counterpart had to be selected by hand. These were radio sources 1, 5, 6, 7, 9 and 10. In figures 4.5 (A and B-configuration maps) and 4.6 (A-configuration maps) $50'' \times 50''$ ($100'' \times 100''$ for source 7) optical images of these radio sources are shown with radio contours overlaid. The contours are all multiples of the rms of the map, $7.5\,\mu$Jy/beam times -2, 2, 4, 6, 8, 16, 32, 64, 128, 192, 256, 320, 384, 448, 512, 576, 640, 704, 768, 832, 896 and 960. The reasons for the selection of the optical counterpart of each source is given below:

- Source 1 is the brightest radio source by almost an order of magnitude. It lies $13.5'$ away from the centre of the field at the very edge of the primary beam. Its brightness, location and angular size caused many problems at the imaging stage, see section 2.2.2. It is clearly a double lobe source (morphologically it just falls into the FRII category, however in the intrinsic R-magnitude/radio luminosity diagram, figure 4.20, it is clearly a FRII source) with the receding jet to the north-east and an approaching jet to the south-west. Examination of figure 4.6-a strongly suggests that the source of the jets is the bright elliptical galaxy about $5''$ north-east of the centre of the image (the image is centred on the position of the peak flux). This is confirmed by the higher resolution MERLIN observations (see figure 4.7) which show a bright core on the elliptical galaxy and highest surface brightness areas of the approaching jet to the south-west.

- Source 5 is perhaps the most aesthetically pleasing. It is a head-tail radio source which is a type of source thought to be associated with the movement of a jet source through a cluster in which the lobes of the jets are swept back by the intra-cluster medium. The actual source of the swept back lobes is the elliptical galaxy at the centre of figure 4.6-b at the bright point or 'head' of the radio source. There is evidence for a cluster in the optical image with an overdensity of reasonably bright galaxies within $10 - 20''$, but more compellingly there is an extended, faint, soft X-ray source in the *XMM* data with its centre only $10''$ away from the 'head' of the head-tail source (this source is also seen in the original *ROSAT* survey and by *Chandra*). From figure 4.5-b (the combined A and B-configuration data) it is clear that this source would be defined as a narrow angle head tail source.

- Source 6 is another double lobe radio source with a slightly brighter approaching lobe to the north-west and a fainter receding lobe to the south-east. The radio contours overlay 3 galaxies, but from figure 4.6-c) it is clear that the likely candidate is the middle brightest source with the other 2 being coincident background or foreground galaxies. The radio emission to the east is certainly a separate source associated with diffuse emission from the coincident extremely bright elliptical.

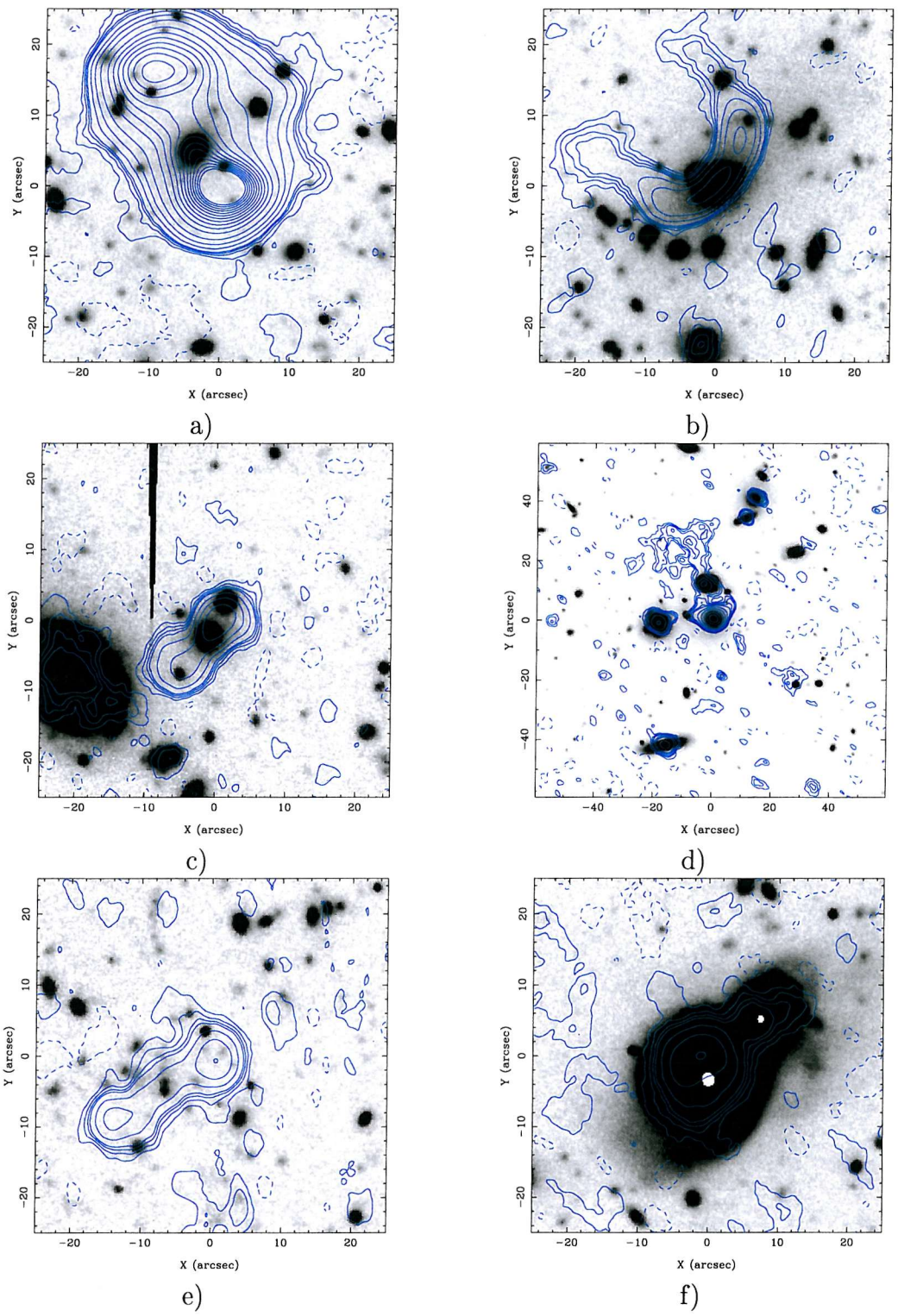


Figure 4.5: $R$– band images of the extended radio sources: 1, 5, 6, 7, 9 and 10 with radio contours from a naturally weighted A and B-configuration map at 7.0 $\mu$Jy/beam × -2 (dashed), 2, 4, 6, 8, 16, 32, 64, 128, 192, 256, 320, 384, 448, 512, 576, 640, 704, 768, 832, 896 and 960. Note that d) is $100'' \times 100''$ whilst all the others are $50'' \times 50''$ square.

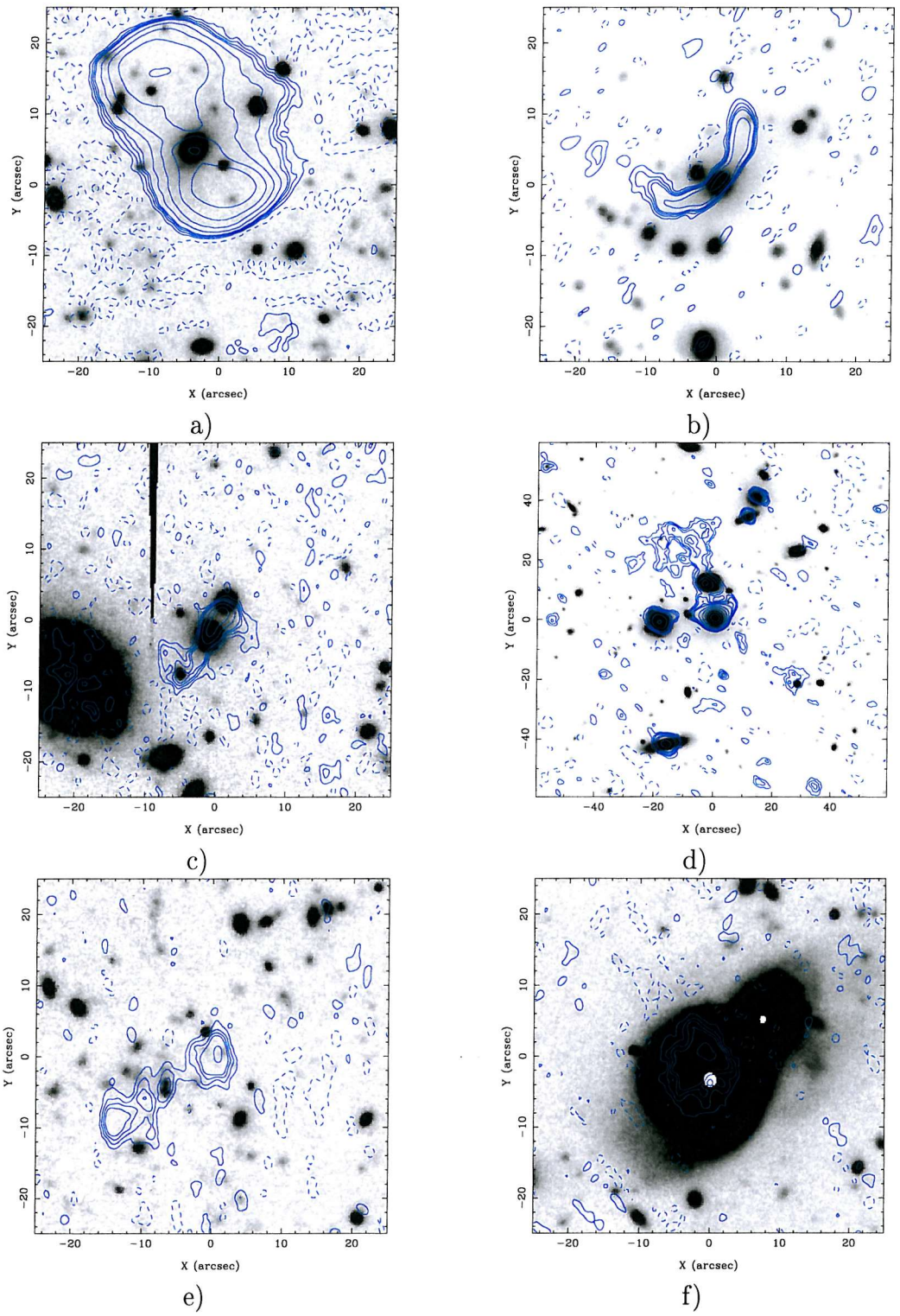


Figure 4.6: $R$– band images of the extended radio sources: 1, 5, 6, 7, 9 and 10 with radio contours from a naturally weighted A-configuration map at 7.0 $\mu$Jy/beam × -2 (dashed), 2, 4, 6, 8, 16, 32, 64, 128, 256, 512 and 1024. Note that d) is $100'' \times 100''$ whilst all the others are $50'' \times 50''$ square.

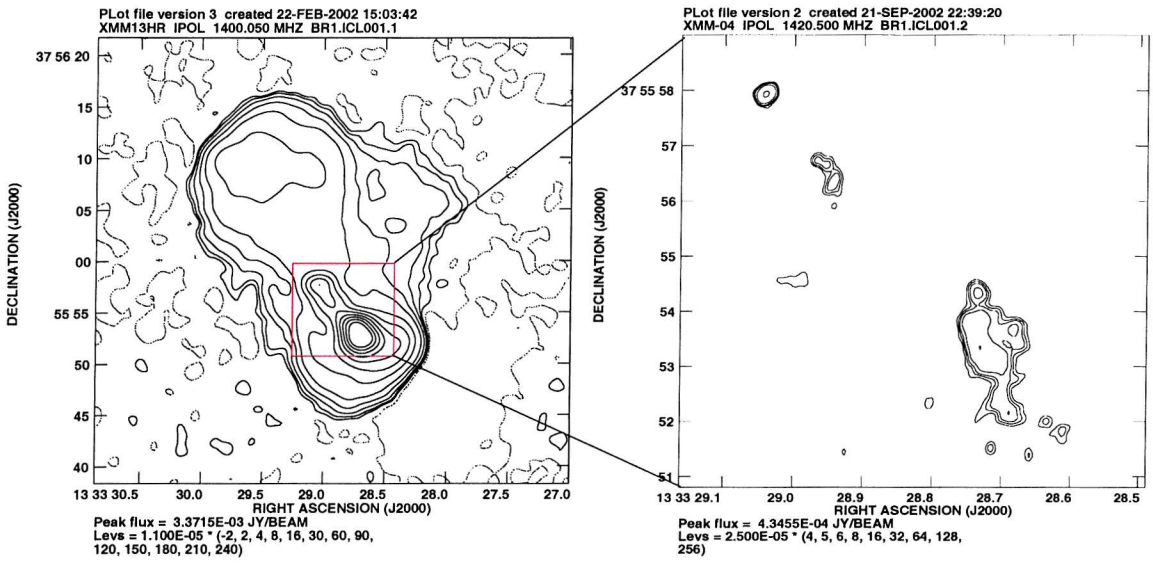


Figure 4.7: Radio source one displayed from the VLA data (left) and MERLIN data (right). The higher resolution MERLIN does not detect most of the extended emission as its higher resolution renders it less sensitive to low surface brighter emission. Only the bright hotspot of the approaching jet to the south-west is detected as well as an unresolved core component.

- Source 7 is shown using a larger image ($100'' \times 100''$) as it is by far the most complicated radio source. Source 7 is the one right in the centre of the field overlaying an elliptical galaxy. However there is considerable extended emission to the north which arcs round to the east, and includes two further galaxies, see also bottom left quadrant of figure 2.5. This region is discussed in more detail in section 5.5.2.

- Source 9 is a further double lobe radio source and would be morphologically classified as an FRII. However as there is no redshift for this source it is not possible to confirm its position in the intrinsic R-magnitude/radio luminosity diagram, figure 4.20. Figure 4.6-d) indicates that the source is associated with the galaxy at the central hotspot, believed to be the core.

- Source 10 is clearly associated with the underlying spiral galaxy which is bright enough to be saturated in the deep Subaru image. It is interesting to note that the combined, lower resolution, A and B-configuration data figure 4.6-e) detects emission from the nearby galaxy to the north-west whereas the A-configuration does not, figure 4.5-e)

### 4.1.4 The $B-$band data

The $B-$band data was observed using the Wide Field Camera (WFC) on the 2.5m Issac Newton Telescope (INT) with an exposure time of 1200s (data provided courtesy of Scott Croom). The WFC is a prime focus instrument for the INT consisting of 4 thinned EEV $2k \times 4k$ CCDs. The CCDs have a pixel size of $13.5\mu$m corresponding to $0.33''$/pixel. The arrangement of 3 CCDs lying side by side with one lying above two of these is such that a square area of $\sim 34'$ is covered minus a small corner. The Kitt Peak B filter was used.

This observation was photometric with seeing of $1''$. The final image was again analysed with SExtractor software and which found objects down to a non-confused limit of $B \sim 25.5$. Again a stellarity parameter was also reported. Optical counterparts were found in an identical fashion as that of the $R-$band data (i.e. within a $2''$ radius). Here 296 out of 462 radio sources were found to have $B-$band counterparts.

### 4.1.5 Colour distribution

An interesting diagnostic of a possible emission mechanism for the faint radio population is the $B-R$ colour distribution relative to that of the general population of galaxies. A relatively blue colour could be an indication of star-formation, whilst a relatively red colour is an indication of dust. A previous study (Roche, Lowenthal & Koo, 2002) found that the radio detections generally had similar colours to an optically selected sampled of galaxies in the same field (including radio detections), and concluded that if the faint radio galaxies are of a similar type to that of the field, star-forming galaxies, then they suffered little ($\Delta(B-R) < 0.5$ mag), or no additional reddening.

To investigate this possible effect, $B-$band counterparts for all Subaru $R-$band sources were found by using a $2''$ detection radius (when more than one counterpart was found then either the nearer was taken if there was one obviously closer or else the one with more similar stellarity was taken). A subregion of the Subaru field was used defined by the $30'$ diameter of the VLA field and the edge of the region missed by the non-operational Subaru CCD in the lower left of figure 4.1. From the same region all radio sources with $R-$band and $B-$band counterparts were chosen. Figure 4.8 compares the $B-R$ distribution of all radio IDs, 258 in total, with that of all 37579 galaxies (including the radio IDs) as a function of $R-$band and $B-$band .

The effects of the detection limits of each image are clear. In figure 4.8a) the effect of the $B \sim 26.5$ limit is obvious in the upper right of the plot where at faint $R-$band magnitudes there is a significant selection effect against red objects

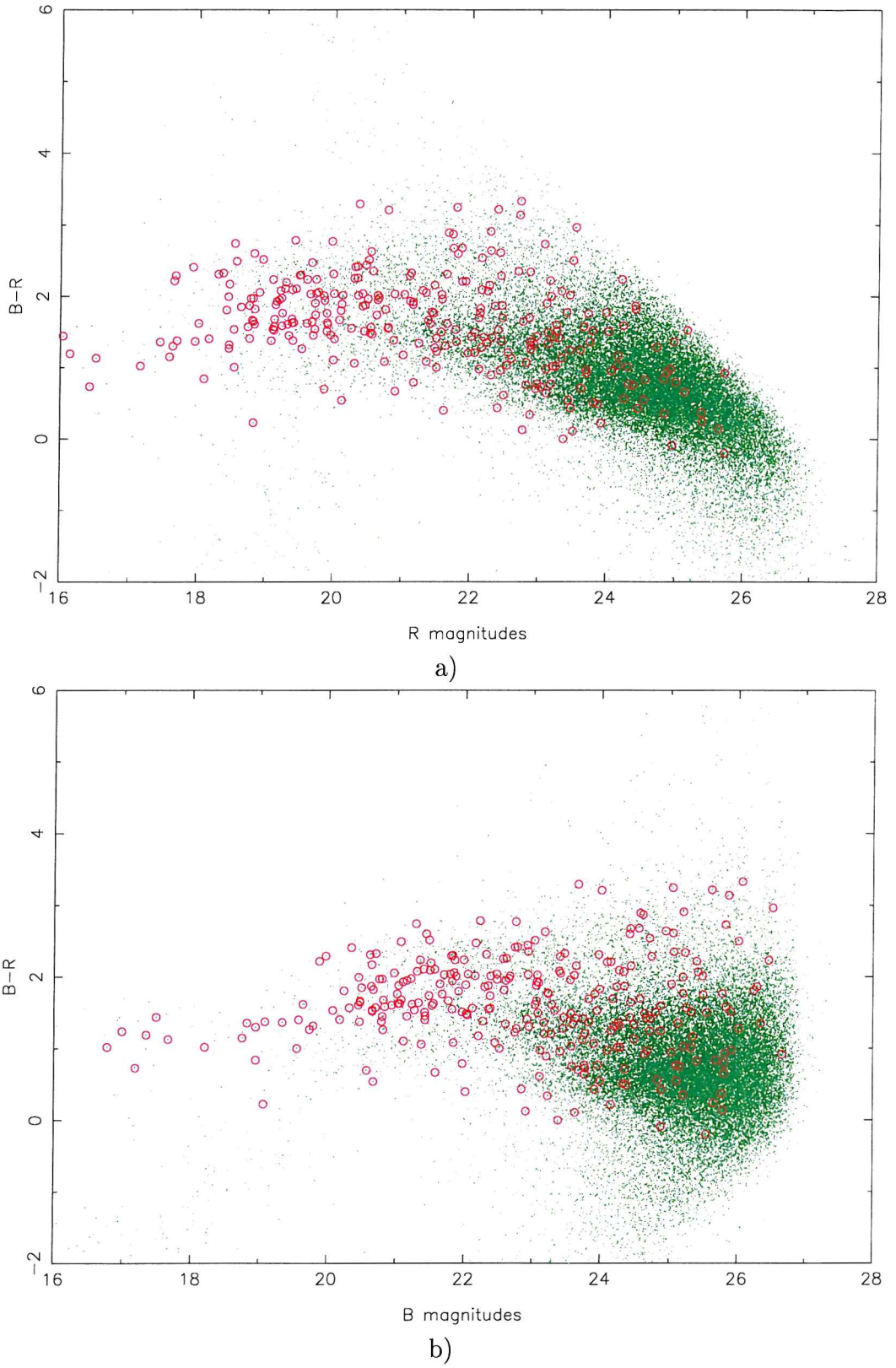


Figure 4.8: The $B-R$ colours of all optical sources with $R$–band and $B$–band detections plotted against $R$–band magnitude and $B$–band magnitude. The selection effects in both plots are obvious (see section 4.1.5). Optical counterparts of radio sources are marked with an open circle.

Table 4.1: Results of KS test on the distribution of different samples

| Sample | Field | | Radio | | $\delta$mean | D | P |
|---|---|---|---|---|---|---|---|
| | no. | mean | no. | mean | | | |
| $20 < B < 25$ | 14522 | 0.94 | 219 | 1.64 | 0.70 | 0.40 | $< 0.001$ |
| $Rstel < 0.9$ | 13337 | 0.92 | 210 | 1.68 | 0.76 | 0.26 | 0.056 |
| $Rstel < 0.5$ | 12003 | 0.98 | 201 | 1.70 | 0.72 | 0.26 | 0.056 |
| $Rstel > 0.9$ | 1182 | 1.15 | 8 | 0.71 | -0.44 | 0.38 | 0.085 |
| $20 < B < 22.5$ | 1135 | 1.51 | 99 | 1.77 | 0.26 | 0.28 | 0.032 |
| $22.5 < B < 25$ | 13387 | 0.89 | 120 | 1.54 | 0.65 | 0.38 | 0.001 |
| $F_{1.4\,\mathrm{GHz}} < 100$ | 14522 | 0.94 | 138 | 1.66 | 0.72 | 0.40 | $< 0.001$ |
| $F_{1.4\,\mathrm{GHz}} > 100$ | 14522 | 0.94 | 80 | 1.62 | 0.68 | 0.42 | $< 0.001$ |

(i.e. they're not detected). A similar effect is seen in the lower right of figure 4.8b) where at very faint $B$–band magnitudes very blue objects are not selected. However the area of parameter space missed is much smaller in this case and if a limit of $B \sim 25$ is taken then a virtually complete sample is obtained. In both figures at brighter fluxes there is a scattering of very blue objects which are either quasars or mis-identifications. What is clear from both plots is that the radio sources are systematically redder than the field galaxies at fainter fluxes. To quantify this, eight sub-samples from a complete sample of radio and optical sources with $R < 26.5$ and $20 < B < 25$ were examined. The faint limit is to avoid missing too many faint, very blue sources (it is possible that some faint, very blue sources with $B - R \leq 0$ are missed due to $R$–band source confusion starting at $R \sim 25$). The bright limit is chosen so as to avoid being biased by the possibly mis-identified, bright, blue objects (figure 4.8).

The $B - R$ colour distribution for the eight selected sub-samples are shown in figure 4.9. The first sub-sample (figure 4.9-a)) shows all the sources selected in $20 < B < 25$ range. The next 3 subsamples are divided according to $R$–band stellarity ($R$–band was chosen as it was slightly deeper and therefore the stellarity is more accurate to fainter magnitudes). Figure 4.9-b) includes all the sources with stellarity $< 0.9$, figure 4.9-c) includes all the sources with stellarity $< 0.5$ and figure 4.9-d) includes all the sources with stellarity $> 0.9$. The sources were then divided by optical and radio flux. Figure 4.9-e) includes all the sources with $20 < B < 22.5$, figure 4.9-f) includes all the sources with $22.5 < B < 25$, figure 4.9-g) includes all the sources with radio flux $< 100\,\mu$Jy and figure 4.9-h) includes all the sources with radio flux $> 100\,\mu$Jy.

It is clear that there is a skew between the distributions of the optically selected sample and the radio selected sample in both figures. In all cases except for the high stellarity sample ($Rstel > 0.9$), it seems that the radio selected sources are redder than the non-radio selected sources of a similar magnitude. To quantify this the Kolmogorov-Smirnov (KS) Comparison Test (Press et al., 1992) was used which tests whether two sets of data are drawn from the same distribution function

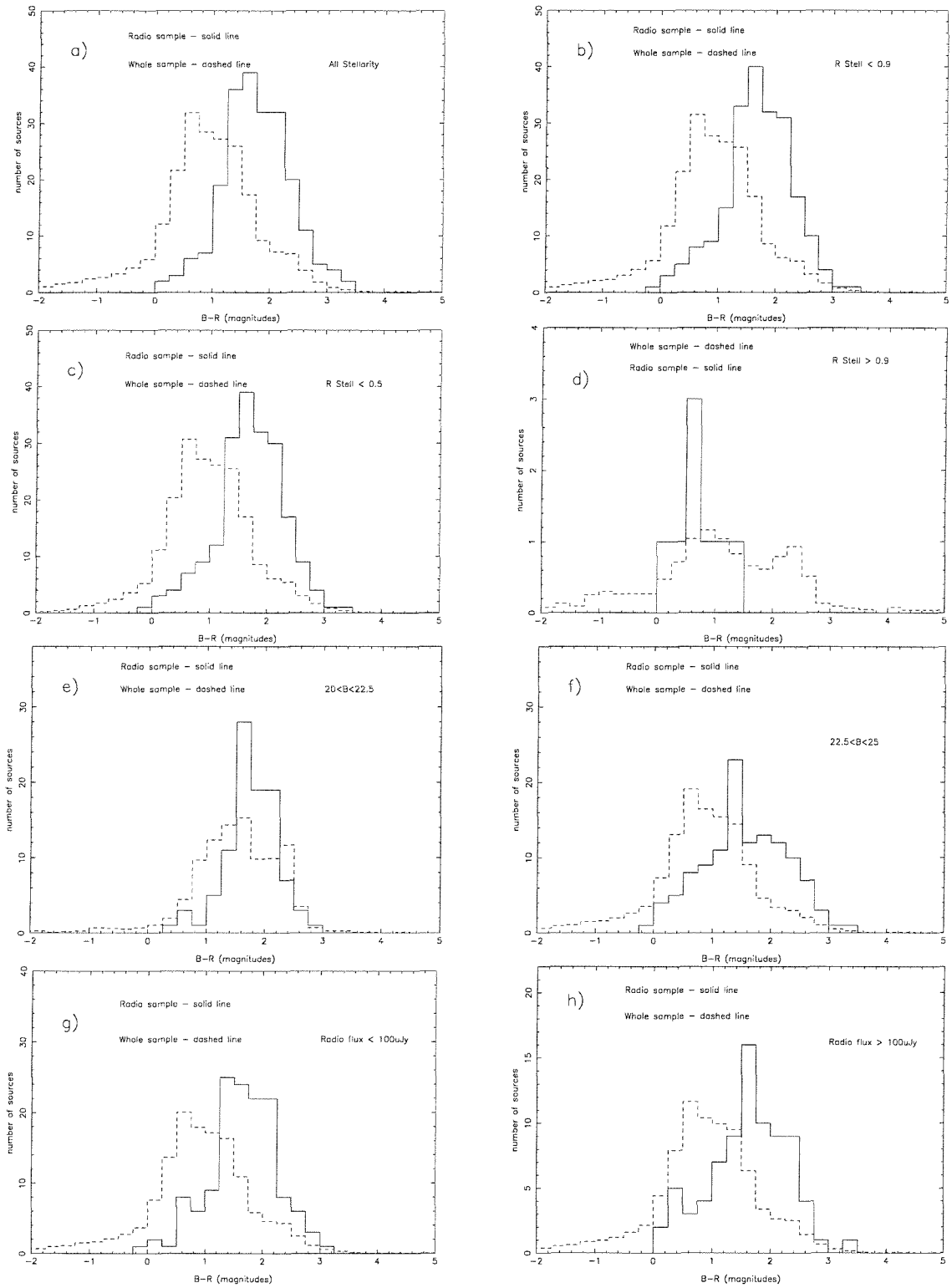


Figure 4.9: The distribution of colours of radio sources for eight selected sub-samples (solid lines) with the distribution of colour for similarly selected optical sources (dashed line), normalised to the same total number of sources.

or not. It works by converting both distributions into a cumulative distribution and then finding $D$, the maximum value of the absolute difference between the two cumulative distributions normalised to one. This value corresponds to a KS statistic (Press et al., 1992) which gives the significance level of an observed value of $D$ as a disproof of the null hypothesis that the distributions are the same. In other words it is the probability that if you randomly picked each distribution from the same parent population that you get the two distributions observed, so a low value indicates a low probability that the differences are random. The results of this analysis are presented in table 4.1.

The high stellarity plot shows a noticeably different distribution of $B-R$ colours for the field galaxies compared to all the other plots, figure 4.9-d). The distribution of optically selected sources in this plot is probably a combination of quasars with $B-R \sim 1$ and fore-ground stars with $B-R \sim 2-3$. Undoubtedly a high fraction of the radio selected, unidentified, blue, 'stellar' sources are quasars. Despite the high stellarity radio sub-sample having only eight sources (and hence low number statistics coming into play) it is probable that most if not all are quasars (at least 3 of these sources have been spectroscopically identified as such - see section 4.2.1). However the slightly high probability of the null hypothosis is due to the low number statistics in the radio selected sample (8 sources). There is a big change in the difference in mean colours going from the $20 < B < 22.5$ subsample to the $22.5 < B < 25$ subsample, however this is largely due to the mean colour of the the optically selected galaxies getting more blue. This is probably the detection of the faint blue galaxy population (Shanks et al. 1984) which is noticeable in the bottom left of figures 4.8a) and b). Additionally there is little indication that sources with fainter radio fluxes ($< 100\,\mu$Jy) are redder than brighter sources ($\Delta(B-R) \sim 0.04$mag).

Georgakakis et al. (1999) found that in a selected sample of radio sources from the Phoenix Deep Field (Hopkins et al., 1998) for which they have $V$, $R$ and $K-$band magnitudes the $V-R$ and $R-K$ colours are consistent with a small amount of extinction (including a small fraction of galaxies with evidence of higher extinction) compared to the predictions of evolutionary models of Bruzual & Charlot (1993). They also concede that the reddening could also be caused by the presence of an underlying evolved stellar population in addition to main sequence stars.

Richards et al.(1999) notice a similar reddening of radio objects relative to field galaxies by plotting $I-K$ against $I$ magnitude for sample of source from the Hubble Deep Field and the SSA13 field. They note that at fainter $I-$band magnitudes ($> 21$) the radio sources are redder than the field galaxies and that the optically fainter radio sources have redder colours reaching $I-K \sim 3$ at $I = 24$ mag.

The analysis presented here does not find that there is any significant change in the mean colour of radio sources as a function of $B-$band magnitude. The discrepancy of the distribution of radio galaxies with that of optically selected sources is due to the emergence of a population of faint blue galaxies (not detected at radio

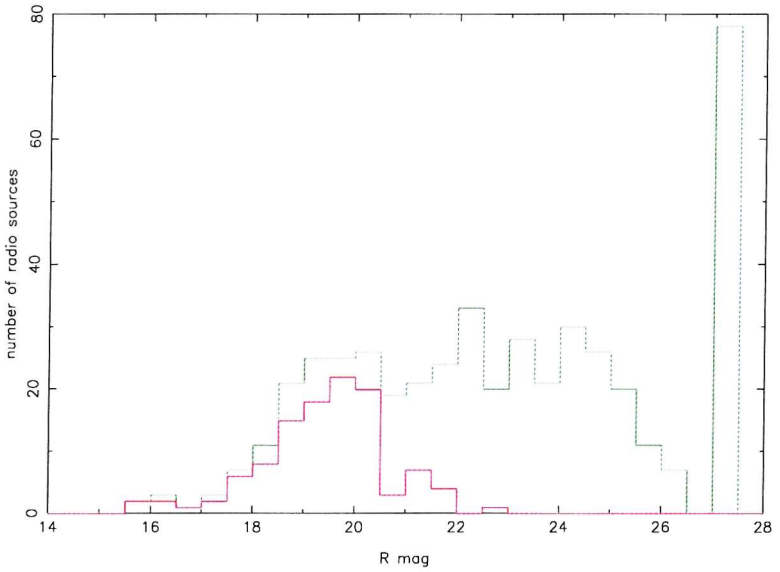


Figure 4.10: The $R$–band magnitude of radio sources with optical counterparts and those also with confirmed optical spectra shown underneath. Sources with no $R$–band counterparts are given a nominal value of $R \sim 27$.

wavelengths) causing the mean colour of the optically selected galaxies to become more blue with fainter $B$–band magnitudes.

### 4.1.6 General Properties of the Radio/Optical sample

Of 462 radio sources 385 were found to have $R$–band optical counterparts to the confusion limit of $R \sim 27$. This means this the radio survey is optically 83% complete which is comparable to other deep radio surveys with deep optical imaging (e.g. Richards, 2000, was $\sim$ 80% complete in $I$–band to a limit of $I_{AB} \sim 25$). In figure 4.10 a histogram shows the distributions of $R$–band magnitudes for the radio sources with optical counterparts. The final bin at $R \sim 27$ with 77 optical sources is for sources with no optical counterpart found to that limit. The roughly constant number of $R$–band counterparts over $19 \leq R \leq 25$ seem to indicate the presence of several populations of radio sources. The tail off at $R \sim 24 - 27$ is due to confusion of optical sources close to the detection limit and incompleteness of the optical catalogue. It is probably not physical. More than likely there is a roughly flat distribution of radio sources at fainter $R$–band magnitudes. The lower histogram indicates the number of counterparts with optical spectra (these are examined further in section 4.2.1). Figure 4.11 shows a similar histogram for the $B$–band data. Here there are only 296 counterparts to radio sources, a completeness of 64%.

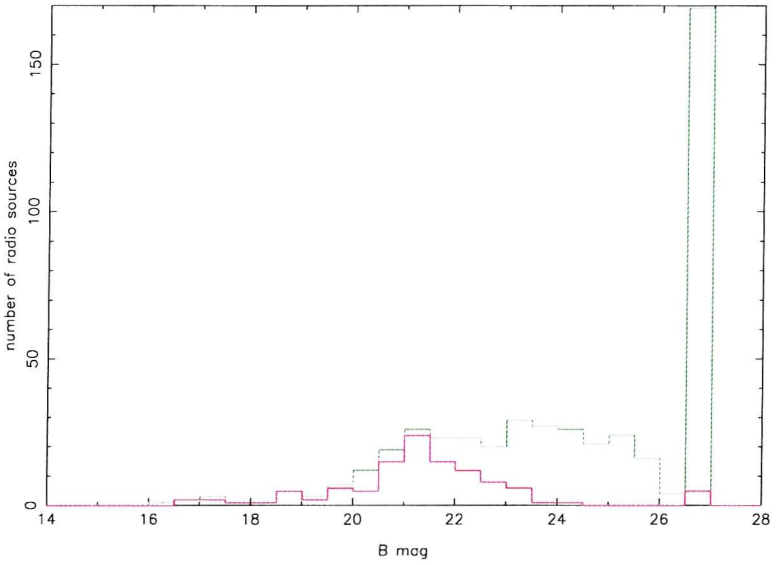


Figure 4.11: The $B-$band magnitude of radio sources with optical counterparts and those also with confirmed optical spectra shown underneath. Sources with no $B-$band counterparts are given a nominal value of $\sim$ 26.5. Note there are far more sources without $B-$band counterparts than without $R-$band counterparts, due to shallower imaging available in $B$.

#### 4.1.6.1 The Radio to Optical flux ratio of the Radio Sources

Sources first discovered by radio surveys were naturally the brightest radio sources with a very large radio to optical flux ratio. It was later discovered that virtually all galaxies emit at radio wavelengths albeit most normal galaxies relatively very little. The radio continuum contributes $< 10^{-4}$ of the bolometric luminosity of normal galaxies (Condon, 1992). Their radio emission is in the form of synchrotron radiation from relativistic electrons and free-free emission from HII regions. Only young stars more massive than $8\,M_{\odot}$ produce supernovae whose remnants are thought to accelerate most of the relativistic electrons in normal galaxies and these stars also ionise the HII regions (Condon, 1992). There is recent evidence, including the original *ROSAT* survey (M$^{c}$Hardy et al., 1998), that star formation and AGN activity can occur within the same galaxy with varying relative contributions to bolometric flux. Recently a value $L_{radio}/L_{optical} = 10$ has been taken to separate 'radio loud' quasars from 'radio quiet' quasars (Kellermann et al. 1989 and Ho & Peng 2001). This radio-loud/radio-quiet classification is strictly only defined for quasars while the sample presented here contains a mixture of different class of object (e.g.radio galaxies, starbursts, clusters etc.). The distribution of radio loudness is examined.

The traditional definition in the literature of 'radio loudness' (Kellermann et al., 1989) is the ratio of the flux at 5 GHz to the flux in $B-$band (both in mJy). However

as this radio survey is most complete at 1.4 GHz and in $R$–band the radio loudness is defined thus in this analysis:

$$RadioLoudness, R_O = \frac{f_{1.4\,\mathrm{GHz}}}{f_\nu(R)} \tag{4.1}$$

The optical magnitude to flux conversions are calculated using the constants defined in Fukugita et al. (1995). The optical flux is defined

$$\log(f_\nu(m_x)) = -0.4m_x + \log(f_\nu(0)) \tag{4.2}$$

where $f_\nu(m_x)$ is the flux in $\mathrm{W\,m^{-2}\,Hz^{-1}}$ and the relative flux is multiplied by a correction factor ($f_\nu(0)$, the absolute spectral irradiance for mag=0, also in $\mathrm{W\,m^{-2}\,Hz^{-1}}$). This definition is assuming a certain filter. The Cousins filter was used for the $R$–band exposure and the Kitt-Peak filter for the $B$–band . Hence Fukugita et al. give $f_\nu(0) = 3.02 \times 10^{-23}\,\mathrm{W\,m^2\,Hz^{-1}}$ for $R$–band and $f_\nu(0) = 4.02 \times 10^{-8}\,\mathrm{W\,m^2\,Hz^{-1}}$ for $B$–band leading to (in units of Janskys):

$$\log(f_\nu(m_R)) = -0.4R + 3.480 \tag{4.3}$$

and

$$\log(f_\nu(m_B)) = -0.4B + 3.604 \tag{4.4}$$

It is possible to show that the divide between 'radio loud' and 'radio quiet' can also be defined from equation 4.1 as $R_O = 10$ by extrapolating the traditional definition (which uses 5 GHz and $B$–band ) to 1.4 GHz and $R$–band assuming an average radio spectral index of $\alpha = 0.75$ and a mean $B - R$ colour of 1.64 (see section 4.1.5). Therefore if

$$\frac{f_{5\,\mathrm{GHz}}}{f_\nu(m_B)} = 10 \tag{4.5}$$

$$f_{1.4\,\mathrm{GHz}}\left(\frac{5}{1.4}\right)^{-0.75} = 10 \times 10^{-0.4B+3.604} \tag{4.6}$$

$$\log(f_{1.4\,\mathrm{GHz}}) - 0.41465 = 1 - 0.4(R + 1.64) + 3.604 \tag{4.7}$$

$$\log(f_{1.4\,\mathrm{GHz}}) = -0.4R + 4.36265 \tag{4.8}$$

$$\log(f_{1.4\,\mathrm{GHz}}) = -0.4R + 3.48 + 0.88265 \tag{4.9}$$

giving:

$$\frac{f_{1.4\,\mathrm{GHz}}}{f_\nu(m_R)} = 7.63 \sim 10 \tag{4.10}$$

This then gives a relationship which can be used to divide the 'radio louds' and 'radio quiets' in 1.4 GHz flux/$R$–band space:

$$\frac{f_{1.4\,\mathrm{GHz}}}{f_\nu(m_R)} = 10 \tag{4.11}$$

Now putting in the expression for optical flux.

$$\log(f_{1.4\,\mathrm{GHz}}) = 1 + (-0.4R + 3.604)) \tag{4.12}$$

and then for radio flux $S_{1.4\,\mathrm{GHz}}(\,\mu\mathrm{Jy}) = 10^6 \times f_{1.4\,\mathrm{GHz}}$

$$\log(S_{1.4\,\mathrm{GHz}} \times 10^{-6}) = 4.604 - 0.4R \tag{4.13}$$

where $10^{-6}$ is the conversion from $\mu$Jy to Jy gives,

$$\log(S_{1.4\,\mathrm{GHz}}) = 10.604 - 0.4R \tag{4.14}$$

The radio flux against R magnitude is plotted in figure 4.12. The relationship above is plotted as a line separating the 'radio quiets' from the 'radio louds'. It is clear that for a given R magnitude it is possible to have a wide range of radio fluxes, i.e. from the detection limit (30 $\mu$Jy) to several tens of mJys. There is no obvious separation between the radio louds and the radio quiets, suggesting that the radio/optical flux ratio has a continuous distribution across radio flux and $R$ magnitudes for radio selected sources. This is confirmed by figures 4.13 and 4.14 which are both shown with the $f_{1.4\,\mathrm{GHz}}/f_\nu(R) = 10$ dividing line. It appears that of the optically detected sources, around half are radio loud and half are radio quiet.

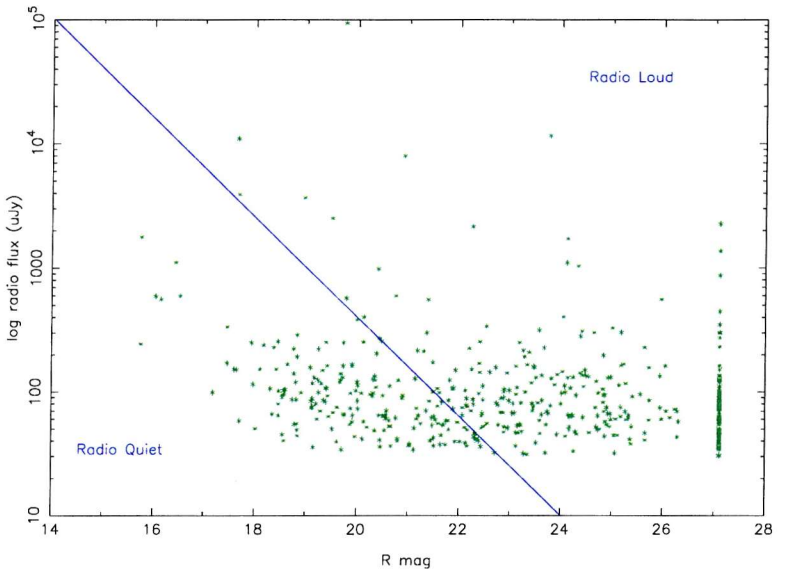


Figure 4.12: Distribution of $R$– band magnitude of optical counterparts to the radio sources. Sources with no optical counterpart have been assigned a maximum value of $R \sim 26.75$. The diagonal line shows the division between radio loud and radio quiet as defined by having the ratio of radio to optical monochromatic fluxes equalling 10.

Early surveys of the quasars, selected by their relative UV excess, found that only 5-10% are radio loud. This is the standard picture in the literature and even relatively recent survey have found a dichotomy in radio loudness for quasars (Kellermann et al., 1989). Recent evidence for Seyferts (Ho and Peng, 2001) suggests that instead of around 4% being radio loud, as previously thought, closer to $\sim$ 50% are radio loud (i.e. $R_0 > 10$). However the sample presented here is selected on radio luminosity so that it is more than likely that many radio quiets are not included, biasing this distribution to roughly half loud and half quiet.

Using radio loudness as parameter to study AGN does have some problems. It strictly pertains to the radio/optical ratio of the nucleus, but even in resolved sources it is difficult to differentiate between the flux of the nucleus and that of the host galaxy (which may be emitting optically due to stars and at radio wavelengths due to supernova remnants). Miller et al. (1990) suggest defining radio loud as any object with a 5 GHz intrinsic luminosity, $P_{5\,\mathrm{GHz}} > 10^{25}\,\mathrm{W\,Hz^{-1}}$. However as the radio emission mechanism is more than likely linked to other sources of energy from the central engine, then the *relative* radiative output in the radio band is considered to be more meaningful (Ho and Peng, 2001).

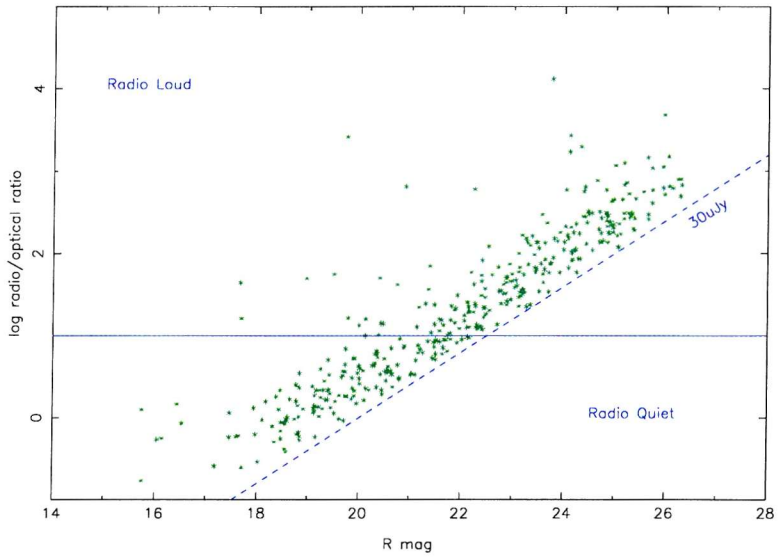


Figure 4.13: A plot of the log radio/optical flux ratio as a function of R magnitude. The radio loud/radio quiet cut is shown at $R_{radio/optical} = 10$, see text. The lack of sources in the lower right corner is due to the 30 $\mu$Jy radio survey limit indicated by the dashed line.

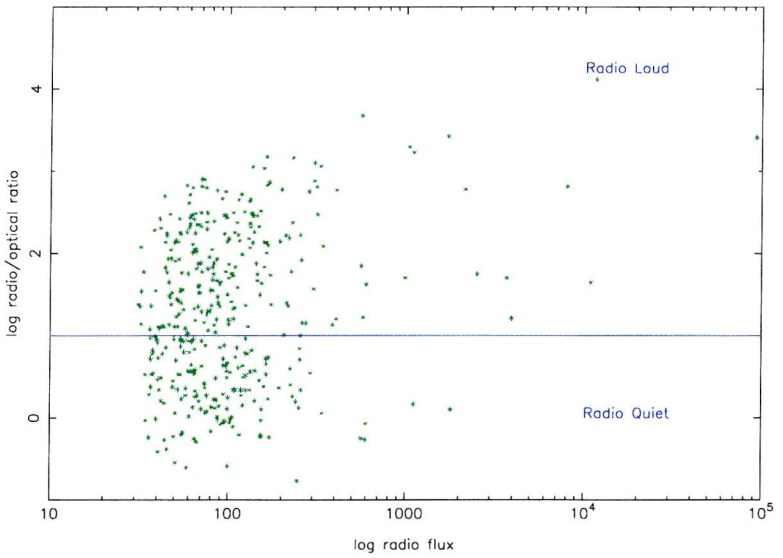


Figure 4.14: The distribution of the log radio/optical flux ratio as a function of radio flux. This figure shows that over the whole range of radio fluxes radio bright and radio quiet galaxies are detected.

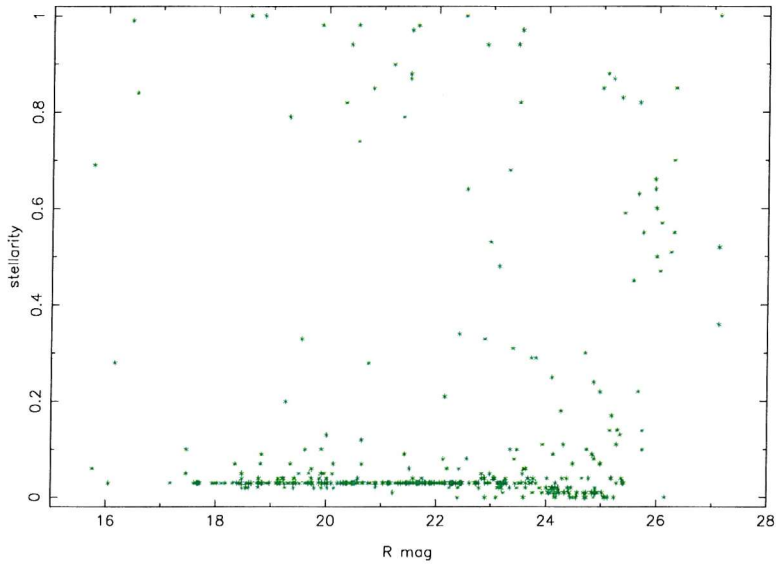


Figure 4.15: The distribution of the stellarity value against R magnitude for all optical counterparts to the radio sources. This figure shows that whilst there are many optical counterparts which are star like, the vast majority are resolved galaxies.

#### 4.1.6.2 The stellarity

The stellarity parameter is an indication of how the confident the SExtractor software is that an optical source is star-like, or unresolved. Figure 4.15 shows the distribution of all radio sources with $R$–band counterparts. It is clear that the vast majority are resolved (i.e. have a stellarity less than 0.9) and are therefore galaxies. We would expect AGN to have a stellarity value close to one if no 'halo' is seen.

## 4.2 The Optical Spectra

Optical spectra are extremely useful in studying contributors to the radio and X-ray background. Not only do identified spectra give you redshifts and hence absolute optical magnitudes and radio luminosities, but the details of the spectra also give you clues to the astrophysical processes going on in a galaxy and how obscured the nucleus is.

### 4.2.1 The Data

As the 13hr field has been investigated for a decade, the various optical spectra have been obtained from many different observations and on different telescopes. Most

have been obtained toward the end of the time spent on this thesis when a final list of radio sources was defined. Some optical spectra date back to observations identifying optical counterparts to the *ROSAT* sources (M$^{c}$Hardy et al., 1998). The positions were later checked with *Chandra* IDs as the positions on the *ROSAT* error boxes were of the order of 5″. In cases where the *ROSAT* ID was confirmed that ID was used, or alternative IDs from unpublished data from the *ROSAT* observations were used (if confirmed by the *Chandra* and *VLA* positions).

There were three main sources of optical spectra:

- Pre-existing spectra from the original *ROSAT* survey from a variety of sources (including unpublished data)
- Spectra from observations taken with the RGO Wide Field Fibre Optical Spectrograph (WYFFOS) on the William Hershel Telescope (WHT) on La Palma in 1999.
- Further observations from the 9th May 2002 on WHT with WYFFOS.

The WYFFOS spectra had already been calibrated and had provisional IDs. However they were carefully inspected again and more identifications were made or corrected.

#### 4.2.1.1 Identification of optical spectra and determination of redshift

The optical spectra were identified by the emission or absorption lines and occasionally by the continuum break at $\sim$ 3950Å. The spectra were given one of three classifications: broad line galaxies (referred to henceforth as BLAs, but obviously could be Seyfert I or Broad Line Radio Galaxies), narrow emission line galaxies (NELGs) and absorption line galaxies (GALs). Each ID of a spectra was given a quality value depending on how confident the result was; 3=definite (several features with agreeing redshifts), 2=probable (at least two features with agreeing redshift, e.g. OII line and continuum break), 1=possible (one reasonable feature) and 0=tentative (one slightly uncertain feature). As the quality of the spectra varied redshifts were determined from measuring the wavelength of the maximum or minimum values of the emission/absorption lines (and averaging them if more than one were present). For sources with many features the redshift was found by averaging the values found for each feature, and the statistical errors are less than 1%. For sources with one feature the error is around a few percent.

### 4.2.2 The results

The list of all 111 radio sources with optical spectra of confirmed optical counterparts is presented in table 4.2. The contribution they make to the total number of optical counterparts is shown in fig 4.10. It is clear that the sample is reasonably complete to a limit of $R \sim 20.5$. In table 4.2 the first column is the source number followed by the Right Ascension and then declination, the eighth column is the $R-$band magnitude, the ninth column is the source's redshift, the tenth column is the ID (GAL=galaxy, NELG=Narrow Emission Line Galaxy and BLA=Broad Line AGN), the eleventh column is the Quality factor of the ID (explained in the previous paragraph) and final columns notes the lines and features seen in the spectrum (R indicates that the ID of the source was taken from the *ROSAT* catalogue paper (M$^{c}$Hardy et al., 1998) (or from unpublished data concerning that work).

### 4.2.3 The Spectroscopic Sub-sample

To a limit of $R < 20.5$, optical spectra for 96 out of 124 radio sources are available (i.e. an 77% completeness). This sample was named the 'spectroscopic' sub-sample and their properties were investigated more closely[1]. Here a few properties of the sub-sample are examined.

### 4.2.4 Distribution of properties with redshift

In this section the distribution of stellarity, colour and radio loudness are examined as a function of redshift. These are shown respectively in figures 4.16, 4.17 and 4.18.

Figure 4.16 shows that (as expected) most radio objects are generally red except for Broad Line AGN which are bluer (as expected if most are quasars). It is interesting to note that until the Broad Line AGN are detected at high redshift there is a slight trend that more distant objects are redder. However this is mainly due to K-correction effects. This is the redshifting of the Spectral Energy Distribution of the observed source due to the cosmological expansion of the universe which causes a particular passband (in this case $R$ and $B-$band ) sampling a part of the spectrum at shorter wavelengths. Specifically a typical galaxy spectrum will be observed to be redder after the $B-$band bandpass passes through the continuum break at $\sim$ 3950Åwhich occurs at $z \sim 0.1$ (i.e. the observed $B-$band magnitude decreases and a hence a redder spectrum is observed). Also the lack of particularly blue sources

[1]The 15 sources with optical spectra, but not included in this sample ($R > 20.5$) are; 63, 69, 121, 159, 175, 209, 257, 290, 298, 305, 325, 382, 412, 415, 436.

Table 4.2: Full list of optical counterparts to radio sources with optical spectra. Each radio source is accompanied by its position, $R$-mag of optical counterpart, redshift, spectroscopic classification, a quality factor (to indicate the confidence in a spectra, 3=definite, 2=probable, 1=possible, 0=tenuous) and the emission/absorption lines observed. R indicates that the ID of the source was taken from the *ROSAT* catalogue paper (M$^c$Hardy et al., 1998) or from unpublished data concerning that work

| Source | Right Ascension hh mm ss | Declination ° ′ ″ | R mag | z | ID | Q | lines |
|---|---|---|---|---|---|---|---|
| 1 | 13 33 29.0400 | 37 55 57.9000 | 19.744 | 0.688 | NELG | 2 | OII |
| 3 | 13 34 38.4961 | 38 06 27.0060 | 17.654 | 0.235 | NELG | 3 | R |
| 5 | 13 33 59.9508 | 37 49 11.6365 | 17.674 | 0.257 | GAL | 3 | R |
| 6 | 13 34 57.6500 | 37 50 29.4000 | 18.959 | 0.384 | NELG | 3 | OII |
| 10 | 13 35 25.3400 | 38 05 33.9000 | 15.743 | 0.068 | NELG | 3 | R |
| 13 | 13 34 13.5711 | 37 45 39.3040 | 16.43 | 0.061 | NELG | 3 | H$\alpha$,H$\beta$,SII,OII,OII |
| 16 | 13 34 58.3925 | 38 04 29.8780 | 20.400 | 1.997 | BLA | 3 | CIV,CIII,SiIV |
| 18 | 13 34 1.5384 | 37 49 10.3570 | 16.521 | 0.062 | NELG | 3 | R |
| 20 | 13 35 16.2916 | 37 56 21.4310 | 16.038 | 0.121 | NELG | 3 | H$\alpha$ |
| 21 | 13 34 42.8462 | 37 57 34.1190 | 19.777 | 0.499 | NELG | 3 | OII,OII |
| 27 | 13 34 51.9969 | 37 57 43.5570 | 20.125 | 1.89 | BLA | 3 | R |
| 28 | 13 34 57.3099 | 37 47 59.0140 | 19.992 | 0.358 | NELG | 3 | OII,H$\alpha$,SII |
| 31 | 13 34 1.3223 | 37 48 29.1610 | 17.453 | 0.061 | NELG | 3 | OII,H$\alpha$,SII |
| 40 | 13 34 26.2601 | 37 56 23.2230 | 18.829 | 0.336 | NELG | 3 | OII,H$\alpha$ |
| 43 | 13 33 48.1941 | 37 53 54.1560 | 20.422 | 0.82 | NELG | 1 | OII |
| 44 | 13 35 14.8138 | 38 01 10.2580 | 20.471 | 0.327 | NELG | 3 | OIII |
| 47 | 13 34 13.6694 | 37 59 44.6950 | 20.119 | 0.476 | NELG | 3 | OII,OIII |
| 49 | 13 33 48.3903 | 37 54 57.5170 | 19.391 | 0.320 | NELG | 3 | H$\alpha$,H$\beta$,OII,OII |
| 50 | 13 35 0.2059 | 37 56 33.1360 | 19.733 | 0.56 | NELG | 3 | OII,OIII |
| 51 | 13 35 31.9092 | 37 45 35.7610 | 17.930 | 0.304 | GAL | 3 | K,H |
| 52 | 13 34 11.5746 | 38 01 19.3580 | 15.743 | 0.062 | NELG | 0 | G,H$\alpha$ |
| 53 | 13 34 22.7381 | 37 55 25.2530 | 18.168 | 0.265 | NELG | 3 | H$\alpha$,H$\beta$,OII,OII |
| 55 | 13 34 41.8190 | 38 00 11.0860 | 18.372 | 1.089 | BLA | 3 | R |
| 59 | 13 34 17.5873 | 37 44 32.9340 | 18.761 | 0.289 | NELG | 3 | H$\alpha$,H$\beta$,OII,OII |
| 60 | 13 35 18.6975 | 37 55 31.6230 | 19.243 | 0.304 | NELG | 3 | H$\alpha$,H$\beta$,OII,OII |
| 63 | 13 35 14.1241 | 37 51 28.1210 | 21.300 | 0.425 | NELG | 1 | OII |
| 68 | 13 33 42.3652 | 38 03 36.1750 | 18.829 | 1.078 | BLA | 3 | MgII CIII |
| 69 | 13 34 47.3743 | 37 59 49.8370 | 21.477 | 0.178 | NELG | 1 | OII |
| 73 | 13 35 29.6392 | 37 51 27.8960 | 19.901 | 0.384 | NELG | 3 | OII |
| 74 | 13 35 0.2941 | 38 01 57.8390 | 18.639 | 0.357 | NELG | 3 | OII |
| 77 | 13 34 49.8819 | 37 53 36.7080 | 19.416 | 0.383 | NELG | 3 | H$\alpha$,H$\beta$,SII,OII,OII |
| 78 | 13 34 24.0034 | 38 00 30.4940 | 19.727 | 0.332 | NELG | 3 | H$\alpha$,OII |
| 82 | 13 34 50.0164 | 37 49 48.1030 | 19.902 | 0.385 | NELG | 3 | H$\alpha$,H$\beta$,OII,OII |
| 88 | 13 34 17.1137 | 38 00 39.9740 | 18.424 | 0.250 | NELG | 3 | H$\alpha$,SIII,OII |
| 89 | 13 35 30.5185 | 38 04 4.9600 | 17.592 | 0.110 | NELG | 3 | H$\alpha$,SII,OII,OII |
| 90 | 13 34 26.5085 | 38 00 27.9660 | 18.099 | 0.164 | NELG | 3 | H$\alpha$,H$\beta$,H$\gamma$,SII,OII,OII |
| 93 | 13 33 36.3772 | 38 02 44.1490 | 17.639 | 0.149 | NELG | 3 | H$\alpha$,OII,OII |
| 96 | 13 34 22.7100 | 37 46 56.9380 | 19.324 | 0.355 | NELG | 3 | H$\beta$,OII,OII |
| 102 | 13 34 45.1068 | 37 55 42.5110 | 19.681 | 0.359 | NELG | 3 | H$\beta$,OII,OII |

Table 4.2: Full list of optical counterparts to radio sources with optical spectra (continued)

| Source | Right Ascension hh mm ss | Declination °′″ | R mag | z | ID | Q | lines |
|---|---|---|---|---|---|---|---|
| 110 | 13 34 33.2043 | 37 55 10.0230 | 20.345 | 0.356 | NELG | 3 | OII |
| 113 | 13 35 24.7184 | 37 51 19.5110 | 19.724 | 0.388 | NELG | 3 | Hα,Hβ,SII,OII,OII |
| 114 | 13 34 57.8357 | 37 50 6.4160 | 19.164 | 0.257 | NELG | 3 | Hα,Hβ,OII,OII |
| 121 | 13 35 48.5251 | 37 54 49.9780 | 21.130 | 0.433 | NELG | 1 | OII,OII |
| 122 | 13 33 44.2948 | 37 57 52.6600 | 20.306 | 0.093 | GAL | 1 | K,H |
| 126 | 13 34 15.6017 | 38 03 4.8830 | 19.680 | 0.431 | NELG | 3 | OII,OIII |
| 129 | 13 34 28.6901 | 37 46 47.3500 | 20.355 | 0.504 | NELG | 1 | OII,OIII |
| 132 | 13 34 11.4252 | 37 52 39.3360 | 19.659 | 0.449 | NELG | 3 | OII |
| 133 | 13 35 16.7322 | 37 51 29.4010 | 20.000 | 0.263 | NELG | 3 | Hα,Hβ,SII,OII,OII |
| 134 | 13 35 6.2358 | 38 02 32.9800 | 18.802 | 0.36 | NELG | 3 | Hα,Hβ,OII,NeV |
| 137 | 13 34 36.8307 | 37 56 20.2370 | 19.131 | 0.250 | NELG | 3 | Hα,Hβ,OII |
| 139 | 13 34 29.9989 | 37 56 40.1700 | 19.301 | 0.291 | NELG | 3 | OII |
| 140 | 13 34 28.9289 | 37 53 32.6630 | 17.965 | 0.223 | NELG | 3 | Hα,Hβ,SII,OII,OII |
| 142 | 13 34 0.0172 | 37 58 55.8490 | 20.014 | 0.385 | NELG | 3 | Hβ,OII,OIII |
| 158 | 13 33 58.7690 | 37 49 52.7380 | 18.300 | 0.253 | GAL | 3 | K,H G MgB |
| 159 | 13 35 23.8249 | 38 03 32.4370 | 21.569 | 0.69 | NELG | 3 | OII |
| 163 | 13 34 46.9403 | 38 04 27.1500 | 18.596 | 0.238 | NELG | 3 | Hα,OII |
| 166 | 13 34 14.3804 | 37 46 47.1240 | 18.57 | .293 | NELG | 3 | OII |
| 168 | 13 34 28.8219 | 37 53 39.9950 | 18.464 | 0.222 | NELG | 3 | Hα,NII,Hβ,HγSII,OII |
| 175 | 13 34 1.0084 | 37 54 5.0760 | 21.613 | 1.64 | BLA | 3 | R |
| 176 | 13 34 29.4289 | 37 52 18.5680 | 19.248 | 0.325 | NELG | 3 | Hα, Hβ,NeV, |
| 177 | 13 34 40.8873 | 38 03 53.6630 | 17.167 | 0.110 | NELG | 3 | Hα, Hβ,NII,SII |
| 179 | 13 34 26.8415 | 38 09 23.9700 | 20.312 | 0.61 | NELG | 3 | OII |
| 180 | 13 34 49.3035 | 38 06 57.7640 | 18.909 | 0.255 | NELG | 3 | Hα |
| 185 | 13 34 23.4723 | 37 49 14.5620 | 20.085 | 0.359 | NELG | 3 | Hα, Hβ,NII,NeV,OII |
| 190 | 13 33 48.6570 | 37 56 11.6550 | 18.536 | 0.19 | NELG | 3 | Hα,Hβ,NII,SII,OII |
| 197 | 13 35 50.9860 | 37 51 31.3120 | 19.43 | .532 | GAL | 3 | K,H G |
| 200 | 13 34 23.6499 | 37 50 55.1640 | 20.300 | 0.479 | NELG | 2 | OI,OII,OIII |
| 202 | 13 34 5.4384 | 37 49 27.9640 | 18.544 | 0.110 | NELG | 3 | Hα,Hβ,SII,OII,OIII |
| 209 | 13 34 1.1388 | 37 53 49.5200 | 22.819 | 1.64 | BLA | 3 | R |
| 211 | 13 34 12.4301 | 38 04 0.3980 | 18.817 | 0.165 | NELG | 3 | OII |
| 220 | 13 34 57.7394 | 37 49 33.9710 | 20.004 | 0.253 | NELG | 3 | Hα,NII,OII |
| 222 | 13 35 21.5985 | 37 55 9.5900 | 19.106 | 0.312 | NELG | 3 | Hα,NII,OII |
| 224 | 13 35 14.3903 | 37 54 57.5410 | 19.388 | 0.304 | NELG | 3 | Hα,OII |
| 235 | 13 35 8.7042 | 37 44 23.8490 | 19.201 | 0.256 | NELG | 3 | Hα,OII |
| 236 | 13 33 59.0424 | 37 49 46.2330 | 18.466 | 0.251 | GAL | 3 | R |
| 247 | 13 35 5.0813 | 37 48 51.4560 | 19.124 | 0.252 | NELG | 3 | Hα,Hβ,OII |
| 248 | 13 35 10.1610 | 37 43 21.4000 | 19.611 | 0.316 | NELG | 3 | OII |
| 256 | 13 33 35.7387 | 37 50 7.1380 | 19.108 | 0.290 | NELG | 3 | OII |
| 257 | 13 34 40.2974 | 37 47 20.6300 | 21.160 | 0.435 | NELG | 1 | OII,OIII |
| 259 | 13 34 23.1352 | 38 04 15.5910 | 19.870 | 1.795 | BLA | 3 | CIV,CII,MhII |
| 260 | 13 34 52.5412 | 37 40 29.0910 | 20.015 | 0.291 | NELG | 0 | OII |
| 269 | 13 34 40.0756 | 37 49 21.3420 | 19.286 | 0.336 | GAL | 3 | K,H |
| 277 | 13 34 15.9943 | 38 06 12.5590 | 19.538 | 0.210 | NELG | 3 | Hα,NII,Hβ,SII,OII,OIII |

Table 4.2: Full list of optical counterparts to radio sources with optical spectra (continued)

| Source | Right Ascension hh mm ss | Declination °′″ | R mag | z | ID | Q | lines |
|---|---|---|---|---|---|---|---|
| 283 | 13 34 12.2207 | 38 04 56.9950 | 19.743 | 0.387 | GAL | 3 | K,H |
| 290 | 13 35 21.8586 | 37 58 26.5270 | 20.542 | 0.382 | NELG | 3 | OII |
| 291 | 13 33 58.1547 | 37 56 56.0100 | 19.916 | 0.269 | NELG | 3 | H$\alpha$.NeIII,OII,OIII |
| 293 | 13 35 28.2003 | 37 50 40.1570 | 19.743 | 0.251 | NELG | 1 | H$\alpha$,OII |
| 295 | 13 34 18.9463 | 37 44 1.0050 | 20.421 | 0.292 | NELG | 2 | H$\alpha$,NII,OII,OIII |
| 298 | 13 35 12.6631 | 38 02 49.8650 | 21.200 | 1.855 | BLA | 3 | R |
| 299 | 13 34 27.5024 | 38 00 31.8840 | 18.465 | 0.164 | NELG | 3 | H$\alpha$,H$\beta$,OII,OII |
| 305 | 13 34 4.9489 | 37 58 0.0140 | 21.502 | 0.615 | NELG | 2 | H$\beta$,OII,OII |
| 307 | 13 34 31.9788 | 37 46 30.2970 | 19.449 | 0.290 | NELG | 3 | H$\alpha$,SII |
| 319 | 13 34 45.4144 | 37 48 56.0960 | 19.221 | 0.340 | NELG | 3 | H$\alpha$,NII,OII |
| 325 | 13 34 8.5614 | 37 57 14.4170 | 21.530 | 0.58 | NELG | 1 | OII |
| 337 | 13 34 1.8237 | 37 53 28.2110 | 19.907 | 0.164 | NELG | 1 | R |
| 348 | 13 35 6.1609 | 37 49 52.4710 | 18.781 | 0.364 | NELG | 3 | R |
| 374 | 13 34 35.0872 | 37 57 52.6840 | 19.515 | 0.308 | GAL | 0 | K,H |
| 382 | 13 34 2.5205 | 37 51 29.3400 | 20.532 | 1.335 | BLA | 3 | CIII,MgII |
| 384 | 13 34 11.4916 | 37 56 19.5070 | 20.345 | 0.296 | NELG | 1 | OII |
| 398 | 13 35 32.9457 | 37 48 5.3350 | 18.543 | 0.305 | GAL | 3 | K,H |
| 409 | 13 35 1.9921 | 37 55 54.2320 | 19.959 | 0.291 | NELG | 3 | H$\alpha$,OII,OIII |
| 412 | 13 35 19.0986 | 37 56 8.7200 | 21.498 | 0.309 | NELG | 3 | OII |
| 415 | 13 35 27.2652 | 37 52 12.1760 | 20.789 | 0.614 | NELG | 3 | OII |
| 416 | 13 34 27.5256 | 37 55 24.4850 | 20.105 | 0.432 | NELG | 1 | OII |
| 421 | 13 34 35.7171 | 38 08 20.0990 | 20.448 | 0.487 | NELG | 3 | H$\beta$,OII,OIII |
| 423 | 13 34 17.5481 | 37 57 22.6499 | 18.575 | 1.14 | BLA | 3 | R |
| 430 | 13 34 36.5972 | 38 05 31.9580 | 19.608 | 0.241 | NELG | 3 | H$\alpha$,NII,H$\beta$,OII |
| 436 | 13 33 54.2749 | 38 00 35.2380 | 21.031 | 0.672 | NELG | 3 | H$\beta$,OII,NeIII |
| 446 | 13 34 51.0992 | 37 52 34.6010 | 20.458 | 0.552 | NELG | 3 | OII |
| 447 | 13 33 35.1936 | 38 01 16.1360 | 19.150 | 0.262 | NELG | 3 | H$\alpha$,OII, |
| 451 | 13 34 38.5704 | 37 56 50.5120 | 19.703 | 0.249 | NELG | 3 | H$\alpha$.H$\beta$,OII |

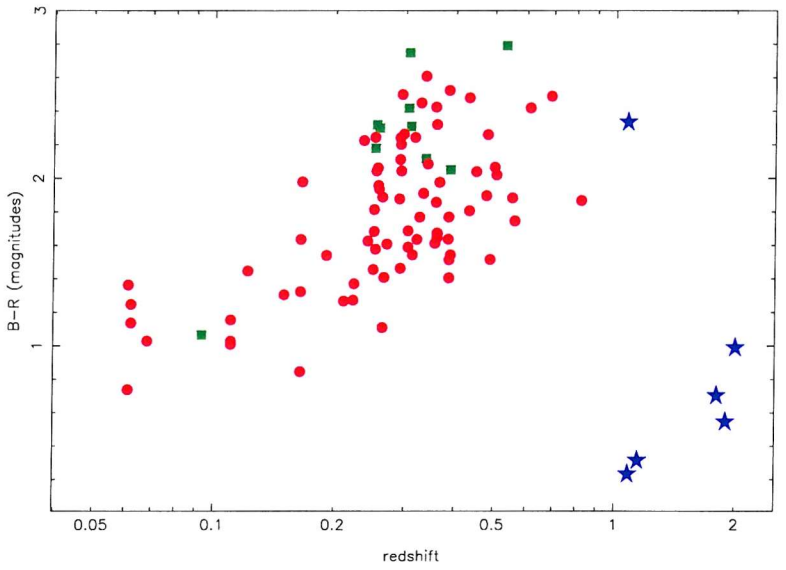


Figure 4.16: The distribution of $B - R$ colour (in magnitudes) with redshift, with Broad Line AGN indicated by blue stars, galaxies by green squares and NELGs by red circles. Note one Broad Line AGN does not have a $B-$band counterpart and is not included and these colours do not have a K-correction applied.

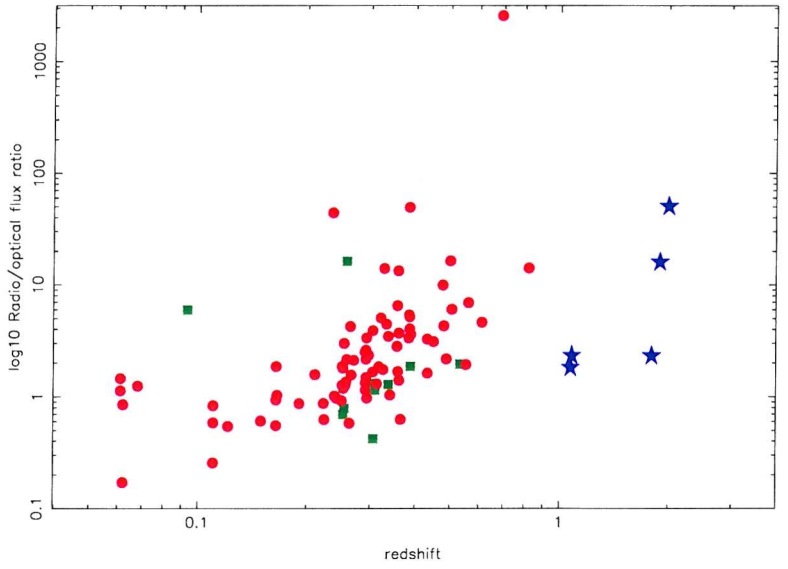


Figure 4.17: The distribution of the Radio/optical flux ratio with redshift, with Broad Line AGN indicated by blue stars, galaxies by green squares and NELGs by red circles. Note one Broad Line AGN has an unusually low radio/optical ratio of 0.3 and is not included in this plot.

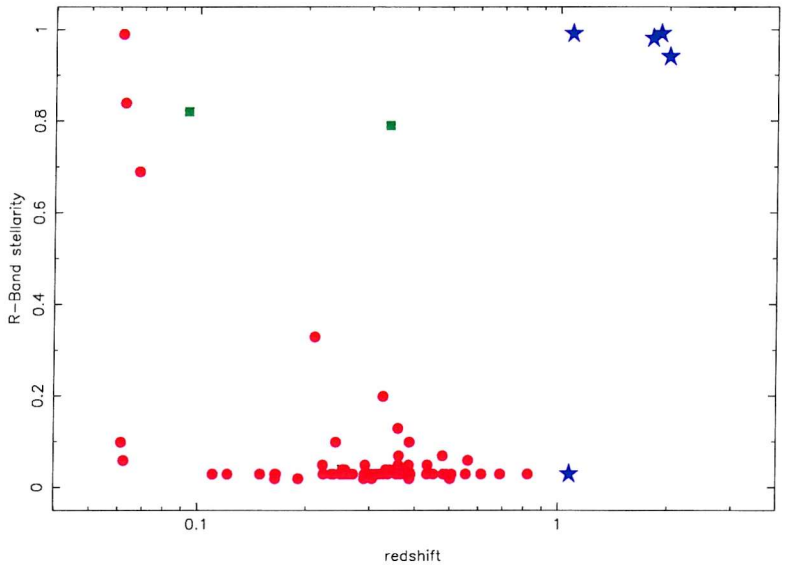


Figure 4.18: The distribution of the $R$– band stellarity with redshift, with broad line AGN indicated by blue stars, galaxies by green squares and NELGs by red circles.

is partly due to the selection effect that all our sources have $S_{1.4\,\mathrm{GHz}} \geq 30\,\mu$Jy and also $R \leq 20.5$. Therefore the sample does not include nearby Broad Line AGN with relatively low radio emission (in fact most quasars, as these Broad Line AGN probably are, are radio quiet, see chapter 1). Also not included on the plot are sources in this sample which do not have $B$– band counterparts (including one BLA).

Figure 4.17 shows that there is a reasonably wide range of scatter of radio loudness with redshift and even amongst one optical spectroscopic class of object. Again there are biases including the fact that many sources with a relatively low radio/optical ratio are excluded by the selection criteria of the spectroscopic sub-sample. The lack of radio loud sources at low redshifts (as seen in this figure) has been known about for a long time (Longair, 1966) and is explained by the evolution of radio sources with time. Current differential radio source counts are discussed in section 2.5 and modelling of the evolution of AGN and star-forming population is presented in Hopkins et al. (1998) and references therein.

Figure 4.18 shows again the expected result that the high redshift radio selected Broad Line AGN are unresolved (presumably as they are probably quasars the host galaxy is outshone by the nucleus). The lack of radio loud objects at low redshift is an indication of the redshift evolution. Virtually all the NELGs and normal galaxies are resolved and their radio emission is either from star formation or the central engine in the nucleus or a mixture of both effects.

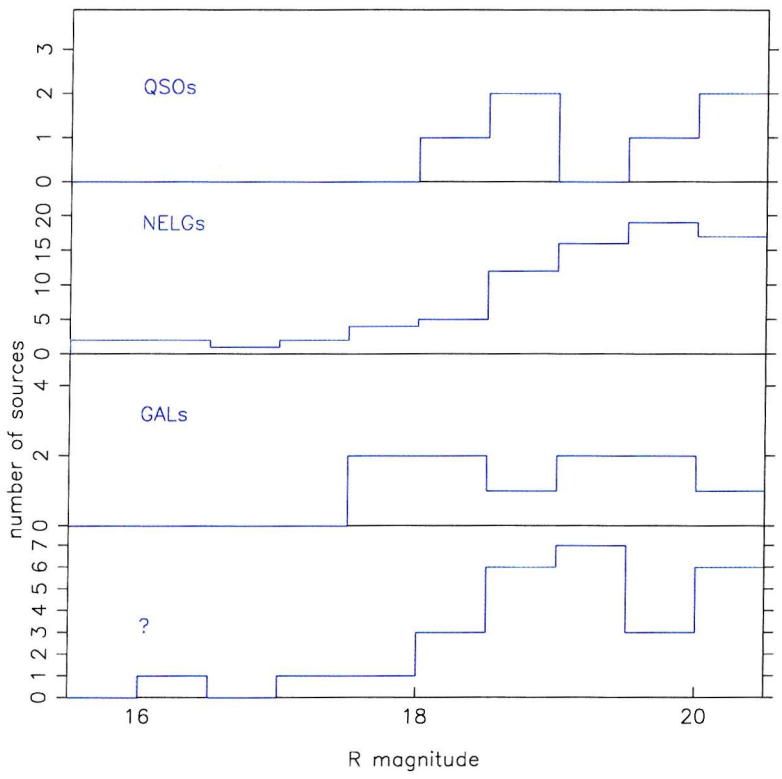


Figure 4.19: The distribution of each optical spectroscopic class of the spectroscopic subsample radio sources by $R$– band magnitude.

### 4.2.5 Distribution of Optical Spectroscopic Class with $R$– band magnitude

In figure 4.19 the distribution of different optical spectral classes of sources in the sub-sample is shown as a function of $R$– band magnitude. Towards fainter $R$– band magnitudes there is a clear increase in the number of NELGs whilst the number of Broad Line AGNs and absorption line galaxies stays roughly constant. The unidentified optical spectra of radio sources approximately increase with fainter $R$– band magnitudes as would be expected as it is harder to identify a lower signal to noise spectrum.

### 4.2.6 Rest frame magnitudes and luminosities

Figure 4.20 shows the rest frame absolute $R$– band luminosity against the intrinsic radio luminosity assuming a standard flat universe with $H_0 = 70$ and $\Omega_m = 0.3$. The solid line at $\log(L_r) = 24.6$ is the FRI/FRII differential break at 178 MHz extrapolated to 1.4 GHz assuming a radio spectral index of $\alpha = 0.75$ (Fanaroff and Riley, 1974). Clearly only one of these radio sources would defined by as a

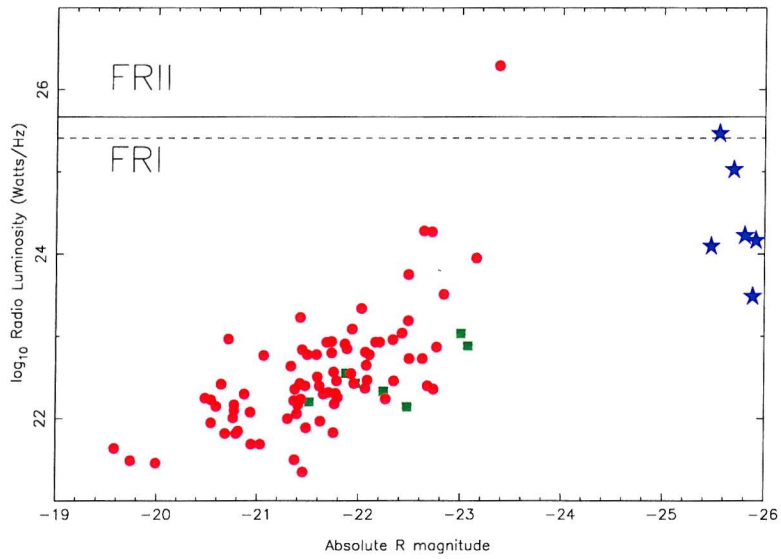


Figure 4.20: Absolute $R$–band magnitude against intrinsic radio luminosity for all radio sources with redshifts in the spectroscopic subsample. The solid line at $\log(L_r) = 24.6$ is the FRI/FRII differential break at 178 MHz extrapolated to 1.4 GHz assuming a radio spectral index of $\alpha = 0.75$ (Fanaroff & Riley, 1974). The dashed line at $\log(L_r) = 25.67$ is the definition of radio loudness from Miller et al. (1990).

FRII by this criterion. The source above the line is radio source 1, which by the morphological definition of FR class is a class II. One other source in the field is morphologically defined as class II, source 10, but no optical spectrum is available, so it does not appear in this figure.

The dashed line at $\log(L_r) = 25.67$ is the definition of radio loudness from Miller et al. (1990), who suggest that all sources with a 5 GHz flux greater than $10^{25}$ W Hz$^{-1}$ should be defined as radio loud. This separating line was extrapolated to 1.4 GHz again assuming $\alpha = 0.75$. By this definition only 2 sources in the spectroscopic sub-sample (source 1 and source 16, a quasar) are radio loud. It should be noted that this sub-sample is biased against including radio loud objects as only objects with $R < 20.5$ have been selected (in an attempt to have a reasonably complete sample with optical spectra). As has been shown in section 4.1.6.1 many objects in this radio survey are radio loud, but most have optical counterparts with $R > 20.5$ (of which most do not have a redshift) and hence are not included in this figure.

### 4.2.7 Distribution in Space

The distribution with redshift of the all radio sources with optical spectra is shown in figure 4.21. The clumpiness is consistent with superclustering on scales $\sim$ 100 Mpc

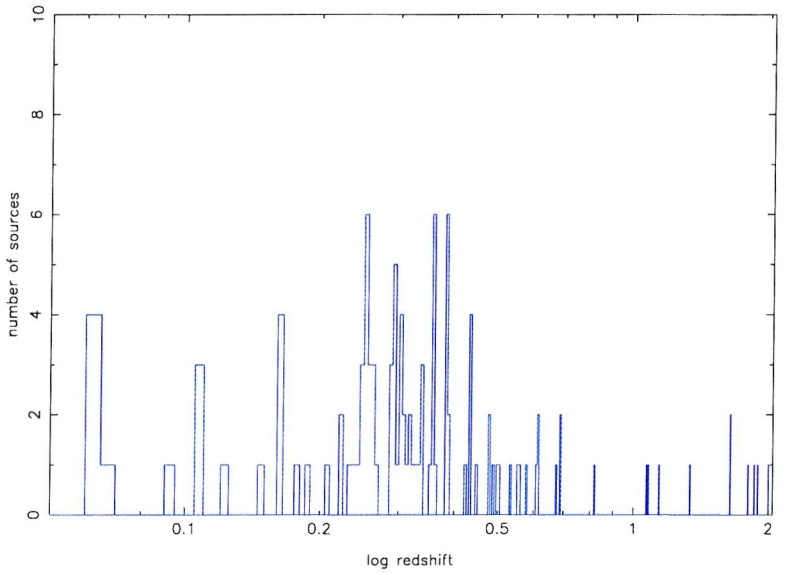


Figure 4.21: Distribution of redshifts for optical counterparts with optical spectra for all radio sources (not including stars).

seen in other pencil beam surveys (Broadhurst et al. 1990 , Benn et al. 1993). Some clumps, $z \sim 0.3$, contain normal galaxies and emission line galaxies suggesting that both populations trace the same distribution of matter on large scales as noticed by Benn et al. (1993). Some of the sources with similar redshifts are separated by distances of over $10'$ suggesting that we are observing filamentary structure within this particular wedge of the sky.

There is also evidence for individual clusters in the data from sources with small angular separations and close redshifts. The area around radio source 5 appears to be part of a cluster with also an additional foreground cluster (see section 5.5.2). Sources 175 and 209 at $z = 1.64$ are separated by $13''$ implying a physical seperation of 80 kpc assuming $H_o = 70\,\mathrm{km\,s^{-1}\,Mpc^{-1}}$ and a flat universe as in section 4.20. Sources 148 and 168 lie within $8''$ of each other at a redshift of $z = 0.223$ which corresponds to a separation of 26 kpc. Sources 60, 222, 224 and 412 all lie within $100''$ of each other all around $z = 0.31$. This implies that they are all within $\sim 400$ kpc of each other in a looser grouping.

## 4.3 Conclusion

The $R$–band optical counterparts to the radio source list have been found to be 83% complete to $R < 27$, comparable to that of other deep surveys at 1.4 GHz with the VLA in A-configuration (e.g.the HDF is $\sim 80\%$ complete in $I$–band to a limit $I_{AB} \sim 25$, Richards et al., 1999). It has been shown that the astrometry of the

optical and radio data is in good agreement with no systematic offsets leading to high confidence in the detection of counterparts. In $B$–band the optical counterparts were 64% complete to $B < 26.5$. There is an approximately constant number of $R$–band counterparts in the range $19 \leq R \leq 25$ suggesting more than one population of sources is present. For a given $R$–band magnitude the radio flux of a source is spread over 3 orders of magnitude and for a given radio flux the radio to optical flux ratio is also spread over 3 orders of magnitude. This implies that several emission mechanisms are probably involved and even within one source as there is no discontinuity in radio or optical properties.

The general field population of galaxies gets bluer on average at fainter $B$–band magnitudes (compared to radio selected galaxies) although there is a larger spread in colours. High stellarity radio sources are much bluer than the high stellarity optically selected galaxies as you are preferentially selecting quasars compared to selecting a combination of quasars and the faint foreground stars (which are on average redder). There is evidence that optically fainter radio sources are bluer by 0.23 magnitudes whilst optically fainter field galaxies are bluer by 0.62 magnitudes. There is little evidence that radio sources $< 100\,\mu$Jy are redder than those $> 100\,\mu$Jy, $\Delta B - R \sim 0.04$.

Of a spectroscopic sub-sample of 93 sources 6 are Broad Line AGN (probably quasars), 8 are galaxies and 89 are Narrow Emission Line galaxies. The stellarity and colour of the quasars confirms the old non-radio selection method to find quasars by looking for blue, unresolved objects. The optical spectra were not of sufficient quality to discern line ratios and similar diagnostics about the emission mechanisms, however examination of the radio morphology, optical morphology and radio spectral indices confirms that both star-formation and activity stimulated by the central engine of an AGN contribute to the background radio emission.

# Chapter 5

# Correlation of Radio sources with X-ray counterparts

In this chapter a brief summary of the *Chandra* X-ray survey is presented. The results of the UK Deep *Chandra* survey are correlated with the radio data from chapters two and three. The method of correlating the X-ray sources with the radio data is explained. General properties of the X-ray/radio sample are examined and examples of particular interest are presented in order to show the value of multi-wavelength surveys in determining the exact nature of faint sources.

## 5.1 Introduction

Full details of the *Chandra* observation are presented in M$^{c}$Hardy et al. (2002) (from which the author takes the *Chandra* survey list), but here the observations are briefly summarized (in sections 5.2.1, 5.2.2 and 5.2.3). In section 5.2.4 the author uses the new accurate X-ray positions from *Chandra* to modify the results of the original *ROSAT* survey (M$^{c}$Hardy et al., 1998) presented in section 1.3. The *Chandra* X-ray catalogue is correlated with the radio catalogue at the end of chapter 2. General properties of the X-ray/radio objects are examined and sources of particular interest are examined more closely.

Table 5.1: Log of *Chandra* observations

| Field Number | Sequence Number | Observation Date | *Chandra* RA | Dec | Roll Angle | Exposure (ksec) |
|---|---|---|---|---|---|---|
| 1 | 900063 | 8 June 2001 | 13 34 13.06 | +37 58 46.0 | 232.20 | 30.18 |
| 2 | 900064 | 9 June 2001 | 13 35 06.19 | +37 50 34.7 | 232.20 | 30.18 |
| 3 | 900065 | 9 June 2001 | 13 35 00.43 | +37 59 54.7 | 232.20 | 28.53 |
| 4 | 900062 | 8 June 2001 | 13 34 18.91 | +37 49 25.9 | 232.20 | 30.39 |

## 5.2 The *Chandra* Observations

### 5.2.1 Observational Details

In order to cover the large majority of the *XMM* (and *ROSAT*) field at small *Chandra* off-axis angles, four pointings were made with the ACIS-I instrument aboard *Chandra*. The log of the observations is listed in Table 5.1. The observations were postponed to avoid a large solar flare and then took place in relatively low background conditions. The 'very faint' observational mode was used in which a 5×5 pixel array is read out around every event, allowing better photon/cosmic ray discrimination than in the standard 3×3 pixel 'faint source' readout mode.

The observations were made consecutively and the roll angle of the observations are identical to within 0.1″. The positions of the pointing centres were adjusted to provide the good coverage pattern shown in Fig. 5.1. There is a known positional offset for any *Chandra* observation which depends on the roll angle. For the roll angle in these observations that offset is $\delta$RA=+1.10″ and $\delta$Dec=+1.14″. These offsets were applied to the data before undertaking the source fitting procedure.

### 5.2.2 Source Extraction

The sources were extracted in the $0.5 - 7.0$ keV band, which was found to give the optimum signal/noise. The detection code is based on an algorithm by Cash (1979), further details are given in M$^{c}$Hardy et al.(1998). Details of its application are given in M$^{c}$Hardy et al.(2002). The algorithm returns a Cash statistic for a suspected source. The detection limit is set at $\chi^2 > 25$ which corresponds approximately to a $5\sigma$ detection. The positional accuracy is extremely good. For sources with an off-axis angle $< 5'$ the optical/X-ray offsets are better than 1″ and are below 2″ at even the largest offset angles (10′).

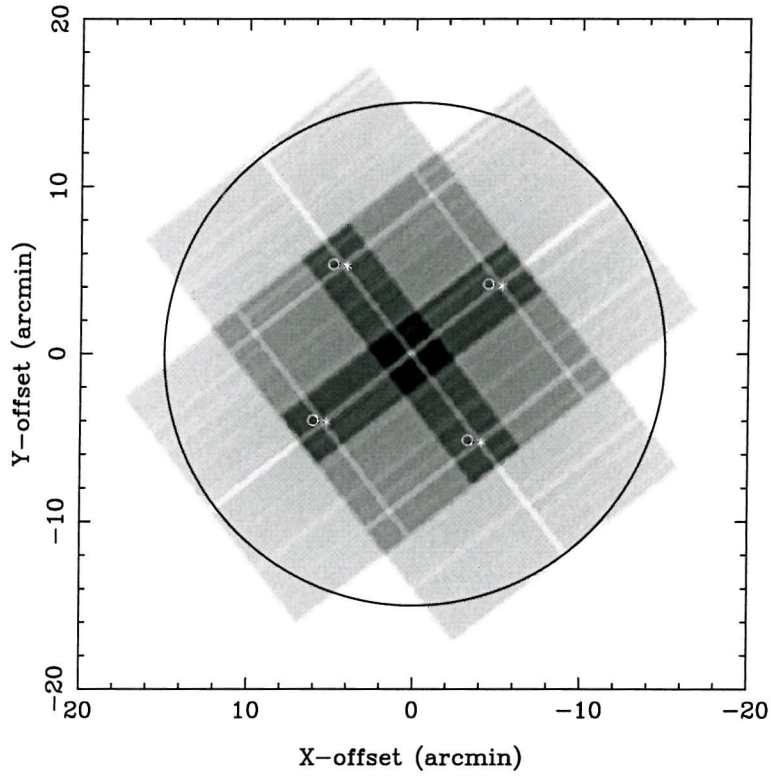


Figure 5.1: Exposure map for the mosaic of 4 *Chandra* pointings. For each pointing the centre of the ACIS-I field is marked by an asterisk and the optical axis of the telescope is marked by a small circle. The 30′ diameter *ROSAT* / *XMM* field of view is marked with the large circle.

### 5.2.3 Results

214 *Chandra* sources were detected above a flux of $\sim 1.3 \times 10^{-15}$ erg cm$^{-2}$ s$^{-1}$ (0.5 – 7 keV). These sources were compared to those found in the original *ROSAT* survey (M$^{c}$Hardy et al., 1998) and identifications of those sources were confirmed, modified, refuted or, in a few cases, were left inconclusive. The full *Chandra* catalogue and correlation with the $R$–band Subaru data is presented in M$^{c}$Hardy et al. (2002).

### 5.2.4 Correction of *ROSAT* results

To complete the initial goal of the radio survey (section 1.3.4), finding radio counterparts to the *ROSAT* survey source list, a corrected version of figure 2.1 showing the X-ray sources divided by optical spectroscopic class (with combined A and B-configuration counterparts) is presented, figure 5.2. The identifications in this figure have been corrected using the *Chandra* identifications (as done in section 6 of M$^{c}$Hardy et al.(2002)) along with optical spectra taken in the WYFFOS observing runs described in section 4.2.1. Figure 5.2 shows the same general trend as figure 2.1 with decreasing numbers of quasars at fainter fluxes and increasing numbers of NELGs. However several *ROSAT* IDs have been refuted with the more accurate positions of the *Chandra* detections. This has led to a larger fraction of sources in the faint flux bin being unidentified. The total number of QSOs has increased from 32 to 37 (including 2 mis-identifications and 7 new correct IDs). The total number of NELGs has decreased from 15 to 10 with 11 mis-identifications and 6 new IDs. The number of clusters has increased by one with one new correct ID. The number of un-identified sources (which do not include sources with no optical counterpart down to $R \geq 26$) has increased from 13 to 29. The increase of 16 un-identified sources includes 2 mis-identified QSOs, 11 NELGs, 1 galaxy and 2 stars. The trends of the figure 2.1 were always dependent on assuming that the unidentified sources did not change the trend significantly (e.g. by all being quasars) and on the exact selection of bin widths and positions in log flux space. The shaded areas now show radio counterparts from the full 1.4 GHz source list from chapter 2.

## 5.3 Correlation of the *Chandra* sources with the 1.4 GHz Radio Data

In this section the sample of 214 *Chandra* sources are correlated with the 1.4 GHz radio data. Initially each *Chandra* source was correlated with the list of 462 sources described in chapter 2. Due to the high positional accuracy of both the X-ray and radio sources a 2″ search radius was sufficient to find counterparts. This method

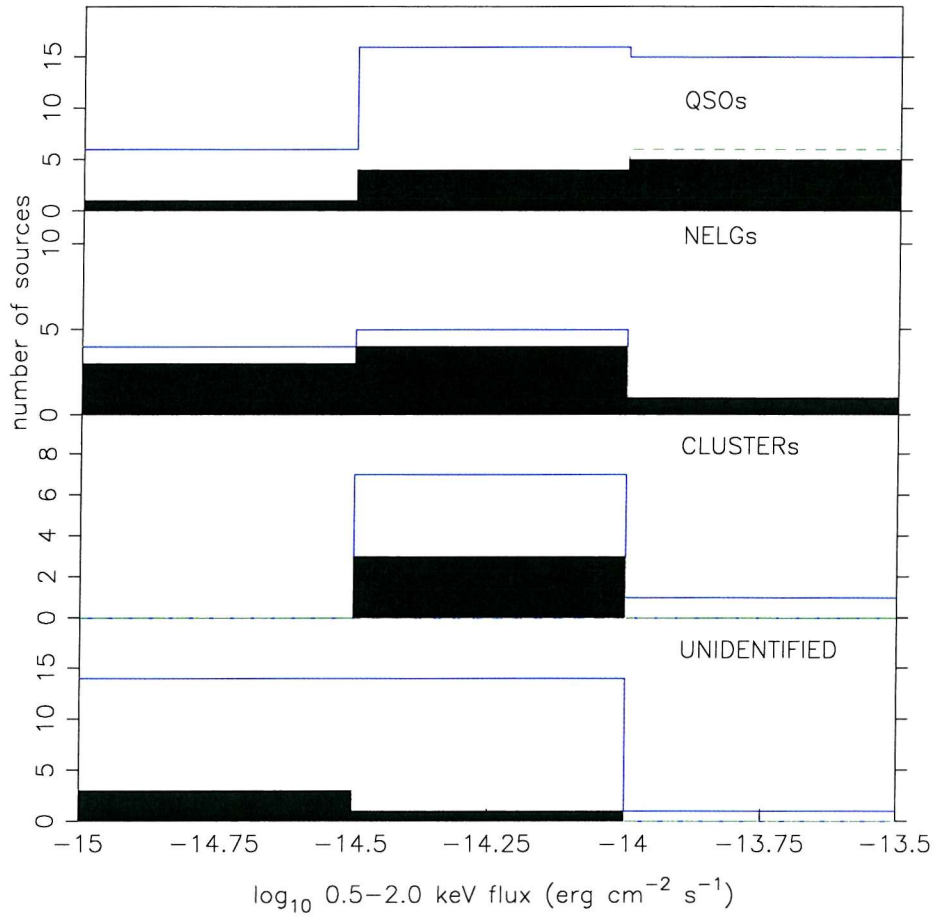


Figure 5.2: Number of *PSPC* sources in the *ROSAT* survey identified with various classes of object (now corrected with more accurate positions from *Chandra*). Shaded areas indicate the fraction of *ROSAT* sources detected in the combined A and B-configuration radio data.

found 51 radio counterparts to X-ray sources. Figure 5.3 indicates the X-ray/radio positional offsets. There is no systematic offset between the two coordinate frames and only 6 sources lie beyond the 1″ radius circle indicating the incredible positional agreement of the independent coordinate frames (Bauer et al., 2002, use a 1″ search radius for a similar VLA/*Chandra* cross-correlation on the HDF-N).

In order to look for more potential radio counterparts (i.e. extended radio sources, or with radio flux $< 4\sigma$) 30″ square 'postage stamps' were made at the positions of every X-ray source. These consist of a Subaru grey-scale $R-$band image superimposed with radio contours in exactly the same fashion as for the 1.4 GHz radio sources (these are presented in section 2 of the Appendix). All potential radio sources that visually appeared to be greater than $3\sigma$ and were within 2″ of the X-ray position were fitted with an elliptical Gaussian using the AIPS task JMFIT, which works in an identical fashion to SAD except that it can be used to fit one source at a time. In this fashion 15 more sources were found. It is possible to estimate the number of spurious X-ray/radio coincidences with the assumption that the noise of the radio data is Gaussian. The number of radio sources above $3\sigma$ in the field can be estimated by the number of 'islands' in the radio map with peaks above $3\sigma$, $\sim 1000$ (from contouring and visual inspection of the maps). The number of these 'islands' expected to be spurious is $(1 - \frac{99.73}{100}) \times 1000 \sim 3$, i.e. from a Gaussian distribution the chance of a $3\sigma$ sources *not* being random in 99.73% and hence about 3 points in a 1000 are expected to deviate from the mean by $3\sigma$ or more. The number of these expected to be coincident with an X-ray source is just the ratio of the search area ($214 \times 2^2\pi$ arcseconds square) to the area of the whole field ($900^2 \times \pi$ arcseconds square) multiplied by the expected number of spurious sources in the field ($\sim 3$). This gives an answer of $3 \times 10^{-3}$ indicating that we expect no random coincidences, but this is with the caveat the noise in the radio maps may not be completely Gaussian. Section 2.3 discussed the statistics of the radio maps further.

One X-ray source (*Chandra* 160) was found to be 10″ to the south-east of the head-tail source (radio source 6). The X-ray source is believed to be associated with a cluster which is consistent with the presence of a head-tail source. Also one X-ray source (*Chandra* 24), located in the far western corner of the south-west *Chandra* pointing, was found to have a radio counterpart outside the 15′ radius field of view of the radio data. In total this gives 68 radio counterparts to the X-ray sources. Examination of the optical/radio 'postage-stamps' of the X-ray sources suggests that there could be further radio counterparts (e.g. *Chandra* sources 12 and 42 could be associated with radio emission that looks like jets). There are also instances of X-ray sources being in close proximity ($\leq 5''$) to extended radio structure with peak fluxes $> 3\sigma$. However these sources and the potential jet sources were not considered firm detections and are not considered further here.

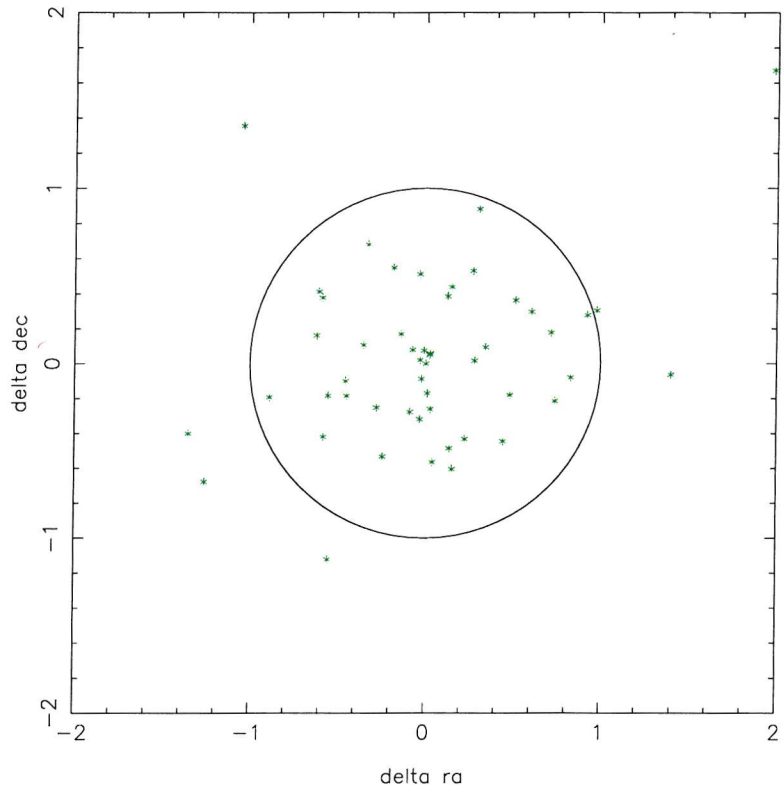


Figure 5.3: Diagram of the offset in RA and dec (asec) of the *Chandra* positions with the radio positions (with a 1″ circle overlaid to show how few of the matches are separated by more than 1″). It is clear there is no systematic error present.

### 5.3.1 Results

In total there are 68 radio counterparts to the 214 *Chandra* sources which corresponds to 31.8%. By comparison, in a radio survey of the HDF-N, Bauer et al. (2002) detect 42% of a sample of 62 *Chandra* X-ray sources taken from a 3′ radius area at the centre of the field. The radio observations of Richards (2000) were used which have a similar detection limit ($5\sigma \sim 40\,\mu$Jy) to the observations presented in chapter 2. However their X-ray observations come from a single 1 Ms *Chandra* exposure which had a detection limit over an order of magnitude deeper than the observations here ($1 \times 10^{-16}\,\mathrm{erg\,cm^{-2}\,s^{-1}}\,(0.5 - 8\,\mathrm{keV})$ compared to $1.3 \times 10^{-15}\,\mathrm{erg\,cm^{-2}\,s^{-1}}\,(0.5 - 7.0\,\mathrm{keV})$) and therefore are probing a slightly different region of parameter space to the analysis presented here. Direct comparisons between these samples is complicated by the different sizes of the surveys (15′ radius compared to 3′), the decrease in radio sensitivity away from the field of view in this survey due to the primary beam attenuation and the non-uniform coverage of this X-ray survey (figure 5.1). However it is clear that X-ray/radio surveys similar to this one and the HDF-N should expect a reasonable fraction of sources to be detected as X-ray and radio sources.

## 5.4 General properties of the X-ray/radio sample

### 5.4.1 Distribution of optical spectroscopic class with X-ray flux

Figures 5.4 and 5.5 show the distribution of different classes of X-ray source with X-ray flux. Figure 5.4 shows the distribution of quasars, NELGs and 'normal' galaxies for 3 X-ray bands. Figure 5.5 shows the same distribution for clusters, stars and unidentified sources. These distribution do not include the brightest X-ray source, a foreground M class star (*Chandra* 1 from M$^{\mathrm{c}}$Hardy et al. 2002 with a flux of $8.00 \times 10^{-13}\,\mathrm{erg\,cm^{-2}\,s^{-1}}\,(0.5 - 8\,\mathrm{keV})$) as it is an order of magnitude brighter than the next brightest X-ray source. The classes are taken from confirmed IDs in the *ROSAT* catalogue paper and from the same set of WYFFOS observations mentioned in section 4.2.1. By far the largest category is '?', unidentified sources. This due to the fact that there has not been enough observing time to do sufficient spectroscopic follow up on the optical counterparts. It is unsurprising that of the brightest X-ray band only 1 out of 26 *Chandra* sources is unidentified, whilst in the faintest band X-ray band 90 out of 110 are unidentified. The trend of decreasing quasar numbers and increasing NELG numbers is therefore largely due to the results of the *ROSAT* survey and until a much larger fraction of sources are identified it is not possible to say if this trend is confirmed or not.

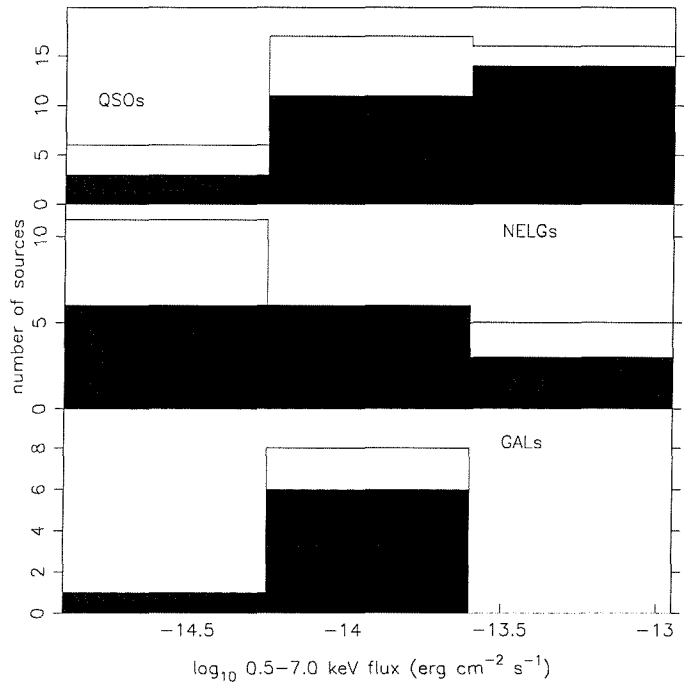


Figure 5.4: Distribution of *Chandra* sources by X-ray flux for sources with different optical spectroscopic class: quasars (QSOs), NELGs and 'normal' galaxies (GALs). Shaded areas indicate where an identification is also detected in the A and B-configuration 1.4 GHz data.

Also shown on both figures is the number of sources with radio counterparts (the shaded histograms). It clear that a large fraction of all classes of objects are detected at radio wavelengths with the except of stars most of which are dwarf Me stars[1].

### 5.4.2 X-ray/Radio flux ratio

Figure 5.6 shows the distribution of X-ray flux (in $\mathrm{erg\,cm^{-2}\,s^{-1}}$) against radio flux density (in $\mu$Jy). Sources with radio counterparts below a $3\sigma$ detection limit of 22.5 $\mu$Jy are marked as upper limits at the bottom of the figure. Identified sources are marked with appropriate symbols; quasars as filled stars, NELGs as squares, normal

[1]Incidentally, the bright M star ($R = 13.7$), *Chandra* one, not included on the plots is detected in the radio ($S_{1.4\,\mathrm{GHz}} \sim 0.1$ mJy). It is known that late M dwarf stars can be variably and persistently active in both X-rays and radio waves (Berger, 2002). It is an HST guide star, GSC0302600937, with $V = 13.83$. From this magnitude the M star and assuming a spectral type of M6 (M3) with an absolute magnitude of 10.50 (13.74), and using m-M=-5+5log(d), it lies at a distance of 45pc (10pc). The true spectral type is unknown, but it's likely that it is bracketed by M3-M6. Curiously it has extended emission to one side. It is not possible to detect an optical counterpart to this extended emission, but it more likely due to background object. Whether this background object contributes to the X-ray emission or not is unknown. The radio/optical image is shown in the section 1 of the Appendix as radio source 195 and as *Chandra* source one.

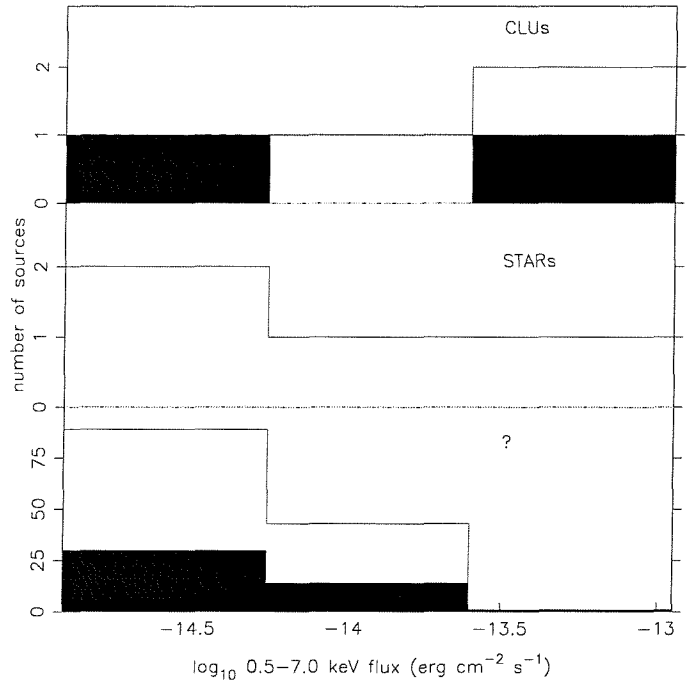


Figure 5.5: Distribution of *Chandra* sources by X-ray flux for sources with different optical spectroscopic class: clusters (CLUs), stars and unidentified sources '?'. Shaded areas indicate where an identification is also detected in the A and B-configuration 1.4 GHz data.

galaxies as circles, clusters as open circles, stars as open stars and unidentified sources as crosses. Here the bright M star with radio emission is included on the far right of the plot. At low fluxes, as noted in the previous section, most sources are as yet unidentified. However of the identified sources it is clear that the three main classes of objects, namely quasars, NELGs and normal, absorption line galaxies, cover almost 3 orders of magnitude in X-ray to radio flux ratio[2]. The large range in X-ray to radio flux ratio in quasars (and the NELGs with possible large AGN contributions) is consistent with observations of classical AGN (e.g. Kellermann et al., 1989 and Brinkmann et al., 2000).

The scatter in the radio/X-ray ratio of AGN is not surprising considering that AGN have been found to be radio loud and radio quiet (depending on orientation, AGN activity, presence of jets etc.), and also X-ray loud and X-ray quiet (depending on AGN activity, amount of absorption etc.). Again variability of objects needs to be considered as the VLA and *Chandra* observations were taken 2.5 years apart. Radio loud AGN have been known to vary on scales of $10 - 20\%$ over a few months in both X-rays and radio waves, so the scatter in the radio/X-ray ratio of the radio loud objects cannot be due to variability. Radio variability is not so well studied in

[2]The radio flux (as opposed to flux density) was calculated using a bandwidth of $14 \times 3.125\,\mathrm{MHz} = 43.75\,\mathrm{MHz}$ which was then used to calculate the X-ray to radio flux ratio (Bauer et al., 2002). Lines of constant X-ray to radio flux ratio are marked on the plot.

radio quiet AGN, e.g. Seyferts, but Wrobel (2000) has shown that they can vary by $20 - 50\%$ over a few months which is consistent with their known X-ray variability (Uttley et al., 2002). It is likely though that the scatter of all objects (radio loud and radio quiet) is real and not due to variability.

The number of matches between the X-ray/radio populations at faint radio and X-ray fluxes is consistent with the detection of 'normal' star-forming galaxies with perhaps little AGN activity at moderate redshifts (Bauer et al., 2002). Figure 5.7 shows the number of X-ray/radio coincidences as a function of radio flux. Below $100\,\mu$Jy the number of coincidences remains high implying that slightly deeper radio observations will continue to find more radio counterparts to X-ray objects. Bauer et al. (2002) come to a similar conclusion noting a steep rise in the number of radio matches to X-ray sources near the limit of their radio survey ($40\,\mu$Jy from Richards, 2000). It is also worth noting that 20 out of 26 of their X-ray/radio matches would have not have been detected below the limit of the *Chandra* survey presented here implying that a deeper X-ray survey would find many more X-ray/radio sources (although this survey covers a much larger area than Bauer et al., 2002).

### 5.4.3 Radio/Optical flux ratio distribution as a function of X-ray flux

Figure 5.8 shows the radio to optical flux ratio, $R_O$, plotted against X-ray flux. $R_0$ is calculated from equation 4.1. For sources without radio detections an upper limit for $R_0$ is calculated using the $3\sigma$ radio limit of $22.5\,\mu$Jy. The two X-ray sources without optical (or radio) detections are not included. Neither is the bright M star (*Chandra* 1/Radio source 195) included as it is about an order of magnitude brighter than the the next brightest X-ray source and has a value of $R_0 \sim 0.01$.

X-ray sources without radio counterparts have $\log(f_X/f_{1.4\,\mathrm{GHz}})$ ratios of four or more indicating that their bolometric luminosity is dominated by X-rays. The number of X-ray/radio matched NELGs at faint X-ray fluxes and radio densities is consistent with the emergence of a normal starforming galaxy population at moderate redshifts (Bauer et al., 2002).

### 5.4.4 Radio spectra of X-ray sources

For 18 sources we have detections at 1.4 GHz and 4.86 GHz. There radio spectra are shown as a function of 1.4 GHz flux in figure 5.9. This is clearly a biased sample to be detected in all three frequencies. As the 1.4 GHz survey is five times deeper than the one at 4.86 GHz sources with flat spectra are being preferentially selected.

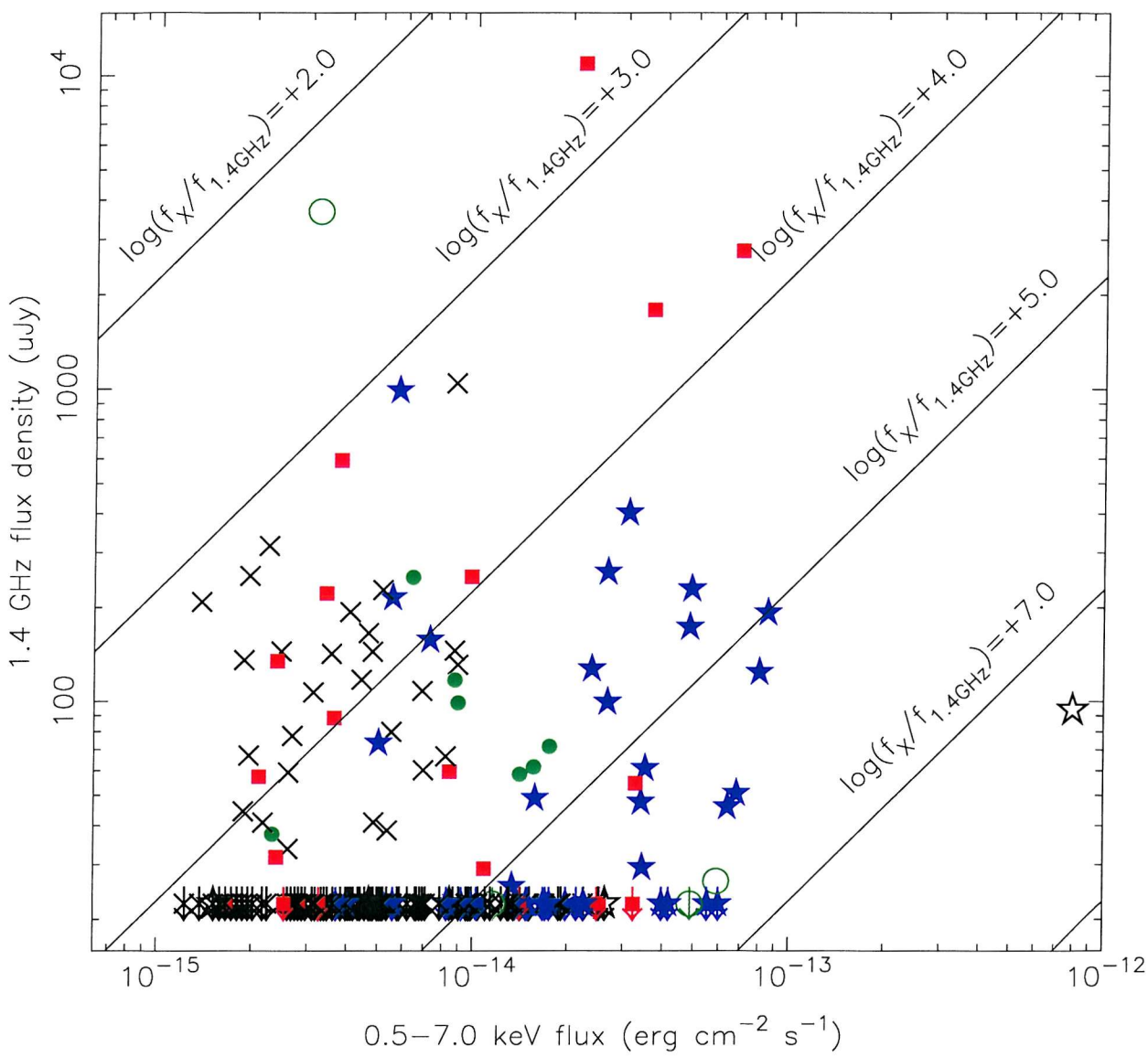


Figure 5.6: The X-ray flux/radio flux density distribution with the class of source indicated by the symbol: quasars (filled stars), NELGs (squares), 'normal' galaxies (circles), stars (open stars), clusters (open sources) and unidentified sources (crosses). X-ray sources with no radio counterparts are shown as upper limits with a radio flux 22.5 $\mu$Jy. The diagonal lines mark lines of constant flux ratio (the radio flux was calculated using a bandwidth of 43.75 MHz, Bauer at al., 2002).

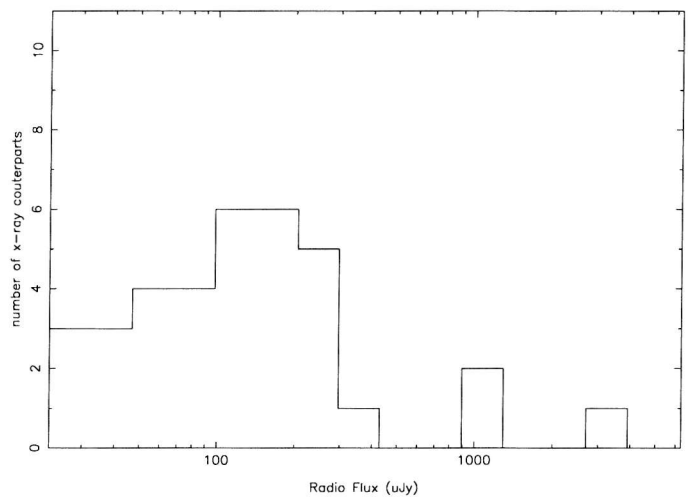


Figure 5.7: The number of *Chandra* X-ray sources with radio counterparts as a function of radio flux.

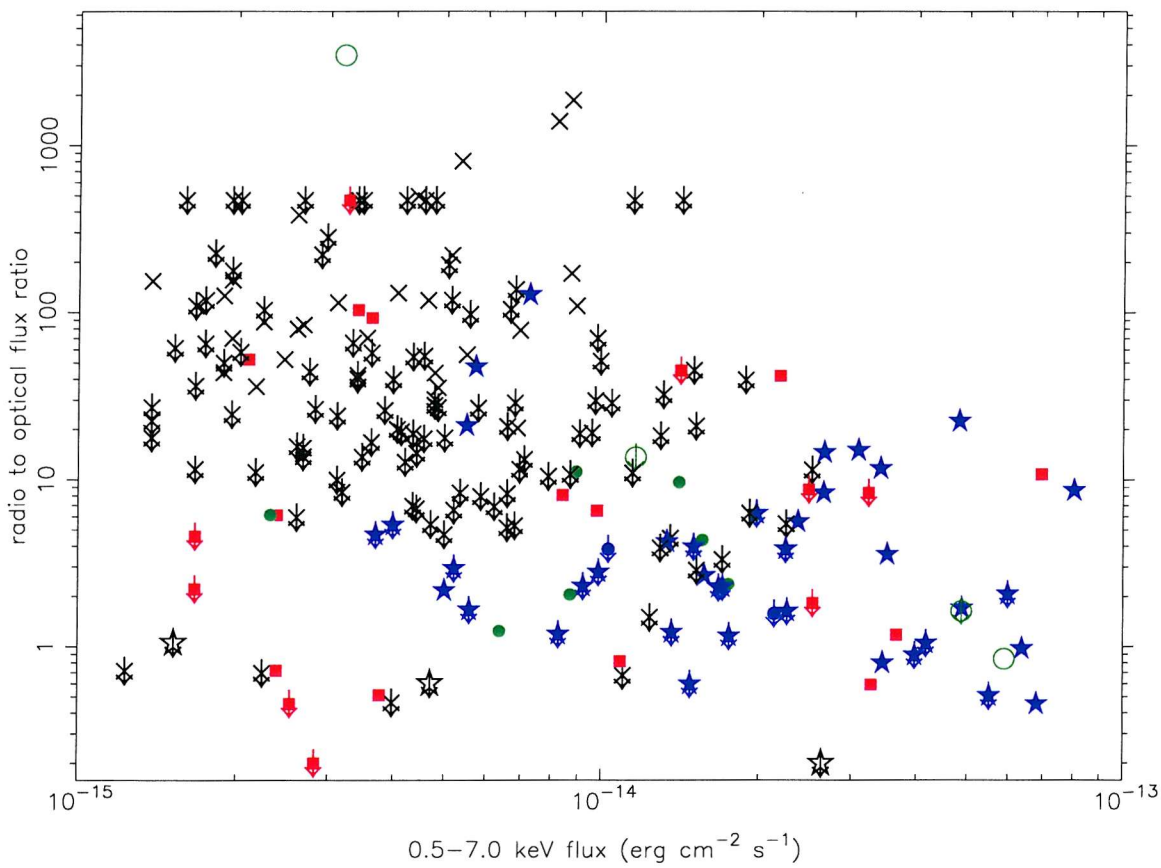


Figure 5.8: The distribution of radio to optical flux ratios against X-ray flux. The class of source indicated by the symbol: quasars (filled stars), NELGs (squares), 'normal' galaxies (circles), stars (open stars), clusters (open sources) and unidentified sources (crosses). X-ray sources with no radio counterparts are indicated as upper limits with flux ratio calculated from the $3\sigma$ radio limit and their $R$–band magnitude.

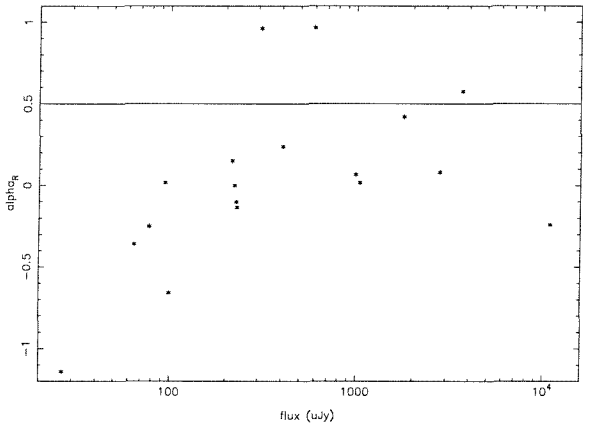


Figure 5.9: The distribution of radio spectral index against 1.4 GHz flux for X-ray sources

## 5.5 The emission mechanism in examples of radio/X-ray correlations

For X-ray/radio sources with enough information over a large portion of its spectral energy distribution and with possibly optical, radio and X-ray spectra it is possible to characterise the emission mechanism(s) in individual sources.

### 5.5.1 *ROSAT* 117

Early analysis of the radio data found a counterpart to a NELG from the *ROSAT* catalogue (M$^{c}$Hardy et al., 1998) (source R117). The spectral energy distribution of R117 was well modelled by a combination of a normal spiral galaxy and a moderate-strength starburst component. The radio emission was found to be extended and trace the faint optical spiral structure seen in $R-$band data (Gunn et al., 2001), see figure 5.10. This source is included in the appendix as radio source 13 with radio contours from the combined A and B-configuration data. The lower resolution of the A and B-configuration data (3.35″) prevents the spiral structure being seen in the postage stamp in the appendix so a high resolution A-configuration contour map is presented here in figure 5.10. This radio map was made with a robustness weighting of R=0 (see section 2.3.1) which gives a resolution of 1.35″. R117 is also detected at 4.86 GHz with a steep spectrum, $\alpha = 0.95$, which is indicative of star formation. However this source is not detected in the *Chandra* observations, which it should be if it were a point source, but it is detected with *XMM* , implying that the X-ray emission is extended consistent with the normal galaxy plus starburst model.

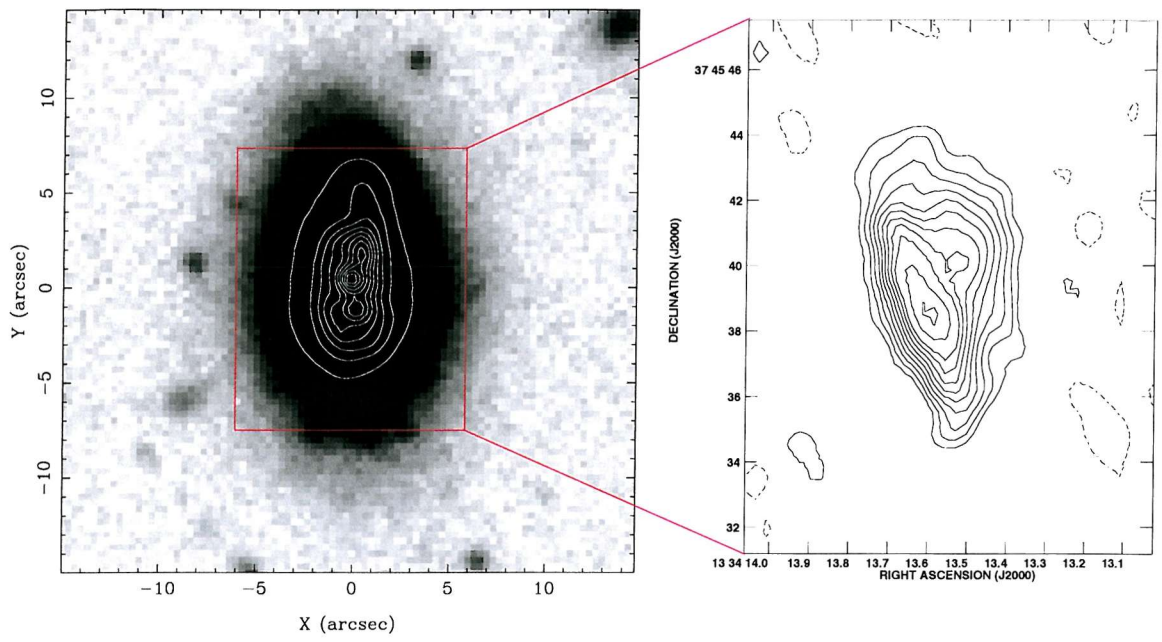


Figure 5.10: Left, an optical $R$– band image from the Canada France Hawaii Telescope of R117 with contours indicating the optical intensity. Right, a radio contour map of *ROSAT* source 117 showing the extended structure tracing the spiral arms of the underlying optical galaxy. The contours are at levels of -2,2,3,4,5,6,7,8,9,10,12,14 times 6 $\mu$Jy/beam.

### 5.5.2 *Chandra* 4

The fourth brightest *Chandra* source was found to coincide with the fifth brightest radio source (see figure 5.11). The original optical detection in the *ROSAT* catalogue was with a NELG at $z = 0.062$ (now associated with radio source 18), but the subsequent positionally accurate detection with *Chandra* suggested that the X-ray emission was associated with the bright elliptical galaxy ($R = 17.7$) coincident with radio source 5. This had been spectroscopically classified as a normal elliptical absorption line galaxy at z=0.257 from original follow-up observations of the *ROSAT* source. This source was also detected at 4.86 GHz and the contour map is presented in figure 5.11. The 4.86 GHz data have a far lower resolution ($14''$) and therefore the emission from the radio source is unresolved. The simplified method of determining radio spectra in section 3.6 finds $\alpha = 0.053$. This may not be strictly correct as it is unlikely that the assumptions in that method are strictly correct if the 4.86 GHz flux includes contributions from the other radio sources nearby (i.e. radio sources 18 and 54). However if it is assumed that at both frequencies there is an unresolved core (hence the peak flux equals the flux of the core) then a very flat spectrum is still obtained, $\alpha = -0.053$. Even allowing for possible uncertainties it is likely that the radio counterpart of *Chandra* 4 has a very flat radio spectrum.

Early results from the XMM survey show this X-ray source to have a very steep

X-ray spectrum. The overall spectral energy distribution from a combination of a flat radio spectrum and a steep X-ray spectrum is indicative of a blazar (i.e. AGN whose emission is dominated by a relativistic jet orientated close to the line of sight, see figure 5.12).

The nature of this whole group of objects is unclear. Sources 18 and 31 may be part of a foreground cluster with redshifts of 0.062 and 0.061 respectively (there are 3 other sources in the field around this redshift, $\Delta z \leq 0.005$, including one about $4.2'$ to the south-east of this area suggesting a large scale filament across the field of view). Sources 5, 158 and 236 all lie at very similar redshifts: 0.257, 0.253 and 0.251 implying that they may be associated. There is no redshift available for source 54 and the nature of the extended emission to the north of it remains unclear.

### 5.5.3 *Chandra* 33

*Chandra* source 33 was also found to be associated with a bright elliptical galaxy ($R = 17.7$) and source 3 (see appendix) from the 1.4 GHz catalogue ($S_{1.4\,\mathrm{GHz}} = 10.94\,\mathrm{mJy}$). It was also detected at 4.86 GHz at $S_{4.86\,\mathrm{GHz}} = 14.76\,\mathrm{mJy}$, giving it a flat spectrum of $\alpha = -0.24$. As a source of particular interest its X-ray spectrum was taken from the *XMM* data. The X-ray spectrum was very similar to that of *Chandra* 4, very steep, but with a small amount of intrinsic absorption. Again the combination of a flat radio spectrum and steep X-ray spectrum with a bright elliptical suggests that it is also a blazar.

So at least two of the bright sources in the combined X-ray/radio sample are blazars. Although it may be possible that this sample is un-representative of the background population as a whole, these results do suggest that blazars do contribute at least in part to the X-ray and radio backgrounds.

### 5.5.4 *ROSAT* 32

*ROSAT* 32 was identified with a pair of interacting spiral galaxies both at moderately low redshift (z=0.068) and both with narrow emission lines. The X-ray centroid was coincident with the larger of the two spirals. Following up this source in the radio an image was made with just A-configuration data initially. The $1.7''$ resolution data indicated that radio emission was coming from the spiral arms. Figure 5.13 shows an HST $I-$band image of the two galaxies overlaid with A-configuration contours. As the radio emission from the spiral arms dominates that from the galaxy, the emission is very likely linked to the bright knots of star formation visible in the $I-$band image. This source was detected as *Chandra* 16, but unfortunately it was so far from the *Chandra* pointing centre that the point-spread function is extended

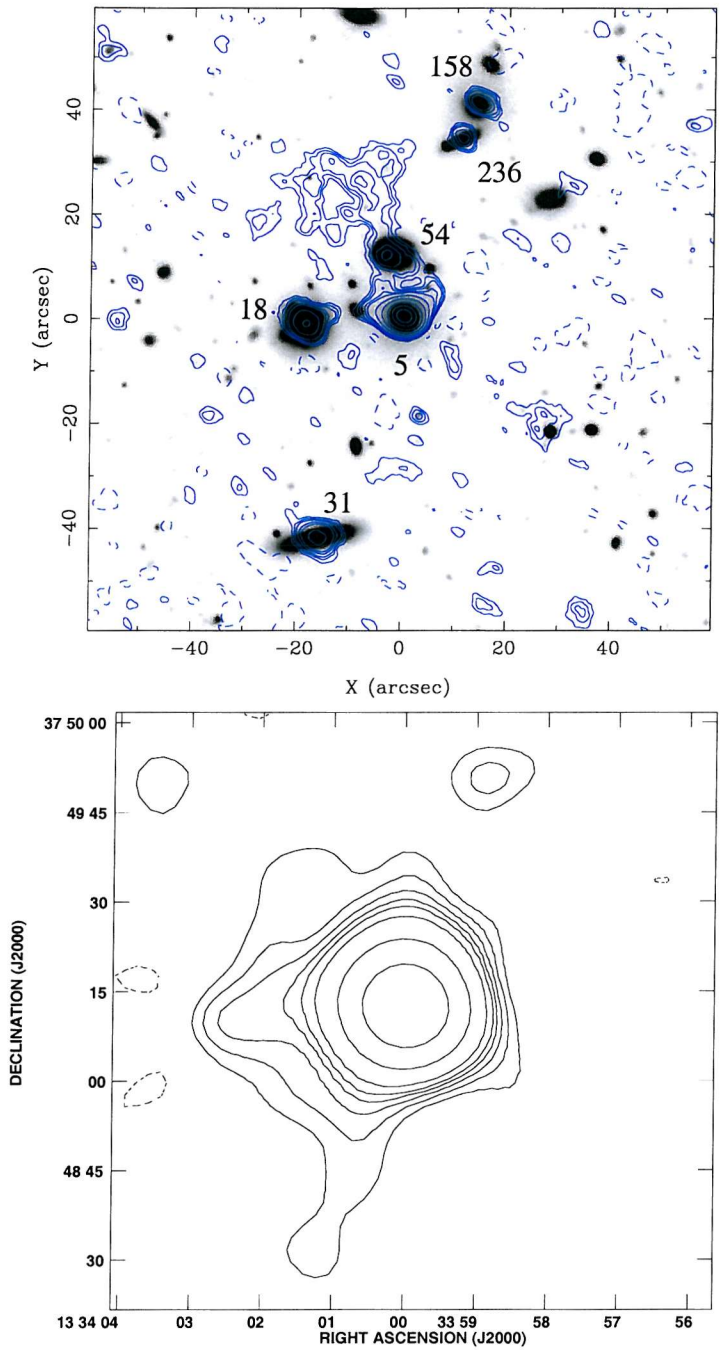


Figure 5.11: Top figure: A 3.35″ resolution, 1.4 GHz radio contour map of the environment around *Chandra* source 4 showing the extended structure overlaid on part of the subaru $R$–band image. The numbers are of the radio sources are from the catalogue in chapter 2 (*Chandra* 4 corresponds to radio source 5). The contours are at levels of -2, 2, 4, 6, 8, 16, 32, 64, 128, 192, 256 times 7.0 $\mu$Jy/beam. Bottom figure: A 14″ resolution, 4.86 GHz radio contour map of the environment around *Chandra* source 4 showing the extended structure. The contours are at levels of -2, 2, 3, 4, 5, 6, 8, 16, 32, 64, 128 times 35 $\mu$Jy/beam.

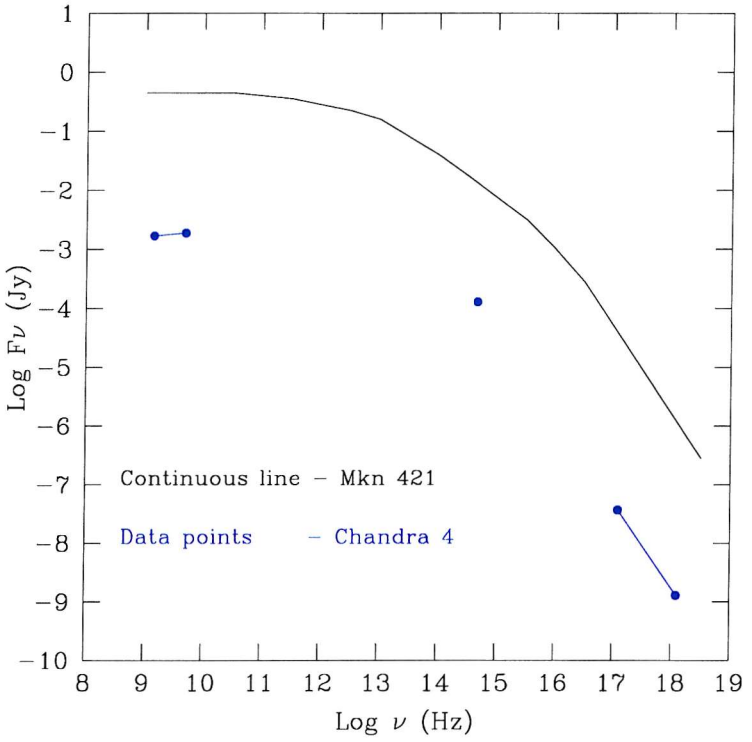


Figure 5.12: The spectral energy distribution of *Chandra* 4, with that of Markarian 421 (a classic example of a BL Lac), shown as comparison.

to about the separation of the galaxies and in the same direction. Although there were hints of possible extended emission it was not possible to say conclusively if the source is extended or not in X-rays and hence if the X-ray emission is from the star-forming regions. Additionally this source falls off the edge of the XMM field of view so the XMM could not help determine more about this source. It is a bright enough X-ray source that it would have been possible to get a reasonable X-ray spectrum which would help determine whether star-formation was the emission mechanism or if there is some contribution from a central engine.

*ROSAT* 32 is shown in the appendix as radio source 10. The 3.35″ resolution image of the A and B-configuration data shows radio emission from both galaxies, but the structure of the spiral arms not resolved. *ROSAT* 32 has a radio spectral index of $\alpha = 0.42$. Star formation is generally associated with a steep spectrum ($\alpha > 0.5$), but it possible that there is a small amount of AGN activity as well as the star formation contributing to this source and the flatter spectrum.

## 5.6 Conclusions

In this chapter it has been shown that there is considerable overlap between the faint X-ray populations and the faint radio populations. Sampling as much of the spectral energy distribution as possible is essential for fully determining the emission mechanisms of the faint objects that constitute the radio and X-ray background. Figures 5.6 and 5.8 show that the faint sources have a wide range of X-ray to radio and radio to optical ratios. Of those sources of each class detected at X-ray and radio wavelengths, the X-ray to radio and radio to optical ratios are distributed over a several orders of magnitude. Additionally for all classes of X-ray sources (e.g. quasars, NELGs etc.) there is a substantial fraction which are also detected at 1.4 GHz. Evidence from this survey and others (e.g. Bauer et al., 2002) suggests that there will increasing overlap between X-ray and radio surveys at fainter detection limits.

It is clear that objects with a whole range of properties and morphologies contribute to the X-ray and radio background. The types of objects range from unresolved QSOs to star-forming, interacting spiral galaxies. Preliminary results for individual objects suggest that we are observing many different emission mechanisms from starbursts to AGN activity to a mixture of both.

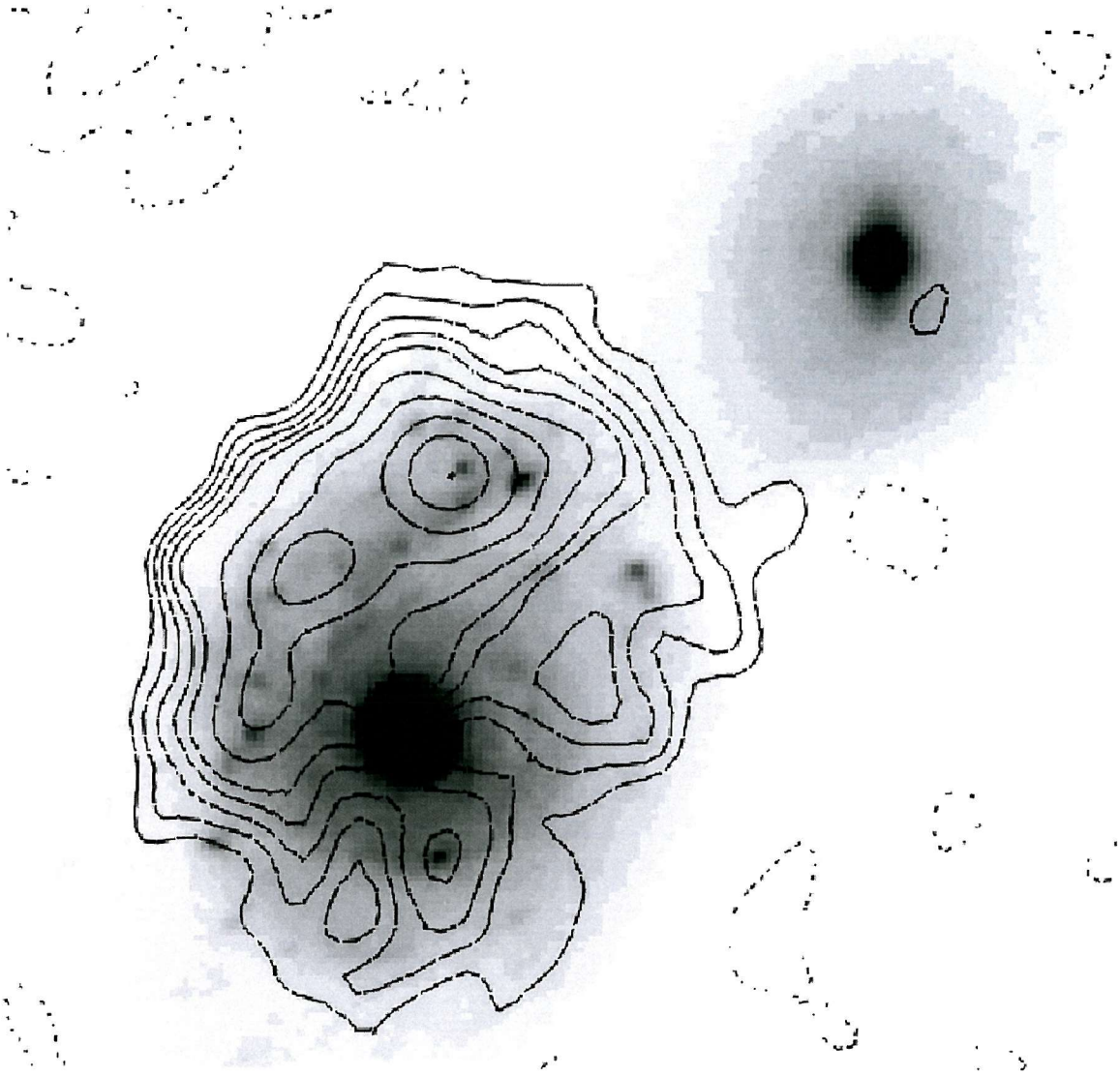

Figure 5.13: A $20'' \times 20''$ HST $I-$band image of source 9 overlaid with radio contours of -2,2,4,5,6,8,10,12,14,16,18 times 11 $\mu$Jy. Note the way the radio emission traces the bright knots of starformation visible in the optical image.

# Chapter 6

# Conclusions

In this chapter the different datasets are summarised. The results of the correlation of the data at different frequencies are presented. The future exploitation of this survey in determining the nature of the faint galaxies is discussed. There is much more data that will contribute to this survey, some already obtained (and briefly mentioned already) and some on guaranteed time still to be taken.

## 6.1 Summary of Data

### 6.1.1 The radio data

From 24hrs of usable data from the VLA, 462 sources were detected to a $4\sigma$ peak flux limit of 30 $\mu$Jy/beam at 1.4 GHz. This makes it one of the deepest radio surveys ever made at this frequency. After correction for software and instrumental bias the Euclidean normalised source counts show an up turn below 1 mJy consistent with other deep surveys (e.g. the Hubble Deep Field, Richards 2000 and the Phoenix Deep Field, Hopkins et al. 1998). The scatter in the counts at sub-mJy fluxes between this survey, the HDF and the PDF is most likely due to real field to field variations in source density.

The survey area was also observed at 4.86 GHz and 116 sources were found above a $3\sigma$ peak flux detection limit of 100 $\mu$Jy/beam , of which 53 had 1.4 GHz counterparts. For these sources it is possible to determine accurate two-point radio spectral indices ($\alpha_R$). For other sources only detected at 1.4 GHz or 4.86 GHz it is possible to obtain upper or lower limits of $\alpha_R$.

### 6.1.2 The optical data

In Chapter 4 the results of the correlation of the radio data with a deep $R-$band Subaru image and a deep $B-$band INT image is presented. Of the radio sources 83% are detected with $R-$band optical counterparts to a limit of $R \leq 27$ (for $B-$band 64% are detected to a limit of $B \leq 26.5$). The radio to optical flux ratios are spread over 4 orders of magnitude with no obvious discontinuity. For 110 sources there are optical spectra from a variety of sources. From a sub-sample of optical counterparts to radio sources with spectral classifications and $R < 20.5$, 96 out of 124 have spectra (77%). This sub-sample contains sources with a wide range of spectral IDs, $B - R$ colours, radio to optical flux ratios and stellarities indicating that the radio sources have a several emission mecahanisms with a range of bolometric luminosities.

### 6.1.3 The X-ray data

The *Chandra* observations detected 214 sources above a flux of $\sim 1.3 \times 10^{-15}$ erg cm$^{-2}$ s$^{-1}$ (0.5 – 7 keV) (M$^{c}$Hardy et al., 2002a). The high positional accuracy of these observations, 1″, has helped confirm or refute the previous optical IDs of counterparts to the original *ROSAT* survey.

## 6.2 Summary of Results

### 6.2.1 Correlation of the Radio and X-ray data

High positional accuracies of the radio, optical and X-ray data (from accurate independent coordinate frames) meant that most correlations were found using a 2″ detection radius. For the radio counterparts to the X-ray sources detections down to a $3\sigma$ limit of 22.5 $\mu$Jy were included (it was estimated that the probability of a $3\sigma$ radio source being randomly coincident with an X-ray source is less than 1% although since the radio maps are not completely Gaussian, this may be an underestimate). Extended sources were found by inspecting the data visually (e.g. in postage stamp format as in the section 2 of the Appendix). Several of the brighter optical counterparts to X-ray sources had optical spectra and a few radio counterparts had two point radio spectra.

This combination of data begins to reveal the exact nature of the faint objects. Certainly for the sources which have a well sampled spectral energy distribution it is possible to begin to have a very good understanding of their character. The high fraction of optically faint sources means that it is difficult to obtain optical spectra

and hence the determination of the nature of a faint object will rely more on the general full band spectral energy distribution.

It has been shown that many different types of objects contribute to the radio and X-ray background including BL Lac objects (radio sources 3 and 5), pure starburst galaxies (radio source 13), galaxies with a possible starburst and AGN component (radio source 10) and normal galaxies at moderate redshift (radio sources 332 at $z = 0.25$ and 436 at z=0.69).

### 6.2.2 Quasars

Quasars have been previously been found to dominate less deep X-ray surveys (Shanks et al. 1991, Boyle et al. 1993). In the *Chandra* survey presented here quasars dominate the identified sources at bright fluxes. The *Chandra* data has been vital in confirming the optical counterpart to a X-ray source previously found by *ROSAT* due to the superior spatial resolution of *Chandra* . 70% of the X-ray detected quasars have radio counterparts with 1.4 GHz fluxes greater than 22.5 $\mu$Jy with radio to optical flux ratios ranging from one to a hundred. Several unidentified X-ray sources with radio counterparts have radio to optical flux ratios around one thousand and are also likely to be quasars.

### 6.2.3 BL Lacs

Several *Chandra* surveys (e.g.Mushotzky et al.,2000) found that a fraction of bright X-ray sources were associated with apparently normal absorption line galaxies for which it was difficult to explain their large relative X-ray luminosity. The deep radio observations at 1.4 GHz and 4.86 GHz indicated that two of these sources (radio sources 3 and 5) had flat radio spectra ($\alpha_R \sim 0$) and core-halo morphologies. Analysis of the X-ray spectra of these objects from *XMM* indicate that they are very steep which is indicative of the tail of the synchrotron emission from a relativistic flow of material along or near the line of sight. This evidence strongly indicates that these objects are BL Lacs.

### 6.2.4 Narrow Emission Line Galaxies

NELGs are the a major constituent of the identified *Chandra* sources and the dominant population of the identified radio sources. Whilst some sources are associated with AGN activity (e.g. radio source 1 which is a lobe dominated FRII radio source also detected in X-rays in the *ROSAT* survey, but not in the *Chandra* survey, indi-

cating that it is either soft, extended or possibly variable in the X-rays) some can be accurately described by starburst emission. *ROSAT* source 117 is detected as a relatively strong radio source and its spectral energy distribution can be modelled well by a combination of a normal spiral galaxy and a moderate strength starburst component (Gunn et al., 2001). The radio emission is extended and appears to trace out the faint optical structure seen in an *R*–band image. *ROSAT* source 117 appears in section 1 of the Appendix as radio source 13.

*ROSAT* source 32 is also detected as a relatively strong radio source (source 10, in section 1 of the Appendix). It is coincident with a pair of low redshift (z=0.068), interacting spiral galaxies. High resolution A-configuration data (figure 5.13) shows that the radio flux is dominated by emission from the spiral arms of one galaxy with very little flux from the nucleus indicating that this is starburst galaxy.

So it appears that NELGs are mixture of starburst galaxies and AGNs, possibly with a contribution from both within one object.

### 6.2.5 Clusters

There were several cluster candidates from the *ROSAT* survey, soft extended X-ray sources with no obvious single optical counterparts. The angular distribution of the radio sources along with some optical spectra indicate that there are clusters in our field as well as large scale structure including filaments that traverse the whole field of view. One cluster candidate (also detected by *Chandra* as source 160) is associated with head-tail radio source, a class of lobe dominated radio sources whose lobes have been swept back by the galaxies relative motion through an intra-cluster medium.

## 6.3 Future potential of this survey

The principle goal of the X-ray surveys (the original *ROSAT* survey and the *Chandra* /*XMM* survye) is to study the astrophysics of the contributors to the hard X-ray background. Additionally these data will also form the basis of a study of the faint radio sources at 1.4 GHz. Many of the current deep extragalactic surveys (e.g. HDF-North and South, PDF, European Large-Area ISO Survey - ELAIS and others) now take advantage of the ability to obtain comparable resolutions in optical, radio and X-ray observations. It is likely that deeper surveys will find increasing overlap between the radio and X-ray background.

### 6.3.1 Existing Data

The survey team have data from *XMM* and MERLIN which is not included in this thesis as it has not been fully correlated with the data presented here. Additionally some of the *ROSAT* and *Chandra* sources have deep $K-$band imaging.

#### 6.3.1.1 *XMM*

The *XMM* observations of this field are in the process of being analysed. The very bright M star (*Chandra* source 1) caused a lot of problems with the XMM detectors. For the brighter sources X-ray spectra are now being obtained which are already beginning to show their worth in identifying emission mechanisms (see chapter 5). Over one hundred of the sources are bright enough to have reasonable quality X-ray spectra from which powerlaw spectra can be obtained. *XMM* will also be able to detect many extended sources (some associated with clusters and already detected with *ROSAT*) which *Chandra* has missed due to its lack of sensitivity to low surfaces brightness objects.

#### 6.3.1.2 MERLIN

As MERLIN only has a $\sim 10'$ field of view, four pointings were used to cover the $30'$ diameter field of view of this survey. Each pointing was of four days duration giving a $1\sigma$ rms noise limit of $15\,\mu$Jy/beam. MERLIN has a larger maximum baseline than the VLA (250 km compared to 36.4 km for the VLA) giving it a much higher resolution ($0.3''$ compared to $1.4''$ for the VLA A-configuration). The higher resolution data will be very useful in looking at the structure of extended sources, finding upper limits to the sizes of unresolved sources and determining brightness temperatures of the radio sources. Compact sources with flat spectra and high brightness temperatures are typical of AGN whereas starburst are resolved and have steep spectral indices.

### 6.3.2 Work to be done with current data

There is is still considerable science to be extracted from this survey. Of primary importance is to gather together as much data as possible for each radio and X-ray source. So far only the brighter sources have been examined in any detail (e.g. chapter five). For each source it is necessary to sample as much as possible of its Spectral Energy Distribution to help determine the emission mechanism(s). It has been shown that at least two bright, optically inactive galaxies are very likely to

be BL Lacs (M$^{c}$Hardy et al., in prep., 2002). The combination of radio spectra and X-ray spectra was crucial in determining their nature. The combination of optical spectra and X-ray spectra from *XMM* will help determine the distribution of absorption in broad-line AGN as a function of luminosity and redshift.

One of the key questions for both the faint radio and X-ray sources is the nature of the Narrow Emission Line Galaxies. There is evidence in the original *ROSAT* survey and in this thesis (section 5.5) that both star-formation and AGN activity play a part both within the whole sample and within individual objects. The *XMM* spectra can be used to distinguish between AGN, perhaps with some absorption, and starbursts which will contribute soft thermal components to the spectra. The radio imaging will provide an independent determination of the star-formation rate to support the X-ray spectral diagnostic. The X-ray diagnostic will also help to distinguish between starburst galaxies (which are characterised by steep radio spectra) and steep spectrum lobe dominated sources at moderate redshifts (i.e. a source at $z \sim 0.5$ with radio lobes that extend $10 - 20\,\mathrm{kpc}$), both of which can be extended to about the same size on the sky, $3 - 4''$.

In the *XMM* data around 20 soft, extended sources have been detected which are strong cluster candidates. This is twice as many as expected from the local cluster X-ray luminosity function and has important implications for cosmology. Clusters could explain the small fraction of X-ray sources with very faint optical sources (as an optical source would not be expected at the exact X-ray position if many optical sources contribute to a single X-ray source). *Chandra* will be useful in removing any possibility of contamination by locating any point sources (e.g. AGN) contributing to the extended soft source. Additionally the two-point correlation function within the X-ray, radio and optical surveys and between them can be studied. This can be important in getting the most out of this data where, due to the very low noise (less than one photon per pixel), half a dozen photons can be considered a reasonable detection in the *Chandra* data.

The survey team are in the process of obtaining further optical spectra of the unidentified X-ray sources (including those with radio counterparts) in order to begin to statistically study the broad band properties of the X-ray sample as a whole.

### 6.3.3 Future Guaranteed Data

This survey has a wealth of data still to be collected, but on guaranteed observing time. These data are listed below and will be collected over the next few years.

#### 6.3.3.1 The Data

1. Deep $K-$band imaging of the 13hr field will be performed using the new wide field imaging camera, WFCAM, on the UK Infra-Red Telescope down to a limit of $K \sim 22$.[1]

2. Observations will be made with SIRTF (NASA's Space Infra-Red Telescope Facility) as part of guaranteed time with two of the instrument groups. Firstly with Giovannio Fazio who is organising the construction of the Infrared Array Camera (IRAC) which covers $3.6 - 8\mu$m and secondly with George Rieke who is organising the construction of the Multiband Imaging Photometer (MIPS) which covers the $24 - 160\mu$m range.

3. There will also be observations at $\sim$ 1mm made with the BOLOCAM instrument at the Caltech Sub-millimeter Observatory (Mauskopf, 2000).

#### 6.3.3.2 Potential of these new data

The potential of using all these data with those previously collected is vast. Just a few of the possibilities are presented here.

The $K-$band data will be very useful in studying the optical-IR spectral energy distribution. With $B, R$ and $K-$band magnitudes it possible to begin to estimate properties of the galaxies, e.g. the amount of absorption of an AGN (if they are bright in X-rays and radio waves, but optically quiet) and rate of starformation. Three photometric measurements are not enough to make a full photometric determination of the redshift of a source (typically at least 4 photometric magnitudes are used, e.g. Gwyn & Hartwick, 1996). However three photometric magnitudes can give you an idea if the spectral energy distribution is consistent with a a certain redshift. For example, Sánchez & González-Serrano (2002) use $R$, $B$ and $K$ magnitudes to investigate the environments of seven radio loud quasars. They find that the quasars tend to inhabit the outer regions of clusters where relative speeds of galaxies are more likely to produce a merger (mergers are currently thought to be a possible origin or feeding mechanism of nuclear activity, Wilson & Colbert, 1995). The analysis of clusters as selected by colour, angular separation and by redshift will also be useful in this survey to investigate other radio sources (e.g. the head-tail source) and clusters as sources of soft X-rays.

With the aim of identifying as many of the sources which contribute to the X-ray and radio backgrounds, the SIRTF and BOLOCAM data will be useful in further sampling the full spectral energy distribution of as many sources as possible. With enough sources of each class it will be possible to study the astrophysics of each

[1]During the viva, the author was informed that these observations were not yet gauranteed as the TAC had not yet come to a decision and WFCAM has yet to see first light.

class as a function of redshift and luminosity. The nature of the Narrow Emission Line Galaxies is of particular interest as they are a major contributor to the X-ray background and are in fact the dominant contributor to the radio background (based on the sources currently identified). Obviously high to signal to noise optical spectra of each X-ray or radio source would be invaluable in quantifying the relative AGN/starburst contribution to bolometric luminosity of each source. However to obtain such spectra for the hundreds of sources contained in the X-ray and radio surveys would take a prohibitively large amount of time on even the largest telescopes. With a well sampled full spectral energy distribution, starburst and AGN components can be modelled to examine what relative contribution best matches the observed SED.

## 6.4 The 1hr field

It has been argued that more than one deep survey is unnecessary in the astronomical community as apart from possible field to field variations in the density of objects, the faint sources observed will all be of similar type. However the faint objects appear to be of many classes with a wide range of relative optical, radio and X-ray properties. Therefore to study the astrophysics of each class as a function of redshift, luminosity and other parameters many objects are needed. This is why a second field at a Right Ascension of 1hour[2] is also in the process of being analysed by the 13hr survey team with a similar wealth of data as this field. This field has 12hrs of VLA A-configuration data, a 200 ks XMM observation and also $4 \times 30$ ks *Chandra* observations in a similar fashion to the 13hr field.

## 6.5 Concluding remarks

The data presented here will form the basis of a very detailed deep multi-wavelength survey. The possibilities of scientific analysis on this survey are legion. Understanding the nature of the faintest X-ray and radio sources detected to data, luminous objects to $z \sim 5$, and how they relate to objects in the local universe, will be imperative for understanding sources that will be detectable with future technological advances at $z = 5 - 10$. At these redshifts the epoch of first galaxy formation and first star formation ('population III' stars) will be probed.

[2]Precise coordiantes of RA 01 45 27 $\delta$ -04 34 42 (J2000).

# Chapter 7

# Appendix

## 7.1 $R$– band Optical counterparts to the radio sources

Here 'postage-stamp' images of the $R$– band counterparts to all 462 radio sources from table 2.2 are presented with contours of the radio flux superimposed. Each postage-stamp is $30'' \times 30''$ square. The radio contours are in multiples of the 7.5 $\mu$Jy/beam rms noise; -2[1], 2, 3, 4, 5, 8, 16, 32, 64, 128, 256, 512, 1024. They are taken from the naturally weighted, combined A and B-configuration display map figure 2.5 and its flanking fields. The optical data are from the Subaru Suprimecam $R$– band deep one hour image discussed in Chapter 4 which has a detection limit of $R \sim 27$ (for non-confused sources). Some radio sources fall on the blank part of the field of view due to the inoperative CCD chip., see section 4.1.1. The 4 numbers at the top of each image are the source number, the peak flux in $\mu$Jy (the sources are in order of decreasing total flux), its distance from the centre of the field in arcminutes and the angle counter-clockwise from north to the centre of the field from the radio source. If the source is coincident with a *Chandra* source then the *Chandra* number is presented in the lower right of the postage-stamp.

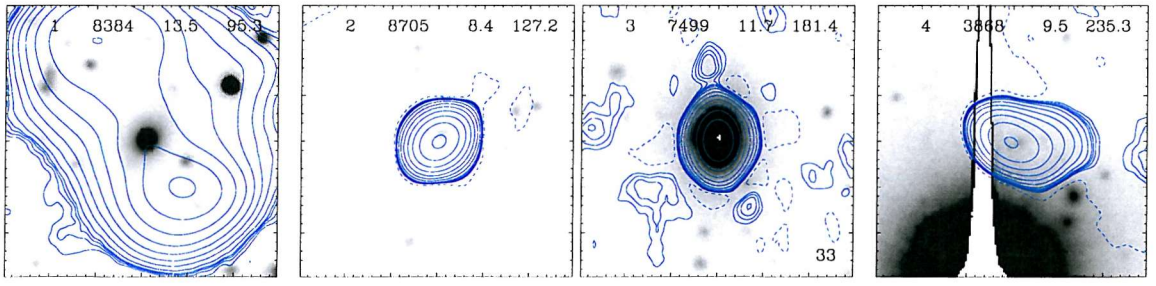


[1]Negative contours are indicated by a dashed line.

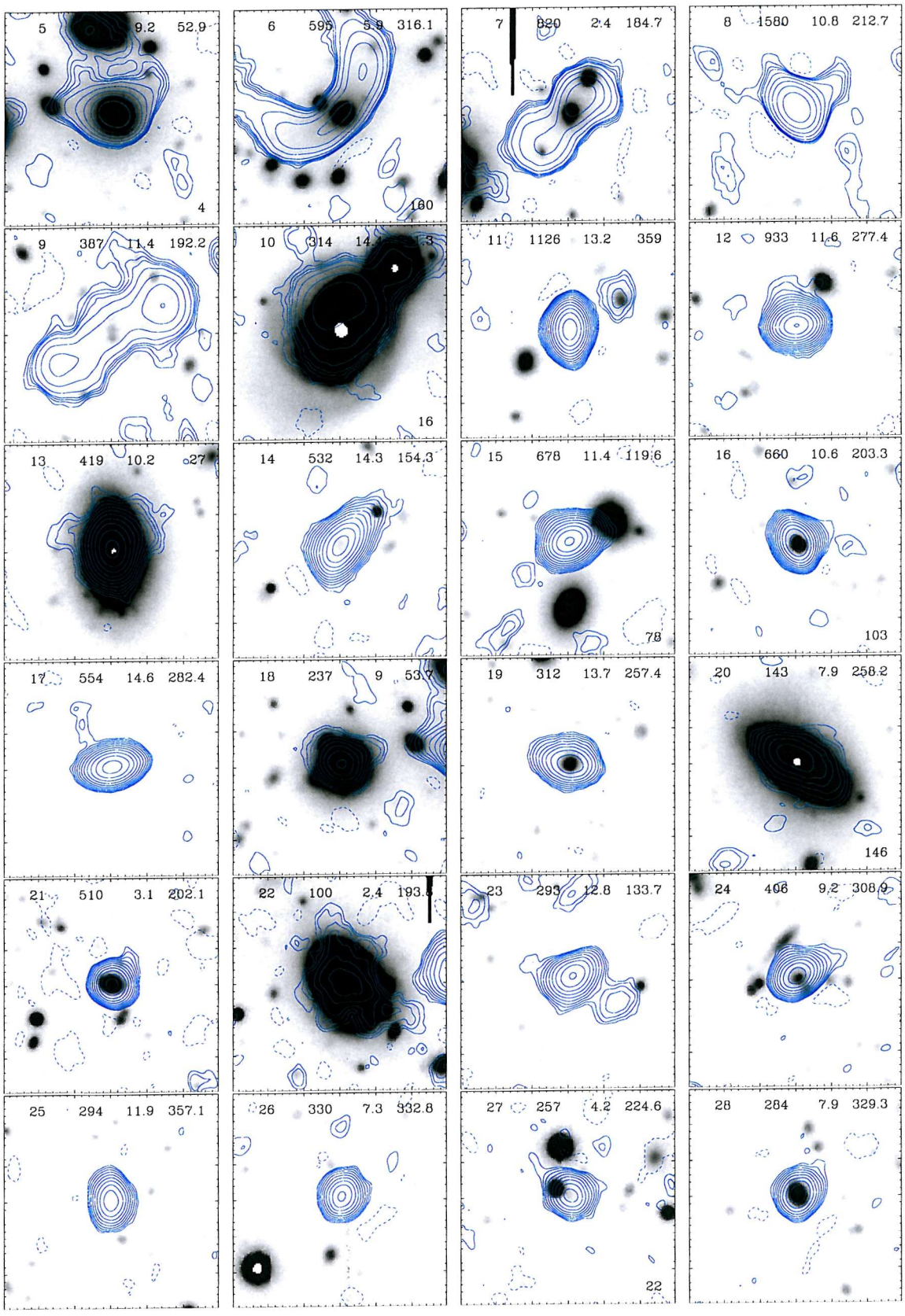
5 9.2 52.9
4
6 595 5.9 316.1
160
7 820 2.4 184.7
8 1580 10.8 212.7
9 387 11.4 192.2
10 314 14.4 3
16
11 1126 13.2 359
12 933 11.6 277.4
13 419 10.2 27
14 532 14.3 154.3
15 678 11.4 119.6
78
16 660 10.6 203.3
103
17 554 14.6 282.4
18 237 9 53.7
19 312 13.7 257.4
20 143 7.9 258.2
146
21 510 3.1 202.1
22 100 2.4 193.6
23 293 12.8 133.7
24 406 9.2 308.9
25 294 11.9 357.1
26 330 7.3 332.8
27 257 4.2 224.6
22
28 284 7.9 329.3

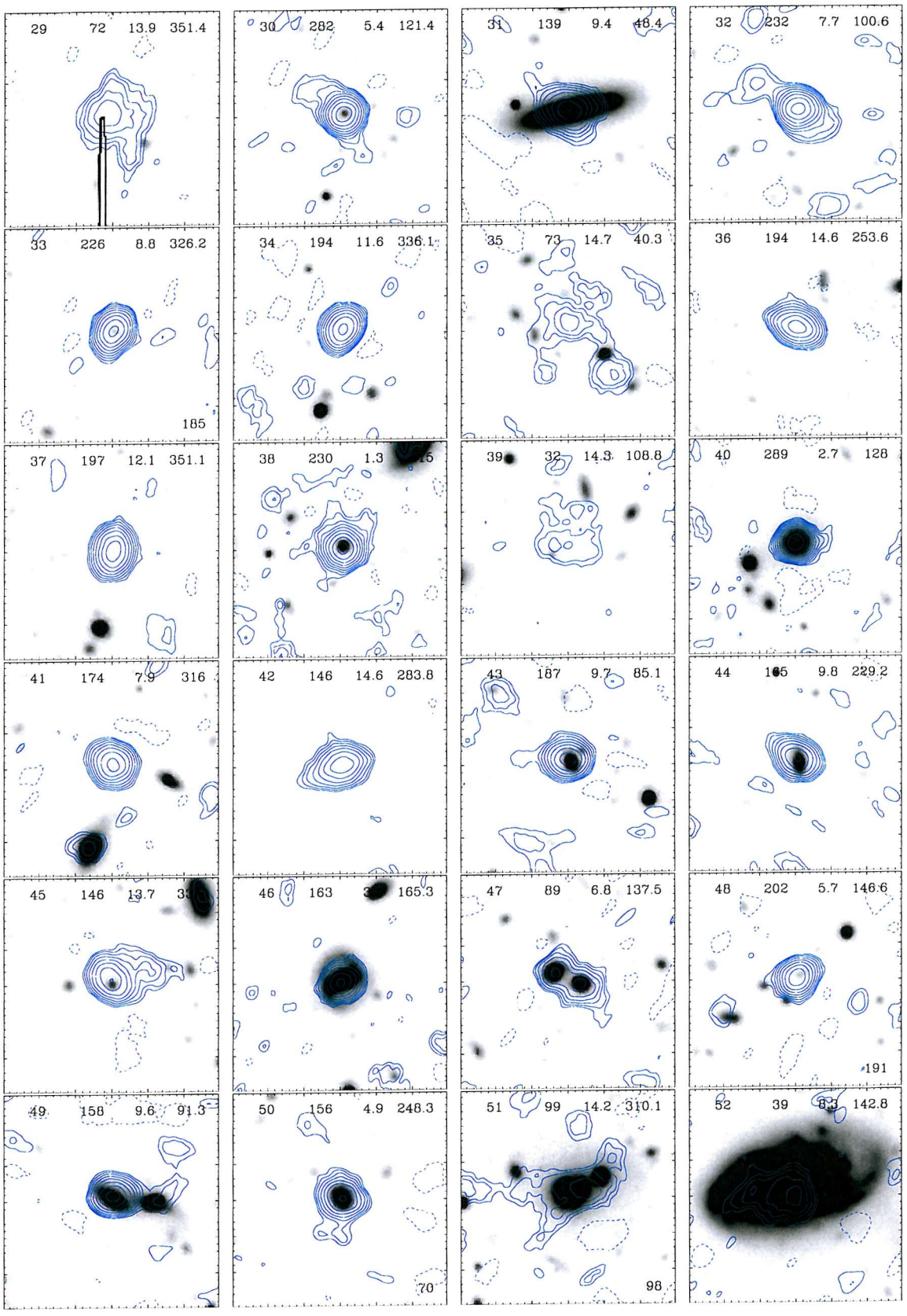
29 72 13.9 351.4
30 282 5.4 121.4
31 139 9.4 48.4
32 232 7.7 100.6
33 226 8.8 326.2
185
34 194 11.6 336.1
35 73 14.7 40.3
36 194 14.6 253.6
37 197 12.1 351.1
38 230 1.3
39 32 14.3 108.8
40 289 2.7 128
41 174 7.9 316
42 146 14.6 283.8
43 187 9.7 85.1
44 165 9.8 229.2
45 146 13.7
46 163 165.3
47 89 6.8 137.5
48 202 5.7 146.6
191
49 158 9.6 91.3
50 156 4.9 248.3
70
51 99 14.2 310.1
98
52 39 142.8

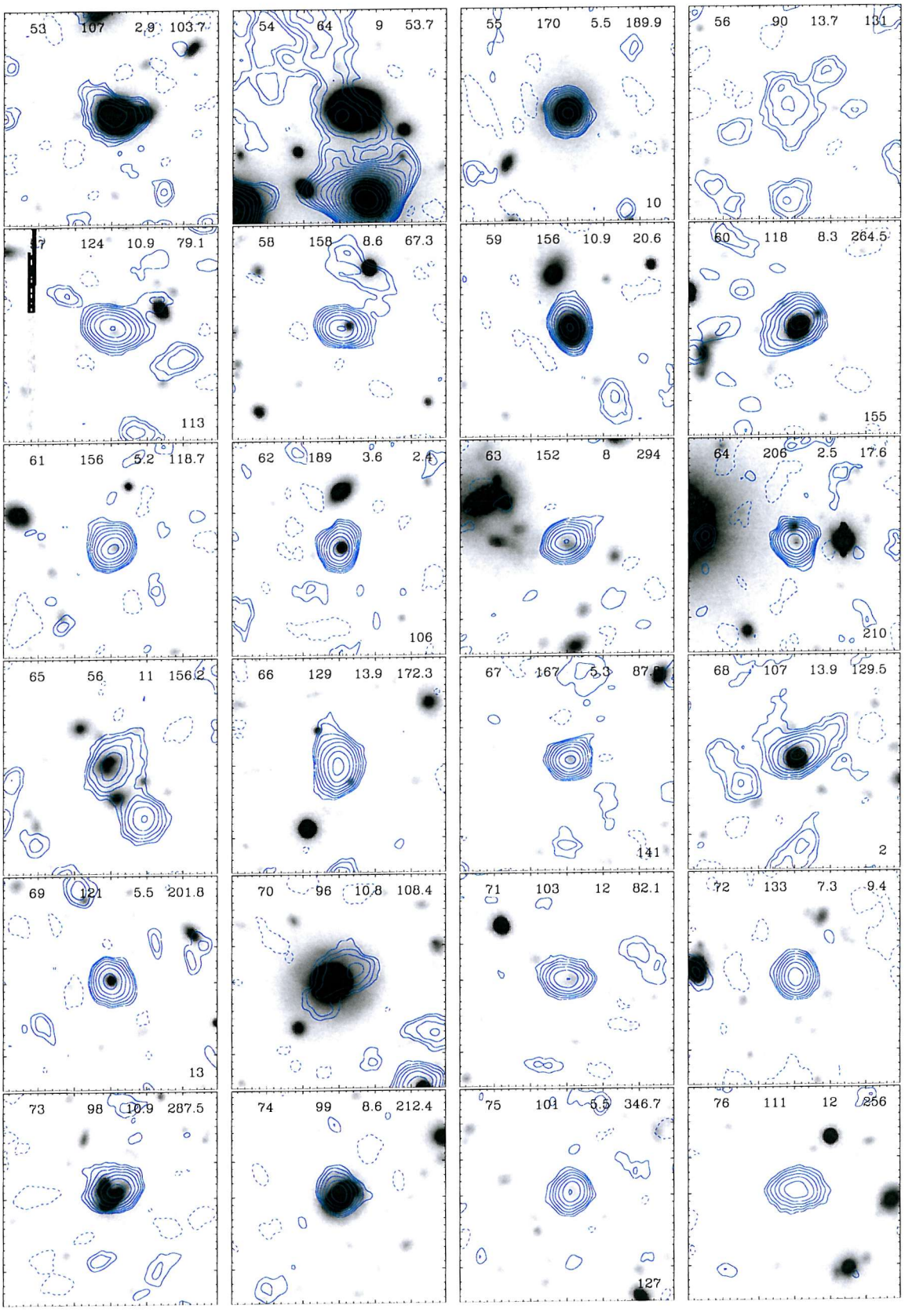
53 107 2.9 103.7
54 64 9 53.7
55 170 5.5 189.9
10
56 90 13.7 131
57 124 10.9 79.1
113
58 158 8.6 67.3
59 156 10.9 20.6
60 118 8.3 264.5
155
61 156 5.2 118.7
62 189 3.6 2.4
106
63 152 8 294
64 206 2.5 17.6
210
65 56 11 156.2
66 129 13.9 172.3
67 167 5.3 87.8
141
68 107 13.9 129.5
2
69 121 5.5 201.8
13
70 96 10.8 108.4
71 103 12 82.1
72 133 7.3 9.4
73 98 10.9 287.5
74 99 8.6 212.4
75 101 5.5 346.7
127
76 111 12 256

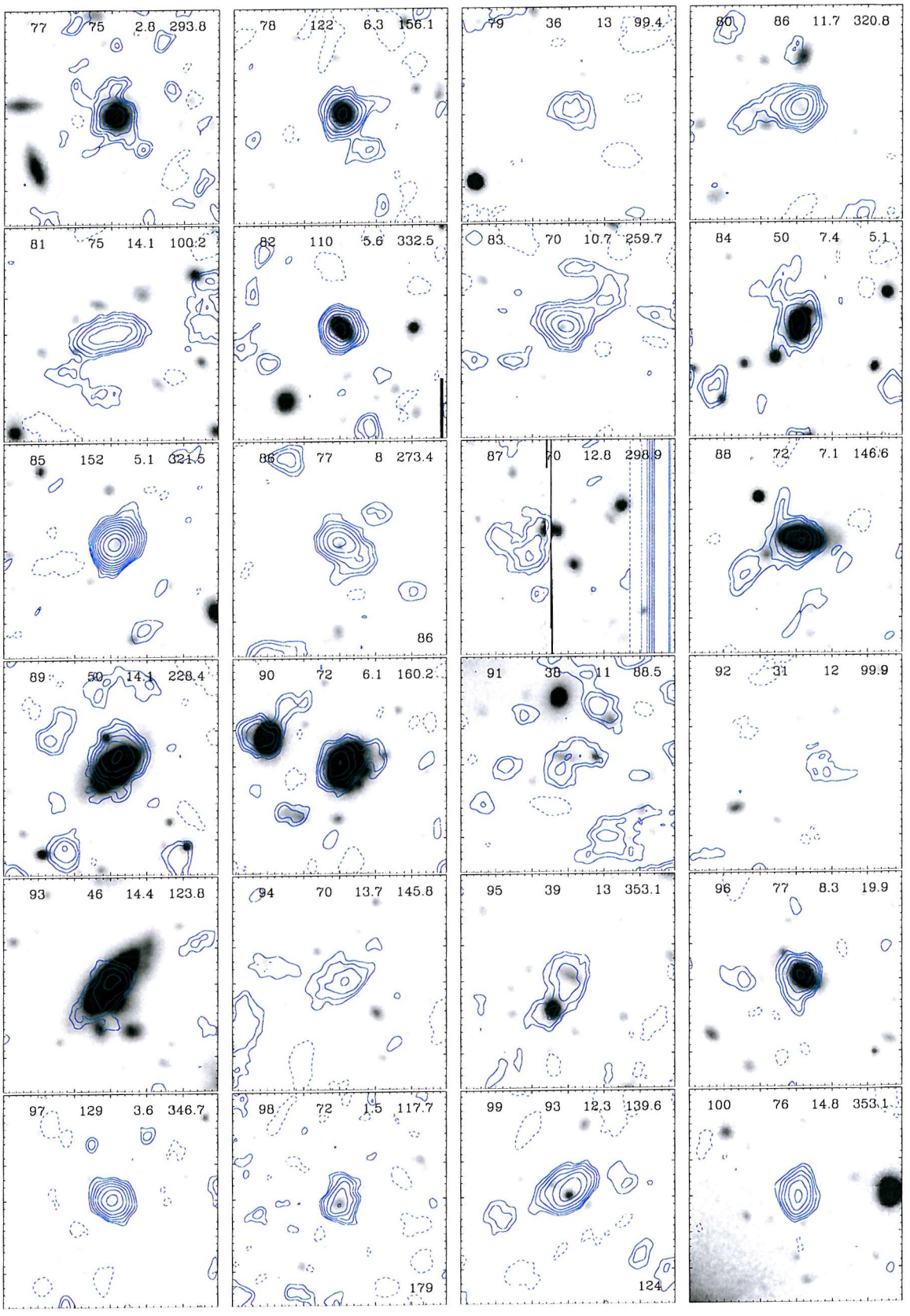
77 75 2.8 293.8
78 122 6.3 156.1
79 36 13 99.4
80 86 11.7 320.8
81 75 14.1 100.2
82 110 5.6 332.5
83 70 10.7 259.7
84 50 7.4 5.1
85 152 5.1 321.5
86 77 8 273.4
86
87 70 12.8 298.9
88 72 7.1 146.6
89 50 14.1 228.4
90 72 6.1 160.2
91 38 11 88.5
92 31 12 99.9
93 46 14.4 123.8
94 70 13.7 145.8
95 39 13 353.1
96 77 8.3 19.9
97 129 3.6 346.7
98 72 1.5 117.7
179
99 93 12.3 139.6
124
100 76 14.8 353.1

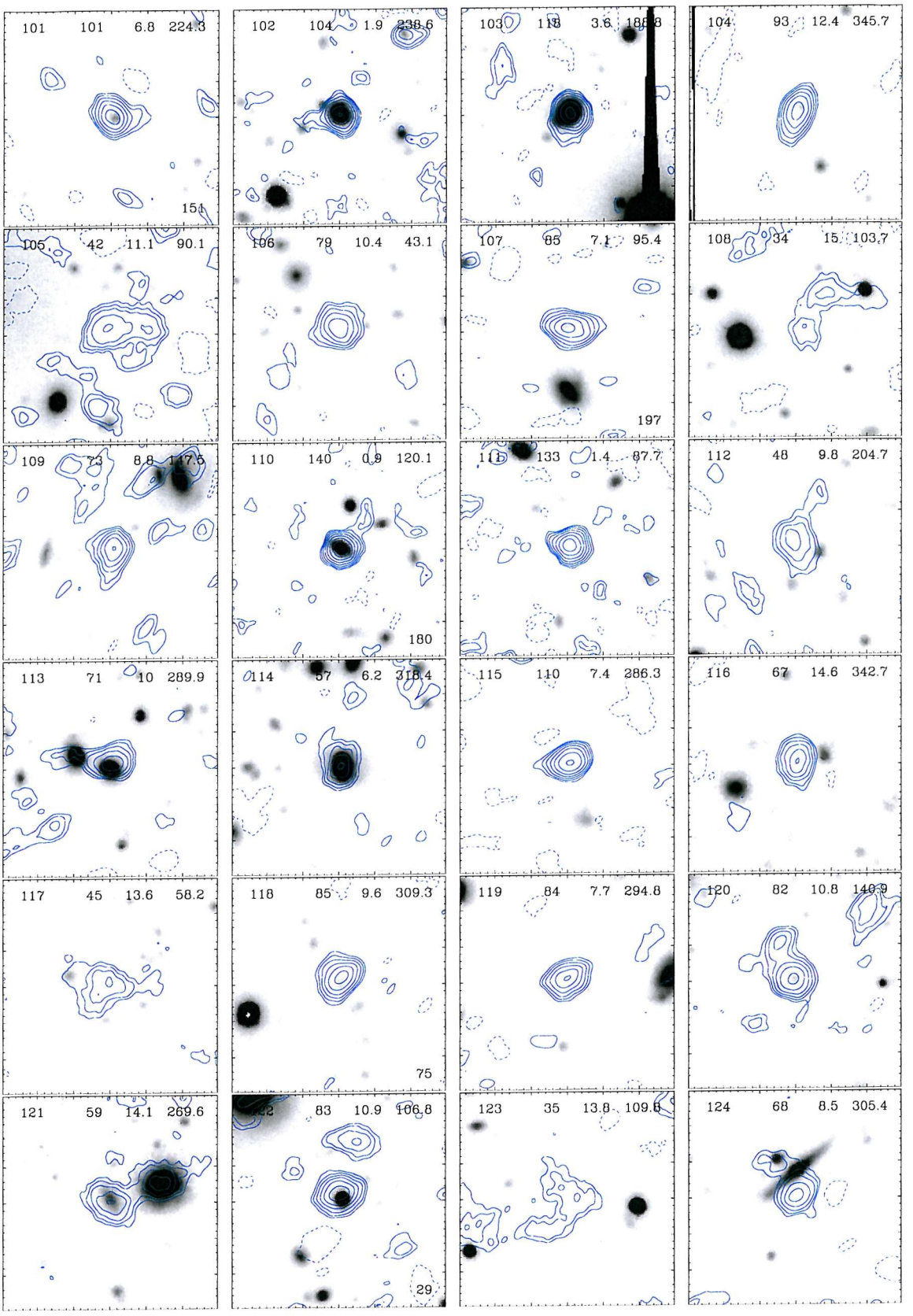
101 101 6.8 224.3
151
102 104 1.9 238.6
103 118 3.6 188.8
104 93 12.4 345.7
105 42 11.1 90.1
106 79 10.4 43.1
107 85 7.1 95.4
197
108 34 15 103.7
109 73 8.8 117.5
110 140 0.9 120.1
180
111 133 1.4 87.7
112 48 9.8 204.7
113 71 10 289.9
114 57 6.2 318.4
115 110 7.4 286.3
116 67 14.6 342.7
117 45 13.6 58.2
118 85 9.6 309.3
75
119 84 7.7 294.8
120 82 10.8 140.9
121 59 14.1 269.6
83 10.9 106.8
29
123 35 13.8 109.8
124 68 8.5 305.4

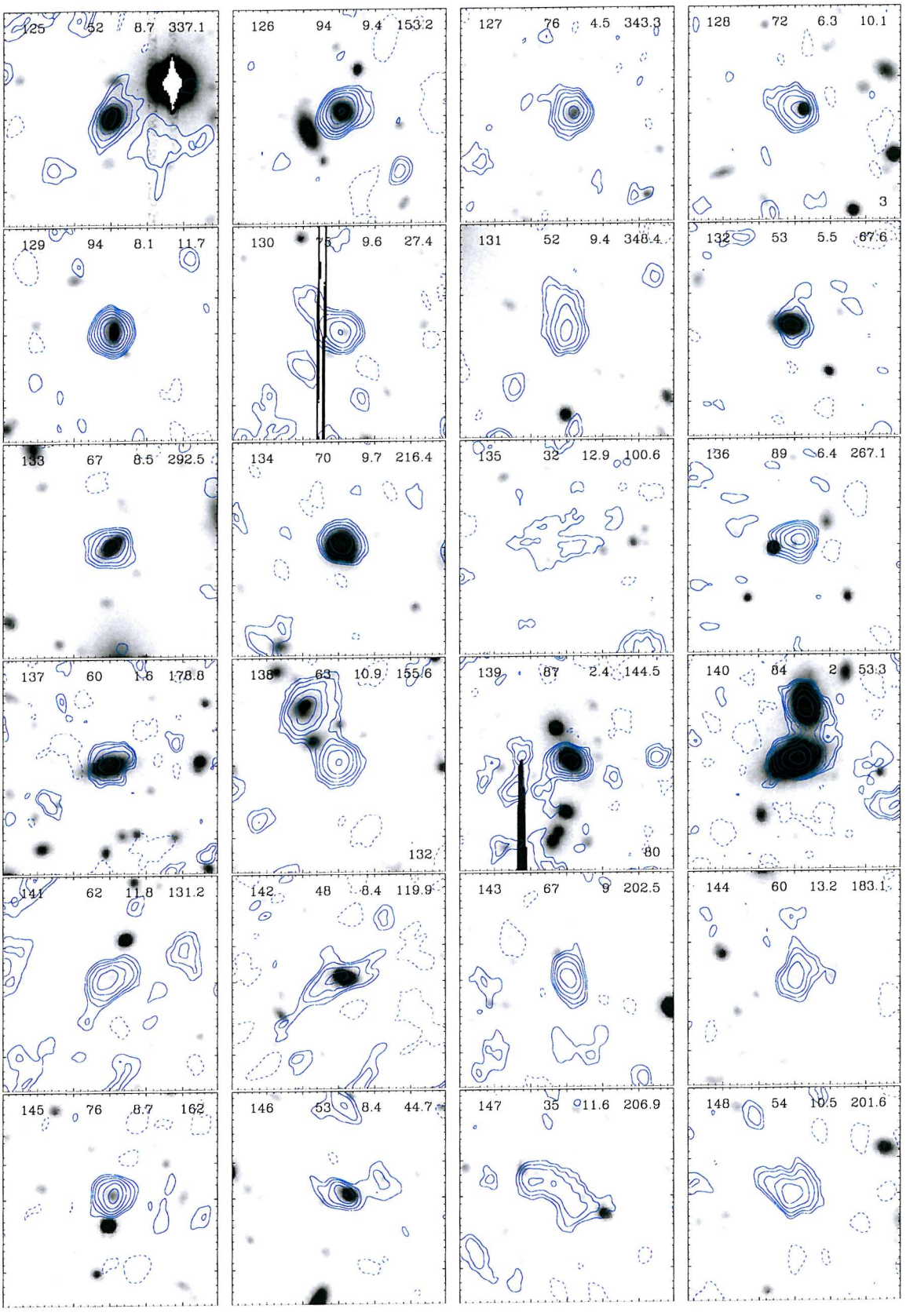
125 52 8.7 337.1
126 94 9.4 153.2
127 76 4.5 343.3
128 72 6.3 10.1
3
129 94 8.1 11.7
130 9.6 27.4
131 52 9.4 348.4
132 53 5.5 67.6
133 67 8.5 292.5
134 70 9.7 216.4
135 32 12.9 100.6
136 89 6.4 267.1
137 60 1.6 178.8
138 63 10.9 155.6
132
139 87 2.4 144.5
80
140 84 2 53.3
141 62 11.8 131.2
142 48 8.4 119.9
143 67 9 202.5
144 60 13.2 183.1
145 76 8.7 162
146 53 8.4 44.7
147 35 11.6 206.9
148 54 10.5 201.6

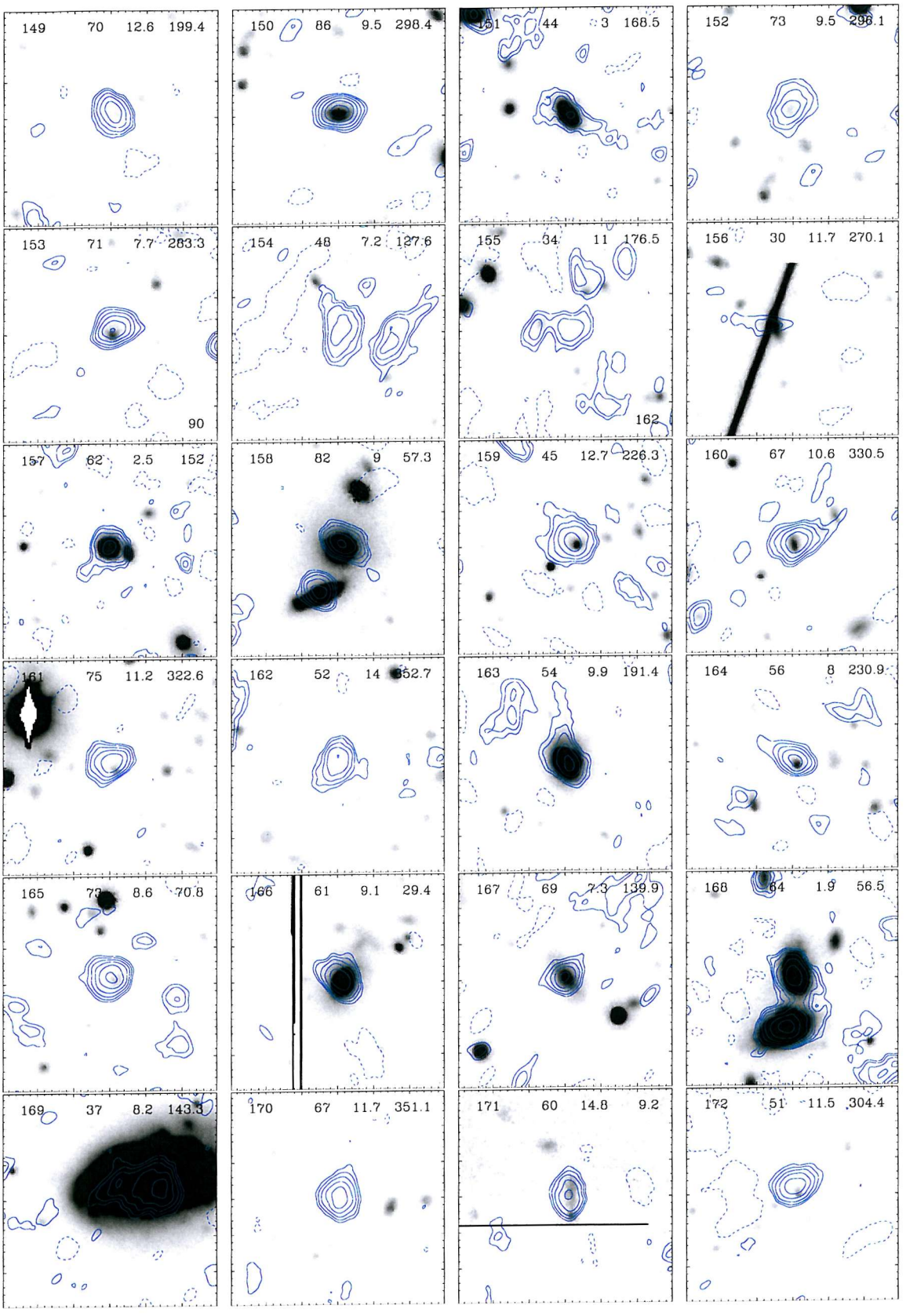
149 70 12.6 199.4
150 86 9.5 298.4
151 44 3 168.5
152 73 9.5 298.1
153 71 7.7 283.3
90
154 48 7.2 127.6
155 34 11 176.5
162
156 30 11.7 270.1
157 62 2.5 152
158 82 9 57.3
159 45 12.7 226.3
160 67 10.6 330.5
161 75 11.2 322.6
162 52 14 352.7
163 54 9.9 191.4
164 56 8 230.9
165 73 8.6 70.8
166 61 9.1 29.4
167 69 7.3 139.9
168 64 1.9 56.5
169 37 8.2 143.3
170 67 11.7 351.1
171 60 14.8 9.2
172 51 11.5 304.4

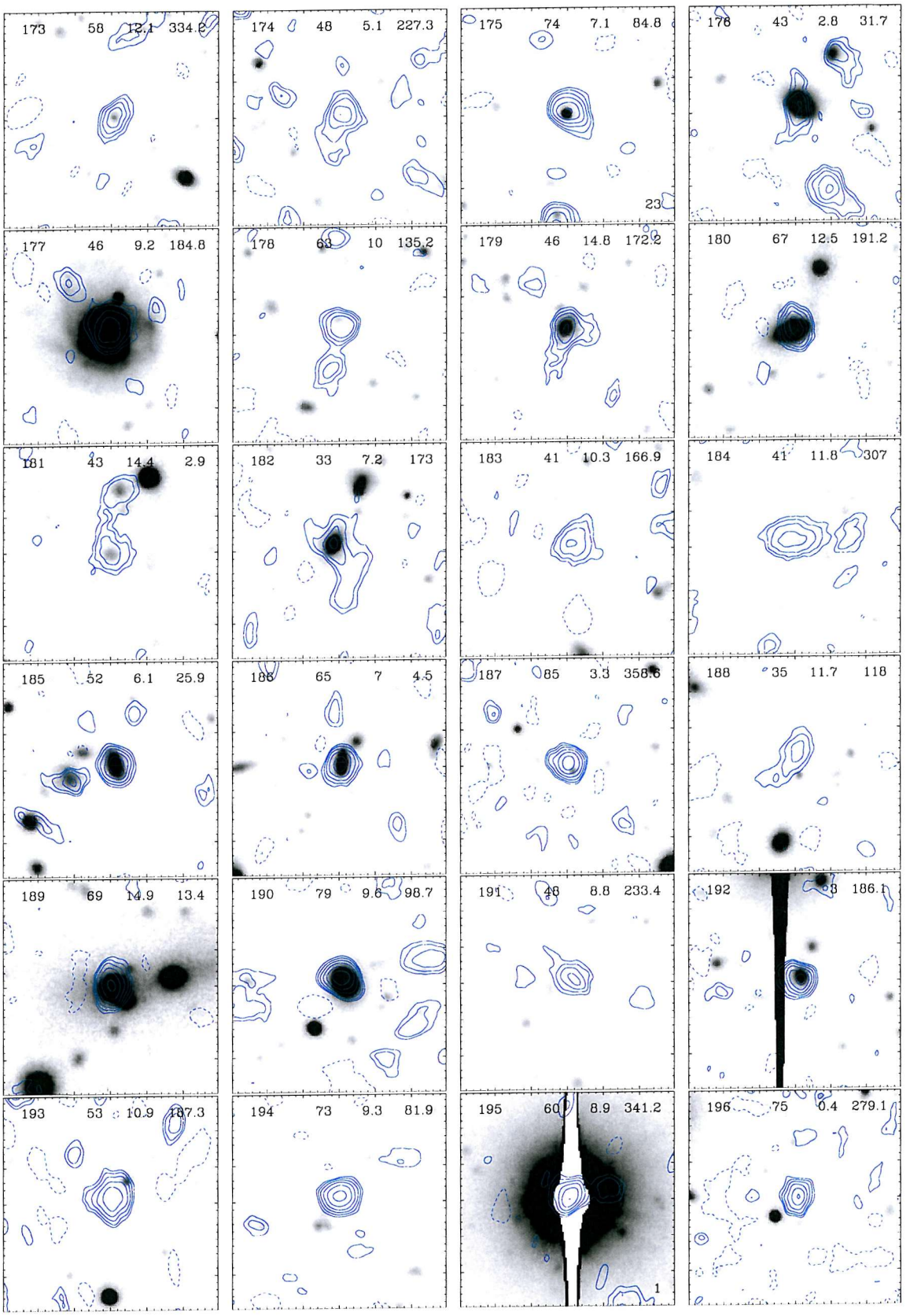
173 58 12.1 334.2
174 48 5.1 227.3
175 74 7.1 84.8
176 43 2.8 31.7
177 46 9.2 184.8
178 63 10 135.2
179 46 14.8 172.2
180 67 12.5 191.2
181 43 14.4 2.9
182 33 7.2 173
183 41 10.3 166.9
184 41 11.8 307
185 52 6.1 25.9
186 65 7 4.5
187 85 3.3 358.6
188 35 11.7 118
189 69 14.9 13.4
190 79 9.6 98.7
191 46 8.8 233.4
192 186.1
193 53 10.9 187.3
194 73 9.3 81.9
195 60 8.9 341.2
196 75 0.4 279.1

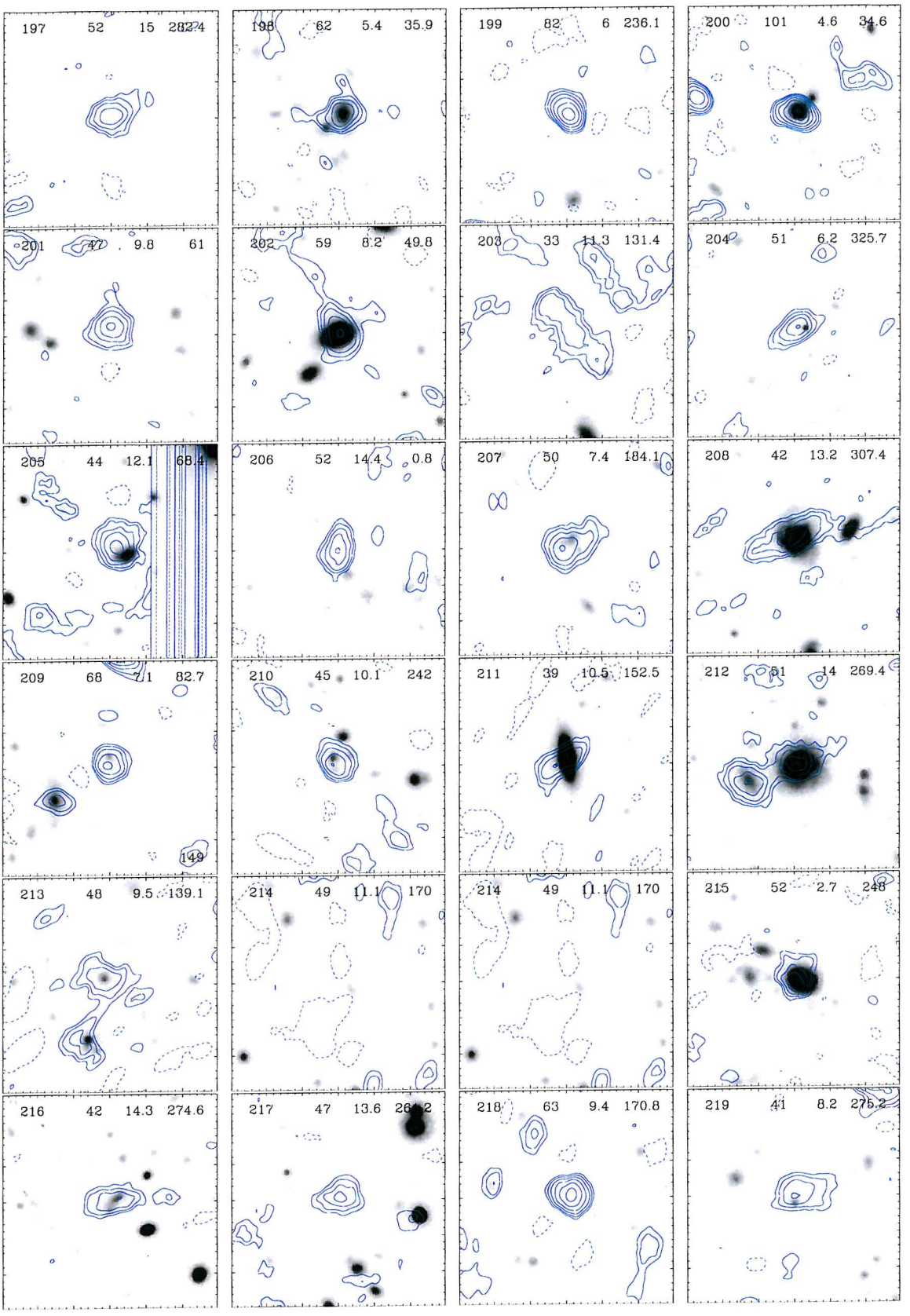
197 52 15 282.4
198 62 5.4 35.9
199 82 6 236.1
200 101 4.6 34.6
201 47 9.8 61
202 59 8.2 49.8
203 33 11.3 131.4
204 51 6.2 325.7
205 44 12.1 68.4
206 52 14.4 0.8
207 50 7.4 184.1
208 42 13.2 307.4
209 68 7.1 82.7
149
210 45 10.1 242
211 39 10.5 152.5
212 51 14 269.4
213 48 9.5 139.1
214 49 11.1 170
214 49 11.1 170
215 52 2.7 248
216 42 14.3 274.6
217 47 13.6
218 63 9.4 170.8
219 41 8.2 275.2

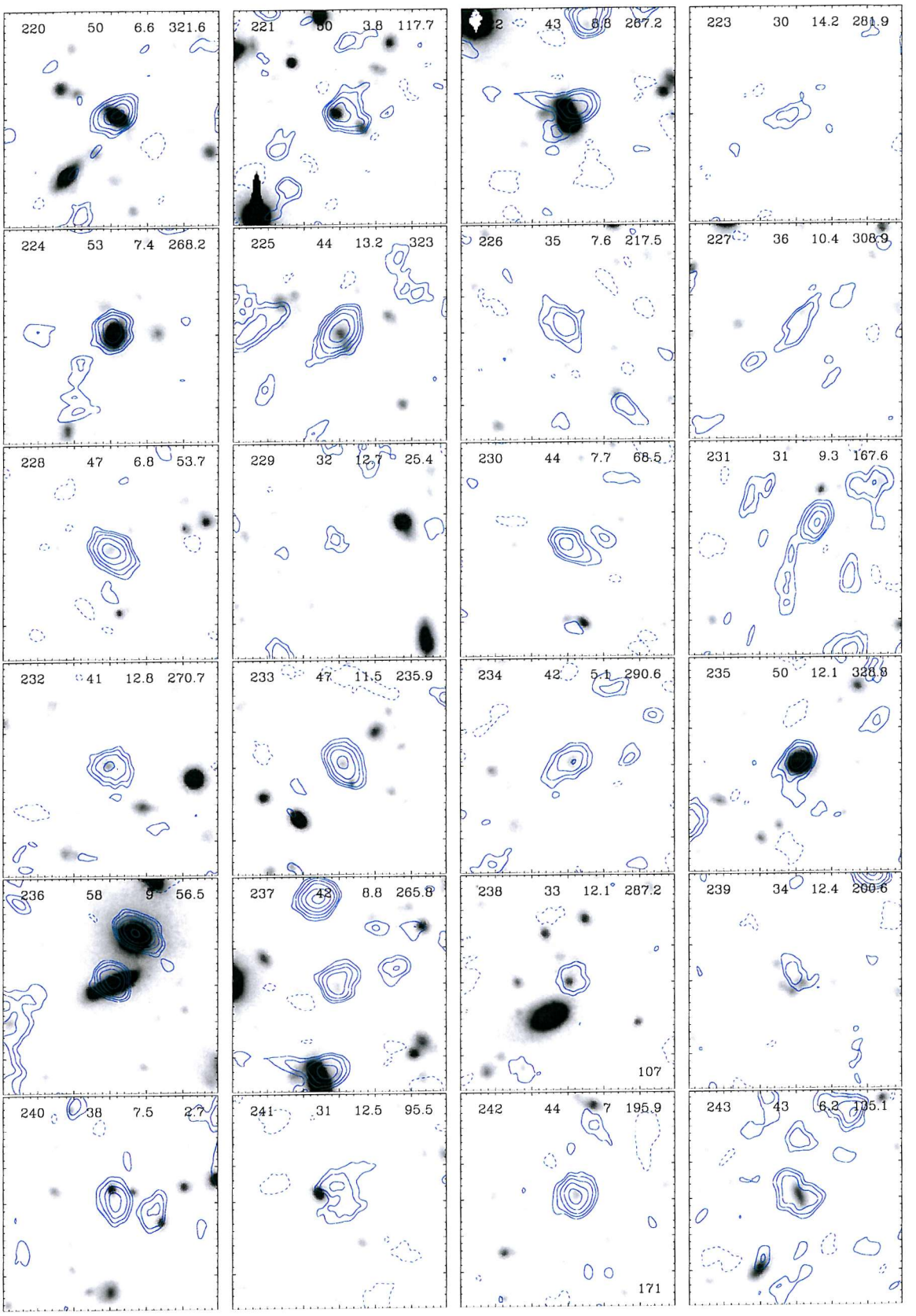
220 50 6.6 321.6
221 50 3.8 117.7
222 43 8.8 287.2
223 30 14.2 281.9
224 53 7.4 268.2
225 44 13.2 323
226 35 7.6 217.5
227 36 10.4 308.9
228 47 6.8 53.7
229 32 12.7 25.4
230 44 7.7 68.5
231 31 9.3 167.6
232 41 12.8 270.7
233 47 11.5 235.9
234 42 5.1 290.6
235 50 12.1 326.8
236 58 9 56.5
237 42 8.8 265.8
238 33 12.1 287.2
107
239 34 12.4 260.6
240 38 7.5 2.7
241 31 12.5 95.5
242 44 7 195.9
171
243 43 6.2 105.1

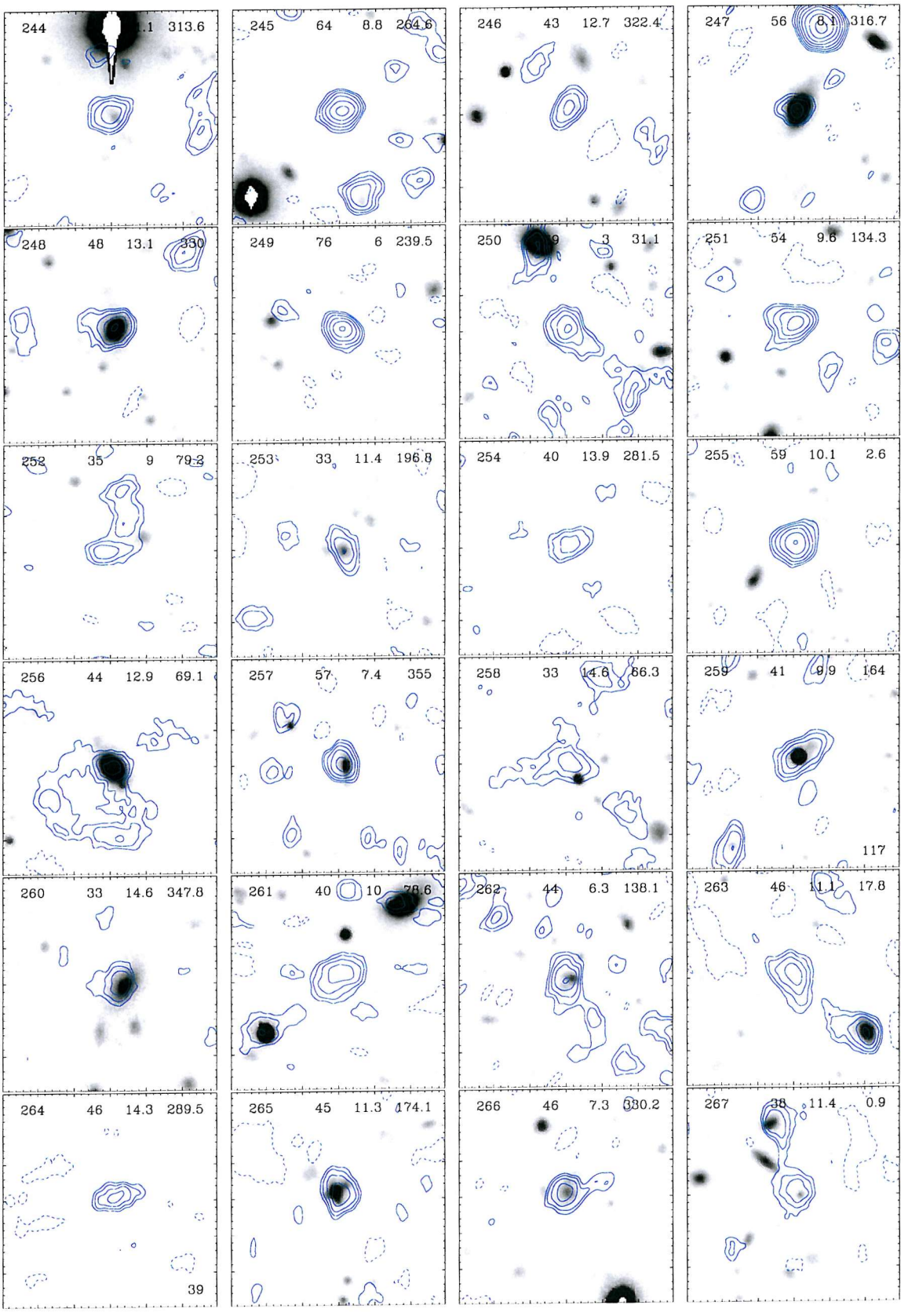
244 313.6
245 64 8.8 264.6
246 43 12.7 322.4
247 56 8.1 316.7
248 48 13.1 330
249 76 6 239.5
250 3 31.1
251 54 9.6 134.3
252 35 9 79.2
253 33 11.4 196.8
254 40 13.9 281.5
255 59 10.1 2.6
256 44 12.9 69.1
257 57 7.4 355
258 33 14.6 66.3
259 41 9.9 164
117
260 33 14.6 347.8
261 40 10 78.6
262 44 6.3 138.1
263 46 11.1 17.8
264 46 14.3 289.5
39
265 45 11.3 174.1
266 46 7.3 330.2
267 38 11.4 0.9

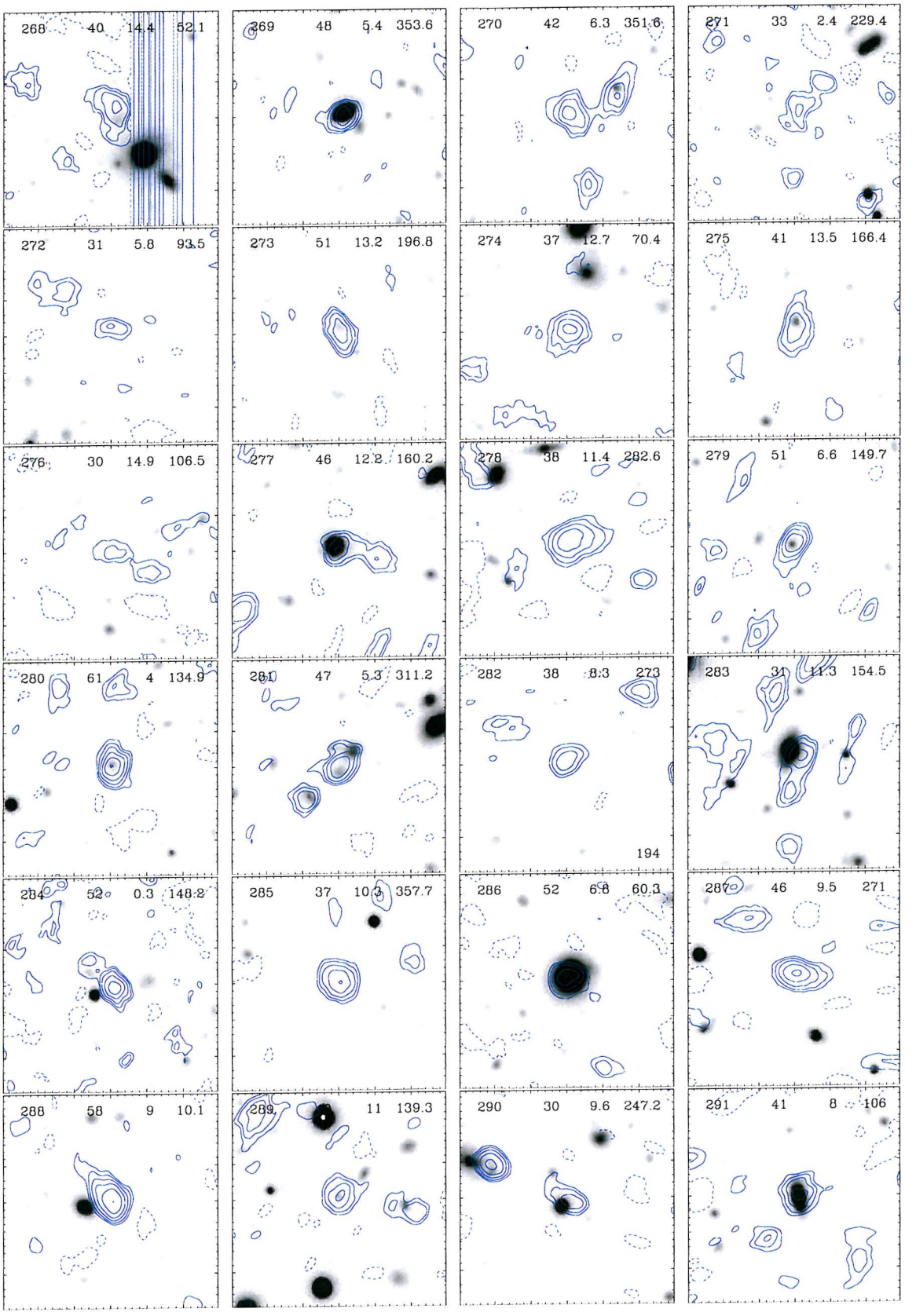
268 40 14.4 52.1
269 48 5.4 353.6
270 42 6.3 351.6
271 33 2.4 229.4
272 31 5.8 93.5
273 51 13.2 196.8
274 37 12.7 70.4
275 41 13.5 166.4
276 30 14.9 106.5
277 46 12.2 160.2
278 38 11.4 282.6
279 51 6.6 149.7
280 61 4 134.9
281 47 5.3 311.2
282 38 8.3 273
194
283 31 11.3 154.5
284 52 0.3 148.2
285 37 10.3 357.7
286 52 6.8 60.3
287 46 9.5 271
288 58 9 10.1
289 11 139.3
290 30 9.6 247.2
291 41 8 106

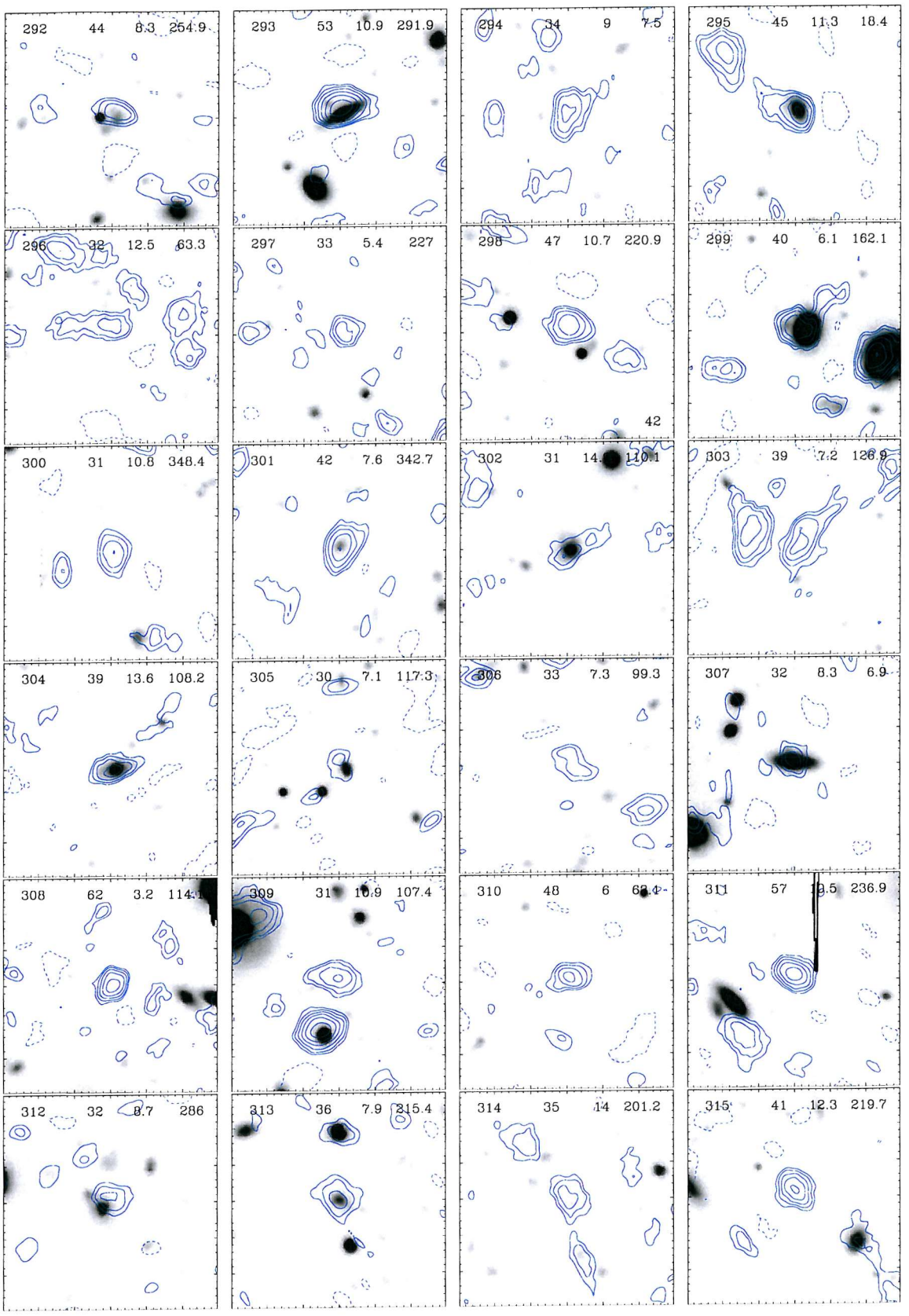
292 44 8.3 254.9
293 53 10.9 291.9
294 34 9 7.5
295 45 11.3 18.4
296 32 12.5 63.3
297 33 5.4 227
298 47 10.7 220.9
42
299 40 6.1 162.1
300 31 10.8 348.4
301 42 7.6 342.7
302 31 14.
303 39 7.2 126.9
304 39 13.6 108.2
305 30 7.1 117.3
306 33 7.3 99.3
307 32 8.3 6.9
308 62 3.2 114.
309 31 10.9 107.4
310 48 6 68.4
311 57 9.5 236.9
312 32 8.7 286
313 36 7.9 215.4
314 35 14 201.2
315 41 12.3 219.7

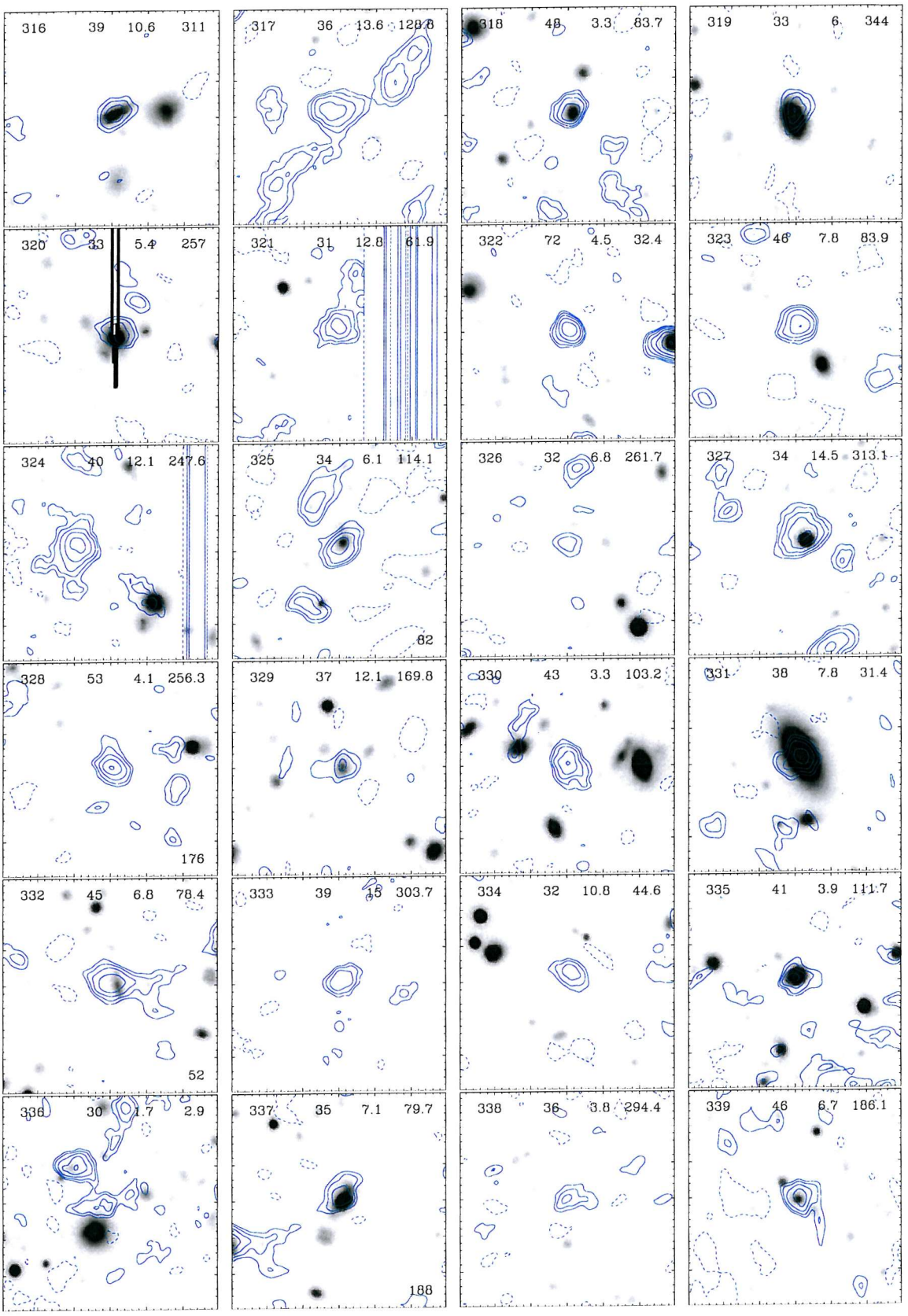
316 39 10.6 311
317 36 13.6 128.8
318 48 3.3 83.7
319 33 6 344
320 33 5.4 257
321 31 12.8 61.9
322 72 4.5 32.4
323 46 7.8 83.9
324 40 12.1 247.6
325 34 6.1 114.1
82
326 32 6.8 261.7
327 34 14.5 313.1
328 53 4.1 256.3
176
329 37 12.1 169.8
330 43 3.3 103.2
331 38 7.8 31.4
332 45 6.8 78.4
52
333 39 15 303.7
334 32 10.8 44.6
335 41 3.9 111.7
336 30 1.7 2.9
337 35 7.1 79.7
188
338 36 3.8 294.4
339 46 6.7 186.1

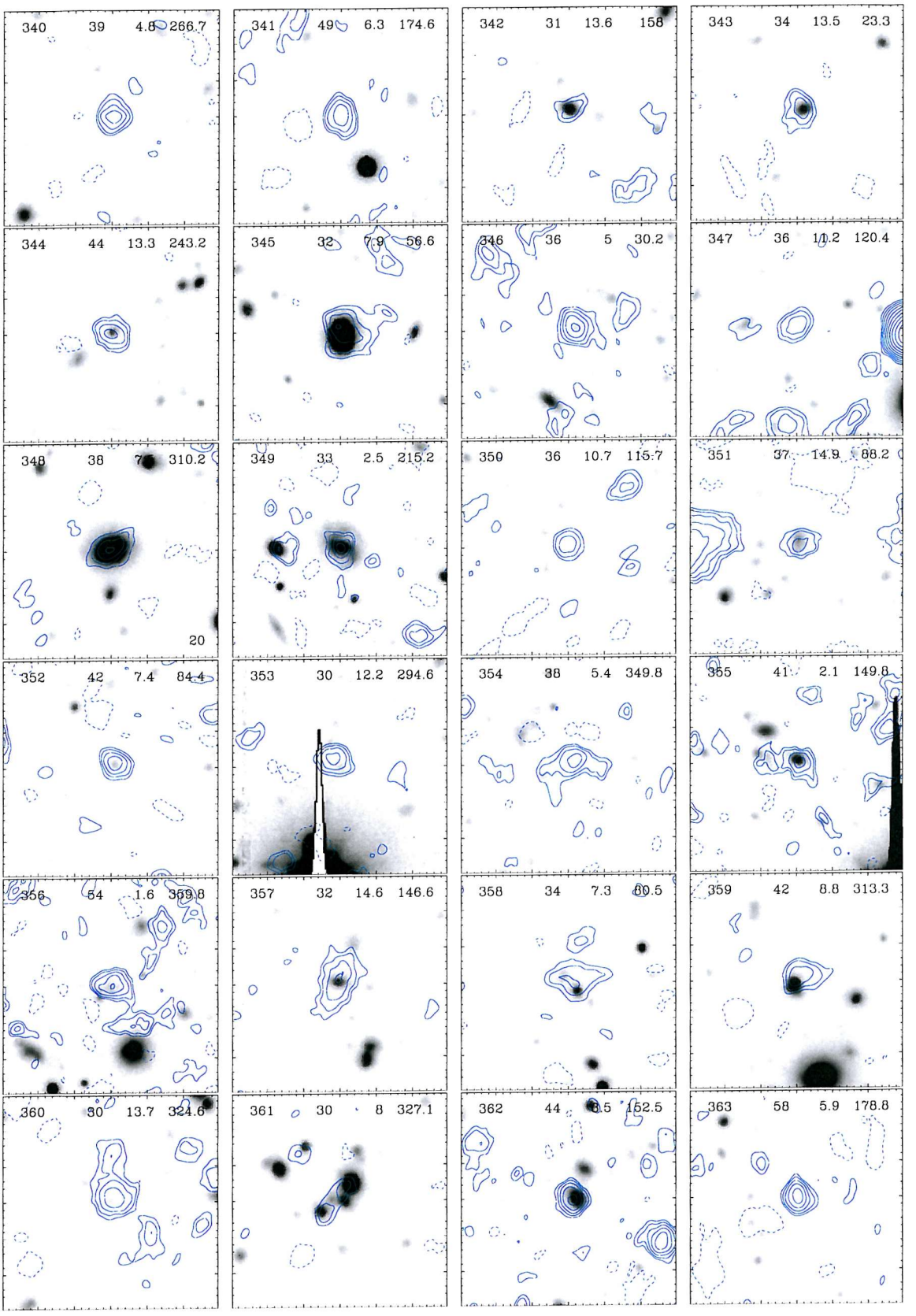
340 39 4.8 266.7
341 49 6.3 174.6
342 31 13.6 158
343 34 13.5 23.3
344 44 13.3 243.2
345 32 7.9 56.6
346 36 5 30.2
347 36 10.2 120.4
348 38 7 310.2
20
349 33 2.5 215.2
350 36 10.7 115.7
351 37 14.9 88.2
352 42 7.4 84.4
353 30 12.2 294.6
354 38 5.4 349.8
355 41 2.1 149.8
356 54 1.6 359.8
357 32 14.6 146.6
358 34 7.3 80.5
359 42 8.8 313.3
360 30 13.7 324.6
361 30 8 327.1
362 44 8.5 152.5
363 58 5.9 178.8

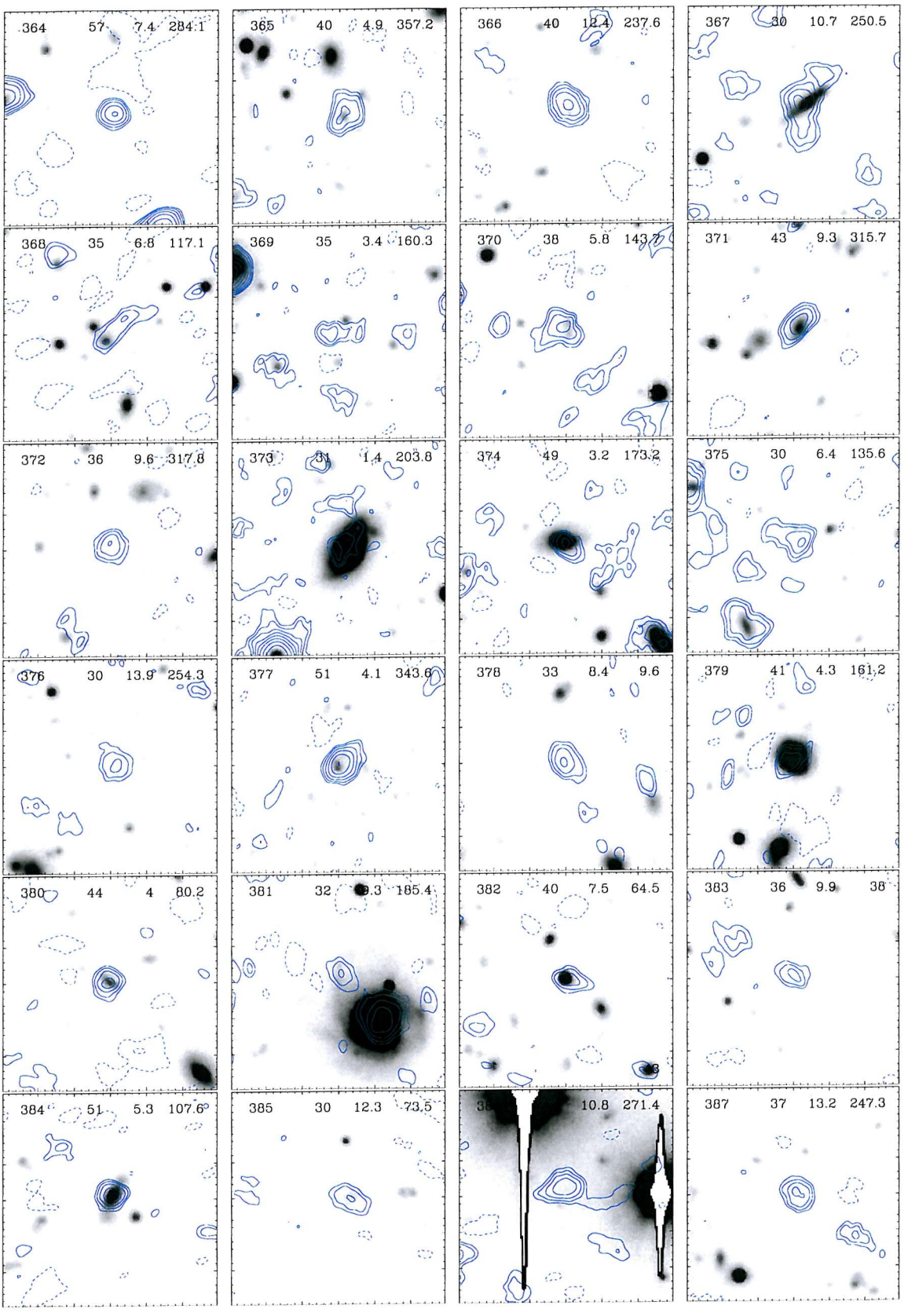
364 57 7.4 284.1
365 40 4.9 357.2
366 40 12.4 237.6
367 30 10.7 250.5
368 35 6.8 117.1
369 35 3.4 160.3
370 38 5.8 143.7
371 43 9.3 315.7
372 36 9.6 317.8
373 31 1.4 203.8
374 49 3.2 173.2
375 30 6.4 135.6
376 30 13.9 254.3
377 51 4.1 343.6
378 33 8.4 9.6
379 41 4.3 161.2
380 44 4 80.2
381 32 9.3 185.4
382 40 7.5 64.5
383 36 9.9 38
384 51 5.3 107.6
385 30 12.3 73.5
10.8 271.4
387 37 13.2 247.3

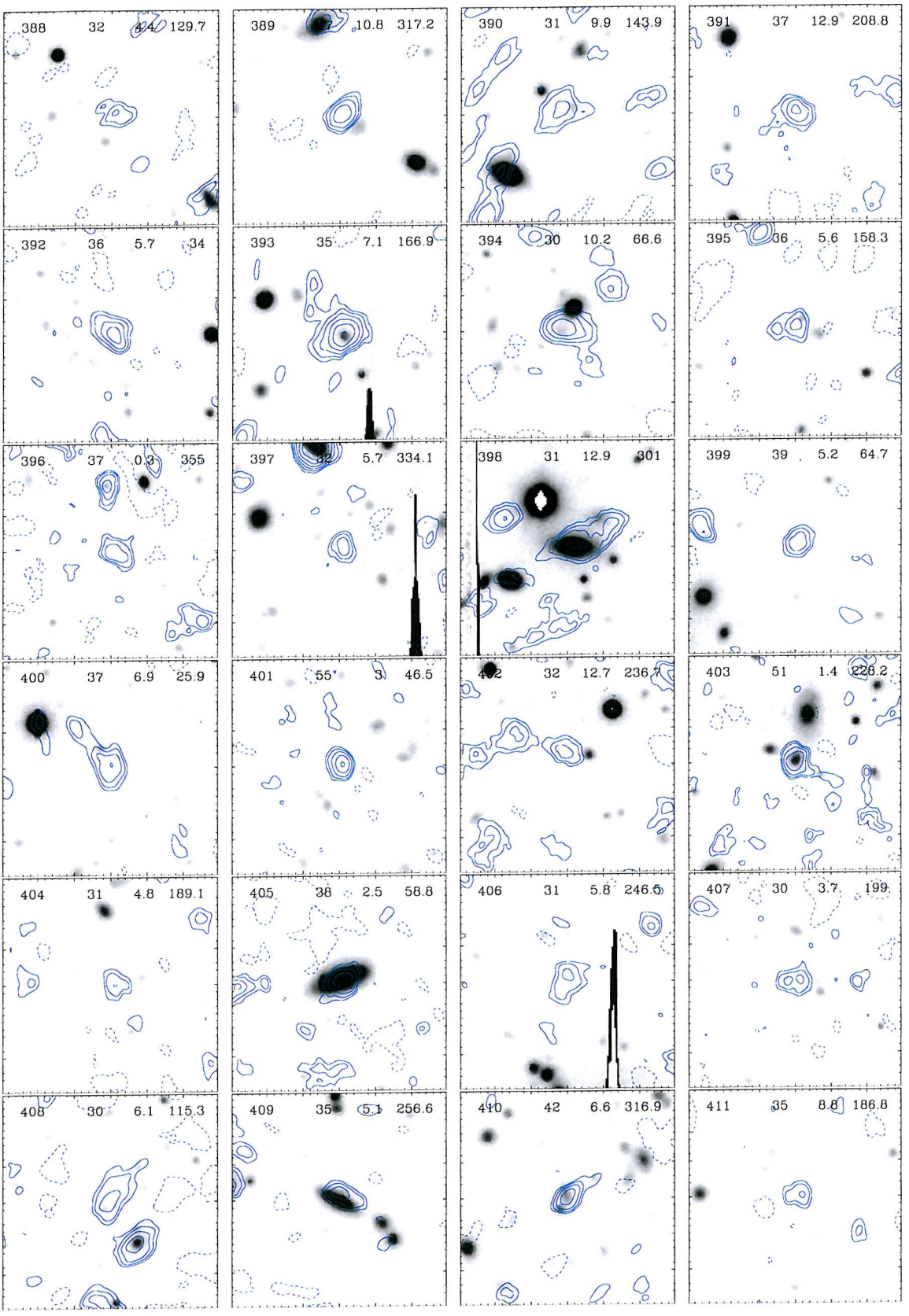
388 32 4.4 129.7
389 10.8 317.2
390 31 9.9 143.9
391 37 12.9 208.8
392 36 5.7 34
393 35 7.1 166.9
394 30 10.2 66.6
395 36 5.6 158.3
396 37 0.3 355
397 5.7 334.1
398 31 12.9 301
399 39 5.2 64.7
400 37 6.9 25.9
401 55 3 46.5
403 51 1.4 226.2
404 31 4.8 189.1
405 38 2.5 58.8
406 31 5.8 246.5
407 30 3.7 199
408 30 6.1 115.3
409 35 5.1 256.6
410 42 6.6 316.9
411 35 8.8 186.8

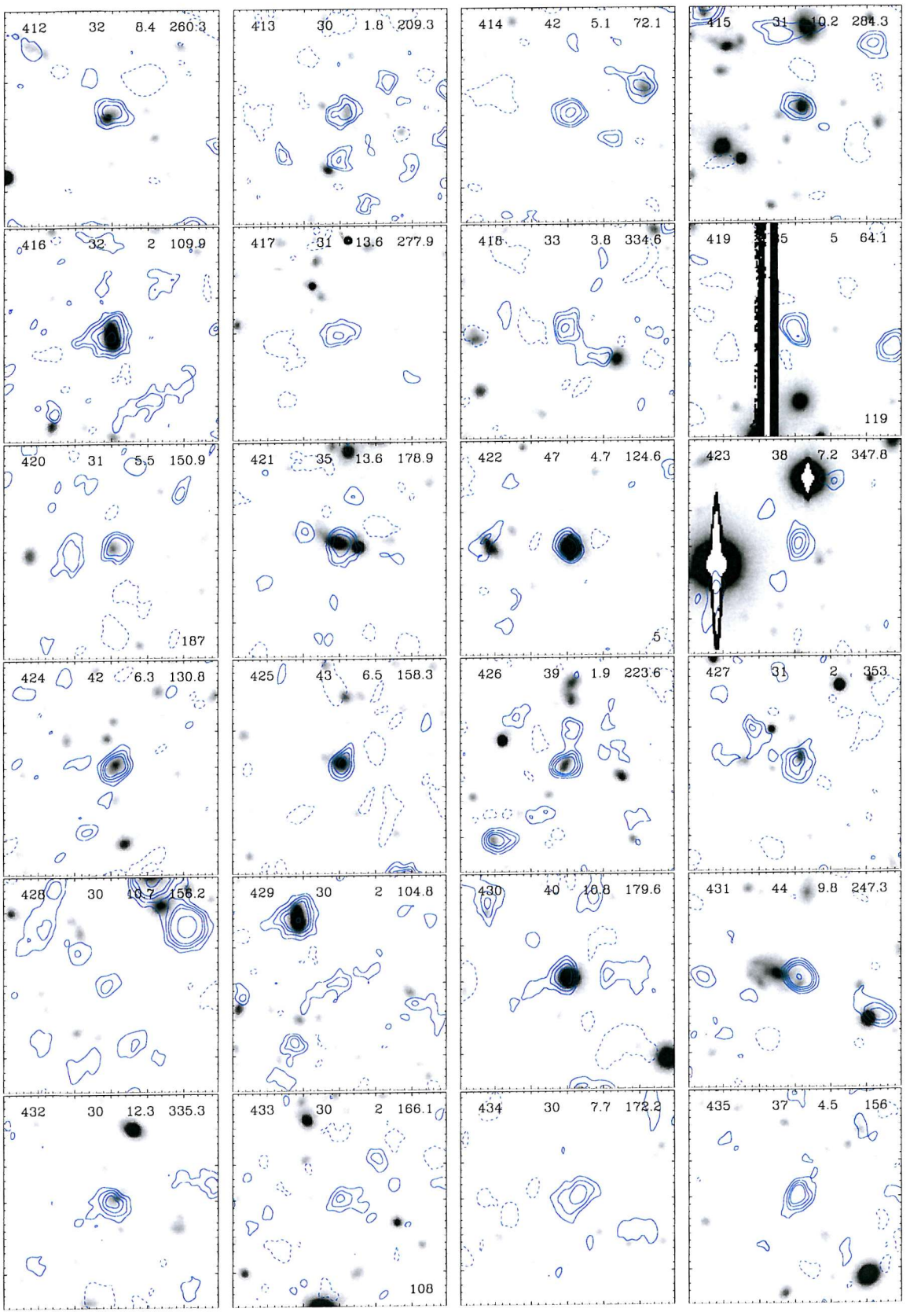
412 32 8.4 260.3
413 30 1.8 209.3
414 42 5.1 72.1
415 31 10.2 284.3
416 32 2 109.9
417 31 13.6 277.9
418 33 3.8 334.6
419 5 64.1
119
420 31 5.5 150.9
187
421 35 13.6 178.9
422 47 4.7 124.6
5
423 38 7.2 347.8
424 42 6.3 130.8
425 43 6.5 158.3
426 39 1.9 223.6
427 31 2 353
428 30 10.7 156.2
429 30 2 104.8
430 40 10.8 179.6
431 44 9.8 247.3
432 30 12.3 335.3
433 30 2 166.1
108
434 30 7.7 172.2
435 37 4.5 156

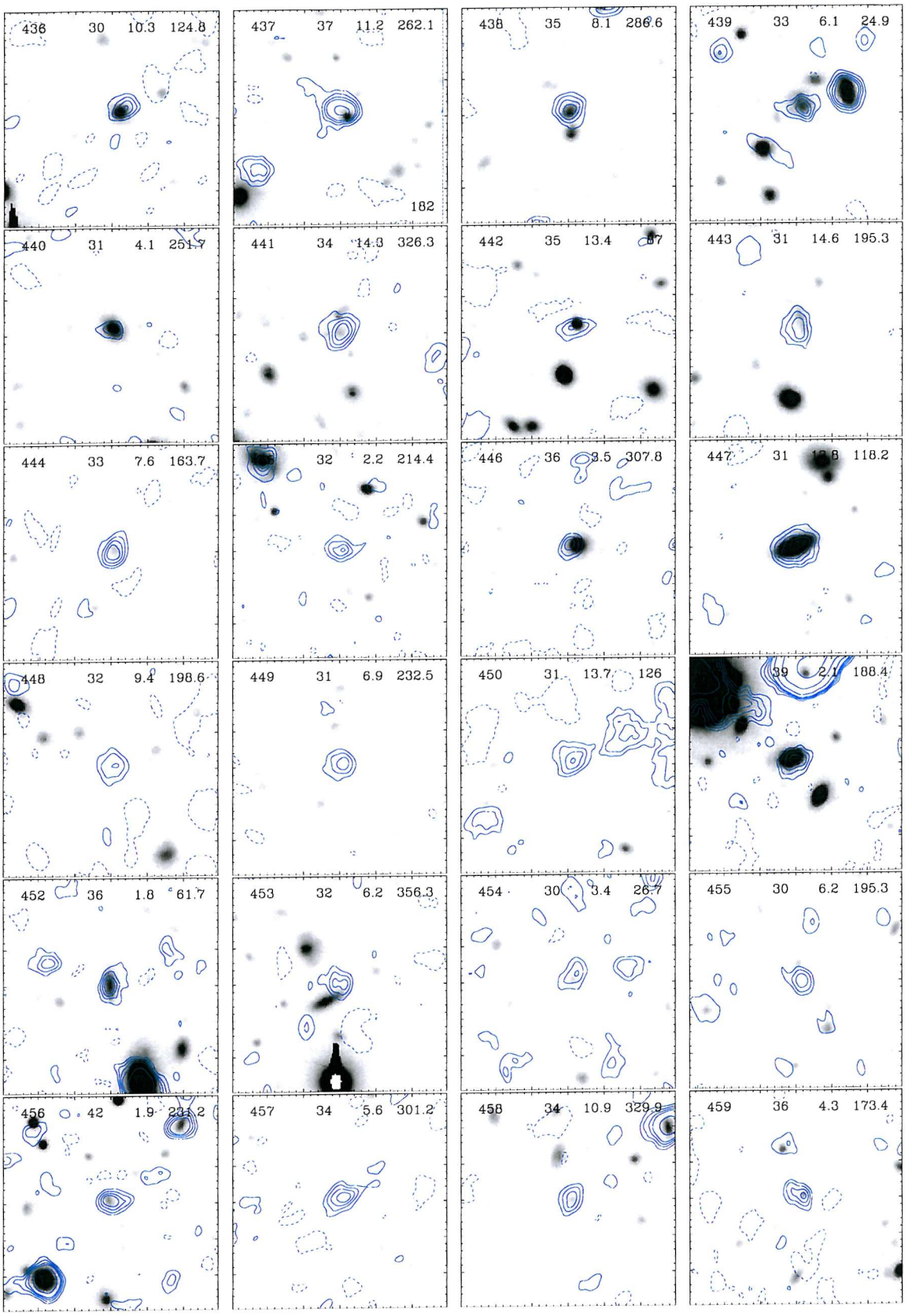
436 30 10.3 124.8
437 37 11.2 262.1
182
438 35 8.1 286.6
439 33 6.1 24.9
440 31 4.1 251.7
441 34 14.3 326.3
442 35 13.4 87
443 31 14.6 195.3
444 33 7.6 163.7
32 2.2 214.4
446 36 3.5 307.8
447 31 188 118.2
448 32 9.4 198.6
449 31 6.9 232.5
450 31 13.7 126
39 2.1 188.4
452 36 1.8 61.7
453 32 6.2 356.3
454 30 3.4 26.7
455 30 6.2 195.3
456 42 1.9 231.2
457 34 5.6 301.2
458 34 10.9 329.9
459 36 4.3 173.4

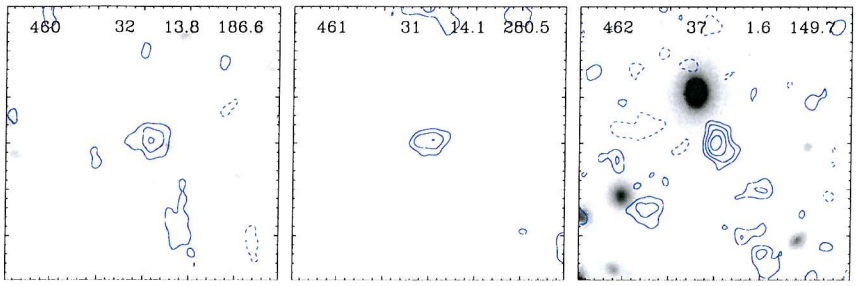
460 32 13.8 186.6
461 31 14.1 280.5
462 37 1.6 149.7

## 7.2 Optical 'postage-stamps' with radio contours of all the *Chandra* sources

Here 'postage-stamp' images of the $R$–band counterparts to all 214 X-ray sources from *Chandra* catalogue paper (M$^{c}$Hardy et al., 2002a) are presented with contours of the radio flux superimposed. Each postage-stamp is $30'' \times 30''$ square. The radio contours are in multiples of the 7.5 $\mu$Jy/beam rms noise; -2[2], 2, 3, 4, 5, 8, 16, 32, 64, 128, 256, 512, 1024. They are taken from the naturally weighted, combined A and B-configuration display maps figure-2.5 and its flanking fields. The optical data are from the Subaru Suprimecam $R$–band deep one hour image discussed in Chapter 4 which has a detection limit of $R \sim 27$ (for non-confused sources). The 4 numbers at the top of each image are the *Chandra* source number (sources are order of decreasing total X-ray flux), the *Chandra* off-axis angle in arcminutes, the source's distance from the centre of the radio field in arcminutes and the angle counter-clockwise from north to the centre of the radio field from the X-ray source.

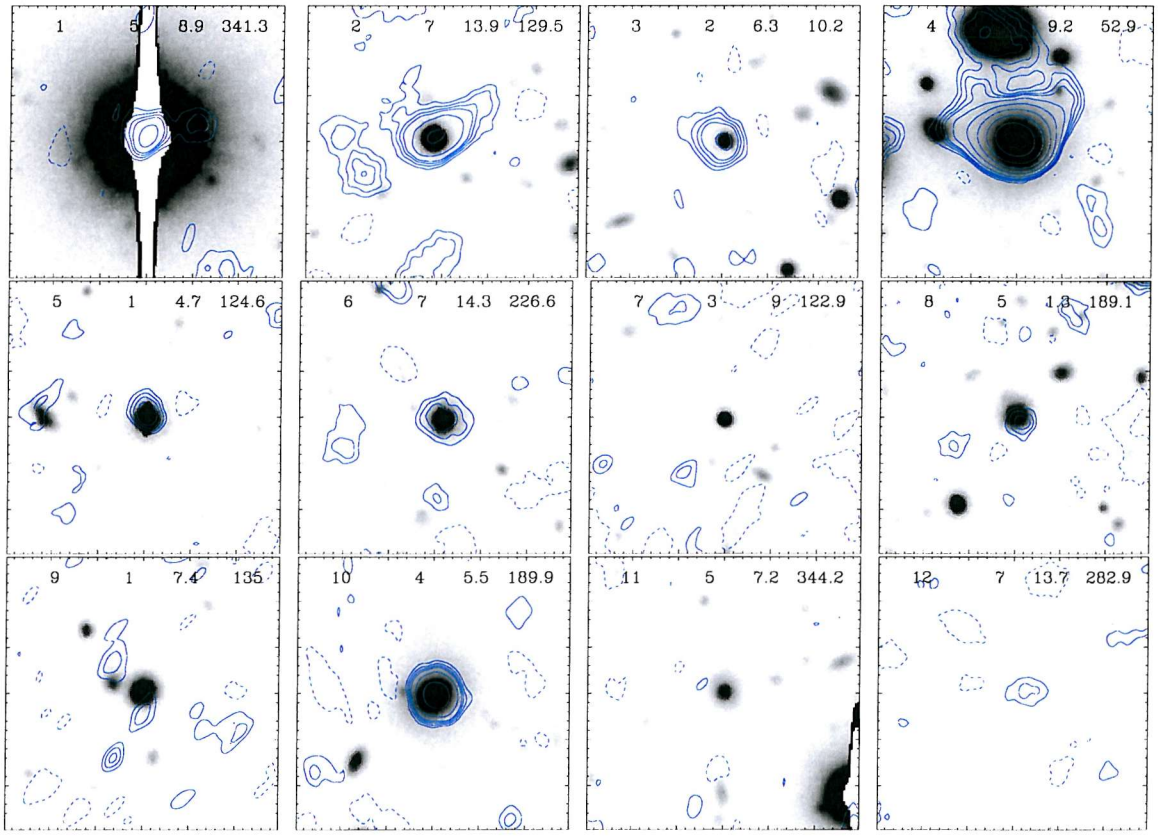


[2]Negative contours are indicated by a dashed line.

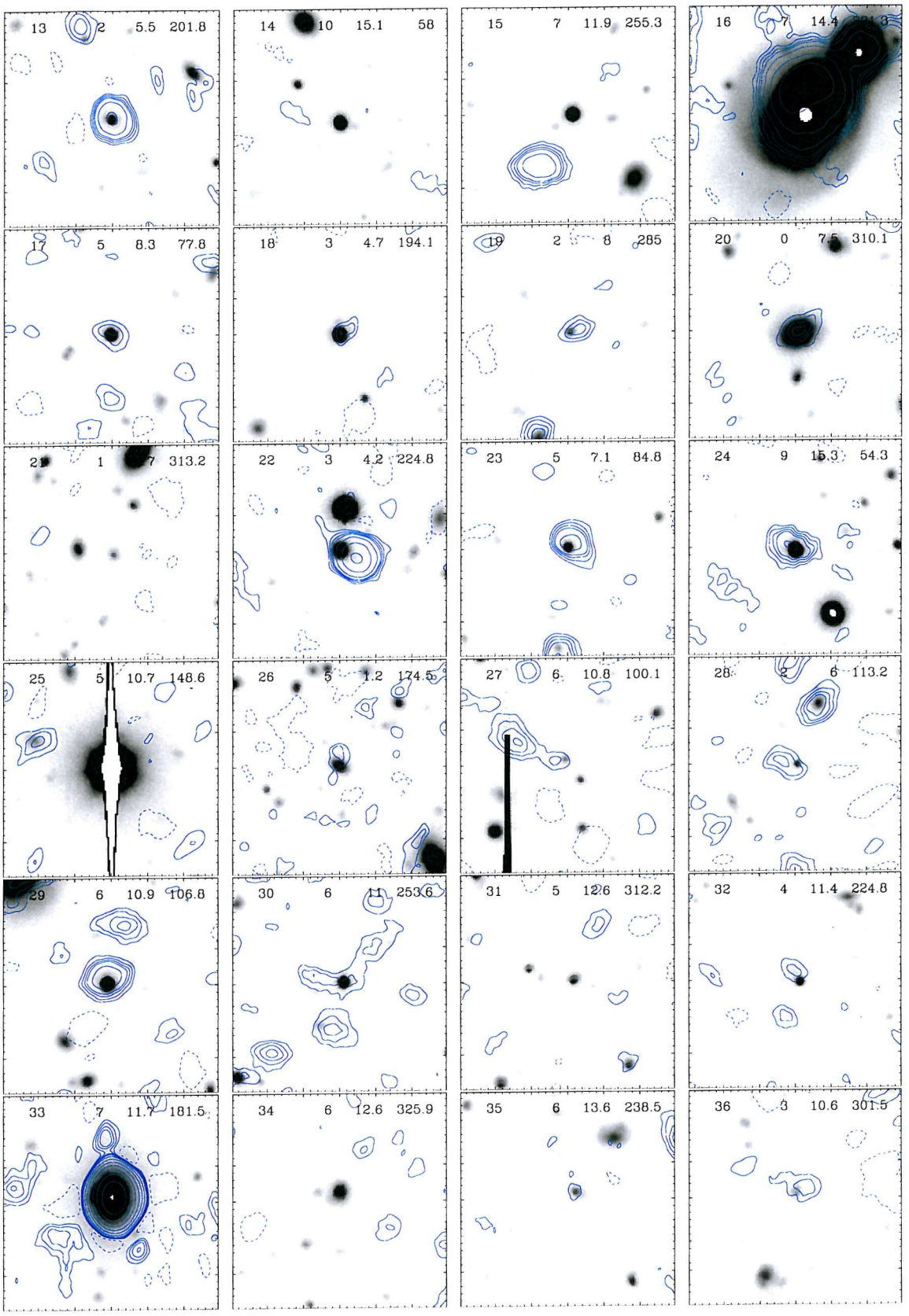
13 2 5.5 201.8
14 10 15.1 58
15 7 11.9 255.3
16 7 14.4
17 5 8.3 77.8
18 3 4.7 194.1
19 2 8 285
20 0 7.5 310.1
21 1 7 313.2
22 3 4.2 224.8
23 5 7.1 84.8
24 9 15.3 54.3
25 5 10.7 148.6
26 5 1.2 174.5
27 6 10.8 100.1
28 2 6 113.2
29 6 10.9 106.8
30 6 11 253.6
31 5 12.6 312.2
32 4 11.4 224.8
33 7 11.7 181.5
34 6 12.6 325.9
35 6 13.6 238.5
36 3 10.6 301.5

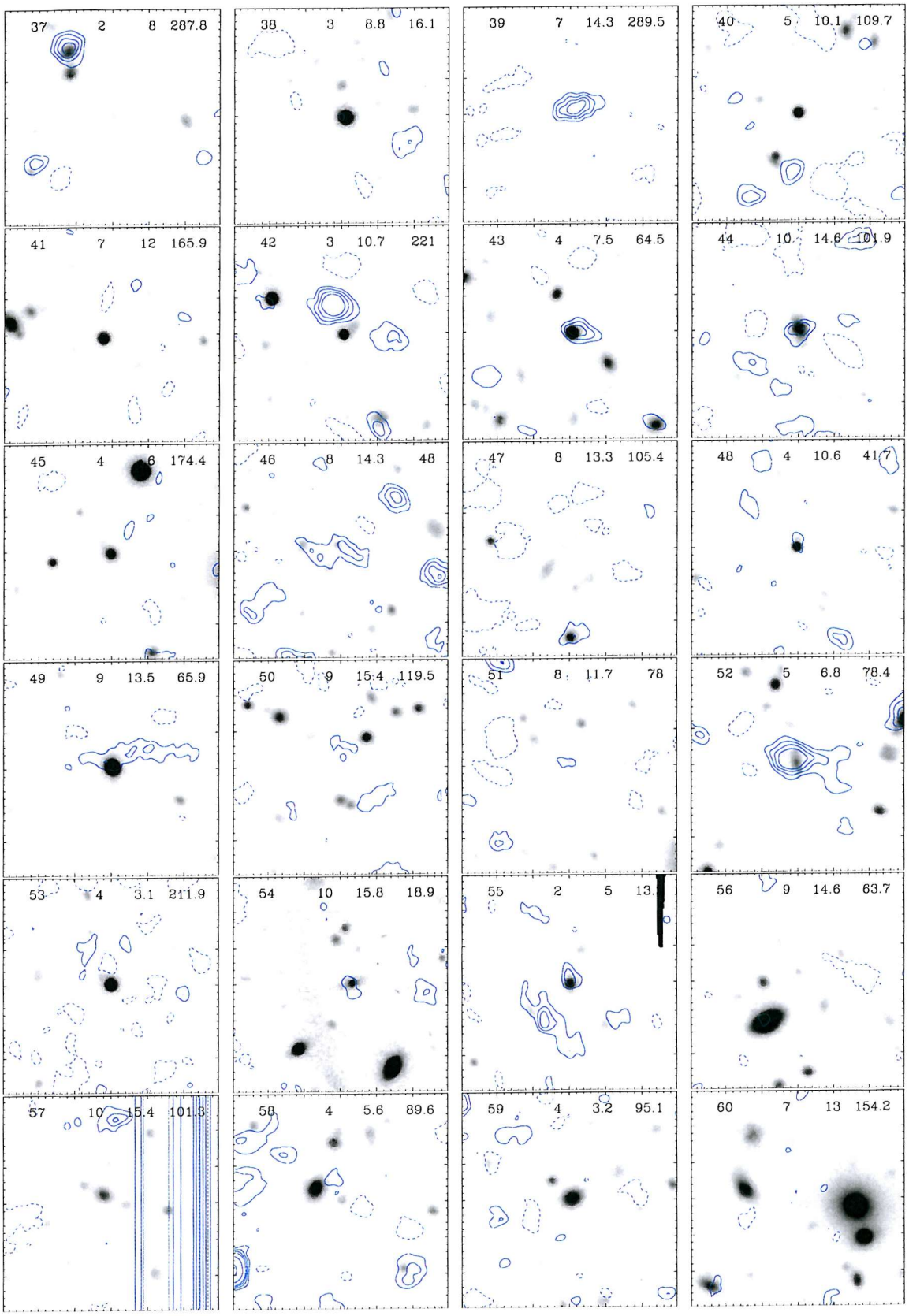
37 2 8 287.8
38 3 8.8 16.1
39 7 14.3 289.5
40 5 10.1 109.7
41 7 12 165.9
42 3 10.7 221
43 4 7.5 64.5
44 10 14.6 101.9
45 4 6 174.4
46 8 14.3 48
47 8 13.3 105.4
48 4 10.6 41.7
49 9 13.5 65.9
50 9 15.4 119.5
51 8 11.7 78
52 5 6.8 78.4
53 4 3.1 211.9
54 10 15.8 18.9
55 2 5 13.
56 9 14.6 63.7
57 10 15.4 101.3
58 4 5.6 89.6
59 4 3.2 95.1
60 7 13 154.2

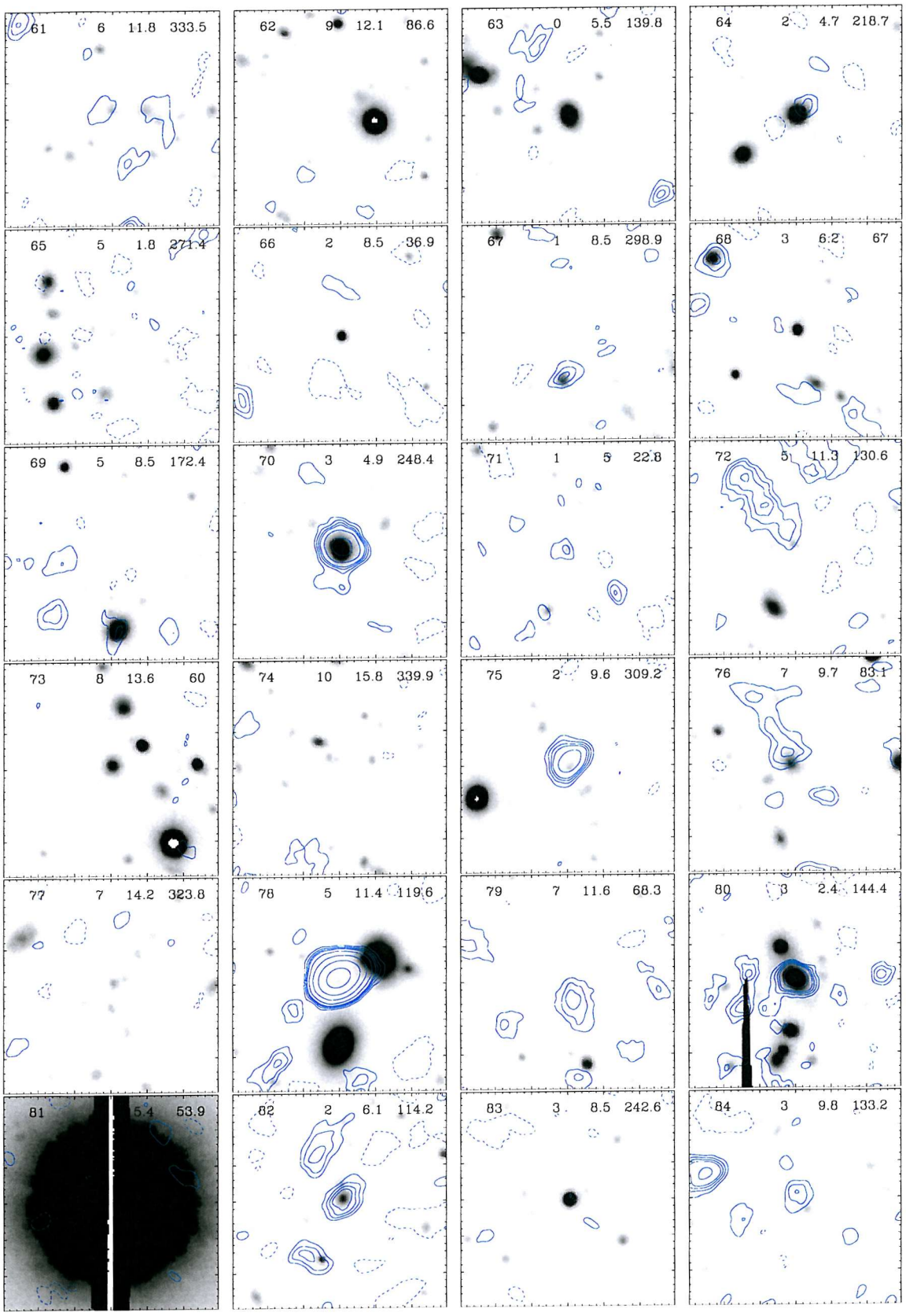
61 6 11.8 333.5
62 9 12.1 86.6
63 0 5.5 139.8
64 2 4.7 218.7
65 5 1.8 271.4
66 2 8.5 36.9
67 1 8.5 298.9
68 3 6.2 67
69 5 8.5 172.4
70 3 4.9 248.4
71 1 5 22.8
72 5 11.3 130.6
73 8 13.6 60
74 10 15.8 339.9
75 2 9.6 309.2
76 7 9.7 83.1
77 7 14.2 323.8
78 5 11.4 119.6
79 7 11.6 68.3
80 3 2.4 144.4
81 5.4 53.9
82 2 6.1 114.2
83 3 8.5 242.6
84 3 9.8 133.2

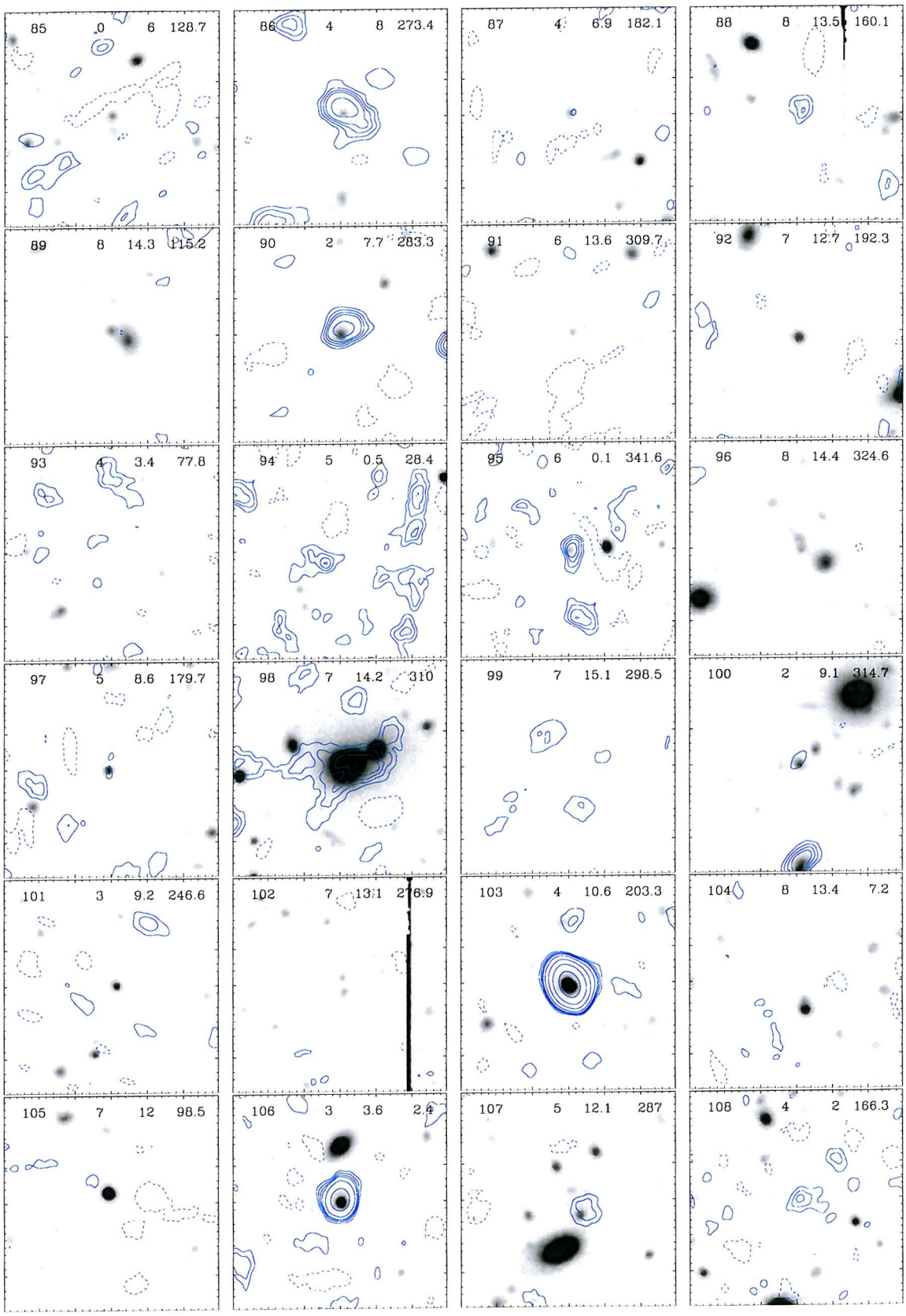
85 0 6 128.7
86 4 8 273.4
87 4 6.9 182.1
88 8 13.5 160.1
89 8 14.3 115.2
90 2 7.7 283.3
91 6 13.6 309.7
92 7 12.7 192.3
93 4 3.4 77.8
94 5 0.5 28.4
95 6 0.1 341.6
96 8 14.4 324.6
97 5 8.6 179.7
98 7 14.2 310
99 7 15.1 298.5
100 2 9.1 314.7
101 3 9.2 246.6
102 7 13.1 276.9
103 4 10.6 203.3
104 8 13.4 7.2
105 7 12 98.5
106 3 3.6 2.4
107 5 12.1 287
108 4 2 166.3

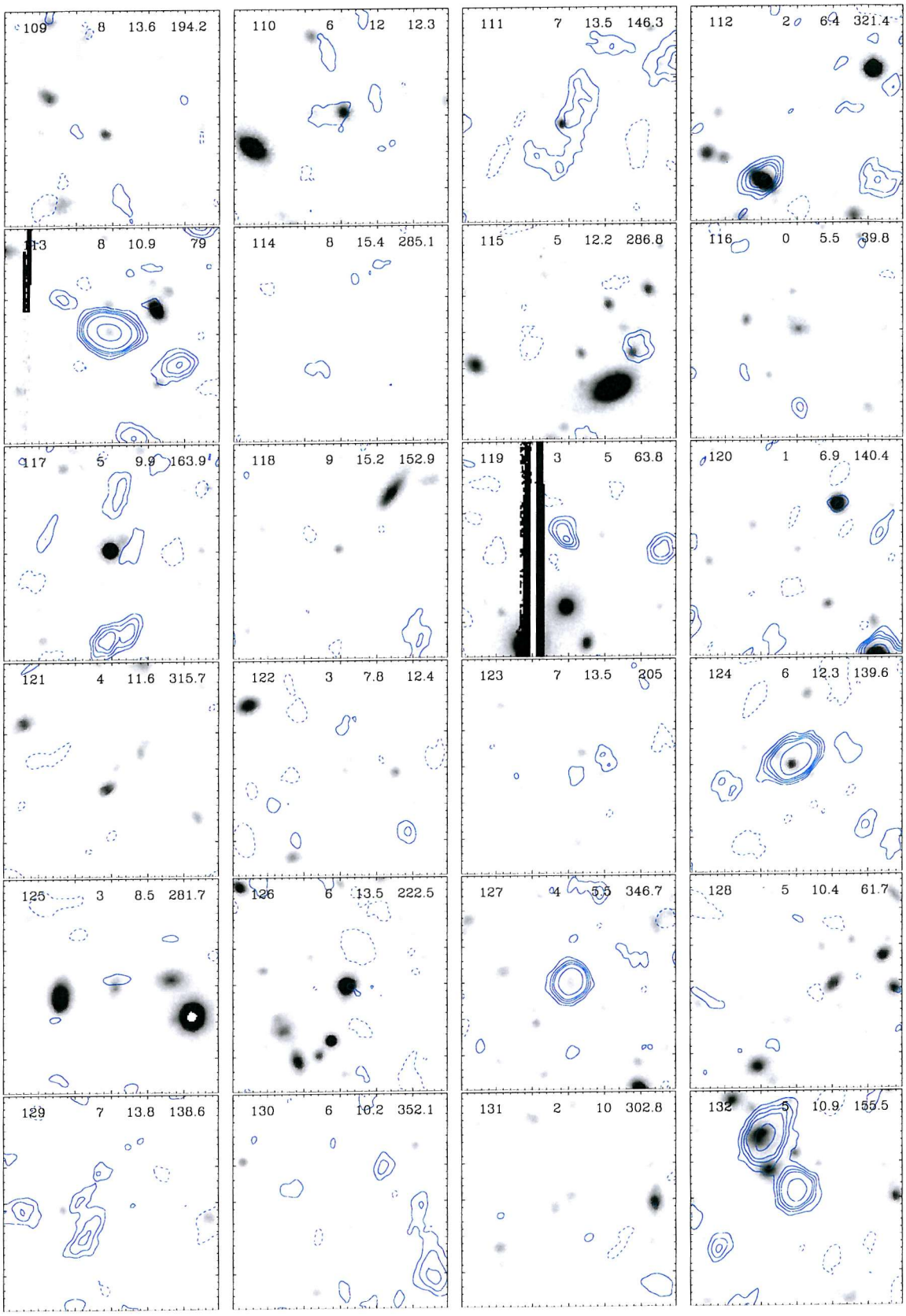
109 8 13.6 194.2
110 6 12 12.3
111 7 13.5 146.3
112 2 6.4 321.4
113 8 10.9 79
114 8 15.4 285.1
115 5 12.2 286.8
116 0 5.5 39.8
117 5 9.9 163.9
118 9 15.2 152.9
119 3 5 63.8
120 1 6.9 140.4
121 4 11.6 315.7
122 3 7.8 12.4
123 7 13.5 205
124 6 12.3 139.6
125 3 8.5 281.7
126 6 13.5 222.5
127 4 5.5 346.7
128 5 10.4 61.7
129 7 13.8 138.6
130 6 10.2 352.1
131 2 10 302.8
132 5 10.9 155.5

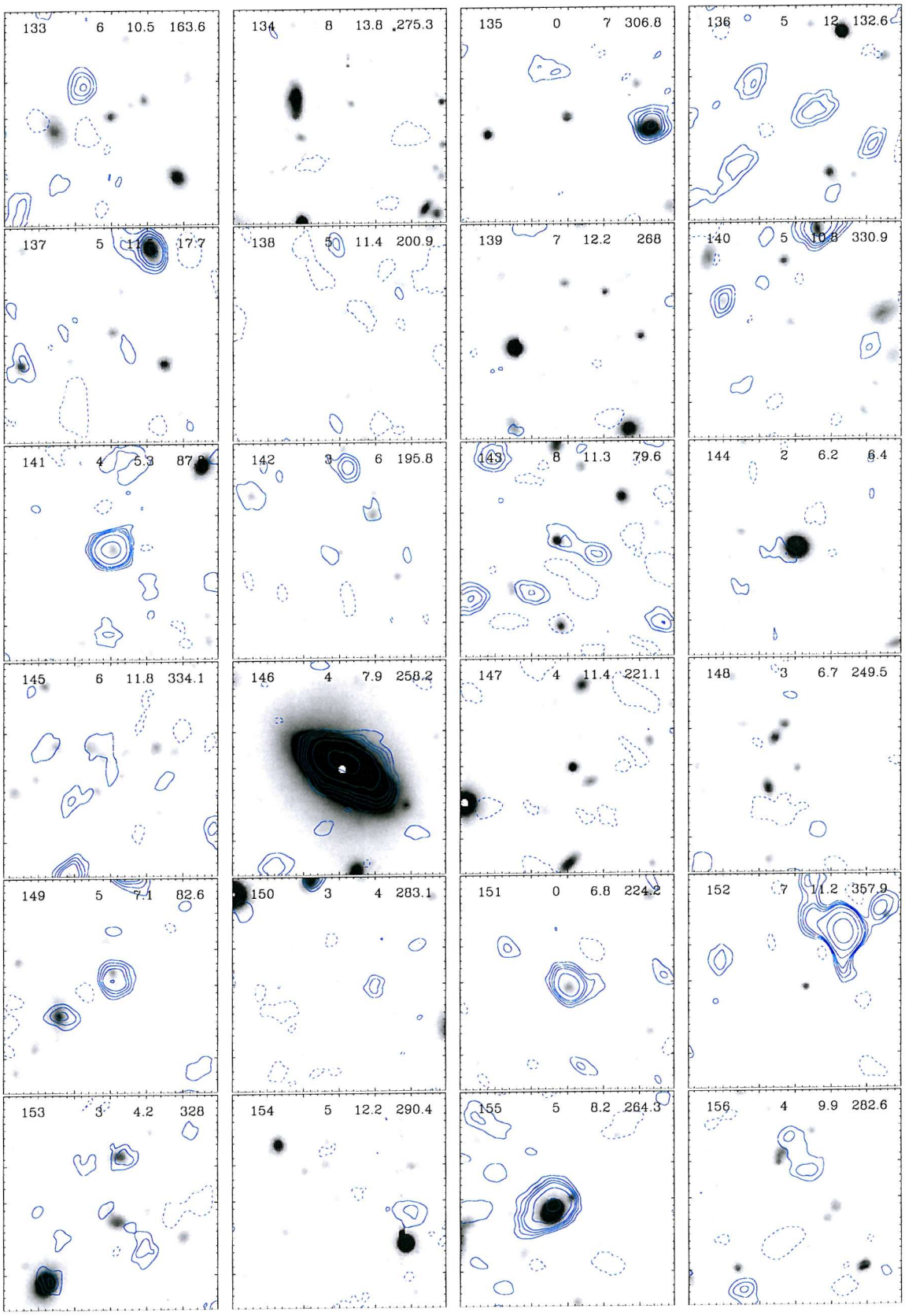
133 6 10.5 163.6
134 8 13.8 275.3
135 0 7 306.8
136 5 12 132.6
137 5 11 17.7
138 5 11.4 200.9
139 7 12.2 268
140 5 10.8 330.9
141 4 5.3 87.8
142 3 6 195.8
143 8 11.3 79.6
144 2 6.2 6.4
145 6 11.8 334.1
146 4 7.9 258.2
147 4 11.4 221.1
148 3 6.7 249.5
149 5 7.1 82.6
150 3 4 283.1
151 0 6.8 224.2
152 7 11.2 357.9
153 3 4.2 328
154 5 12.2 290.4
155 5 8.2 264.3
156 4 9.9 282.6

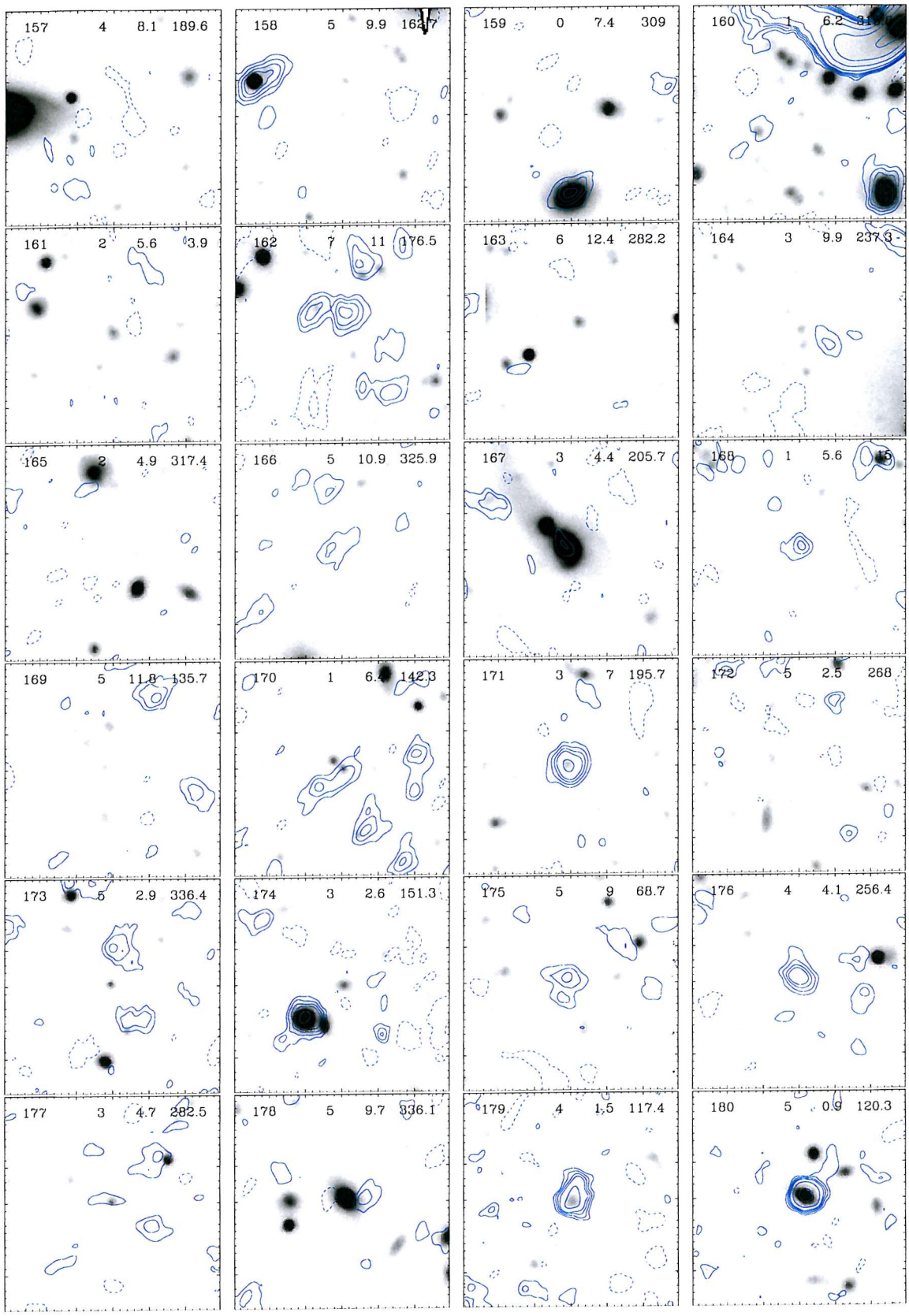
157 4 8.1 189.6
158 5 9.9 162.7
159 0 7.4 309
160 1 6.2 81.3
161 2 5.6 3.9
162 7 11 176.5
163 6 12.4 282.2
164 3 9.9 237.3
165 2 4.9 317.4
166 5 10.9 325.9
167 3 4.4 205.7
168 1 5.6 15
169 5 11.8 135.7
170 1 6.4 142.3
171 3 7 195.7
172 5 2.5 268
173 5 2.9 336.4
174 3 2.6 151.3
175 5 9 68.7
176 4 4.1 256.4
177 3 4.7 282.5
178 5 9.7 336.1
179 4 1.5 117.4
180 5 0.9 120.3

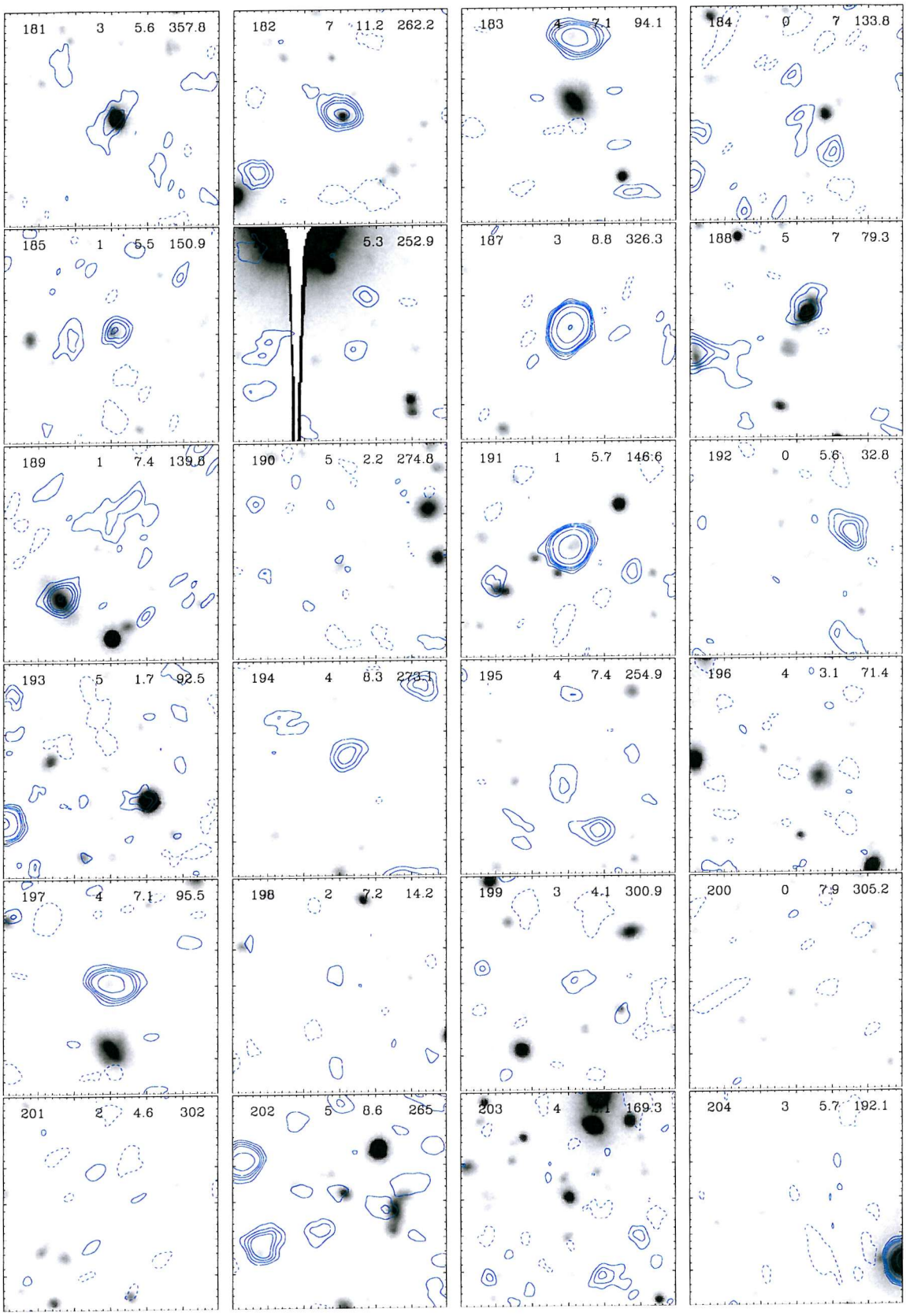
181 3 5.6 357.8
182 7 11.2 262.2
183 4 7.1 94.1
184 0 7 133.8
185 1 5.5 150.9
5.3 252.9
187 3 8.8 326.3
188 5 7 79.3
189 1 7.4 139.8
190 5 2.2 274.8
191 1 5.7 146.6
192 0 5.6 32.8
193 5 1.7 92.5
194 4 8.3 273.1
195 4 7.4 254.9
196 4 3.1 71.4
197 4 7.1 95.5
198 2 7.2 14.2
199 3 4.1 300.9
200 0 7.9 305.2
201 2 4.6 302
202 5 8.6 265
203 4 169.3
204 3 5.7 192.1

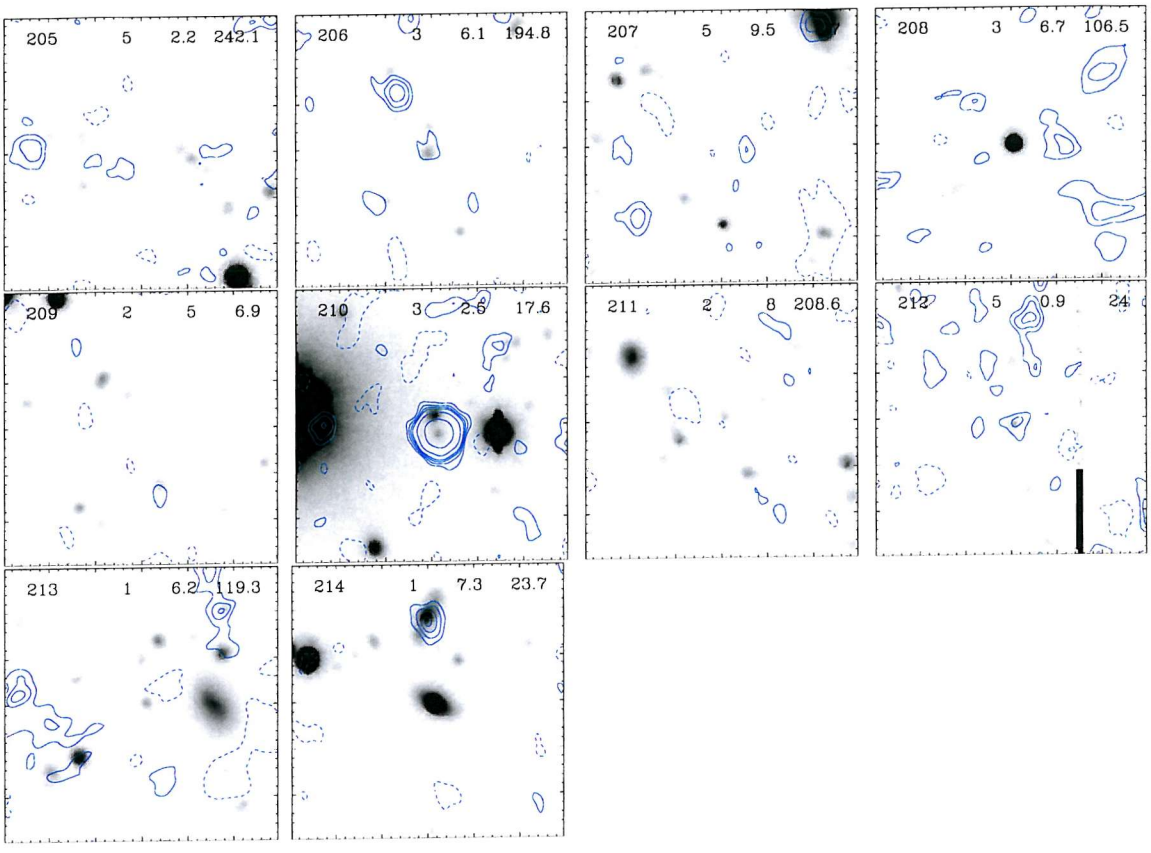
205 5 2.2 242.1
206 3 6.1 194.8
207 5 9.5
208 3 6.7 106.5
209 2 5 6.9
210 3 2.6 17.6
211 2 8 208.6
212 5 0.9 24
213 1 6.2 119.3
214 1 7.3 23.7

# Bibliography

Almaini, O., Shanks, T., Boyle, B. J., Griffiths, R. E., Roche, N., Stewart, G. C., and Georgantopoulos, I.: 1996, *MNRAS* **282**, 295
Antonucci, R.: 1993, *ARA&A* **31**, 473
Antonucci, R. R. J. and Miller, J. S.: 1985, *ApJ* **297**, 621
Bahcall, J. N., Kirhakos, S., and Schneider, D. P.: 1995, *ApJ* **450**, 486
Bauer, F. E., Alexander, D. M., Brandt, W. N., Hornschemeier, A. E., Vignali, C., Garmire, G. P., and Schneider, D. P.: 2002, *ApJLinprep.*
Benn, C. R., Rowan-Robinson, M., McMahon, R. G., Broadhurst, T. J., and Lawrence, A.: 1993, *MNRAS* **263**, 98
Berger, E.: 2002, *ApJ* **572**, 503
Bertin, E. and Arnouts, S.: 1996, *A&AS* **117**, 393
Boyle, B. J., Griffiths, R. E., Shanks, T., Stewart, G. C., and Georgantopoulos, I.: 1993, *MNRAS* **260**, 49
Boyle, B. J., Shanks, T., and Peterson, B. A.: 1988, *MNRAS* **235**, 935
Briggs, D. S.: 1995, *American Astronomical Society Meeting* **27**, 1444
Brinkmann, W., Laurent-Muehleisen, S. A., Voges, W., Siebert, J., Becker, R. H., Brotherton, M. S., White, R. L., and Gregg, M. D.: 2000, *A&A* **356**, 445
Broadhurst, T. J., Ellis, R. S., Koo, D. C., and Szalay, A. S.: 1990, *Nat* **343**, 726
Bruzual A., G. and Charlot, S.: 1993, *ApJ* **405**, 538
Cash, W.: 1979, *ApJ* **228**, 939
Ciliegi, P., McMahon, R. G., Miley, G., Gruppioni, C., Rowan-Robinson, M., Cesarsky, C., Danese, L., Franceschini, A., Genzel, R., Lawrence, A., Lemke, D., Oliver, S., Puget, J.-L., and Rocca-Volmerange, B.: 1999, *MNRAS* **302**, 222
Condon, J. J.: 1992, *ARA&A* **30**, 575
Condon, J. J.: 1997, *PASP* **109**, 166
Fanaroff, B. L. and Riley, J. M.: 1974, *MNRAS* **167**, 31P
Freyer, C.: 2002, *A Knowledgebase for Extragalactic Astronomy and Cosmology*
Fukugita, M., Shimasaku, K., and Ichikawa, T.: 1995, *PASP* **107**, 945
Georgakakis, A., Mobasher, B., Cram, L., Hopkins, A., Lidman, C., and Rowan-Robinson, M.: 1999, *MNRAS* **306**, 708
Ghigo, F. D.: 2002, *Personal Website*
Greenstein, J. L. and Matthews, T. A.: 1963, *AJ* **68**, 279
Greisen: 1999, *The* AIPS *cookbook*
Gruppioni, C., Ciliegi, P., Rowan-Robinson, M., Cram, L., Hopkins, A., Cesarsky,

C., Danese, L., Franceschini, A., Genzel, R., Lawrence, A., Lemke, D., McMahon, R. G., Miley, G., Oliver, S., Puget, J.-L., and Rocca-Volmerange, B.: 1999, *MNRAS* **305**, 297

Gunn, K. F.: 1999, *Ph.D. thesis*, Department of Physics, University of Durham

Gunn, K. F., McHardy, I. M., Almaini, O., Shanks, T., Sumner, T. J., Muxlow, T. W. B., Efstathiou, A., Jones, L. R., Croom, S. M., Manners, J. C., Newsam, A. M., Mason, K. O., Serjeant, S. B. G., and Rowan-Robinson, M.: 2001, *MNRAS* **324**, 305

Gwyn, S. D. J. and Hartwick, F. D. A.: 1996, *ApJL* **468**, L77+

Haslam, C.: 2002, *Personal Website*

Helou, G., Soifer, B. T., and Rowan-Robinson, M.: 1985, *ApJL* **298**, L7

Ho, L. C., Filippenko, A. V., and Sargent, W. L. W.: 1993, *American Astronomical Society Meeting* **25**, 817

Ho, L. C. and Peng, C. Y.: 2001, *ApJ* **555**, 650

Hopkins, A. M., Mobasher, B., Cram, L., and Rowan-Robinson, M.: 1998, *MNRAS* **296**, 839

Ivison, R. J., Greve, T. R., Smail, I., Dunlop, J. S., Roche, N. D., Scott, S. E., Page, M. J., Stevens, J. A., Almaini, O., Blain, A. W., Willot, C. J., Fox, M. J., Gilbank, D. G., and Serjeant, S.: 2002, *MNRAS submitted*

Jannuzi, B. T., Elston, R., Schmidt, G. D., Smith, P. S., and Stockman, H. S.: 1994, *ApJL* **429**, L49

Jansky, K. G.: 1982a, in *Classics in Radio Astronomy*, pp 36–+

Jansky, K. G.: 1982b, in *Classics in Radio Astronomy*, pp 10–+

Jansky, K. G.: 1982c, in *Classics in Radio Astronomy*, pp 23–+

Kellermann, K. I., Sramek, R., Schmidt, M., Shaffer, D. B., and Green, R.: 1989, *AJ* **98**, 1195

Khachikian, E. Y. and Weedman, D. W.: 1974, *ApJ* **192**, 581

Lawrence, A. and Elvis, M.: 1982, *ApJ* **256**, 410

Longair, M. S.: 1966, *MNRAS* **133**, 421

Mather, J. C., Cheng, E. S., Eplee, R. E., Isaacman, R. B., Meyer, S. S., Shafer, R. A., Weiss, R., Wright, E. L., Bennett, C. L., Boggess, N. W., Dwek, E., Gulkis, S., Hauser, M. G., Janssen, M., Kelsall, T., Lubin, P. M., Moseley, S. H., Murdock, T. L., Silverberg, R. F., Smoot, G. F., and Wilkinson, D. T.: 1990, *ApJL* **354**, L37

Mauskopf, P. D. e.: 2000, in *ASP Conf. Ser. 217: Imaging at Radio through Submillimeter Wavelengths*, pp 115–+

McLeod, K. K. and Rieke, G. H.: 1995, *ApJL* **454**, L77

McLure, R. J. and Dunlop, J. S.: 2001, *MNRAS* **327**, 199

McMahon, R. G., Irwin, M. J., and Hazard, C.: 1992, in *X-ray Emission from Active Galactic Nuclei and the Cosmic X-ray Background*, pp 399–407

Miller, L., Peacock, J. A., and Mead, A. R. G.: 1990, *MNRAS* **244**, 207

Miyazaki, S., Sekiguchi, M., Imi, K., Okada, N., Nakata, F., and Komiyama, Y.: 1998, in *Proc. SPIE Vol. 3355, p. 363-374, Optical Astronomical Instrumentation, Sandro D'Odorico; Ed.*, Vol. 3355, pp 363–374

M$^{c}$Hardy, I. M., Gunn, K. F., Newsam, A, M., Mason, K. O., Page, M. J.and Takata,

T., Sekiguchi, K., Cordova, F., Jones, L. R., and Loaring, N.: 2002a, *MNRAS-submitted*

McHardy, I. M., Jones, L. R., Merrifield, M. R., Mason, K. O., Newsam, A. M., Abraham, R. G., Dalton, G. B., Carrera, F., Smith, P. J., Rowan-Robinson, M., and Abraham, R. G.: 1998, *MNRAS* **295**, 641

McHardy, I. M., Seymour, N. S., Newsam, A. M., Gunn, K. F., Mason, K. O., Page, M. J.and Takata, T., Sekiguchi, K., Cordova, F., and Sasseen, T.: 2002b, *MNRAS, in prep.*

Mushotzky, R. F., Cowie, L. L., Barger, A. J., and Arnaud, K. A.: 2000, *Nat* **404**, 459

Norman, C., Hasinger, G., Giacconi, R., Gilli, R., Kewley, L., Nonino, M., Rosati, P., Szokoly, G., Tozzi, P., Wang, J., Zheng, W., Zirm, A., Bergeron, J., Gilmozzi, R., Grogin, N., Koekemoer, A., and Schreier, E.: 2002, *ApJ* **571**, 218

Osterbrock, D. E.: 1981, *ApJ* **249**, 462

Penston, M. V. and Perez, E.: 1984, *MNRAS* **211**, 33P

Perley, R. L., Schwab, F. R., and H., B. A. (eds.): 1986, *Synthesis Imaging*, NRAO

Peterson, B. M.: 1997, *An introduction to active galactic nuclei* , Cambridge: University Press

Prandoni, I., Gregorini, L., Parma, P., de Ruiter, H. R., Vettolani, G., Wieringa, M. H., and Ekers, R. D.: 2000, *A&AS* **146**, 41

Prandoni, I., Gregorini, L., Parma, P., de Ruiter, H. R., Vettolani, G., Wieringa, M. H., and Ekers, R. D.: 2001, *A&A* **365**, 392

Press, W. H., Teukolsky, S. A., Vetterling, W. T., and Flannery, B. P.: 1992, *Numerical recipes in FORTRAN. The art of scientific computing*, Cambridge: University Press, —c1992, 2nd ed.

Rantakyro, F. T., Baath, L. B., Backer, D. C., Booth, R. S., Carlstrom, J. E., Emerson, D. T., Grewing, M., Hirabayashi, H., Hodges, M. W., Inoue, M., Kobayashi, H., Krichbaum, T. P., Kus, A. J., Moran, J. M., Morimoto, M., Padin, S., Plambeck, R. L., Predmore, R., Rogers, A. E. E., Schalinski, C., Witzel, A., Woody, D., Wright, M. C. H., and Zensus, A.: 1998, *A&AS* **131**, 451

Richards, E. A.: 2000, *ApJ* **533**, 611

Richards, E. A., Fomalont, E. B., Kellermann, K. I., Windhorst, R. A., Partridge, R. B., Cowie, L. L., and Barger, A. J.: 1999, *ApJL* **526**, L73

Richards, E. A., Kellermann, K. I., Fomalont, E. B., Windhorst, R. A., and Partridge, R. B.: 1998, *AJ* **116**, 1039

Roche, N. D., Lowenthal, J. D., and Koo, D. C.: 2002, *MNRAS* **330**, 307

Romero-Colmenero, E., Branduardi-Raymont, G., Carrera, F. J., Jones, L. R., Mason, K. O., McHardy, I. M., and Mittaz, J. P. D.: 1996, *MNRAS* **282**, 94

Sánchez, S. F. and González-Serrano, J. I.: 2002, *astro-ph/0209355*

Schmidt, M.: 1963, *Nat* **197**, 1040

Schmidt, M.: 1969, *ARA&A* **7**, 527

Shanks, T., Georgantopoulos, I., Stewart, G. C., Pounds, K. A., Boyle, B. J., and Griffiths, R. E.: 1991, *Nat* **353**, 315

Shanks, T., Stevenson, P. R. F., Fong, R., and MacGillivray, H. T.: 1984, *MNRAS* **206**, 767

Smail, I., Hogg, D. W., Yan, L., and Cohen, J. G.: 1995, *ApJL* **449**, L105+
Smail, I., Owen, F. N., Morrison, G. E., Keel, W. C. and Ivison, R. J., and J., L. M.: 2002, *ApJL, astro-ph/0208434*
Stark, A. A., Gammie, C. F., Wilson, R. W., Bally, J., Linke, R. A., Heiles, C., and Hurwitz, M.: 1992, *ApJS* **79**, 77
Taylor, G. B., Ulvestad, J. S., and Perley, R. A.: 2002, *The Very Large Array Observational Status Summary*
Telfer, R. C., Zheng, W., Kriss, G. A., and Davidsen, A. F.: 2002, *ApJ* **565**, 773
Urry, C. M. and Padovani, P.: 1995, *PASP* **107**, 803
Uttley, P., McHardy, I. M., and Papadakis, I. E.: 2002, *MNRAS* **332**, 231
White, R. L., Becker, R. H., Helfand, D. J., and Gregg, M. D.: 1997, *ApJ* **475**, 479
Wilson, A. S. and Colbert, E. J. M.: 1995, *ApJ* **438**, 62
Windhorst, R., Mathis, D., and Neuschaefer, L.: 1990, in *ASP Conf. Ser. 10: Evolution of the Universe of Galaxies*, pp 389–403
Woltjer, L.: 1959, *ApJ* **130**, 38
Wrobel, J. M.: 2000, *ApJ* **531**, 716

# Acknowledgments

First of all I would like to thank Ian M$^{c}$Hardy for being a wonderful supervisor, guiding me through this challenging, but rewarding project and for encouraging me through it all. I am appreciative of the opportunities I have had to go observing and the skills I have picked up. Secondly I would like to thank Katherine Gunn without whom this thesis would not have been possible especially for helpful comments on this work and for the great help in producing the wonderful pictures in the appendix. I would also like to thank her for being great company in the office and on observing trips. I have had much advice and help on understanding the ways of AIPS and I thank Tom Muxlow for his advice and for teaching me so much at Jodrell Bank. Many others have given useful comments to Ian and I on our deep radio survey; Robert Laing, Rick Perley, Eric Greisen, Steve Rawlings and Martin Hardcastle. I would also like to thank Christian Kaiser, Matt Page, Andrew Newsam and Boris Gänsicke for helpful comments over the last 3 years.

Mike Hill deserves thanks for keeping our computer system going, despite the many events that conspired against it this summer and earlier. Simon Harris also deserves much thanks and credit for helping me sort out any computer problem, large or small, with equal tenacity.

I would like to thank everyone in the Southampton Astronomy group over the last few years who have made it a joy to come to work in such a friendly environment. In particular I would like to Silas, Jon, Dave, Charlotte, Phil, Nick, Will, Carolyn, Anna and Simon for being great company at coffee and in the pub. I also thank my housemates Rich, Ross, Katie, Julie and Jim. I would like to thank the sultans for making my first year one of the best: Scott, Ben, Jo, Lizz and Anna. I thank all my other friends too from Reigate and Oxford.

Finally, I would thank my family for all their love and support, especially Peter, Grandad and Mary, Mum, Dad, Rachel and Charlotte. This is for you. They'll be a quiz later....

Nick October 2002